ADVANCING ULTRAHIGH PRESSURE LIQUID CHROMATOGRAPHY

THROUGH EXTENSIONS OF THEORY AND PRACTICE

by
J. Will Thompson

A dissertation submitted to the faculty of the University of North Carolina at Chapel Hill in partial fulfillment of the requirements for the degree of Doctor of Philosophy in the Department of Chemistry.

Chapel Hill
2006

Approved by:

Advisor: Professor James W. Jorgenson

Reader: Professor Gary L. Glish

Reader: Professor R. Mark Wightman

ABSTRACT

J. Will Thompson

ADVANCING ULTRAHIGH PRESSURE LIQUID CHROMATOGRAPHY

THROUGH EXTENSIONS OF THEORY AND PRACTICE

(under the direction of James W. Jorgenson)

Hydrodynamic Chromatography (HDC) was used as a purification method for packing materials (particles) in the micron to sub-micron range. Using HDC, the relative standard deviation for the size distribution of a batch of packing material was successfully narrowed from 33% to 16%. Subsequent chromatographic evaluation of this material, using capillary ultrahigh pressure liquid chromatography (UHPLC) showed significant improvement in performance and decrease in flow resistance over the unpurified material.

The capillary time-of-flight (CTOF) instrument was envisioned and constructed. This instrument uses the poiseuille flow principle to measure solution viscosity at pressures up to 4000 bar. Another embodiment of this instrument enabled the simultaneous measurement of diffusion coefficient and the solution viscosity up to pressures of 2000 bar. Diffusion coefficient and viscosity data obtained from this instrument allowed for reevaluation of previously collected UHPLC data and provided significant new insight into column performance.

Mobile phase compression was investigated as a source of artificially-inflated retention factor measurements for retained compounds in UHPLC. A special capillary column and dual-UV detector setup was utilized to investigate the actual effects of pressure on retention factor, independent of pressure drop and mobile phase compression. A model was also developed which predicted an artificial increase in retention factor from the linear velocity surge caused by mobile phase compression in isocratic UHPLC. The model and the experimental data collected were in good agreement.

The electrospray current density profiler was designed and built to monitor the intensity of ions inside an electrospray plume. This instrument was successful in differentiating between electrospray needles in good and poor condition, and was utilized to generate the first three-dimensional current density map of a nanoelectrospray plume. The profiler was used in the development of atmospheric pressure ion lenses, which were used to shape nanoelectrospray plumes with the goal of improving ion transmission into a mass spectrometer. Ion transmission into the first orifice of a mass spectrometer with nanoelectrospray was found to be roughly 40% without any lens present, which was a significant deviation from prior literature on ion for micro-electrospray conditions. Improvements in signal using the atmospheric ion pressure lenses were minimal.

the lab. Scott has also become a great friend, and golfing and poker buddy. Since we frequently see things from the opposite side of the coin, our research discussions are usually very fruitful. Working on projects (and occasionally practicing my dart or golf game) with John Eschelbach, Rachel Lieberman and Ted Kaiser has made the last five years fly by. Last but not least in the "coworkers" category, I'd like to thank Sutton's Drug Store, where we have enjoyed many a southern-style bacon cheeseburger for lunch, and probably have discussed more science than I care to admit.

Obviously, none of this is possible without family and God. Thanks to God, for His blessings make all things possible. I would like to thank my parents, Joe and Pat Thompson, for raising me to stay grounded and focused on my goals, and for their many years of care and dedication long before I was able to be out on my own. Caroline, thank you for teaching me how to be a good big brother. I know that I'm still working on it. To my church family, thank you for prayers heaped upon me that I could not have made it through the last five years without. Most importantly, I would like to thank my wife. Bryan, you are my constant source of inspiration, and I look forward to coming home to you every day. I love you.

TABLE OF CONTENTS

LIST OF TABLES

LIST OF FIGURES

LIST OF ABBREVIATIONS AND SYMBOLS

A	van Deemter A-term
A	y-intercept of linear portion of compression event in UHPLC
A	empirical constant in the equation for electric field, $= 0.667$
α	slope of viscosity as a function of pressure
$\mathring{A}$	Angstrom
AA	ascorbic acid
A_p	area of the probe electrode
A_T	total area of the ESI plume
B	van Deemter B-term
β	column phase ratio (stationary phase to mobile phase)
BEH	bridged-ethyl hybrid porous particles
BSA	bovine serum albumin
C	van Deemter C-term
χ	C-term dimensionless factor related to column packing
Cat	catechol, 1,2-dihydroxybenzene
C_m	analyte concentration in the mobile phase
C_s	analyte concentration in the stationary phase
CTOF	capillary time-of-flight
D	diffusion coefficient
D	distance between ESI tip and ground plane
δ	combination of terms that constitutes (kT/6pr)
d_c	diameter of a capillary

D_m	diffusion coefficient in the mobile phase
d_p	particle diameter
ΔP	pressure drop across a column
$d_{p,n}$	number-averaged particle diameter
$d_{p,v}$	volume-averaged particle diameter
$\Delta P1$	pressure sensor 1
$\Delta P2$	pressure sensor 2
d_{pore}	pore diameter of a packing material
Δt	time between detectors
ΔV	change in partial molar volume upon analyte sorption
E	electric field
ε	interparticle porosity
ESI	electrospray ionization
F	volumetric flow rate through a column
ϕ	peak capacity
γ	Interparticle porosity or "obstruction" factor
H	height equivalent to a theoretical plate
h	plate height in reduced parameters
η	Viscosity
η_0	viscosity at atmospheric pressure
H_{cm}	plate height contribution from mobile phase C-term
HDC	hydrodynamic chromatography
H_{min}	minimum plate height

HPLC	high pressure/performance liquid chromatography
HQ	hydroquinone, 1,4-dihydroxybenzene
i_p	electrospray current at the probe electrode
I_T	total electrospray current
J	analyte flux
J	current density inside an ESI plume
$\overline{J}$	average current density inside an ESI plume
k	equilibrium constant or partition coefficient
K	Boltzmann constant
κ	compression factor when using lens on ESI plume
k'	retention factor
k''	retention factor absent of compression effects
k_0'	y-intercept of k' versus pressure plot
L	column length
λ	A-term dimensionless factor related to column packing
λ	ratio of analyte radius to channel radius in HDC
L_m	length of the migration region
Mcat	4-methyl catechol, 4-methyl-1,2-dihydroxybenzene
MS	mass spectrometry
N	number of theoretical plates
NPS	nonporous silica
P	Pressure

PEEK	poly-ether ether ketone (machinable polymer)
PH	precipitated-hardened stainless steel
r	hydrodynamic radius of the analyte
R	ideal gas constant
r_0	radius of capillary (used in CTOF instrument)
r_A	analyte radius in HDC
R_c	channel radius for particle separation in HDC
Res	resorcinol, 1,3-dihydroxybenzene
RSD	relative standard deviation
ρ_{sk}	density of the particle skeleton
σ	standard deviation
σ_B^2	variance from B-term contribution (longitudinal diffusion)
σ_C^2	variance from C-term contribution (mass transfer)
SDS	sodium dodecyl sulfate
SIMS	secondary-ion mass spectrometry
σ_L^2	spatial variance
SPV	specific pore volume of a packing material
SSA	specific surface area of a packing material
σ_t^2	temporal variance
t	Time
T	Temperature
τ	ratio of analyte time to void time in HDC
τ	time constant for compression event in UHPLC

TFA	trifluoroacetic acid
t_m	migration time for an unretained species (dead time)
t_n	elution time of solute n
t_r	retention time
u	mobile phase linear velocity
UHPLC	Ultrahigh Pressure Liquid Chromatography
u_{opt}	optimum linear velocity
UPLC	ultraperformance liquid chromatography
UV1	UV detector 1
UV2	UV detector 2
v	velocity in reduced parameters
V	applied voltage
V_L	lens voltage
V_s	ESI (spray) needle voltage
W	median temporal peak width in a gradient elution chromatogram
w_b	temporal width at base for a chromatographic peak

1   INTRODUCTION

1.1   Van Deemter Theory and the Need for Ultrahigh Pressures

Early in the history of modern liquid chromatography, Calvin Giddings related the ultimate separating power and speed of a chromatographic separation directly to the available pressure drop for pushing fluid through the column.[1]   Based on this, Giddings suggested in 1966 that pressures of up to 10^4 bar (145,000 psi) might someday be used for chromatography. Since that time, chromatographers have been both trying to take advantage of higher pressures experimentally and looking theoretically at what changes might be expected at the ever-increasing pressures used for liquid chromatography.   One practical instrumentation development that is at least partially attributable to Giddings' vision is Ultrahigh-Pressure Liquid Chromatography (UHPLC).   Pioneered in the Jorgenson Lab, UHPLC has utilized pressures up to 7,000 bar with small particles (~1 μm) packed into capillary columns to generate very efficient separations.[2-5]

Of course, increasing the pressure at which a separation is performed does not itself improve efficiency.   It has been shown over the last four decades that the most straightforward way to increase efficiency and decrease analysis time is to decrease the particle size of the column packing material. The price to be paid for these improvements comes in the form of drastically increased pressure.   The efficiency of a particular chromatographic column is typically described with a parameter called the height equivalent

to a theoretical plate, or "plate height" for short, and is given the symbol H. Every

chromatographic column has a mobile phase flow velocity at which it performs most

efficiently, or gives the lowest plate height. Plate height for any given column as a function

of mobile phase flow velocity (u) can be described by the van Deemter equation:

$$H = A + \frac{B}{u} + Cu \qquad (1\text{-}1)$$

where A, B, and C are the coefficients for eddy diffusion, longitudinal diffusion, and mass

transfer, respectively.[6] Decreasing the particle diameter (d_p) affects both the A- and C-terms

of the van Deemter equation as can be seen in the following relationships:

$$A = \lambda d_p \qquad (1\text{-}2)$$

$$B = 2\gamma D_M \qquad (1\text{-}3)$$

$$C = \frac{\chi d_p^2}{D_M} \qquad (1\text{-}4)$$

where λ and χ are dimensionless factors related to the structure of the packed bed, γ is the

interparticle tortuosity or "obstruction" factor, and D_M is the diffusion coefficient of the

analyte in the mobile phase.[6] Due to the A- and C-term dependence, decreasing d_p causes a

linear improvement in separation efficiency per unit column length, and a linear increase in

the optimum mobile phase velocity.

To emphasize this theory graphically, hypothetical van Deemter curves for several

particle diameters were calculated using (1-1) through (1-4), and are presented in Figure 1-1.

For this figure values typical of "well-packed" columns were used for the dimensionless

parameters in equations (1-2) to (1-4); λ, γ and χ were approximated as 0.5, 1, and 0.2,

respectively.[6] The performance for commercial HPLC is indicated in red and encompasses

van Deemter curves for 3.5 μm to 5 μm particles, which are typical particle sizes in

commercial columns. UHPLC with 1 μm particles is shown as the black van Deemter curve. For a five-fold reduction in particle diameter, it becomes obvious from Figure 1-1 that you would expect a 5-fold reduction in minimum plate height (H). Also, the u value at which the column performs the best is five times higher for the UHPLC column, meaning that for the same column length the separation will occur in one-fifth the time.

The separation power of a chromatographic run can be described several ways. For isocratic separations, the total number of theoretical plates (N) is the preferred method. Theoretical plate count is a function of the plate height (H) and the column length (L):

$$N = \frac{L}{H} \tag{1-5}$$

For complex separations gradient chromatography is often utilized, where the mobile phase is changed gradually during the course of a chromatographic run. For gradient separations, the best measure of the separation power is peak capacity (ϕ), defined as:

$$\phi = \frac{t_n - t_1}{W} \tag{1-6}$$

where t_1 and t_n are the elution times of the first and last-eluting component of the mixture, respectively, and W is the median temporal peak width of the peaks in the elution window.[7, 8] In general, the higher the plate count (N) or peak capacity (ϕ) for a particular separation, the higher the number of components that can be resolved in a single chromatogram. Both of these parameters improve with decreasing the diameter of the packing material.

The catch with using smaller particles, of course, is that the pressure required to reach the optimum mobile phase velocity is inversely proportional to the particle diameter cubed. This fact comes from the combination of two relationships. The first defines the pressure required (ΔP) to drive flow at a set linear velocity (u) through a packed bed:

3

$$\Delta P = \frac{180 u \eta L (1-\varepsilon)^2}{d_p^2 \varepsilon^2} \tag{1-7}$$

where L is column length (cm), η is viscosity (poise), and ε is interparticle porosity. The second is a result of the van Deemter behavior of chromatographic columns, in that higher linear velocity is required to reach the optimum linear velocity (u_{opt}) for smaller particles:

$$u_{opt} \propto \frac{1}{d_p} \tag{1-8}$$

The combination of (1-7) and (1-8) results in the proportionality:

$$\Delta P_{opt} \propto \frac{1}{d_p^3} \tag{1-9}$$

Thus the development of UHPLC was born not out of the aspiration to utilize higher pressures, but out of the desire to access the efficiency gains that were theoretically possible with smaller stationary phase particles. Commercial instrumentation at the time research in UHPLC began was only capable of roughly 6,000 psi (400 bar). In the past ten years custom-built pumps have been designed in our lab and others to allow isocratic UHPLC at pressures as high as 100,000 psi (7,000 bar) and gradient UHPLC up to 60,000 psi (4,00 bar).[3, 9-19]

1.2   State-of-the-Art in UHPLC

As is obvious from the above discussion of van Deemter theory, particle technology has been central to the development of UHPLC. In addition to being the right size (~ 1 μm), the particles should have a narrow size distribution in order to provide efficiently packed columns. In addition, the particle material must have high mechanical strength to prevent bed collapse under high mobile phase stress.[20] The importance of these parameters to

4

chromatographic performance will be more fully discussed in Chapter 2. Until very recently the only particles available that met these criteria were nonporous silica spheres, which were used almost exclusively in UHPLC from 1997 to 2004.[3, 9, 11, 13, 16, 19, 21, 22] The appearance of the first sub-2 μm porous silica material suitable for capillary UHPLC occurred in 2003 when 1.5-μm BEH (bridged-ethyl-hybrid) material from Waters Corporation was made available to our lab.[17] Chapter 2 of this dissertation is based on research toward decreasing the size of the porous material available for UHPLC to 1 μm and smaller.

The excellent performance characteristics of the 1.5-μm BEH material as demonstrated in the Jorgenson lab led to its commercialization in a slightly larger particle size, as 1.8-μm particle packed columns with the name Acquity™ (2004). Waters Corporation recently made the first significant improvement in pumping technology in three decades, as the Acquity™ Ultra-Performance LC (UPLC) system is capable of roughly three times the pressure of a typical HPLC pump (15,000 psi, or 1000 bar). An expected performance comparison of UPLC (1.8-μm particles) with HPLC and UHPLC is shown in Figure 1-1. UPLC is significantly better than HPLC, but UHPLC using 1.0-μm particles shows another factor of 2 improvement in speed and efficiency over the newly-commercialized technology. Other column manufacturers have recently joined in the production of sub 2-um material, with six vendors introducing new particles in this size range at Pittcon 2005.[23] To date, only one other manufacturer makes a HPLC pump capable of producing linear gradients at a run pressure of 15,000 psi (Jasco XLC), and the newly-introduced Agilent 1200 Series claims 9,000 psi. Unfortunately, instrumentation for capillary or nano-scale LC is lagging somewhat behind large-bore analytical scale

instruments; the Waters nanoAcquity (2006) is the first elevated-pressure nano-LC instrument to reach the market, with a pressure limit of 10,000 psi.

1.3   The Importance of Capillary-Scale UHPLC

The recent developments in commercial column and pump technology serve to identify that the trend toward smaller particles in liquid chromatography has been extended once again. Citing the benefits of UHPLC and the recent commercial UPLC hardware advances to 15,000 psi capability, commercial chromatography at 45,000 psi should be possible in the future. It is likely that pressures at this level will only be useful for capillary columns, however. This is because joule heating in a column (Power, in watts) is the product of flow rate and pressure drop, and is based on the relationship:

$$Power = 0.1 F \Delta P \qquad (1\text{-}10)$$

Where the flow rate (F) is in *mL/sec* and the pressure drop (ΔP) is in *bar*. Joule heating can give rise to a radial temperature gradient, causing radial changes in solution viscosity and analyte diffusion coefficient, and thus degrade chromatographic performance.[19] Colon and coworkers have shown that when using 1.5-µm particles in a 1-mm i.d. stainless steel column, joule heating is not particularly problematic up to pressures of 20 kpsi.[24] Exceeding this column diameter or pressure drop would start to degrade the chromatographic performance. Above roughly 20,000 psi, small-diameter capillary columns become a much more attractive option because the volumetric flow rate (and thus heat generation) scales with the column diameter squared (see equation (1-10)).   In addition, the higher aspect ratio (surface area to volume) of capillaries assists heat dissipation. UHPLC in capillary columns up to 150-µm inner diameter has not shown any negative effects from joule heating, even with pressures as high as 80,000 psi.[11]

Another practical benefit for using capillary columns over traditional stainless steel is with applications requiring mass spectrometric detection. Nano-ESI-MS (flow rates below ~10^2 nL/min) has been shown to have drastically improved sensitivity over ESI-MS at higher volumetric flow rates. Capillary liquid chromatography has therefore become a very popular option for researchers interested in very complex samples that require interfacing with MS, particularly samples of biological origin (mixtures of proteins or metabolites). Part of the research described in this dissertation deals with optimizing the nano-ESI coupling between capillary UHPLC and mass spectrometry to give the best sensitivity and dynamic range possible. This research is more focused on mass spectrometry than chromatography, so for consistency it is presented at the end of the dissertation (Chapter 6).

1.4   Other Consequences of Ultrahigh Pressures

In addition to developing practical UHPLC instrumentation which allows the use of micron and sub-micron particles for liquid chromatography, the Jorgenson lab has also been interested in developing an in-depth understanding of chromatographic theory at ultrahigh pressures. For instance, it has been noted that observed C-terms for capillary UHPLC are somewhat higher than typical values for well-packed standard bore chromatography columns.[2, 5, 25] Possible packing structure effects as well as mobile phase compression at ultrahigh-pressures have been investigated in our lab, and have led to partial explanation of this elevated C-term.[5, 18] Other chromatographic parameters affected by pressure which are examined in this dissertation are viscosity (η), solute diffusion coefficient (D_M), and capacity factor (k').

1.4.1   Solution Viscosity

Knowledge of the mobile phase viscosity is important to the understanding of the behavior of chromatographic columns through the calculation of linear velocity (u) and interparticle porosity (ε) via Equation (1-7). Bridgman was the first to investigate the effects of extreme hydrostatic pressure on viscosity of fluids, and he found that up to pressures of ~7,000 bar almost all liquids exhibit a nearly linear increase in viscosity with pressure.[26] The notable exception is water at low temperatures (below 25°C), which actually exhibits the opposite trend (decrease in viscosity) from atmosphere to approximately 1,000 bar. Unfortunately for chromatographers, Bridgman and many others who studied viscosity at high pressures were mostly interested in pure liquids, as the physics of mixtures was often deemed too complex for interpretation. Therefore, ultrahigh pressure viscosity data for mixtures of acetonitrile/water as used in liquid chromagraphy was very difficult to find. Chapter 3 of this dissertation discusses a method which was developed to determine viscosity values of mixtures at pressures up to 50,000 psi (3500 bar).

1.4.2 Diffusion Coefficient

The importance of analyte diffusion coefficient (D_M) to the evaluation of column performance is indicated by its presence in the *B*- and *C*-terms of the van Deemter equation (see (1-3) and (1-4)). A helpful way to compare the performance of two or more columns run under different conditions is to use so-called *reduced* van Deemter parameters.[27] The reduced plate height (h) is defined as:

$$h \equiv \frac{H}{d_p}$$

(1-11)

The reduced linear velocity (v) is defined as:

$$v \equiv \frac{ud_p}{D_M} \qquad\qquad (1\text{-}12)$$

The reduced-parameter van Deemter equation can then be obtained by substituting into the combination of equations (1-1) through (1-4):

$$h = \lambda + \frac{2\gamma}{v} + \chi v \qquad\qquad (1\text{-}13)$$

Provided the correct d_p and D_M values were used in (1-11) and (1-12), the reduced parameters in (1-13) can then be used to make a fair comparison of columns packed with different sized particles. Atmospheric pressure diffusion coefficient values cannot be expected to be accurate at ultrahigh pressures because of the heavy dependence of D_M on solution viscosity and intermolecular forces, which will likely be disturbed at ultrahigh pressures. The desire to have accurate diffusion coefficients for column evaluation is the motivation behind the research presented in Chapter 4.

1.4.3   Capacity Factor

Chromatographic separation is enabled by the partitioning of an analyte to and from the stationary phase as the solute is carried along by the mobile phase in a column. Separation occurs because of small differences in solutes' relative affinity for the stationary phase and mobile phase. For a given solute, the partition coefficient (K) defines this affinity:

$$K = \frac{C_S}{C_M} \qquad\qquad (1\text{-}14)$$

where C_S and C_M are the equilibrium concentrations of the solute in the stationary and mobile phase, respectively. The partition coefficient is measured indirectly in a chromatogram in the form of a retention factor (k'). With respect to K, retention factor is defined as:

$$k' = K \frac{V_s}{V_m} \qquad\qquad (1\text{-}15)$$

where V_s and V_m are the volumes of the stationary and mobile phase in the column, respectively. Chromatographically, k' of a solute of interested is typically measured as a function of the solute retention time (t_r) and the void time of the column (t_M) in an isocratic run:

$$k' = \frac{(t_r - t_M)}{t_M}$$
(1-16)

The measured k' might change as a function of pressure for a number of reasons. First, elevated pressure might cause an actual change in the partition coefficient (K) or phase ratio (V_s/V_m) in the column. In addition, at the pressures used in UHPLC aqueous mobile phases are compressible, so this might cause an error in the measured t_r or t_M values. Chapter 5 examines k' as a function of pressure, and looks to discern between real changes in equilibrium constant and changes which are from an artifact due to mobile phase compression.

1.5   Dissertation Scope

As discussed above, ultrahigh pressure liquid chromatography is a technique which has come to some degree of maturity over the past decade. The aim of this dissertation, as indicated in the title, is to extend both the practice of UHPLC and our understanding of liquid chromatography at ultrahigh pressures. Practical aspects addressed in my dissertation research were the pursuit of suitable porous particles in the 1-μm and sub-micron range (Chapter 2), and the improvement of the sensitivity of the nanoESI-MS interface (Chapter 6). The general goal of both of these projects was to improve the applicability of UHPLC to very complex mixtures. Projects undertaken to more fully understand the special properties of chromatography at ultrahigh pressures were the measurement of viscosity (Chapter 3), analyte diffusion (Chapter 4), and mobile phase compression effects (Chapter 5).

1.6 References

(1)   Giddings, J. C. *Sep. Science* **1966**, *1*, 73-80.

(2)   MacNair, J. E.; Patel, K. D.; Jorgenson, J. W. *Anal. Chem.* **1999**, *71*, 700-708.

(3)   MacNair, J. E.; Lewis, K. C.; Jorgenson, J. W. *Anal. Chem.* **1997**, *69*, 983-989.

(4)   Mellors, J. S.; Jorgenson, J. W. *Anal. Chem.* **2004**, *76*, 5441.

(5)   Patel, K. D.; Jerkovich, A. D.; Link, J. C.; Jorgenson, J. W. *Anal. Chem.* **2004**, *76*, 5777.

(6)   Snyder, L. R.; Kirkland, J. J. *Introduction to Modern Liquid Chromatography*, 2nd ed. ed.; Wiley: New York, 1979.

(7)   Dolan, J. W.; Snyder, L. R.; Djordjevic, N. M.; Hill, D. W.; Waeghe, T. J. *J. Chrom A.* **1999**, *857*, 1-20.

(8)   Giddings, J. C. *Anal. Chem.* **1967**, *39*.

(9)   Tolley, L.; Jorgenson, J. W.; Moseley, M. A. *Anal. Chem.* **2001**, *73*, 2985-2991.

(10)   Shen, Y.; Zhang, R.; Moore, R. J.; Kim, J.; Metz, T. O.; Hixson, K. K.; Zhao, R.; Livesay, E. A.; Udseth, H. R.; Smith, R. D. *Anal. Chem.* **2005**, *77*, 3090-3100.

(11)   Patel, K. D.; Jerkovich, A. D.; Link, J. C.; Jorgenson, J. W. *Anal. Chem.* **2004**, *2004*, 5777-5786.

(12)   Monroe, M., University of North Carolina at Chapel Hill, Chapel Hill, NC, 2002.

(13)   MacNair, J. E.; Patel, K. D.; Jorgenson, J. W. *Anal. Chem.* **1999**, *71*, 700-708.

(14)   Xiang, Y.; Liu, Y.; Stearns, S. D.; Plistil, A.; Brisbin, M. P.; Lee, M. L. *Anal. Chem.* **2006**, *78*, 858-864.

(15)   Xiang, Y.; Maynes, D. R.; Lee, M. L. *J. Chrom A.* **2003**, *991*, 189-196.

(16)   Wu, N.; Lippert, J. A.; Lee, M. L. *J. Chrom A.* **2001**, *911*, 1-12.

(17)   Mellors, J. S.; Jorgenson, J. W. *Anal. Chem.* **2004**, *76*, 5441-5450.

(18)   Jerkovich, A. D.; Mellors, J. S.; Thompson, J. W.; Jorgenson, J. W. *Anal. Chem.* **2005**, *77*, 6292.

(19)   Jerkovich, A. D.; Mellors, J. S.; Jorgenson, J. W. *LC-GC* **2003**, *21*, 600-610.

(20)   Neue, U. D. *HPLC Columns: Theory, Technology, and Practice*; Wiley-VCH, Inc.:
         New York, NY, 1997.

(21)   Lippert, J. A.; Xin, B.; Wu, N.; Lee, M. L. *J. Microcol. Sep.* **1997**, *11*.

(22)   Anspach, J. A.; Maloney, T. D.; Brice, R. W.; Colon, L. A. *Anal. Chem.* **2005**, *77*,
         7489-7494.

(23)   Majors, R. E. *LC-GC* **2005**, *23*, 248-265.

(24)   Colon, L. A.; Cintron, J. M.; Anspach, J. A.; Fermier, A. M.; Swinney, K. A. *Analyst*
         2004, *129*, 503-504.

(25)   Knox, J. H. *J. Chrom A.* **2002**, *960*, 7-18.

(26)   Bridgman, P. W. In *The Physics of High Pressure*; Andrade, E. N. d. C., Ed.; G. Bell
         and Sons, Ltd.: London, 1931, pp 330-356.

(27)   Giddings, J. C. *Unified Separation Science*; John Wiley & Sons, Inc.: New York, NY,
         1991.
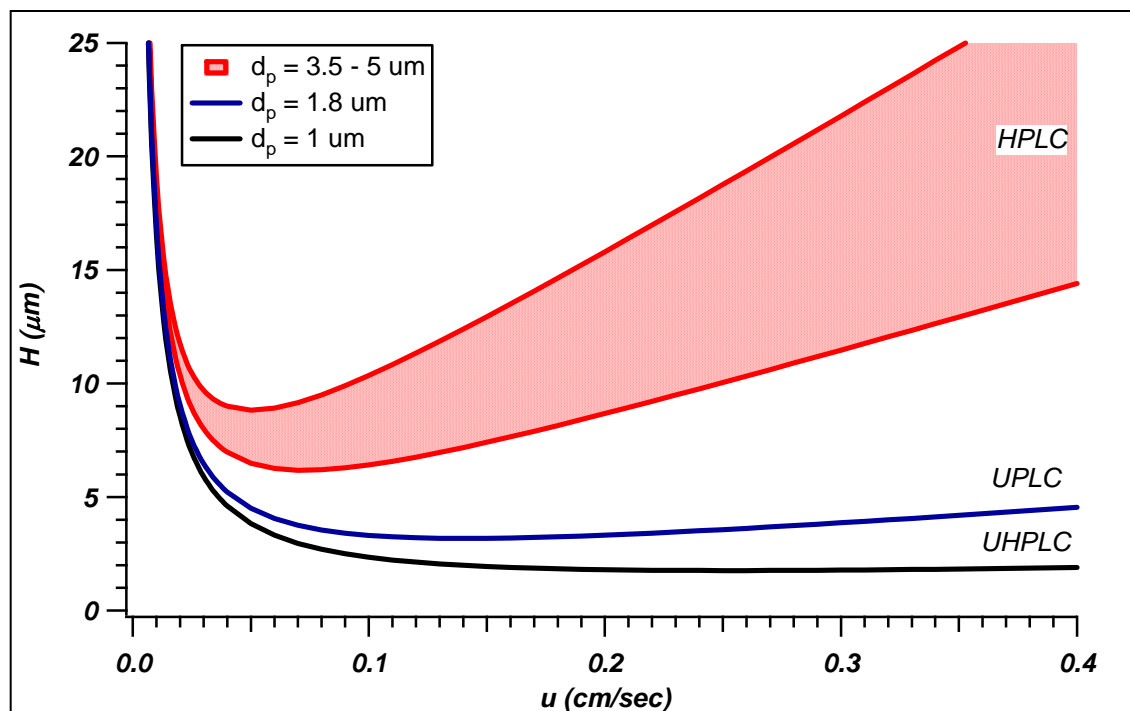
Figure 1-1: Hypothetical van Deemter curves for HPLC, UPLC, and UHPLC. Curves were calculated using Equations (1-1) through (1-4), with values of 0.5, 1, and 0.2 for λ, γ, and χ, respectively. D_M was set to 8.0×10^{-6} cm^{2}sec^{-1}. Particle sizes characteristic of the respective techniques are listed in the legend.

2   HYDRODYNAMIC CHROMATOGRAPHY FOR THE PURIFICATION OF MICRON AND SUB-MICRON PACKING MATERIALS

2.1   Introduction

Properties of the packing material used in a liquid chromatography column are the most important aspect of obtaining an efficient separation. According to Equations (1-1) through (1-4), as the particle size decreases more efficient separations are typically obtained; a rule-of-thumb from empirical observations of "well-packed" chromatography columns is that the plate height at the van Deemter optimum (H_{min}) should be roughly twice the particle diameter:[1]

$$H_{\min} \approx 2d_p \qquad\qquad (2\text{-}1)$$

In order for this rule to hold true, many factors pertaining to the packing material and the way it is packed into a column must be controlled. Column packing density and the size distribution of the particles play a significant role in obtaining a chromatographic column that performs well. Packing density is largely a function of the pressure used to pack a column, and the desire for densely-packed columns is the main reason most commercial columns are packed at pressures well above their highest intended run pressure.[1] As will be explained more fully later, a narrow particle size distribution is thought to be more favorable for generating efficient columns.

UHPLC has been successful in obtaining very efficient separations (by the standard set forth in Equation 2-1) for nonporous silica particles as small as 0.9 μm, and porous particles as small as 1.5 μm.[2-5] Development of porous packing materials useful for UHPLC in our lab has been done through collaboration with Waters Corporation. Since 2002, scientists at Waters have provided us with a variety of porous particles with many different characteristics, including silica type, particle diameter and distribution, pore diameter, and surface modification (stationary phase). A complete list of the particles obtained through this collaboration and their important characteristics is presented in Appendix A.

The work in this chapter is dedicated toward the goal of obtaining porous stationary phase particles in the micron and sub-micron size-range by means of hydrodynamic chromatography. The reasons for wanting porous particles of this size and the details of the research performed using hydrodynamic chromatography as a size-classification technique will be discussed.

2.1.1 Particles Used in UHPLC

Figure 2-1 shows 1.0-μm nonporous silica particles, the material that has been the most extensively used for UHPLC in the literature.[4, 6-9] Nonporous silica was very attractive to early experimenters in UHPLC because it has extreme strength (from its nonporous nature) and a narrow size distribution (~2% RSD of d_p). The narrow size distribution is a result of the synthesis, commonly referred to as the Stöber process.[10] This synthesis is a one-step condensation of tetraethylorthosilicate in a water/ethanol/ammonia mixture. Highly monodisperse nonporous silica particles between 0.05 μm and 2 μm in diameter can be synthesized in this manner. The characteristics of common nonporous silica particles historically used for UHPLC in our lab are also given in Appendix A.

The main drawback of using nonporous silica particles for chromatography is that they have a very low surface area. As a result only a relatively small amount of analyte can be loaded onto the column before the peaks broaden due to mass-overloading. The relative loadability of a packing material can be expressed in the form of a column's phase ratio (β):

$$\beta = (1 - \varepsilon) \frac{SSA}{SPV + \dfrac{\varepsilon}{\rho_{sk}}} \qquad (2\text{-}2)$$

where SSA is the specific surface area of the particles (m^2/g), SPV is the specific pore volume of the particles (mL/g), ε is the interparticle porosity and ρ_{sk} is the skeleton density of the particle material (g/mL). Phase ratio (β) is described as the surface area of the packing material per unit volume of mobile phase in a column. Assuming $\varepsilon = 0.4$, a column packed with 1-µm nonporous silica particles will have $\beta \approx 9$ m^2/mL. We have observed detrimental column overloading when performing gradient LC-MS of complex mixtures; when a larger quantity of analyte is injected onto a nonporous silica column to improve MS signal the chromatographic efficiency suffers substantially.[11]

Because porous particles have much higher surface area, they typically have phase ratios on the order of 200 m^2/mL packed bed or higher.[1] The first sub 2-µm porous particles appropriate for use with UHPLC, called bridged-ethyl-hybrids (BEH), were provided to us by the Waters Corporation in 2003. Figure 2-2 is a SEM image of the 1.5-µm BEH particles, which were shown to have roughly 30 times the loading capacity of 1.0-µm nonporous silica, and gave excellent chromatographic results.[2, 12] Detailed characteristics for these BEH particles (lot KHG-6-55) are listed in Appendix A.

The synthesis procedure for porous BEH material, as with most porous chromatographic media, results in a large amount of particle size heterogeneity.[13] Figure 2-3

shows a batch of BEH particles that has not been size-classified. The particle sizes in this SEM image range from ~5 μm to < 0.1 μm. In order to be used for chromatography, the particles must then be size-classified into smaller size ranges. We received several batches of BEH material from Waters Corporation with average particle sizes between 0.5 and 0.9 μm which contained a significant amount of fines (very small particles), resulting in size distributions of roughly 30% RSD. Neue has suggested that chromatographic material should have a relative standard deviation (RSD) of 15% or less to provide efficient chromatography.[1] We have therefore been interested in size-classifying these particles in order to generate 1-μm BEH particles with a narrow size distribution for use in UHPLC.

2.1.2 Size-Classification Methods for Particles in the 1-μm Size Regime

As can be seen by comparing the BEH particles in Figures 2-2 and Figure 2-3, some form of size-classification was required in order to get the 1.5-μm BEH particles into a narrow size distribution. Several particle size-classification techniques are frequently used in the chromatographic particle industry, but the exact procedures are closely guarded trade secrets. A brief overview of several of the methods is given below, but first it is important to understand why a narrow size distribution is favorable.

The particle size distribution affects two main chromatographic performance characteristics, efficiency and flow resistance. In general, the flow resistance of a chromatographic column scales with the simple number-averaged particle diameter ($d_{p,n}$), which is calculated by the formula:

$$d_{p,n} = \frac{\Sigma d_{p,i} n_i}{\Sigma n_i} \tag{2-3}$$

The performance of a column (plate height) has been correlated to the volume-averaged particle diameter ($d_{p,v}$), which is an average that takes into account the fact that the larger particles take up more volume than the smaller ones:[1]

$$d_{p,v} = \frac{\sum d_{p,i} d_{p,i}^3 n_i}{\sum d_{p,i}^3 n_i} \qquad \text{(2-4)}$$

For a batch of particles that are all exactly the same size, $d_{p,v}$ and $d_{p,n}$ would be equal, which would seem to be the ideal situation. For any real particle size distribution, $d_{p,v}$ will be larger than $d_{p,n}$. Therefore, for a column containing a large range of particle sizes the unfortunate scenario results where performance scales with the larger particles, while the flow resistance more closely reflects the smaller particles.

Classic methods of preparative size-classification that are effective in the 10^{-4} to 10^{-7} m size regime are sieving, sedimentation, and elutriation.[14] Using a series of metal mesh screens in tandem, sieving can be performed to give fairly narrow size distributions (RSD~20%) for particles down to approximately 10 μm.[14] A liquid phase sieving method utilizing track-etched polycarbonate membranes was recently developed in our lab and was shown to be capable of purifying particles in the 1-2 μm size-range.[5] However, this method was only able to generate very small quantities of particles and the porous particles showed signs of fragmentation because of the ultrasonication used to keep the particles suspended.

All sedimentation methods employ the principle that the gravitational force exerted on a particle is proportional to its diameter cubed. Sedimentation in a static fluid offers a simple method of particle size determination or purification for particles in the 1 to 100 μm range.[14] However, this method is slow because very small particles have slow settling speeds, and obtaining narrow size-cuts can be difficult. Centrifugation is a method

developed to increase the gravitational force on the particles and therefore increase the speed and efficiency of the separation. Centrifuges used in tandem have been used to separate particles from greater than 10 μm down to less than 10 nm.[14] Centrifugation suffers from the limitation that obtaining narrow size-cuts of particles requires expensive specialized equipment.

Elutriation is a specialized sedimentation technique in which particles are suspended in a liquid flow that is exactly opposite to their sedimentation velocity. To do this, a long funnel-shaped reservoir is used and solvent is introduced from the bottom. The liquid flow velocity is different at each point in the reservoir because of the gradually increasing diameter, and therefore particles in the reservoir of different size each have a specific equilibrium position where the forces are balanced. Particles between roughly ~2 μm and 100 μm can be separated in this type of device.[14] By fine adjustment of the liquid flow rate, very narrow size distributions of particles (RSD ~ 10%) can be obtained via elutriation. The disadvantage for the technique is that the settling velocity for particles near 1 μm is so slow that it becomes impractical.

Hydrodynamic chromatography (HDC), also called "separation by flow", was demonstrated by Hamish Small in the early 1970's to be useful for size-classification of colloid suspensions containing particles from roughly 50 nm to 3 μm in diameter.[15, 16] Although HDC has been used as an analytical technique for size-classification, no reports in the literature were found using HDC as a technique for preparative purification. Because of the difficulties associated with using the previously discussed techniques to purify particles in the micron to sub-micron range and the relatively small quantities of material needed to pack capillary columns, HDC was investigated as a method for this purpose.

2.2   Hydrodynamic Chromatography

HDC is a separation method based on the parabolic shape of the laminar flow profile in a tube or between the particles in a packed bed. The "separation-by-flow" mechanism was first presented in theory by DiMarzio and Guttman, and subsequently demonstrated by H. Small.[15-19] HDC is akin to size-exclusion chromatography (SEC) in that the largest analytes elute first, but the separation mechanism is completely different. In SEC, analyte molecules are separated by their comparative ability to sample the pore volume of a large-pore stationary phase; the largest analytes (which have limited diffusion into the pores) are eluted first. SEC therefore requires a relatively high solute diffusivity for efficient separations, and is restricted to a maximum analyte size of a few hundred kilodaltons (~10 nm, or a large protein). HDC has no such dependence on solute diffusivity because the separation occurs entirely in the mobile phase, and therefore is applicable for analytes from small proteins to ~3 µm colloids.

2.2.1   Open-Tube HDC

As stated above, HDC separates particles by size based on laminar flow of mobile phase in a tube. Figure 2-4 is a schematic showing how separation-by-flow is thought to occur in an open tube. In this figure, the blue dotted line represents the laminar flow profile of pressure-driven flow in a capillary and the red dots represent analyte particles of different sizes. The smallest particle is able to sample all flow regimes in the capillary, including the slow-flow region near the capillary wall. The larger particles are excluded from the slow-flow region near the wall and therefore experience a higher average flow rate. The "exclusion" model therefore predicts the elution order of largest to smallest particles.[20-23] A

small-molecule marker is typically used to measure the dead-time (t_m) of a HDC column, and the elution time of other analytes (t_r) is related to the void marker by the ratio, tau (τ):

$$\tau = \frac{t_r}{t_m} \qquad (2\text{-}4)$$

τ therefore always has a value less than one.[23]

The diameter of the open tube determines the dynamic range of the separation, or the target analyte size-range. Analytes that are too large will not undergo proper HDC if they either clog the tube or sample more than half of the laminar flow profile. Analytes that are too small effectively sample all the flow-regions and will not be resolved from the small-molecule void volume marker. The ratio of the analyte radius (r_A) to capillary radius (R_c) is given the symbol λ and defined as:

$$\lambda = \frac{r_A}{R_c} \qquad (2\text{-}5)$$

In general, the useful dynamic range of λ for a tube of any given R_c is $0.02 < \lambda < 0.3$.[21] Capillary HDC has been demonstrated using capillary diameters from less than 1 μm to greater than 500 μm.

The optimal capillary radius (R_c) can be calculated by rearranging (2-5) and inserting the target analyte size. The analyte particles we are interested in purifying range from approximately 200 nm to 1.5 μm in diameter. Assuming $\lambda = 0.25$ for the largest particles ($r_A = 0.75$ μm), the minimum limit of R_c is calculated to be 3 μm. Assuming $\lambda = 0.02$ for the smallest particles ($r_A = 0.1$ μm), the maximum limit of R_c is calculated to be 5 μm. We would therefore expect to be able to perform size-classification of our particles via HDC with an open-tube capillary with diameter roughly 8 μm. However, because of the low

throughput, open-tube HDC is typically an analytical tool and is not suited for generating a sufficient quantity of particles to use as packing material.

2.2.2 Packed-Column HDC

As first demonstrated by Small, a packed column can be used to perform HDC because a laminar flow profile similar to that shown in Figure 2-4 is generated between the particles of the packing material.[15, 16, 19] The hydraulic radius of the "capillaries" generated by the space between the packing material is also denoted R_c:

$$R_c(packed) = \left(\frac{\varepsilon}{1-\varepsilon}\right)\frac{d_p}{6}$$

(2-6)

Where d_p is the diameter of the packing material and ε is the interparticle porosity.[24, 25] Using $\varepsilon = 0.4$ and substituting (2-6) into (2-5), the packing material diameter suitable for packed-column HDC of our analyte particles (200 nm to 1.5 μm) is 36 μm.

An exclusion model similar to that applied to open-tubular HDC can be applied to packed-column HDC.[19, 23] Figure 2-5 is a schematic for visualization of this model; it can be seen in the figure that the smaller red particle can sample a larger amount of the volume between the particles, and therefore its elution volume (and retention time) will be higher than for the larger particles. Cheng developed a model for "surface and geometrical exclusion" that enables calculation of the elution time (τ value) of an analyte in an HDC column, given the values for r_A, R_c, ε, and sphere coordination number n:[23]

$$\tau = 1 - \left[\left(\frac{1-\varepsilon}{\varepsilon}\right)\left(3\frac{r_A R_c^2}{R_c^3} + 3\left(1-\frac{n}{4}\right)\frac{r_A^2 R_c}{R_c^3} + \left(1-\frac{n}{2}\right)\frac{r_A^3}{R_c^3}\right)\right]$$

(2-7)

For a typical random-packed column ε and n can be approximated as 0.4 and 8, respectively. R_c is calculated for any given packing material diameter using (2-6). Using (2-7), a

theoretical particle diameter versus τ plot can be calculated. Figure 2-6 shows such a plot for a HDC column packed with 34 μm particles. The τ value is only carried out to a minimum of 0.8 because this is where the analyte particles start to become too large to properly elute through the packed bed.[25] From this model it appears that a column packed with 34 μm particles would be effective at performing HDC for particles in the 1.5 μm to ~300 μm size range.

Packed-column HDC was originally applied as an analytical tool for the size-classification of different polymers.[15, 16, 19] This application typically used ~20 μm ion exchange resins packed into columns several meters long, and an aqueous mobile phase containing a small amount of surfactant and phosphate buffer (pH~7). More recently, HDC has employed nonporous silica particles as small as 1 μm for the separation of very small polystyrene standards and macromolecules.[24-27] A commercial instrument called PL-PSDA (Polymer Laboratories, UK) is now available which uses two different "cartridges" packed with nonporous beads to perform particle size analysis with 0.1% accuracy from 5 nm to 3 μm.[28]

2.2.3 Efficiency, Peak Capacity and Dynamic Range in Packed Column HDC

Efficiency and dynamic range are intertwined in HDC in an interesting way that is not typical of other chromatographic methods. The particle size of the packing material determines the target range of analytes to be separated, as shown in equations (2-5) through (2-7). Typical minimum plate heights in packed-column HDC are slightly better than that expected for HPLC, with H_{min} usually reaching ~$1.6d_p$ as opposed to ~$2d_p$ for HPLC.[26] Unlike HPLC, the particle diameter cannot be reduced in HDC in order to improve efficiency of a particular separation, because of the direct dependence of the separation mechanism on

particle diameter. Therefore the only way to improve the number of theoretical plates for HDC is to increase the column length. The typical byproduct of this predicament would be that the run times become longer for applications requiring more efficient HDC separations.

Fortunately, the van Deemter curve for HDC of large analytes in packed columns is almost flat; this is a result of the combined effect of low analyte diffusivity (thus a low B-term) and a conspicuously low C-term.[26] The reason for the C-term being almost non-existent for packed-column HDC is not well understood but has been observed consistently in the literature.[24, 26, 27, 29, 30] The benefit of the very low C-term, of course, is that the columns can be run at high flow rate without losing efficiency. The limiting factor for speed in HDC separations of colloids is generally from either pressure limitations of the equipment used or fear of shear degradation of the analytes at high mobile phase velocity.

Peak capacity is limited in HDC, since the separation occurs in the region between $0.8t_m$ and t_m for every column. HDC is performed isocratically, so improvement in peak capacity can only be made by increasing the efficiency of the column. Therefore by approximating the separation window as $0.2t_m$ and substituting in equation (1-6) for peak capacity, we find that peak capacity in HDC is:

$$\phi_{HDC} \approx \frac{0.2t_m}{W} \qquad (2\text{-}8)$$

Width at the base (W) can be approximated from the number of theoretical plates (N) and the dead time of the column:[14]

$$W \approx \frac{4t_m}{\sqrt{N}} \qquad (2\text{-}9)$$

Substituting (2-9) into (2-8) we reach a simplified expression to estimate the peak capacity for an HDC column:

$$\phi_{HDC} \approx 0.05\sqrt{N} \qquad\qquad (2\text{-}10)$$

For HDC columns with 5,000 and 50,000 plates, the expected peak capacity is therefore 3.5 and 11.2, respectively.

It is obvious from the above peak capacity calculation that HDC is not well-equipped to perform separations of very complex mixtures. However, the fact that all separation occurs prior to the dead time can be used to gain a throughput advantage for preparative methods. Multiple injections can be performed within the dead-time of the column (up to ~ 4) such that over a large number of injections, essentially four separations can be performed per column void time.

2.3   Experimental

2.3.1   HDC Instrument Configuration

A Waters 600 Quaternary HPLC pump (Waters Corporation, Milford, MA) was used for solvent delivery. Typical flow rates were between 2.5 and 10 mL/minute. Injections were performed with either a 0.42 mL, 0.8 mL, or 1.0 mL sample loop on a VICI electronic injector (Valco Instruments Co., Inc.). HDC columns (described below) were attached to the injector using 0.005 in. i.d. PEEK tubing. The outlet of the column was coupled to a ~1 m section of 600 μm o.d., 300 μm i.d. fused-silica capillary (Polymicro Ltd., Phoenix, AZ) with a window burned in the polyimide coating to allow detection. Detection was performed by UV absorbance/turbidity using a Linear UVis 200 detector equipped with a capillary flowcell (Thermo Electron Corp., Waltham, MA). For analyses using acetone as the mobile phase, detection was performed at 330 nm and 9-methyl anthracene was used as the deadtime marker. When aqueous buffers were used, detection was performed at 214 nm and ascorbic

acid was used as the deadtime marker. The fused silica capillary was then run to either an automated fraction collector (Fraction Collector II, Waters Corp.) or to waste.

2.3.2   HDC Column Packing

Based on the calculations as shown in Section 2.2.2, 36 μm particles were determined to be the optimum size packing material for our HDC separation. Glass beads listed as "32-38 μm" were ordered from Whitehouse Scientific (part number GP0035, Whitehouse Scientific Ltd, Chester, UK). The particles were sized by SEM to be 34 ± 6 μm. The beads contained fines from the sieving process, which were removed by 5 suspensions and sedimentation in water. The beads also contained metal shavings presumably from the metal mesh used for sieving, and these were removed using a magnetic stir bar. The particles were suspended in water and stirred with the stir bar, the bar was removed and shavings discarded, and the process was repeated until no shavings were present upon removing the stir bar. The particles were then rinsed several times with ~200 mL methanol, and placed in a 100°C oven to dry overnight. Prior to packing, the particles were poured through a 150 μm metal sieve to break up aggregates.

After attempts to slurry-pack the particles in water and methanol, dry packing was found to give the best chromatographic results. The beads were dry-packed into 25-mm i.d. glass columns (Omnifit, Western Analytical, Wildomar, CA), by pouring approximately 5 cm of material into the column and tapping vertically until settling ceased. The process was repeated until the desired column length was reached (data from both ~17 cm and ~46 cm columns is reported here). An adjustable endfitting containing a 25 μm porous polyethylene (PE) frit was then tightened in place to remove as much dead-volume as possible. The shortest length possible (typically ~40 cm) of 0.0625 in. i.d. PEEK tubing was used to couple

the inlet of the column to the injector. The tubing was run down inside the adjustable inlet fitting until it just rested on the inlet frit, in order to remove as much extra-column volume as possible. The column was filled with water from the inlet at a flow rate of ~2 mL/minute, with the inlet down so that air could escape from the column outlet. The flow rate was increased to approximately 10 mL/min for 20 minutes to promote bed compression. If a gap was generated at the column inlet during this time, it was removed by tightening the adjustable inlet fitting.

2.3.3   Column Preparation, Acetone Mobile Phase

It was desirable that HDC purifications of the C18-bonded BEH material be performed in acetone because that is the preferred packing solvent for the BEH material. Therefore a method of HDC column pretreatment was developed which allowed for acetone to be used as the mobile phase. For conditioning, the column was flushed with approximately five column volumes of the following mobile phases, starting with 50 mM ammonium acetate with 0.25 M NaCl at pH 5 in water, followed by 2.5 mM sodium dodecyl sulfate in water, followed by DI water, and finally acetone. The column was allowed to sit overnight in acetone prior to use.

2.3.4   Column Preparation, Aqueous Mobile Phase

As will be presented in the results, the column pretreatment followed by using acetone mobile phase had a limited time over which it was useful. After approximately 15-20 runs the column had to be reconditioned because of inconsistent retention. Experiments were also performed with aqueous mobile phase containing surfactant, as is more typical in the literature. For these experiments, the column was equilibrated in a mobile phase of 0.5 mg/ml sodium dodecyl sulfate (SDS) with between 5 mM and 10 mM sodium phosphate

dibasic, at pH 7.0.   Equilibration was allowed for roughly 10 column volumes prior to analyte injection.

2.3.5   Chemicals

ACS grade sodium chloride (NaCl) and sodium phosphate monobasic (NaH_2PO_4), and HPLC grade acetone from Fisher Scientific (Fair Lawn, NJ) were used as received. Ammonium acetate (NH_4CH_3OOH) from EM Sciences (Gibbstown, NJ) and ultra pure sodium docecyl sulfate (SDS) from MP Biomedicals, Inc (Solon, OH) were used as received. Water for mobile phases was obtained from a Nanopure ultrapure water system (Barnstead International, Dubuque, IA).   Ascorbic acid and 9-methyl anthracene, used as deadtime markers, were used as received from Aldrich Chemical Company (Milwaukee, WI).

2.3.6   Size Standards and Analyte Particles

For experiments performed in acetone mobile phase, all particles were bonded with C18. C18-bonded particle size standards had to be used with acetone mobile phase because acetone and silica have a very similar refractive index, such that the bare silica particles were invisible to detection by turbidity.   Nonporous silica standards of 0.6-μm and 1.05-μm diameter were synthesized in our lab via the Stöber process,[10] and bonded with octadecyltrimethoxysilane (C18) using a method described previously.[5]   C18-bonded nonporous silica with 1.5-μm diameter was from Micra Scientific (EiChrom Industries, Inc., Darien, IL).   The analyte particles were "0.8 μm" BEH that had been bonded with C18 stationary phase, with a $d_{p,n}$ of 0.76 ± 0.26 μm measured by SEM (Waters Corp., Milford, MA).   All particles were suspended in acetone at concentrations between 3 mg/mL and 10 mg/mL via vortex and sonication.

For experiments performed in SDS-water mobile phases, the size standards used were bare silica. Nonporous silica standards of 0.3 μm, 0.6 μm, and 0.9 μm were synthesized in our lab using the Stöber process.[10] Nonporous silica with 1.5-μm diameter was from Micra Scientific (EiChrom Industries, Inc., Darien, IL). The analyte particles were the same "0.8-μm" BEH material as mentioned above. Nonporous bare silica standards were easily suspended in the SDS-water mobile phase via vortex and sonication. The C18-bonded BEH particles were very difficult to suspend in the aqueous mobile phase, so the following process was used: The particles were first suspended at a concentration of ~10-15 mg/mL in acetone. A equal amount of the SDS-water mobile phase was added to the acetone-particle slurry, and the mixture was vortexed. The slurry was then centrifuged, mobile phase decanted, and the particles resuspended in a mixture with a slightly higher SDS-water to acetone ratio. The process was repeated (~6X) until the particles were suspended in SDS-water only, and the solution was sonicated to provide final suspension of the particles. Once the C18 particles had sorbed enough SDS into the stationary phase, the BEH particles proved to be very well-suspended in the SDS-water mixture. However, it was impossible to know the final particle concentration exactly because of the losses associated with the many steps in the suspension process.

2.3.7 Particle Size Analysis

Images of nonporous silica standards, as well as pre- and post-purification analyte particles were taken using one of two Scanning Electron Microscopes. Early size analyses were performed using a Cambridge S200 SEM in the UNC Dental School. This instrument has reported resolution of 5-10 nm. Later experiments used a Hitachi 4700 FE-SEM in the UNC Department of Chemistry. This instrument has a resolution between 1.5 and 2.1 nm.

Pictures were evaluated using Image J image analysis software (http://rsb.info.nih.gov/ij/) to measure the particles. Statistical analysis and graphical presentation of the measurements was performed in Microsoft Excel and Igor Pro 4.08 (Wavemetrics Inc., Lake Oswego, OR).

2.4   Results

2.4.1   HDC Packing Material and Predicted Chromatograms

Figure 2-7 shows an SEM image of the "32-38 μm" glass beads purchased for use as packing material in the HDC column. Analysis of this image and others revealed a $d_{p,n}$ for these particles of 34±6 μm. To compare this packing material to the analyte particles we intending to separate, an SEM image was taken with both 34 μm glass beads and sub-micron BEH material on the same SEM stub. Figure 2-8 is an image which helps to visualize how an HDC separation might take place in a packed column. The three large particles in the image are oriented much as they might be in a packed bed. The voids between them therefore are probably similar to that in an HDC column packed with this material. It is obvious that the analyte particles are much smaller than these voids, but that the largest of the analyte particles would be excluded from the regions near the edges of the voids, much like was hypothesized in Figure 2-5.

Using equations (2-5) through (2-7), hypothetical chromatograms were generated for columns packed with 34 μm glass beads, with different N values. For each of four different column lengths equation (2-1) was used to give a conservative estimate of the plate height and then (1-5) was used to calculate N. The void time was calculated using an inner diameter of 25 mm, with $\varepsilon = 0.4$ and a flow rate of 5 mL/min. The width at base for the peaks in the chromatogram was calculated for a dead-time marker using (2-9), and the retention time for

each analyte particle diameter was calculated using (2-7). Chromatograms were modeled for five different diameters in addition to the dead-time marker:, 0.1, 0.3, 0.6, 0.9, and 1.2 μm. The signal intensities at each time position for the chromatograms were then added to give a hypothetical chromatogram if all five particle sizes were injected on the column.

The resulting chromatograms are presented in Figures 2-9 (A) through (D) for plate counts of 4600 (25 cm), 9200 (50 cm), 18400 (100 cm) and 36,800 (200 cm), respectively. The individual particle chromatograms are shown as red traces, and the combined chromatograms are shown in blue. Obviously the best resolution between the particle sizes comes with the highest plate count column. Baseline resolution of particles between 1.2 and 0.3 μm was predicted to occur by the time the plate count reached 18,600 (Figure 2-9C). Because the dynamic range for the packing material selected is optimized for these larger particles, the 0.1 and 0.3 μm particles were still not baseline resolved with 36,800 plates (Figure 2-9D) and the 0.1 μm particles still largely coelute with the deadtime marker. On the other hand, even with the low plate count of 4600 as shown in Figure 2-9A, 1.2 μm particles are expected to be baseline resolved from the 0.6 μm particles. Using a fraction collector, we expected from these simulations to be able to use a ~20-cm long HDC column packed with 34 μm particles to drastically improve the size distribution of BEH porous particles. The target product BEH particles had a nominal diameter near 1 μm, but contained a large amount of material less than 0.7 μm that we desired to remove.

2.4.2　HDC of　Particle Size Standards in Acetone

After pretreatment of a 17-cm HDC column as described in 2.3.3, injections of several C18-bonded nonporous silica particle size-standards were performed, each with 9-methyl anthracene as a deadtime marker. Figure 2-10 shows an overlay of three particle

standard chromatograms, with 0.6-μm, 0.9-μm, and 1.5-μm nonporous silica. For all three injections, the deadtime marker gave N ~ 3,000, which corresponds to H~56.7 μm. The reduced plate height therefore was ~1.6, which corresponds to what has been seen in the literature for packed-column HDC.[26, 30] The plate counts for the size-standards was somewhat lower, which can be explained by the fact that the retention time for larger species is shorter, as well as the possibility of some polydispersity in the size of the standards.[26] Note also that each peak in this chromatogram is somewhat tailed; we believe this arises from inefficient distribution of the sample at the head of the column near the inlet frit, and possibly also inefficient collection of the eluent at the outlet frit. It should be noted that although similar amounts of each particle size were injected, the signal was much lower for the 1.5-μm particles. The reason for this is unknown, but it may have something to do with different particle synthesis or bonding procedure since the 1.5-μm particles were purchased and the 1.05 and 0.6-μm particles were synthesized in our lab.

From these chomatograms it can be seen that there is some overlap in the elution profile for the 1.5-μm and 0.6-μm particles, even though these were predicted to be completely resolved in the geometric exclusion model. The τ values for the three analytes used with our HDC column do not exactly follow the theory; the actual τ values were 0.90, 0.867, and 0.855 for 0.6-μm, 0.9-μm, and 1.5-μm particles, respectively. Exclusion theory as modeled in Figure 2-6 predicts values of 0.922, 0.872, and 0.811. The actual elution profile therefore places the particle retention somewhat closer together than predicted. This is primarily due to the fact that the pure exclusion model does not take into account parameters like size-distribution of the packing material and interactions between analyte particles,[23] which are very difficult to quantify.

In addition to the 5mL/minute flow rate as used in the chromatograms shown in Figure 2-10, runs were also performed at flow rates of 2.5 mL/minute and 10 mL/minute acetone. No significant change in plate count or retention (τ value) was observed by performing the separation faster or slower. This fits with literature observation of little or no van Deemter C-term being present in packed-column HDC, and argues for using the highest possible flow rate for performing these separations. With a flow rate of 10 mL/min, the pressure was approaching the operational limit for our glass columns (150 psi), so 5 mL/min was chosen as the preferred flow rate.

Even though the behavior of the HDC column was not exactly as theoretically predicted, the HDC mechanism did work to size-classify the particles in that the larger particles eluted first and the smaller particles eluted last. Therefore we decided to move forward with this column to see if a batch of porous BEH particles could be purified by performing an injection on column and collecting fractions of the eluting particles.

2.4.3 HDC Purification of BEH Particles in Acetone

Figure 2-11 shows the elution profile for an injection of approximately 10 mg of "0.8 μm" BEH particles (batch KDW-3-159), along with 9-methyl anthracene as the void marker. From prior SEM analysis, we knew that the raw material injected had a $d_{p,n}$ value of 0.76 ± 0.26 μm. The BEH peak in the HDC chromatogram shown in Figure 2-11 was noticeably broader than that of the particle size standards shown in Figure 2-10, due to the polydispersity of the sample and the large amount injected on the column. The peak maximum was at ~6.5 minutes; this was between the values for the 0.6-μm and 0.9-μm particle standards.

Fractions were taken at 0.3-minute intervals, starting at 6.0 minutes and extending for eight fractions. Fractions of interest from an HDC mechanism perspective were 1-3, and fractions 4-8 were taken mainly to observe the size distribution of the particles present in the chromatographic "tail". All fractions were sized by SEM imaging and fractions 4-8 were found to be of about the same composition as the starting material. SEM images and the accompanying histograms for Fractions 1-3 are shown in Figures 2-12 through 2-14. It is obvious from the SEM images alone that the earlier fractions have a larger average particle size and a smaller number of fines. The number averaged particle diameter ($d_{p,n}$) calculated from fractions 1 through 3 were 0.95 ± 0.21 µm, 0.86 ± 0.23 µm, and 0.68 ± 0.23 µm, respectively. The volume averaged particle diameter ($d_{p,v}$) for these fractions was 1.05 µm, 1.02 µm, and 0.87 µm, respectively.

Several key observations arise from analysis of the data presented in figures 2-11 through 2-14. First, packed-column HDC on a 17-cm column was able purify roughly 10 mg of ~0.76 µm BEH starting material with 33% RSD into a few mg of 0.95 µm BEH material with 22% RSD, within about five minutes. This is a much shorter cycle time than observed for the liquid-phase sieving device previously described in our lab,[5] and immediately brings to mind the option of performing sequential injections to purify quantities of material suitable for packing. It was also evident that although the absolute standard deviation was roughly the same for fractions 1-3 (approximately ± 0.2 µm), the relative standard deviation increases as the average particle size gets smaller, from 22% for fraction 1 to 27% for fraction 2, and 34% for fraction 3. From previous data for porous-particle UHPLC with 1.5-µm BEH particles, we believe a particle size RSD near 10% may be small enough to permit good chromatographic performance.[2] It was therefore apparent that although fraction 1 showed

the highest degree of purification from HDC, even further purification was desired in order to obtain particles suitable for packing into chromatographic columns.

In order to obtain enough particles to run a second level of purification, two more HDC separations of the raw material (KDW-3-159, "0.8 μm" BEH) were performed, with fraction 1 collected and pooled for each of these chromatograms. After the three fractions were pooled (approximately 4.5 mL total volume), they were centrifuged down and resuspended in 1 mL acetone. Two second-level purification HDC runs were performed, and the first half of the eluting analyte peak was collected and pooled for each of these runs. The final product of this second purification step was approximately 5 mg of material. Figures 2-15 through 2-18 highlight the purification ability of two passes through the 17-cm HDC column, using appropriate fraction collection. Figures 2-15 and 2-16 are SEM images of the pre- and post-HDC purified "0.8 μm" BEH material. Figures 2-17 and 2-18 are the respective histograms showing the particle size distributions. From the histogram analysis, it is easy to see that the majority of the sub-0.8 μm fines have been removed by HDC purification. With two HDC cycles, the BEH material was purified from 0.76 ± 0.26 μm to 1.05 ± 0.16 μm, for an improvement from 33% to 16% RSD.

2.4.4 Chromatographic Performance of Purified 1.0-μm BEH Material

The approximately 5 mg of 1.05-μm BEH material obtained from the HDC purifications described above were used to pack a 10.1 cm x 30-μm i.d. capillary column. A longer column was desired, but the amount of particles recovered from this small-scale separation was only enough to pack this short column. For comparison, a 25.3 cm x 30-μm i.d. column was packed with the "0.8-μm" BEH raw material (pre-purification). A van Deemter performance analysis was performed on each column, and the results are presented

in Figure 2-19. H_{min} for the raw material was roughly 3.8 μm, which is very poor for a 0.8-μm nominal particle diameter ($h \sim 5$). H_{min} for the purified (1.05-μm) material was 2.4 μm, giving $h \sim 2.3$. This reduced plate height compares very well with commercial HPLC columns, but previous capillary columns packed with 1.5-μm BEH material have given $h \sim$ 1.6. We believe the performance discrepancy between the 1.5-μm BEH particles and our HDC-purified 1.05-μm BEH particles may have to do with the larger relative size distribution (11% for 1.5-μm and 16% for 1.05-μm) or the inability to pack the 1.05-μm material as efficiently as the larger particles because of pressure limitations. It is also possible that these two pheonomena are intertwined, with the small amount of fines remaining in the 1.05-μm material impeding the packing process because of their high flow resistance.

A second telling feature of the chromatographic performance of the purified versus non-purified "0.8-μm" BEH particles is flow resistance. Recall from the introduction that the flow resistance of a packed column scales with the number-averaged particle diameter ($d_{p,n}$), which is heavily influenced by having small particles (fines) in the particle size distribution.[1] Figure 2-20 is a plot of linear velocity versus pressure applied per unit column length. The plot is effectively a flow-resistance comparison, where a column with a higher flow resistance will show a shallower slope (less flow per unit force). By substituting the values for u, ΔP, and L from the data shown in Figure 2-20, using the appropriate viscosity and setting $\varepsilon = 0.4$, the effective particle diameter can be calculated using equation (1-7). The result from this sort of analysis is that the effective particle diameter of the "0.8-μm" BEH particles is 0.66 μm, while for the 1.05-μm HDC-purified material it is 0.83-μm. Since flow resistance is proportional to particle diameter squared, the HDC purification resulted in a

58% reduction in column flow resistance in addition to improving chromatographic performance.

2.4.5 HDC Purification of BEH Particles in SDS-water

There was an unfortunate limitation to the HDC purification performed in acetone, in that the retention reproducibility was poor because the column had to be pre-conditioned with SDS and eventually (after ~30-40 column volumes of acetone) would need to be reconditioned. Retention-time shift led to problems when batch-style purifications were attempted to obtain larger particle quantities. Therefore several attempts were made to use an SDS-water based mobile phase similar to that which has been discussed previously in the literature for HDC.[15, 16, 19] Based on the work of H. Small, we attempted the purification of the "0.8-μm" BEH raw material in an SDS-water based mobile phase. A new, longer column was packed with the 34 μm glass beads, with final length of 45.8 cm and 25-mm inner diameter. Buffers containing 0.5 mg/mL SDS and varying amounts of monobasic sodium phosphate (0 to 10 mM) were used at pH 7. The column was first evaluated with ascorbic acid as the deadtime marker and then with 0.3, 0.6, 0.9, and 1.5 μm bare silica particles (nonporous). Ascorbic acid typically gave $N \sim 7000$ on this column, corresponding to an h value of 1.8.

As noted in the literature, the relative retention (τ values) of the particle size standards using an aqueous buffer is heavily dependent on the ionic strength of the solution.[16] Particles of any given size move through the column slower (τ increases) as the ionic strength increases, because the double layer thickness decreases thereby lowering the "exclusion volume" for any given particle size. With our column packed with 34 mm glass beads, this shift occurred for all particle sizes. For the 0.9-μm diameter particles τ changed

from 0.946 in 10 mM phosphate to 0.879 in a mobile phase with no phosphate. With no phosphate present, the 1.5-μm standard was prevented from eluting off the column. An intermediate mobile phase composition of 5 mM phosphate was determined to be appropriate for HDC purification of the "0.8-μm" BEH material.

Figure 2-21 shows a chromatogram in which 19 consecutive injections containing "0.8-μm" BEH raw material and ascorbic acid were performed every 5 minutes with a flow rate of 5 mL/minute. Injections are marked by the black triangles in Figure 2-21. In this series of injections approximately 100 mg of starting material was purified in roughly two hours. Because of the excellent retention-time reproducibility afforded by this buffer system, fraction collection was set to start at 5 minute intervals and collect appropriate fractions of the eluting peak. In this way, the SDS-water system proved to have a distinct advantage over the acetone-based system. The retention reproducibility can be verified by looking at Figure 2-22, in which the first 15 injections from the chromatogram in Figure 2-21 are overlayed. Five fractions of ~1.5 mL each were collected from each injection, and the collected fractions were pooled. Fraction 2 was the "target" fraction, and SEM analysis of this fraction revealed $d_{p,n} = 0.98 \pm 0.22$ μm. Thus HDC-purification through this column with fraction collection gave very similar results as a single pass through the acetone-based system, but with much better retention reproducibility.

However, purification of reversed-phase particles in an SDS-water buffer does have its limitations. First, the C18-bonded particles are very difficult to suspend in the aqueous-surfactant mobile phase, and losses of particles from flocculation during the suspending effort lowers the overall throughput of the method. In addition, the particles must have the SDS removed from them after they are purified in order to perform reversed-phase UHPLC

with the particles. This removal might occur either after packing the purified particles into a column, which means they must be packed in SDS-water and then have the SDS removed by cycling appropriate mobile phases through the column. Alternatively, the SDS could be removed prior to packing by washing the particles with appropriate solvents. Both SDS removal options add an extra step which has proven difficult to put into practice. The SDS-water buffer system also causes larger on-column loss of analyte particles during the HDC separation, which decreases the quantitative recovery of particles with each run, lowers the HDC column lifetime, and decreases sample purification throughput. The reason on-column losses are higher for HDC in the SDS-system compared to the acetone-based system are unknown.

It appears that HDC purification of chromatographic media in the 1-μm size range would be assisted by a method with a combination of the attributes of the acetone-based system and the SDS-water based system. Several other particle types and possible column chemistries for the glass beads are currently under investigation.

2.5   Conclusions and Future Directions

We have shown that packed-column hydrodynamic chromatography (HDC) is a viable technique for purification of HPLC packing materials in the micron to sub-micron range. A column-conditioning routine was developed which allowed HDC purification of C18 bonded porous BEH particles to be performed using acetone as the mobile phase. The purified material, compared to the raw BEH material, showed an improved size distribution and drastically improved chromatographic performance and flow resistance.

Unfortunately, the improvements in size-distribution via HDC to date have not yielded a batch of ~1-μm porous particles with RSD ~ 10%, which is the ultimate goal for this work. The best obtained so far is RSD ~ 15%. We hope that improving the size distribution down to the 10% range will yield the first capillary columns with plate heights lower than 2 μm for porous particle UHPLC. Work is ongoing to improve the size distribution even further by using longer, more efficient HDC columns (~1 meter +) and different column chemistries, such as ion-exchange resins.

2.6   References

(1)   Neue, U. D. *HPLC Columns: Theory, Technology, and Practice*; Wiley-VCH, Inc.: New York, NY, 1997.

(2)   Mellors, J. S.; Jorgenson, J. W. *Anal. Chem.* **2004**, *76*, 5441-5450.

(3)   MacNair, J. E.; Lewis, K. C.; Jorgenson, J. W. *Anal. Chem.* **1997**, *69*, 983-989.

(4)   MacNair, J. E.; Patel, K. D.; Jorgenson, J. W. *Anal. Chem.* **1999**, *71*, 700-708.

(5)   Mellors, J. S., University of NC at Chapel Hill, Chapel Hill, NC, 2005.

(6)   Jerkovich, A. D.; Mellors, J. S.; Jorgenson, J. W. *LC-GC* **2003**, *21*, 600-610.

(7)   Anspach, J. A.; Maloney, T. D.; Brice, R. W.; Colon, L. A. *Anal. Chem.* **2005**, *77*, 7489-7494.

(8)   Jerkovich, A. D.; Mellors, J. S.; Thompson, J. W.; Jorgenson, J. W. *Anal. Chem.* **2005**, *77*, 6292.

(9)   Patel, K. D.; Jerkovich, A. D.; Link, J. C.; Jorgenson, J. W. *Anal. Chem.* **2004**, *2004*, 5777-5786.

(10)   Stöber, W.; Fink, A.; Bohn, E. *J. Colloid Interface Sci.* **1968**, *26*, 62-69.

(11)   Monroe, M., University of North Carolina at Chapel Hill, Chapel Hill, NC, 2002.

(12)   Thompson, J. W.; Mellors, J. S.; Eschelbach, J. W.; Jorgenson, J. W. *LC-GC North America* **2006**, *24 (S4)*, 16-20.

(13)   Wyndham, K.; O'Gara, J.; Walter, T.; Glose, K.; Arpin, N.; Hudalla, C.; Yuehong, X.; Izzo, G. *Pol. Mat. Sci. Eng.* **2002**, *87*, 275-276.

(14)   Karger, B. L.; Snyder, L. R.; Horvath, C. *An Introduction to Separation Science*; John Wiley & Sons: New York, 1973.

(15)   Small, H.; Langhorst, M. A. *Anal. Chem.* **1982**, *54*, 892A-898A.

(16)   Small, H. *J. Colloid Interface Sci.* **1974**, *48*, 147-161.

(17)   DiMarzio, E. A.; Guttmann, C. M. *Macromolecules* **1970**, *3*, 131, 681.

(18)   DiMarzio, E. A.; Guttmann, C. M. *J. Polym. Sci. B* **1969**, *7*, 267.

(19)   Small, H. *Acc. Chem. Res.* **1992**, *25*, 241-246.

(20)   Noel, R. J.; Gooding, K. M.; Regnier, F. E.; Ball, D. M.; Orr, C.; Mullins, M. E. *J. Chrom.* **1978**, *166*, 373-382.

(21)   Tijssen, R.; Bos, J.; van Kreveld, M. E. *Anal. Chem.* **1986**, *58*, 3036-3044.

(22)   Tijssen, R.; Bleumer, J. P. A.; van Kreveld, M. E. *J. Chrom.* **1983**, *260*.

(23)   Cheng, W. *J. Chrom.* **1986**, *362*, 309-324.

(24)   Stegeman, G.; Kraak, J. C.; Poppe, H. *J. Chrom. A* **1993**, *657*, 283-303.

(25)   Stegeman, G.; Oostervink, R.; Kraak, J. C.; Poppe, H.; Unger, K. K. *J. Chrom.* **1990**, *506*, 547-561.

(26)   Stegeman, G.; Kraak, J. C.; Poppe, H. *J. Chrom. A* **1993**, *634*, 149-159.

(27)   Venema, E.; Kraak, J. C.; Poppe, H.; Tijssen, R. *J. Chrom A.* **1996**, *740*, 159-167.

(28)   Meehan, E.; Tribe, K. In *Particle Sizing and Characterization*; Provder, T., Texter, J., Eds.; American Chemical Society, 2004; Vol. 881, pp 175-183.

(29)   Stegeman, G.; van Asten, A. C.; Kraak, J. C.; Poppe, H.; Tijssen, R. *Anal. Chem.* **1994**, *66*, 1147-1160.

(30)   Stegeman, G.; Kraak, J. C.; Poppe, H. *J. Chrom.* **1991**, *550*, 721-739.
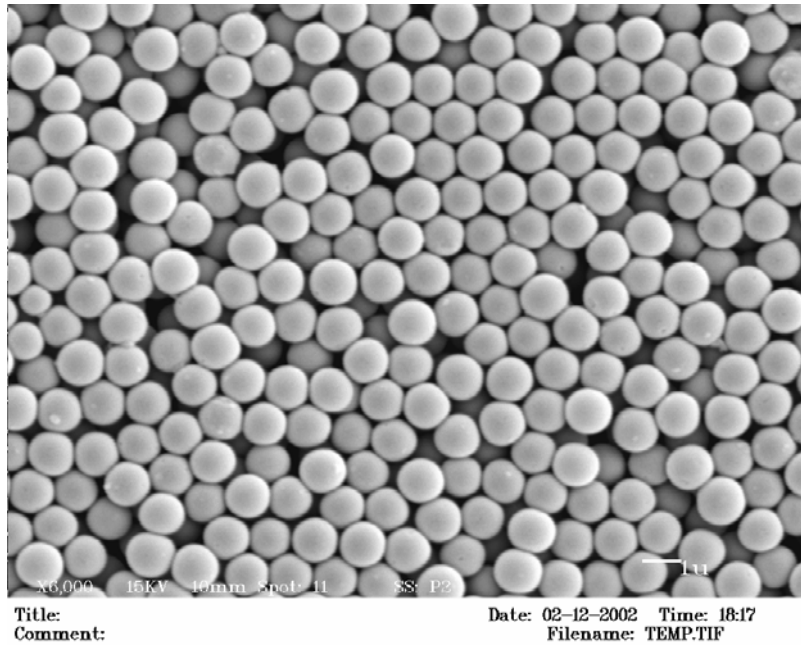
Figure 2-1: SEM image of 1.0 μm nonporous silica particles. Magnification, 6,000X. Synthesis via the Stöber method results in particles with a very narrow size distribution. Image obtained with a Cambridge S200 SEM.
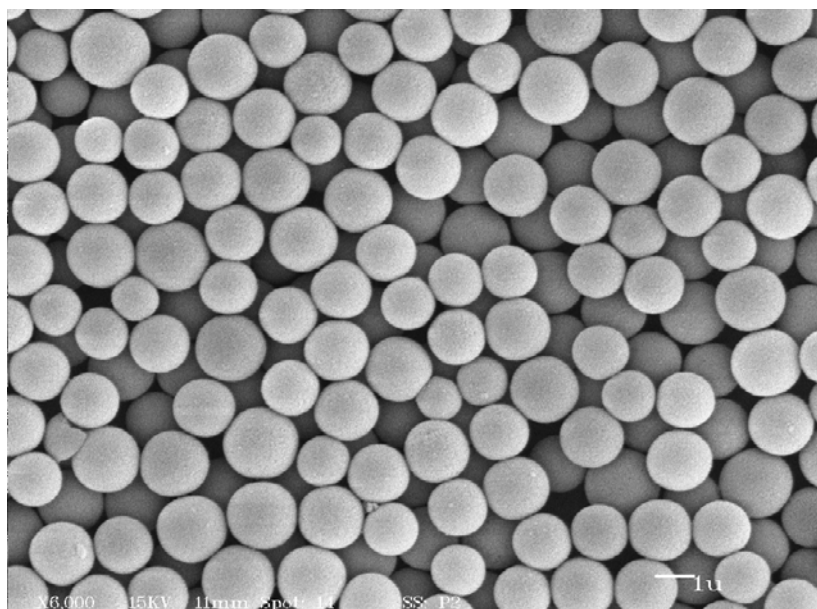
Figure 2-2: SEM image of 1.5-µm BEH particles, size-classified in a proprietary manner by Waters Corporation. Magnification, 6,000X. Image obtained with a Cambridge S200 SEM.
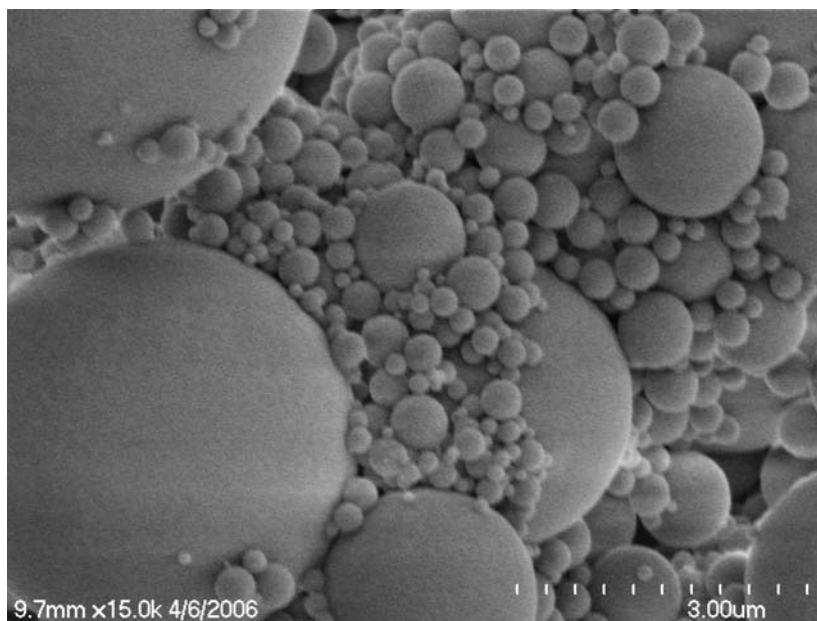
Figure 2-3: SEM image of bridged-ethyl-hybrid porous particles from Waters Corporation, prior to any size-classification. Magnification, 15,000X. Particles in this SEM range from ~5 µm to < 0.1 µm. Image obtained with a Hitachi 4700 FE-SEM.
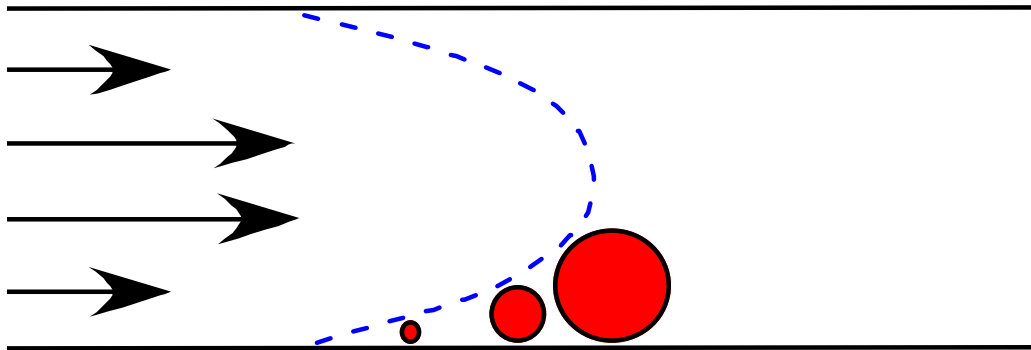
Figure 2-4: Open-tubular model for hydrodynamic chromatography. The larger particles are excluded from the slower flow near the walls to a larger degree than the smaller particles, therefore the largest particles move the fastest.
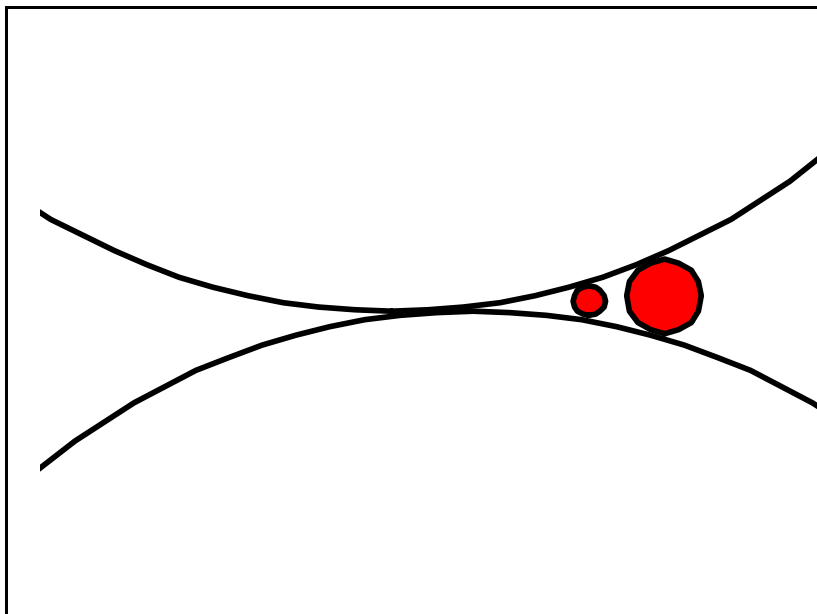
Figure 2-5: Exclusion model for packed-column hydrodynamic chromatography. Large white particles represent the packing material, and the small red particles represent analyte particles. The smaller red particle can sample a larger volume of the space between the spheres, and is therefore predicted to elute later in the exclusion model.
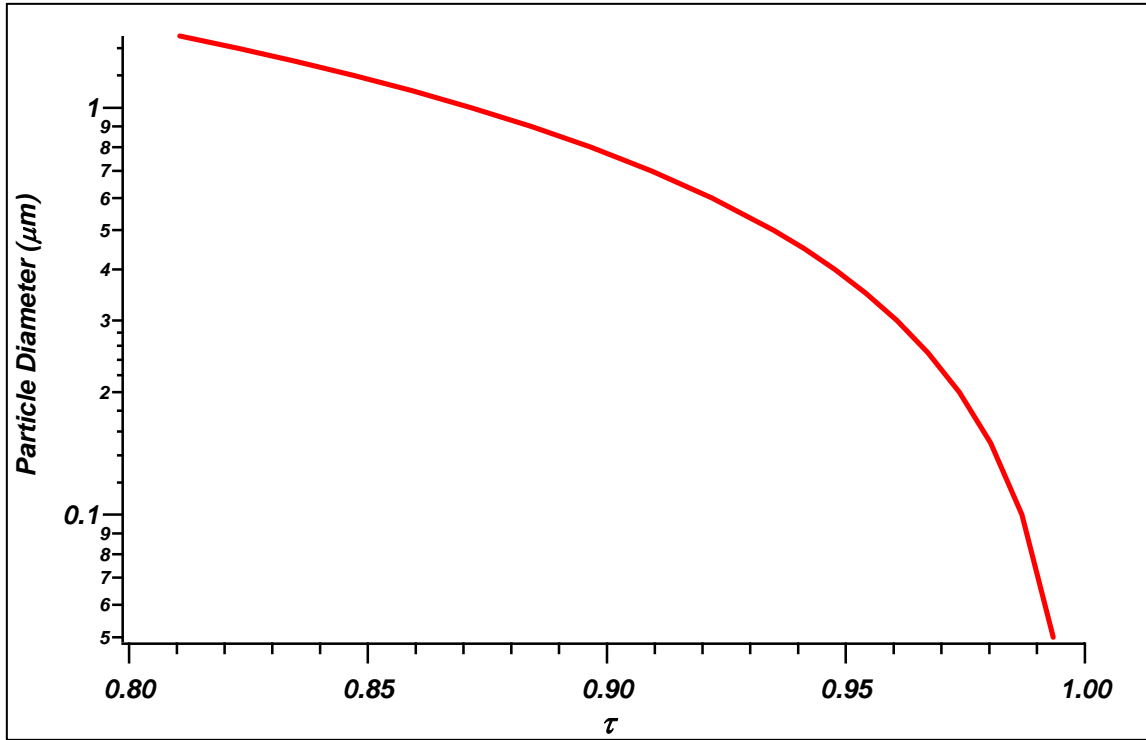
Figure 2-6: Hypothetical analyte particle diameter versus Tau plot for a HDC column packed with 34 μm particles. Calculated from geometrical exclusion theory with equation (2-7).
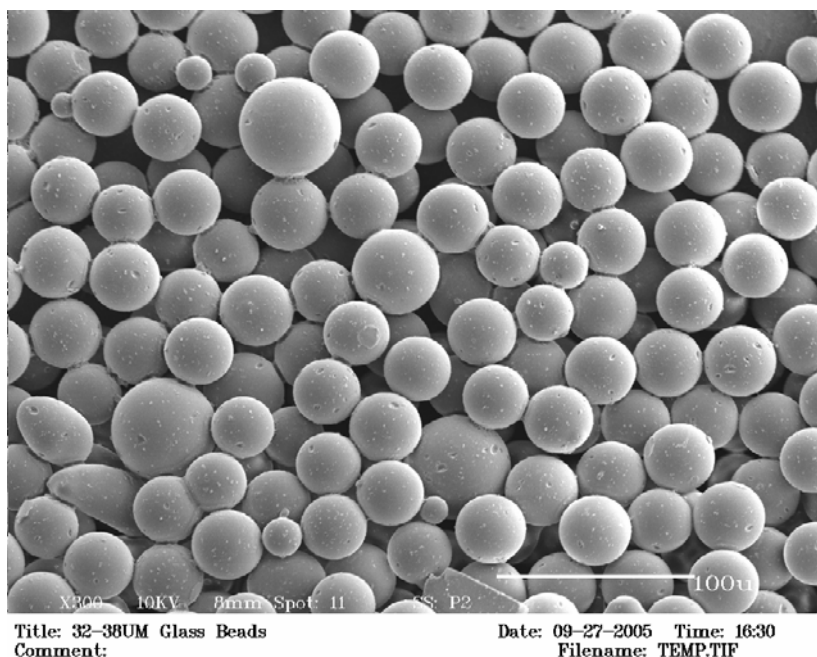
Figure 2-7:   SEM Image of 32-38 μm glass beads from Whitehouse Scientific used as packing material for the HDC column.   Particle diameter measured from this image was 34±6 μm. Magnification, 300X. Image obtained with a Cambridge S200 SEM.
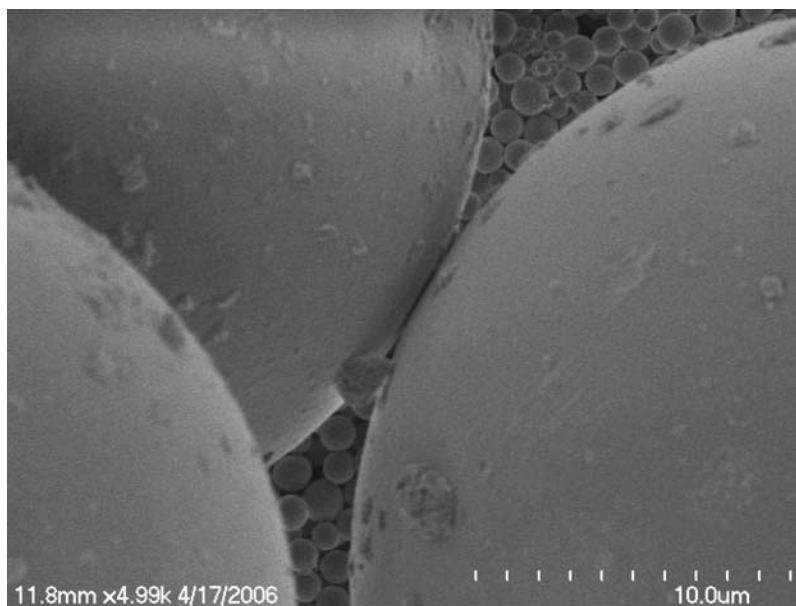
Figure 2-8: SEM image at 5,000X of the 34 μm HDC packing material (large particles) on the same SEM stub as the "0.8 μm" BEH material, which was a typical analyte. This image serves to help visualize the relative size of the voids between the packing material that an analyte may experience in an HDC separation.   Image obtained with a Hitachi 4700 FE-SEM.
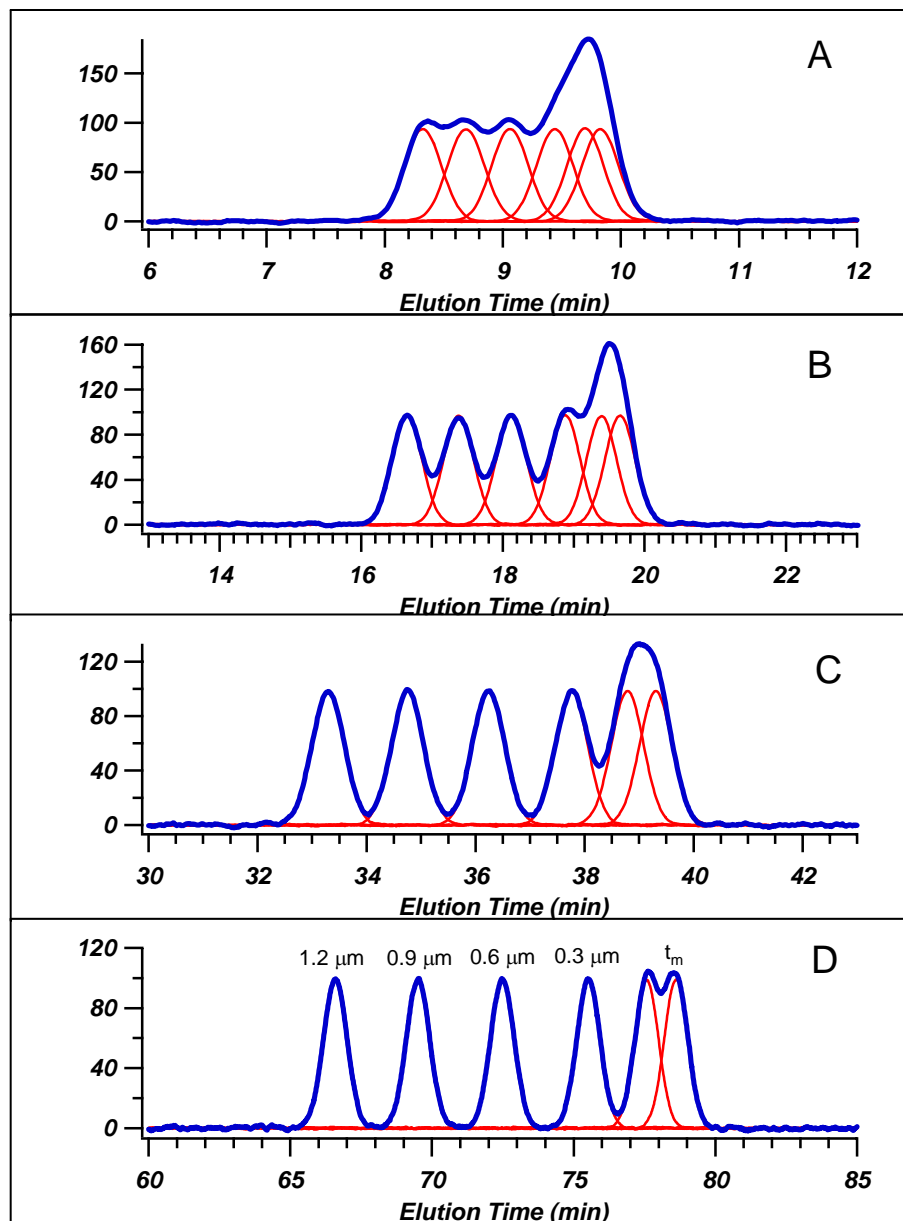
Figure 2-9: Hypothetical chromatograms calculated using the exclusion model for HDC, for size standards on columns of varying length packed with 34-μm particles. The individual chromatograms for each particle size are shown in red, and the predicted chromatogram for a mixture of all particles is shown in blue. The analyte diameters modeled, in order of first to last eluting, are 1.2 μm, 0.9 μm, 0.6 μm, 0.3 μm, 0.1 μm, and small molecule marker. Column lengths and plate counts are (A) 25 cm column, N= 4600; (B) 50 cm column, N= 9200; (C) 100 cm column, N= 18400; (D) 200 cm column, N= 36800.
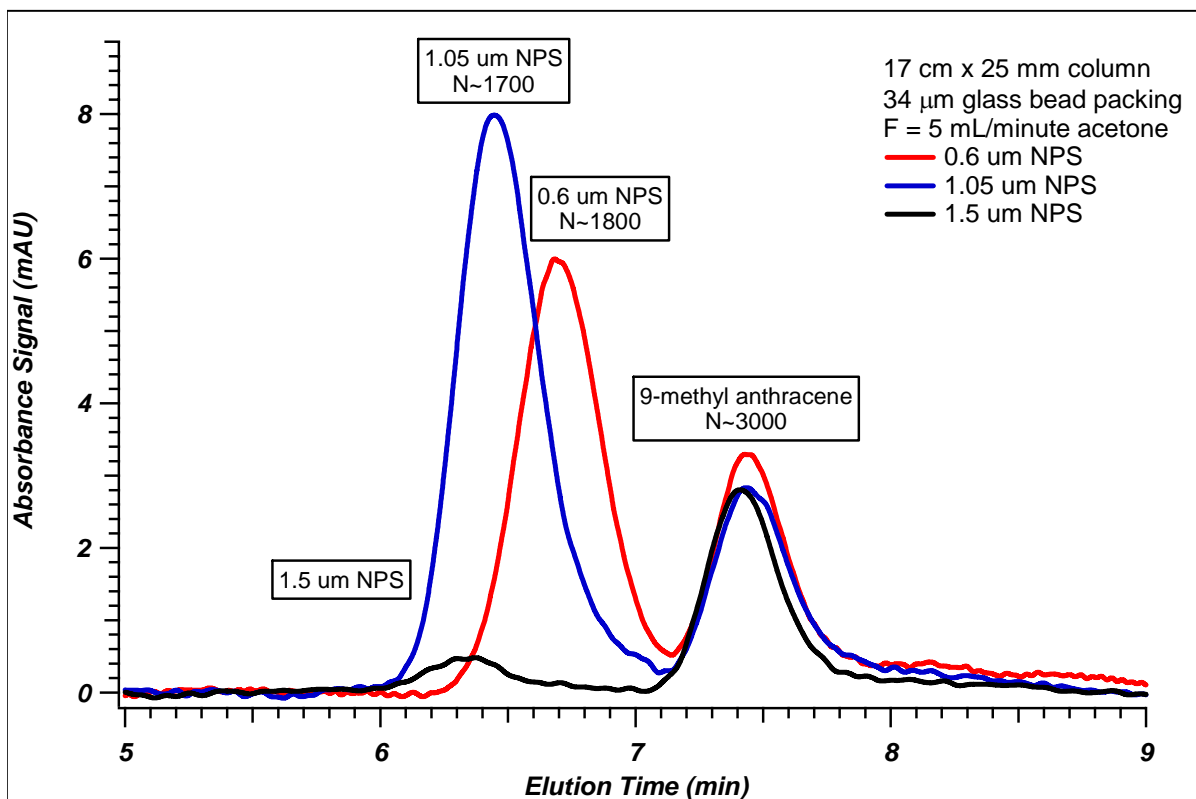
Figure 2-10: HDC Chromatograms of three particle size standards and a void marker, 9-methyl anthracene on a 17-cm long 25-mm diameter glass column packed with 34 μm glass beads. Detection was performed by UV absorbance/turbidity measurement at 330 nm. For this separation, the column had been preconditioned as stated in section 2.3.3; the mobile phase was acetone and the flow rate was 5 mL/min.
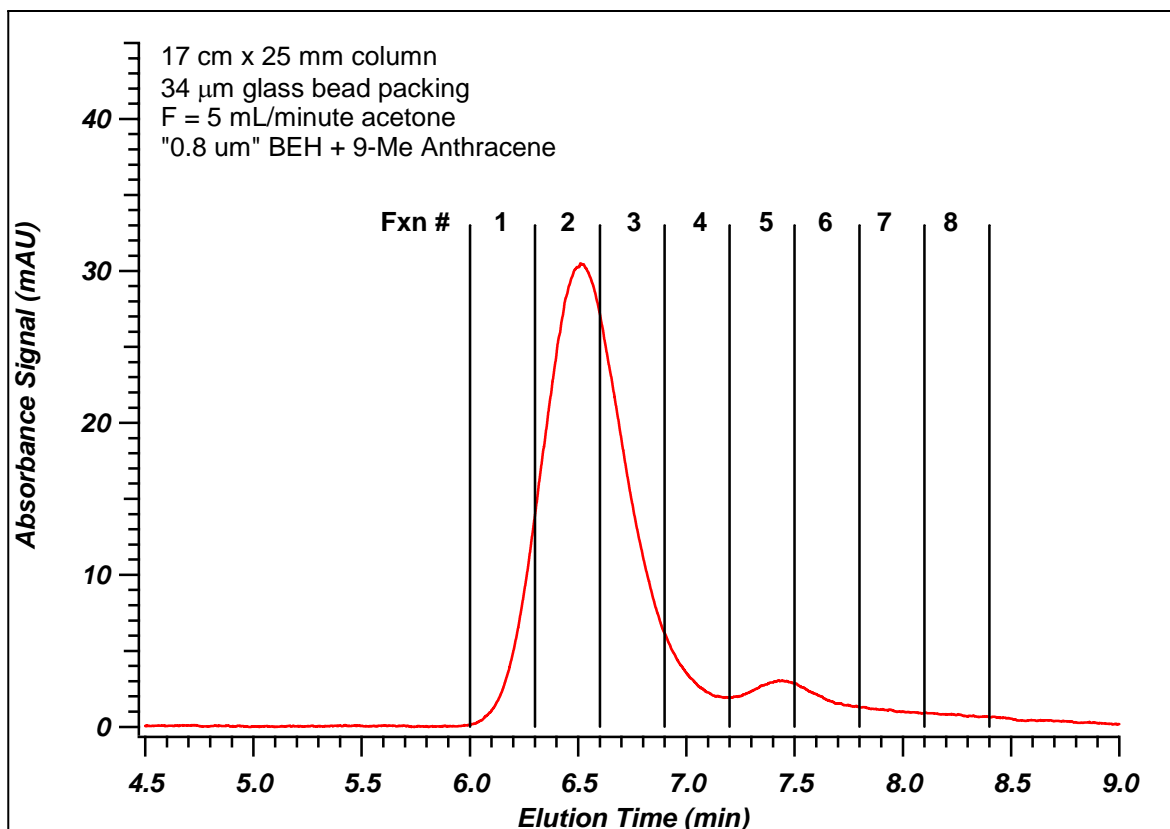
Figure 2-11: HDC Chromatogram of "0.8 μm" BEH, batch KDW-3-159 and 9-methyl anthracene as a void marker. 10 mg of particles was injected on-column. Eight 0.3-minute fractions were collected, although the majority of the true HDC occurred over the first three fractions. Detection was performed by turbidity measurement (UV absorbance signal at 330 nm). Mobile phase was acetone and the flow rate was 5 mL/min.
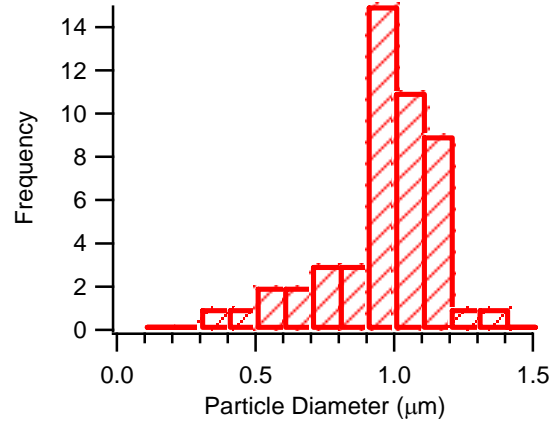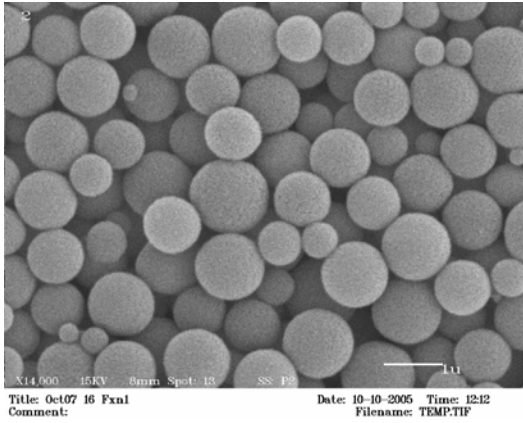
Figure 2-12:   SEM image and particle size histogram for Fraction 1 of the HDC chromatogram shown in Figure 2-11. $d_{p,n}$ for Fraction 1 was 0.95 μm ± 0.21 μm.
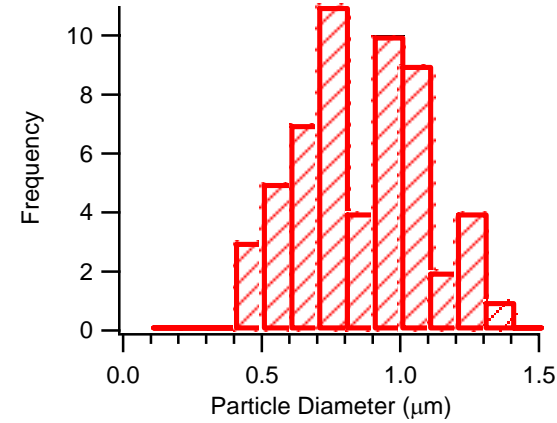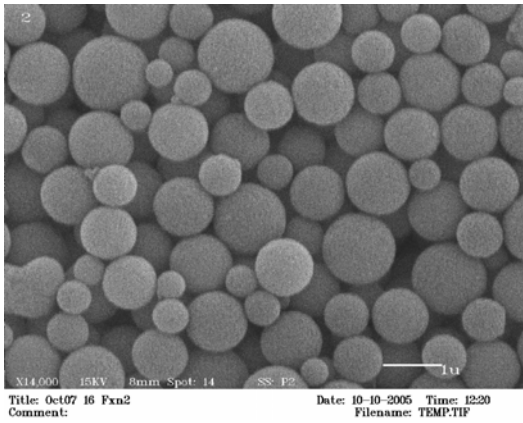
Figure 2-13:   SEM image and particle size histogram for Fraction 2 of the HDC chromatogram shown in Figure 2-11. $d_{p,n}$ for Fraction 2 was 0.86 μm ± 0.23 μm.
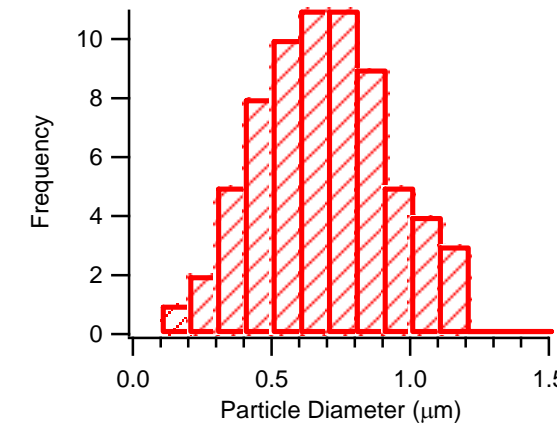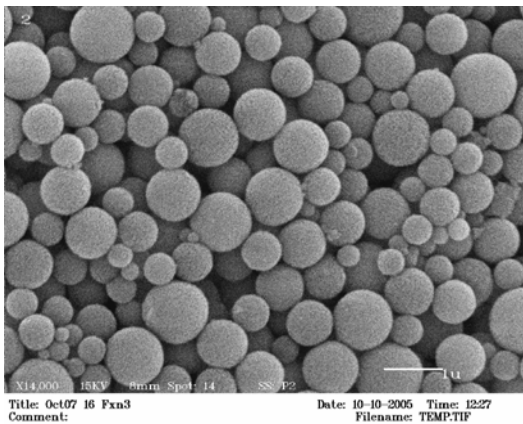
Figure 2-14:   SEM image and particle size histogram for Fraction 3 of the HDC chromatogram shown in Figure 2-11. $d_{p,n}$ for Fraction 3 was 0.68 μm ± 0.23 μm.
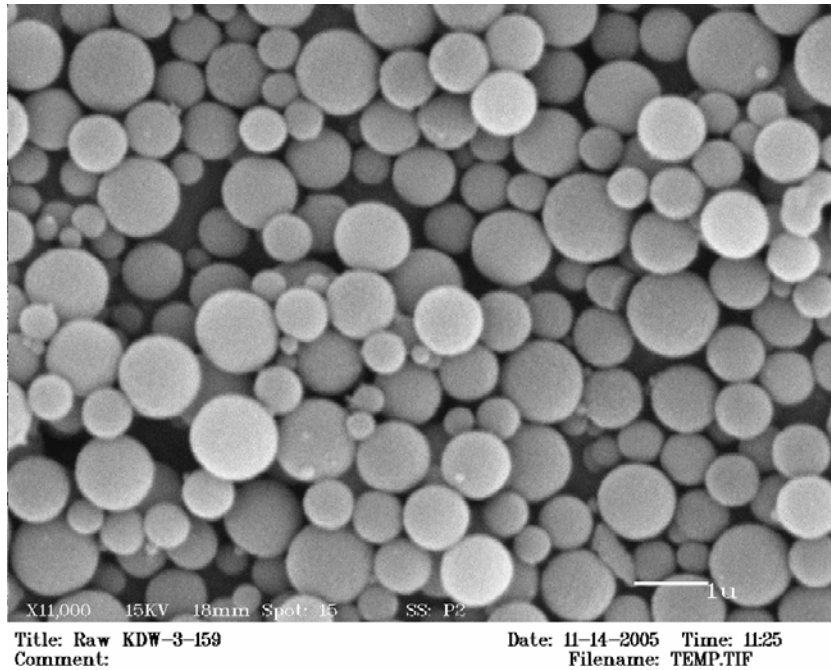
Figure 2-15: SEM Image of "0.8 μm" BEH material (batch KDW-3-159) prior to purification via HDC. $d_{p,n}$ was 0.76 ± 0.26 μm, and $d_{p,v}$ was 0.97 μm. The corresponding histogram is shown in Figure 2-17.
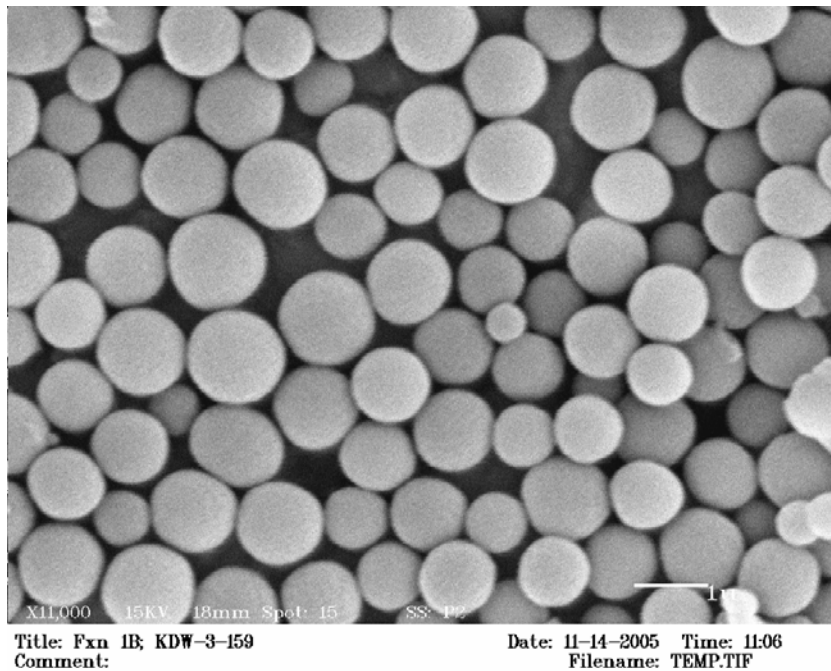
Figure 2-16: SEM Image of "0.8 μm" BEH material (batch KDW-3-159) after two HDC cycles with appropriate fraction collection, on the 17 cm x 25 mm column packed with 34 μm glass beads. $d_{p,n}$ was 1.05 ± 0.16 μm, and $d_{p,v}$ was 1.05 μm. The corresponding histogram is shown in Figure 2-18.
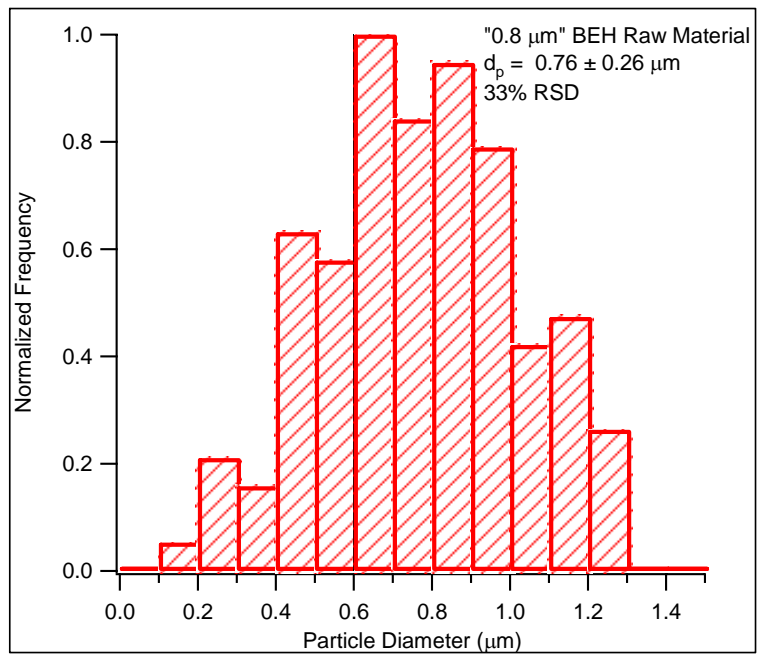
Figure 2-17: Histogram of "0.8 μm" BEH material (batch KDW-3-159) prior to purification via HDC. $d_{p,n}$ was 0.76 ± 0.26 μm, and $d_{p,v}$ was 0.97 μm. Histogram was calculated using the SEM image shown in Figure 2-15.
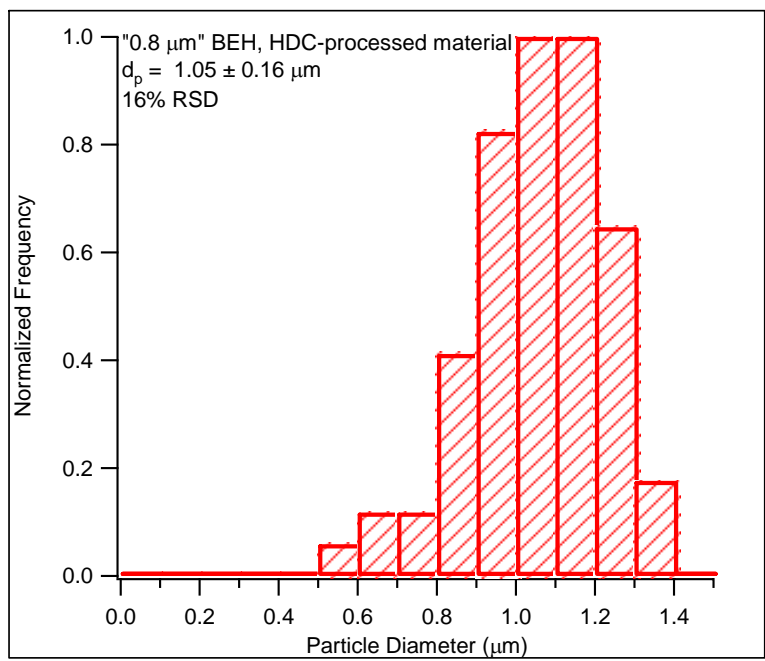
Figure 2-18:   Histogram of "0.8 μm" BEH material (batch KDW-3-159) after two HDC cycles with appropriate fraction collection. $d_{p,n}$ was 1.05 ± 0.16 μm, and $d_{p,v}$ was 1.05 μm. Histogram was calculated using the SEM image shown in Figure 2-16.
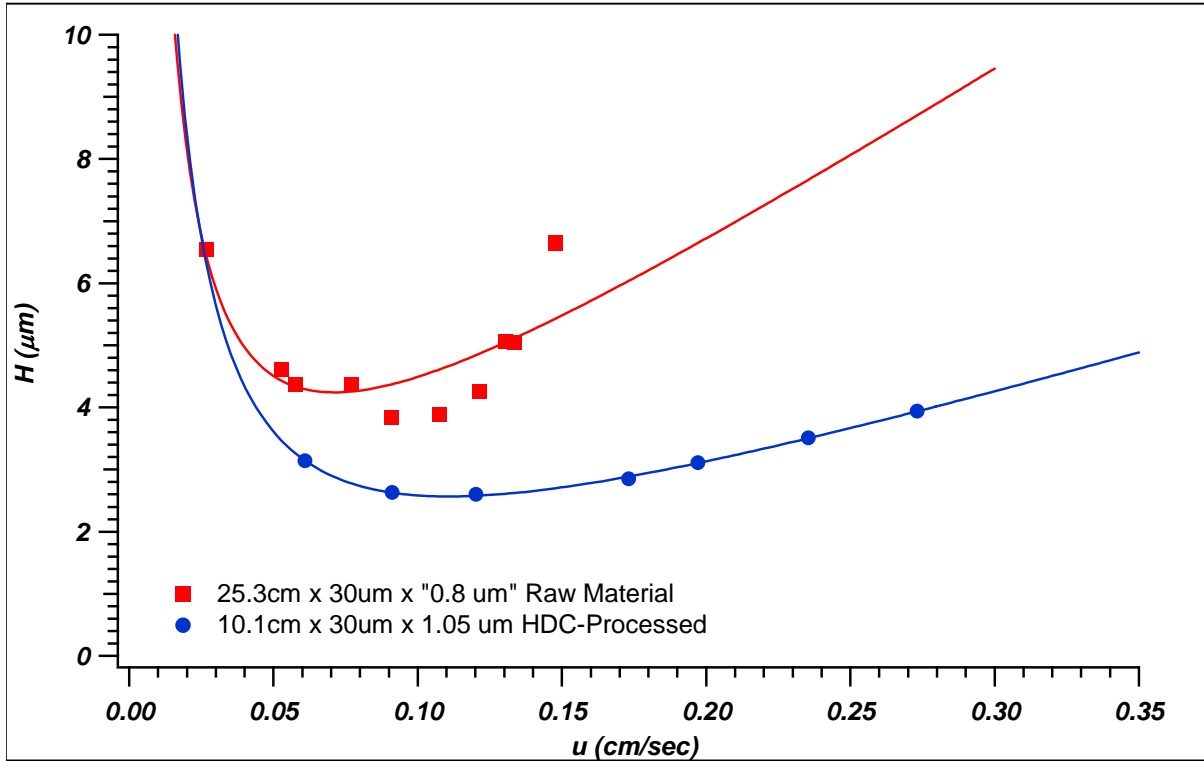
Figure 2-19: van Deemter column performance analysis for two columns, one packed with the "0.80-μm" BEH raw material (■), and one with the 1.05-μm HDC-purified BEH material (●). The minimum plate height was roughly cut in half using the purified particles, even though the average particle size was larger.
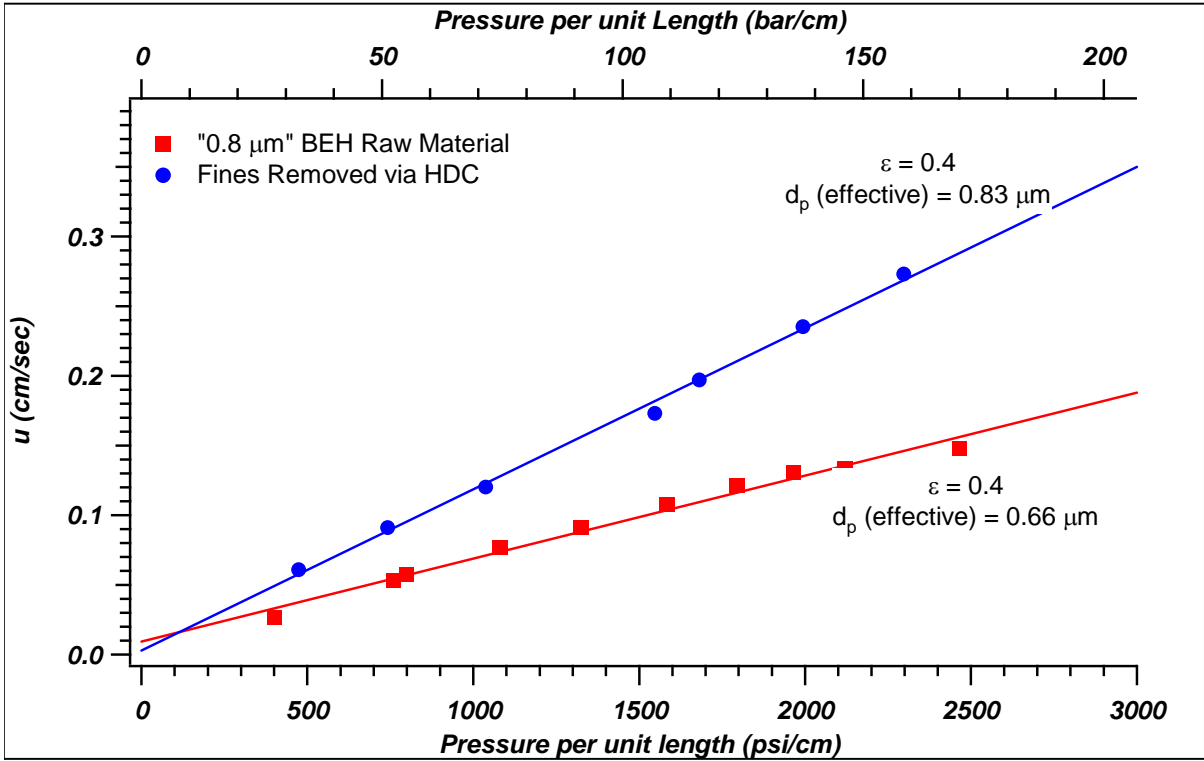
Figure 2-20: Linear velocity as a function of pressure per unit column length. This serves as a comparison of flow resistance per unit column length for the "0.8-µm" BEH raw material (■) and the HDC-purified 1.05-µm BEH material (●). Removal of fines resulted in a 58% decrease in the flow resistance.
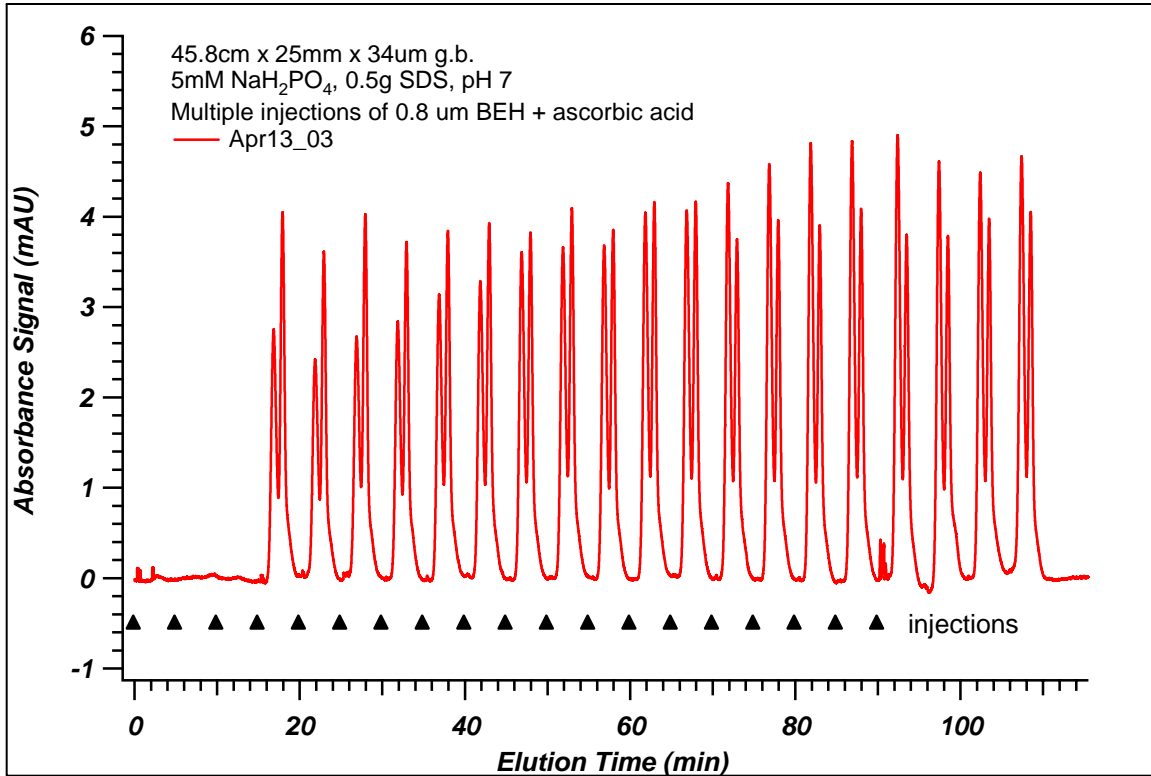
Figure 2-21: HDC chromatogram of "0.8-μm" BEH raw material and ascorbic acid, showing 19 consecutive injections on a 45.8 cm column packed with 34 μm glass beads. Mobile phase was 5 mM sodium phosphate monobasic with 0.5 mg/mL SDS at pH 7; F = 5 mL/min.
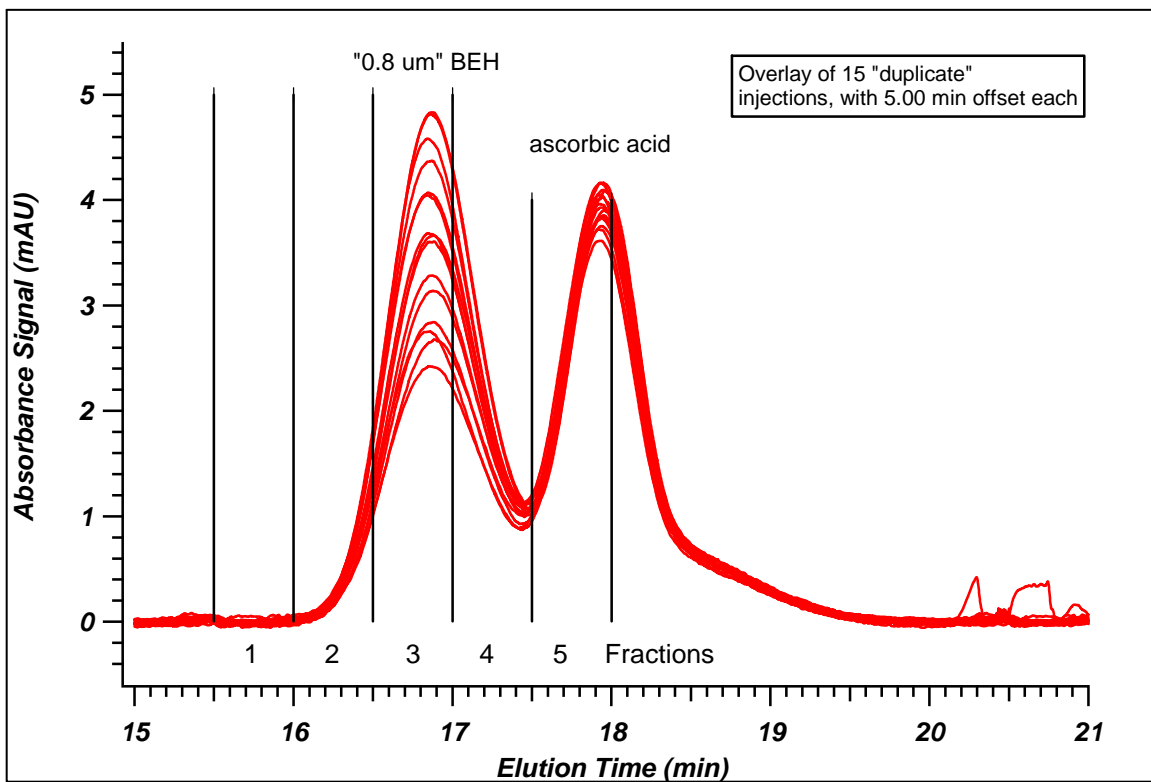
Figure 2-22: Overlay of 15 injections from a HDC chromatogram of "0.8-µm" BEH raw material and ascorbic acid, on a 45.8-cm column packed with 34 µm glass beads. Mobile phase was 5 mM sodium phosphate monobasic with 0.5 mg/mL SDS at pH 7; F = 5 mL/min. Fractions collected at 0.5 minute intervals, as indicated.

3   CAPILLARY TIME-OF-FLIGHT VISCOMETER

3.1   Introduction

The motivation for investigating mobile phase viscosity at ultrahigh pressures (>1500 bar) was twofold. First, the diffusion coefficient of an analyte in the mobile phase affects the *B* and *C*-terms of the van Deemter equation, as discussed in Chapter 1. Mellors dedicated a good portion of his doctoral dissertation to developing a method to directly measure analyte diffusion coefficients at ultrahigh-pressures, so that our capillary chromatography columns could be properly evaluated using reduced parameters.[1]   The stopped-flow method he developed was very accurate, albeit extremely time-consuming (~1 measurement/24 hours). The Stokes-Einstein Equation predicts that a solute's diffusion coefficient should be inversely proportional to solution viscosity, so we hoped that if we could develop a quick way to determine viscosity of mobile phases at elevated pressure, this could be correlated to give the diffusion coefficients at elevated pressure. A second motivation was due to the inability to accurately predict column dead times and interparticle porosity (ε) values for isocratic UHPLC, without the proper mobile phase viscosity.

3.1.1   Historical Perspective

Commercially-available HPLC pumps have a pressure limitation of a few hundred bar, and physical parameters such as solvent viscosity and compressibility have historically been taken as constants as a function of pressure for a given mobile phase.[2-4] The Jorgenson

lab has performed UHPLC with pressures up to 7000 bar, and under these conditions those same physical parameters can undergo significant changes.[4-8]

Viscosity has been known to vary strongly with hydrostatic pressure for the better part of a century.[9] The viscosities of most pure liquids at standard temperature and pressure are well-documented, and a number of studies have looked at pressure effects on the viscosity of pure liquids, following the pioneering work of Bridgman.[9-13] However, modern chromatography is rarely performed in pure solvents, and more often employs binary or ternary solvent mixtures. A few authors have published atmospheric pressure viscosity values for mixtures of the most commonly used solvents in reversed-phase liquid chromatography, methanol-water and acetonitrile-water.[8, 14-17] Since traditional HPLC uses pressures below a few hundred bar, the atmospheric pressure viscosity values of these mixtures can usually be used for flow calculations with only small errors.

A number of studies have focused on the effects that high hydrostatic pressure can have on chromatographic features such as hold-up volume, retention volume, and retention time.[4, 18-24] One of the most noticeable chromatographic effects due to viscosity change at elevated pressure is nonlinear increase in volumetric flow rate with applied pressure, as observed frequently in our lab.[25] In 2005, Martin and Guiochon published an extensive examination of the effects of high pressure on liquid chromatography and essentially said that no high pressure viscosity data for solvent mixtures typically used in HPLC was available in the literature.[8]

3.1.2 Methods for Measuring High Pressure Viscosity

3.1.2.1 Falling-Body Viscometer

At the outset of the experiments described in this chapter, we were not aware of any work in the literature looking at the viscosity of acetonitrile/water or methanol/water mixtures at ultrahigh pressures. When our experiments were finished and we were conducting a second literature search, two papers in the literature were found that addressed high pressure viscosity for methanol/water mixtures[26, 27], and one paper examined viscosity of acetonitrile/water mixtures at high pressures.[28] The references utilized falling-body viscometers, in which the viscosity of a fluid is determined by the time it takes for a body of known mass to fall a specified distance through the fluid of interest. A major drawback of this technique is that the density of the fluid of interest at all pressures must be known exactly, and therefore must be determined by a separate and difficult experiment, or gathered from the literature.[27] The aforementioned papers were located in physical chemistry journals and had been overlooked in the chromatographic literature. A publication based on the research in this chapter was submitted to the *Journal of Chromatography A* with the tenets of making the data contained in those papers apparent, and presenting a new method of viscosity measurement at ultrahigh pressures which does not require knowledge of the solution density.[29]

3.1.2.2 Open-Tube Poiseuille Viscometer

Previously, ultrahigh-pressure viscosity measurements in our lab have been made in a simple fashion by measuring the flow rate through a capillary, and utilizing the Poiseuille relationship. A cartoon example of how this is performed is shown in Figure 3-1. A stopwatch can be used to simply measure the time it takes the fluid flowing out of an open-tube capillary of known diameter to fill a 10-μL calibrated glass pipette.

Using this setup, under 4800 bar of inlet pressure the viscosity of a 50/50 (v/v) acetonitrile-water mixture was observed to increase by 34%.[25] Since the pressure drop across the column is essentially linear, this corresponds to a viscosity increase of 34% over an average pressure increase of 2400 bar, as pointed out recently.[8] Measuring viscosity in this way, as an average over a large pressure drop, has an inherent flaw. Changes in viscosity that occur over small pressure ranges (i.e., a few hundred bar) are lost by "averaging" the viscosity over a large pressure drop. Pure water and mixtures with high percent water are expected to exhibit a nonlinear response of viscosity to pressure, so averaging over a large pressure range (≥1 kbar) would be particularly problematic for these solvents.[10, 11] Additionally, with a large pressure drop across an open tube, heat generation due to flow can contribute to error in viscosity measurements.

3.1.3   Motivation for the Capillary Time-of-Flight Viscometer

It was therefore desirable to develop a method for measuring the pressure dependence of viscosity for solvent mixtures commonly used in liquid chromatography. Open tube-style viscometers utilizing the Poiseuille equation were intrinsically appealing because of the theoretical simplicity, our access to this equipment, and our experience with capillary columns. This chapter describes the development of a novel method for measuring solution viscosity up to 3500 bar, using the time-of-flight of a conductive front through an open tube capillary which can be pressurized from both ends. Once the best instrument design was determined, the viscosity of methanol-water and acetonitrile-water mixtures in decade volume percent increments were measured from atmosphere to 3500 bar using the capillary time-of-flight (CTOF) viscometer.

The design of the CTOF viscometer was based upon several important general ideas that should be described here for clarity. First, all viscometers based on flow through a capillary require a pressure drop to drive the flow. Therefore, all viscometers based on this principle measure an average viscosity over a pressure range. The intent of this work was to measure viscosity over a large pressure range (up to 3500 bar). Viscosity was therefore measured using a relatively small and consistent pressure drop (~200 bar) but at a variable average pressure. For example, viscosity of a solution at 400 bar was determined by having the inlet at 500 bar and the outlet at 300 bar. Likewise, viscosity at 2500 bar would be determined by having the inlet at 2600 bar and the outlet at 2400 bar.

In addition, there must be a way to determine the flow rate through the capillary. Of course, this required some fundamental difference in the solutions at either end of the viscometer. In this instrument, linear velocity of the mobile phase was determined using conductivity detectors. Conductivity was chosen because small differences in conductivity can be detected easily using on-column detectors, and the very low salt concentration utilized (<0.025 M) has been shown to have only slight effects on viscosity (<1% error).[30, 31]

3.2 Experimental

3.2.1 Capillary Time-of-Flight Viscometer Principle

The capillary time-of-flight (CTOF) viscometer described herein is based on the Poiseuille flow principle which says that, under laminar flow conditions, the linear velocity of a fluid (u) through a capillary tube with radius r_0 follows the relationship:

$$u = \frac{r_0^2 \Delta P}{8 \eta L} \tag{3-1}$$

where ΔP is the pressure difference between the inlet and the outlet, η is fluid viscosity, and L is length of the capillary. Viscometers based on Hagen-Poiseuille are probably the oldest form of viscosity measurement.[9, 32] Instead of measuring volumetric flow rate, the capillary time-of-flight viscometer measures the linear velocity of a fluid by passing a conductive front through a known length of capillary; a simple rearrangement of equation (3-1) can then be used to calculate viscosity of the solution:

$$\eta = \frac{r_0^2 \Delta P}{8uL} \qquad (3\text{-}2)$$

3.2.2   Solution Preparation

All solutions were prepared at 25 ± 0.5 °C by mixing HPLC-grade acetonitrile and methanol (Fisher Scientific, Fair Lawn, NJ) with Nanopure water (Barnstead-Thermolyne, Dubuque, IA). Composition was varied from 100% organic to 100% water in 10% steps by volume. For the viscosity determinations using pure water and acetonitrile/water mixtures, trifluoroacetic acid (TFA) (Sigma-Aldrich, St. Louis, MO) was used at 0.1% and 0.02% by volume for the high- and low-conductivity mobile phases, respectively. However, after performing the experiments for pure water and acetonitrile/water mixtures, I observed that TFA gave no conductivity signal in pure acetonitrile. Therefore, for pure acetonitrile, pure methanol and methanol/water mixtures, lithium perchlorate (Sigma-Aldrich, St. Louis, MO) was used at 20 mM and 5 mM for high- and low-conductivity mobile phases, respectively. The high- conductivity mobile phase was always prepared by enriching an aliquot of the low conductivity mobile phase to the desired concentration in order to ensure uniform solvent composition. Experiments were performed at ambient lab temperature, which was 25 ± 0.5 °C for all experiments and typically ± 0.1 °C for each individual viscosity determination.

3.2.3   Capillary Time-of-Flight Viscometer: Early Instrument Design

Initially, the CTOF viscometer was designed and implemented with a setup as shown in Figure 3-2. The idea was simple: Pump 1 would be used to drive the fluid forward, the two pressure sensors on the ends of the capillary would give the difference in pressure between the ends of the capillary, and the two conductivity detectors would give the migration time between two accurately measured points on the capillary. Once a forward migration was performed, Pump 2 could be engaged to drive the front backwards, and the experiment was repeated. In this experiment, ideally the two 75,000 psi pneumatic amplifier pumps (Model DSXHF-903, Haskel, Inc., Burbank, CA) were to be matched and the pressure sensors (150,000 psi, Model PX91PO, Omegadyne, Stanford, CT) were to be matched. These assumptions turned out to be critically flawed.

There were several problems with this system, the most significant of which was that the pressure gauges were not nearly accurate enough. The gauges were capable of measuring pressures to 150,000 psi (10,300 bar), with an error listed as ±0.25% from the manufacturer. This equates to ±375 psi error in the pressure reading. Since were aiming to measure a pressure drop across the capillary of ~2000 psi, this meant we could expect around ±19% error. Indeed, this was the case, as data obtained with this system (not shown) were wildly erratic and irreproducible.

The problems associated with the first CTOF configuration shown in Figure 3-2 were addressed in several ways. First, an instrument was designed that needed only one pressure sensor and one pump to measure the pressure at the inlet and outlet; therefore the system was self-referencing and any systematic error between the two pressure sensors could be eliminated. Second, a new pressure sensor (Model 602160-2, Senso-Metrics Inc., Simi

Valley, CA) that was 75,000 psi-capable, with error on the order of ± 25 psi, was obtained from Dr. Ken Patel at Sandia National Labs.

3.2.4 Capillary Time of Flight Viscometer: Components and General Operation

In the final configuration of the CTOF viscometer, only one pump and one pressure sensor were required. As shown in Figure 3-3, pressure generation with the CTOF viscometer was performed by a pneumatic amplifier pump (Model DSXHF-903, Haskel, Inc., Burbank, CA). By connecting this pump to a dual-arm valve (Part Number 60-15HF2, HiP, Inc., Erie, PA), both sides of the viscometer could be pressurized using a single pump. The bomb used in this system was an in-house machined column packing bomb with a volume of roughly 2 mL, as previously described.[6] Figure 3-4 is a photograph of the instrument. In the photograph, the capillary is present, although not plainly visible because of its small size.

The system, including the capillary, was first flushed with the low-conductivity mobile phase from the reservoir, with the capillary removed from the bomb. The pressure was released, and the fitting was then tightened into the bomb and both valves opened, so that both ends of the capillary were at atmosphere. A front (increase in conductivity) was then pushed through the capillary by closing the valve at Arm 2 and increasing the pump pressure by roughly 200 bar (see Figure 3-3). During this step, flow occured from Arm 1 into Arm 2. However, the flow rate was exceedingly small (~200 nL/min), and the volume of pressure sensor 2 (Model PX91PO, Omegadyne, Stanford, CT) was sufficiently large (~ 1 mL) so that no increase in pressure was observed at the outlet (pressure sensor 2).

The pre- and post-migration pressures were measured using pressure sensor 1 (Model 602160-2, Senso-Metrics Inc., Simi Valley, CA) to give the pressure drop across the

capillary.   The pressure reading prior to migration of the front was used as the initial pressure. The average pressure at sensor 1 during migration of the front was used as the final pressure. The function of pressure sensor 2 was simply to ensure that no pressure change occurred in Arm 2 of the system during the forward migration. Only the forward migration was used for viscosity determinations to eliminate systematic error resulting from the use of two different pressure sensors.

After the high-conductivity front passed the second detector, the valve at Arm 2 was opened to equilibrate the pressure at both ends of the capillary, and therefore stop flow through the capillary. The front was pushed backward by closing the valve at Arm 1 and increasing the pressure another 200 bar. After the reverse migration, both valves were opened to allow the pressure to equilibrate before performing the experiment at the next higher pressure. Viscosity measurements were therefore performed in roughly 400 bar steps from an average pressure of 100 bar to 3500 bar. A detail of instrument operation should be mentioned here for completeness; we discovered empirically that in order to generate sigmoidal fronts in the second forward migration, a pause time of approximately 2 minutes was needed after the reverse migration. This time allowed for appropriate mixing of the analyte in the bomb with the fluid that had just been introduced via reverse migration. Without this "equilibration" pause, tailed fronts were more likely to be observed.

3.2.5   Conductivity Detection and Signal Processing

A 12-µm inner-diameter, 360-µm outer-diameter fused silica capillary (Polymicro Technologies, Inc., Phoenix, AZ) was cut to 230 cm and threaded through two contactless conductivity detectors. The capillary was secured at each end using ultrahigh pressure capillary fittings as described previously.[7]   The contactless conductivity detectors were

based on published examples and built in our laboratory.[33, 34] Using an excitation frequency of 10 V_{pp} at 100 kHz from a waveform generator (Model DS335, Stanford Research Systems, Sunnyvale, CA), changes in the conductivity of the solution at each detector were observed and summed through a simple op-amp adder circuit (using op-amp Model OPA 602AP, Digikey, Thief River Falls, MN). Measurement of the length of capillary between the detectors with a meter stick (± 0.1 cm) allowed for the accurate determination of solution velocity. The detectors were placed 30 cm from either end of the capillary in order to avoid error in the velocity measurement that might have occurred due to solvent compression immediately following an increase in pressure.[33] The 100 kHz portion of the conductivity signal was amplified using a lock-in amplifier (Model 391A, Ithaco, Ithaca, NY), and acquired at 51 Hz through a digital acquisition board (Model BNC-2090, National Instruments Corp., Austin, TX) using a program written in LABVIEW 6 (National Instruments Corp., Austin, TX) on a personal computer (Dell Dimension XPST700r, Dell Inc., Austin, TX).

3.2.6   Viscometer Calibration

Either accurate determination of the average capillary diameter, or calibration of the diameter using a known value, was crucial since calculation of the measured viscosity varies with the square of capillary diameter. If the diameter of the capillary given by the manufacturer was ±1 μm, a capillary of roughly 10 μm would give an unacceptable ±20% error. The viscosity of water at 25ºC and atmospheric pressure was chosen as a reliable literature value to calibrate our instrument. To calibrate the capillary diameter, the viscosity of water was determined as a function of pressure. The capillary radius used in Eqn 3-2 was adjusted until the atmospheric pressure viscosity value given by the CTOF viscometer (as the

y-intercept of viscosity versus pressure) matched the accepted viscosity of water, 0.89 cP. The average diameter was determined to be 12.4 μm, and this value was used for the remainder of the experiments.

3.3   Results

3.3.1   Viscometer Raw Data

The procedure for performing viscosity measurements was described in the experimental section. Figure 3-5A shows a typical pressure trace during the forward and reverse migration of a conductive front. The dip in pressure sensor 1 at ~13.8 minutes was a reproducible artifact from the action of closing the Arm 2 valve.   In this experiment, the pump pressure was then increased by 240 bar at 13.95 min, to cause forward migration of the high-conductivity mobile phase. Note that there was no significant drift in pressure sensor 2 during the forward migration, indicating no pressure change at the outlet of the capillary.

The migration of the front past each of the contactless conductivity detectors is shown in Figure 3-5B (top). An increase in conductivity was observed as the mobile phase switched from low- to high-conductivity at the dectector. These fronts were sigmoidal and had widths less than one second, so once differentiated (Figure 3-5B, bottom), Gaussian fits provided a very accurate measure of the linear velocity for use in Eqn 3-2 (<0.1% error). After the front migrated past both detectors, the valve at Arm 2 was opened, the valve at Arm 1 was closed (14.65 min), and the pump pressure was increased by 170 bar (14.7 min). The conductivity decreased (Figure 3-5B, top) as the front migrated in reverse past the two detectors. Once the front was pushed back through the capillary, both valves were opened (15.9 min), and

pressure equilibration was allowed at a pressure roughly 400 bar above the previous "starting" pressure.

3.3.2 Instrument Novelty and Measurement Error

A small capillary inner diameter (~12μm) was chosen for several error-reducing reasons in this experiment. This configuration reduced band broadening (providing sharp fronts), had a low volumetric flow rate to minimize heating effects, and had high flow resistance to allow for a relatively short capillary (~2 m) to be used with the desired ~200 bar pressure drop.

Pressure measurement was the largest contributor to error in using the CTOF viscometer, simply because the inherent pressure measurement error in a gauge capable of ultra-high pressures was fairly large (~5 bar). Unfortunately, a differential pressure gauge capable of measuring a pressure difference with an accuracy of a few bar at a total pressure of several thousand bar is not commercially available. To overcome this restriction, a setup was devised which used valves to allow the use of one pressure gauge to measure pressure at the inlet and the outlet of the capillary.

In the self-referencing setup depicted in Figure 3-3, pressure sensor 1 was used to measure both the initial and final pressure. In the example shown in Figure 3-5A, the initial pressure was taken from pressure sensor 1 in the region between 13.8 min and 13.95 minutes. The final pressure was the average pressure during the migration between detector 1 and 2, at roughly 14.1 and 14.6 minutes. The pressure drop across the capillary used in Eqn 3-2 was the difference between the two values (~240 bar), and the pressure at which the viscosity was determined was the average of the two values (~1200 bar). This operation procedure and its resultant ultra-high pressure capability is the novelty of the currently described viscometer.

With this procedure the error in the pressure measurement was expected to be roughly 3%. Since error in time-of-flight measurement was very small and the capillary diameter was calibrated, the determined fluid viscosity at ultrahigh pressure was expected to be within 3% of the actual value.

3.3.3 Data Analysis

Figure 3-6 shows examples of two sets of viscosity versus pressure data obtained using the capillary time-of-flight viscometer. Figure 3-6A is the viscosity versus pressure data for water. Note that the data has two seemingly independent linear regions, one below and one above 1000 bar. A nonlinear increase in the viscosity of water with pressure has been well-documented in the literature.[9-11] In cases where nonlinear response was observed, the data could be closely fit with two linear regressions, one including data taken at pressures below 1000 bar, and another between 1000 bar and 3500 bar. This was performed for water and is shown as the dotted line in Figure 3-6A. This type of interpolation, using two linear regressions, was only required for pure water, 10/90 v/v acetonitrile/water, 20/80 v/v acetonitrile/water, and 10/90 v/v methanol/water. For these mixtures, the y-intercept of the low-pressure region (up to 1000 bar) gave the atmospheric pressure viscosity.

Figure 3-6B shows the viscosity versus pressure data and single linear regression fit for 50/50 (v/v) acetonitrile/water. The linear regression follows ideal behavior as typically reported in the literature,[8, 12, 13, 26, 35, 36] and was observed for all mixtures with less than 80% water. For this type of data, the y-intercept of the linear regression gave the atmospheric pressure viscosity. Note that in comparing Figures 3-6A and 3-6B, there appears to be more scatter in the data for pure water; this is an artifact of the finer graduation of the y-axis in Figure 3-6A.

3.3.4 Instrument Validation: Viscosity of Pure Solvents as a Function of Pressure

Since there is literature available for the viscosity of pure water, methanol, and acetonitrile under high pressures, these substances provide a means of validating the performance of the CTOF viscometer. Figure 3-7 is a plot of viscosity versus pressure for pure water. Included in the plot are two duplicate data sets collected on the CTOF viscometer at 25ºC, as well as the values reported recently by Harris, determined by a falling-body viscometer.[10] The viscosity values show good agreement, and are within roughly 1-2% at all pressures from atmosphere to 3500 bar.

Figure 3-8 shows two data sets for 100% methanol at 25ºC collected on the CTOF viscometer, and literature values from three falling-body experiments, including Isdale at 25 ºC, Kubota at 25ºC, and Bridgman at 30ºC.[9, 26, 27] The slope and intercept for our CTOF viscosity determination and Isdale's falling-body experiment are virtually identical. The variation between Kubota's data and the other reported values are within the expressed error of 2.5% by Kubota et al.[26] Bridgman's atmospheric pressure viscosity value is predictably lower, since this data was acquired at 30ºC. The slopes of the viscosity versus pressure curves are 0.24 cP/kbar, 0.25 cP/kbar, 0.27 cP/kbar, 0.26 cP/kbar for Thompson, Isdale, Kubota, and Bridgman, respectively.

Figure 3-9 is a similar plot for pure acetonitrile at 25ºC. Two duplicate viscosity determination experiments using the CTOF viscometer are shown as experimental data. No literature data was available at 25ºC for comparison. Data from a falling-body experiment performed by Ueno et al. up to ~2 kbar at 30ºC is plotted as well. The solid line plotted for literature comparison is the slope and intercept for acetonitrile at 30ºC, from the Smithsonian Physical Tables and recently referenced by Martin.[8] The SPT literature values acknowledge

71

an approximate error of ±5% below 1 kbar and possibly greater at higher pressures.[8] The atmospheric pressure viscosity value for pure acetonitrile obtained from the CTOF viscometer, 0.34cP, is consistent with the literature.[8, 14, 16, 17]

3.3.5   Instrument Validation: Atmospheric Pressure Viscosity for Mixtures

Viscosity measurements were made for mixtures of methanol-water and acetonitrile-water at 10 percent volume increments, from roughly 100 bar to 3500 bar. The y-intercept of each of these data sets was reported as the atmospheric pressure viscosity. Figures 3-10 and 3-11 show the viscosity versus percent by volume water for mixtures with methanol and acetonitrile, respectively. For the methanol-water mixtures shown in Figure 3-10, the CTOF viscometer data lies well within the range of literature values determined by other methods, including falling-body, Cannon-Fenske, and Ubbelohde viscometers.[4, 14, 17, 26] As with other methods, the CTOF viscometer found the maximum viscosity at atmospheric pressure to occur between 50 and 60 percent water by volume (1.56 cP).

For mixtures of acetonitrile/water, the CTOF viscometer data shown in Figure 3-11 agrees well with the data from papers by Abbott, Aminabhavi, and Colin.[16, 17, 37] Data from Huss agrees well with the other literature at high and low percentages of water, but disagrees considerably in the range from 20 to 80 percent water.[14]

3.3.6   High Pressure Viscosity for Mixtures

Linear fits to all experimental viscosity versus pressure plots were performed as shown in Figure 3-6 and discussed previously. The slope and intercept values for methanol-water and acetonitrile-water mixtures are reported in Tables 3-1 and 3-2, respectively. This table gives the slope (α) in units of cP/kbar and the intercept (η_0) in cP. As mentioned

previously, the intercept is the atmospheric pressure viscosity. The slope corresponds to how much the viscosity of a solution increases as a function of the applied pressure.

A single linear fit was appropriate for all tested solvents except the aforementioned pure water, 10/90 v/v methanol/water, 10/90 v/v acetonitrile/water and 80/20 v/v acetonitrile/water. Interestingly, all of these solvents showed a change in slope at around 1000 bar. Two slope and intercept values were therefore given for these mixtures in Tables 3-1 and 3-2. It is important to note that for the solvents that demonstrated dual-linear regions, the intercept (η_0) value Table 3-1 for the high-pressure region (1000-3500 bar) has no physical significance. It is provided only to allow viscosity calculation for these solvent mixtures above 1000 bar.

Data from Tables 3-1 and 3-2 were used to generate contour plots to graphically display the viscosity of methanol-water and acetonitrile-water mixtures at pressures up to 3500 bar. The resultant contour plots are shown in Figure 3-12 (methanol-water) and Figure 3-13 (acetonitrile-water). Data reported by Isdale et al. was used to generate a similar contour plot for methanol-water mixtures up to 3100 bar, and this was displayed as dashed lines in Figure 3-12.[27] Agreement between data obtained using the CTOF viscometer and the falling-body method was excellent, as is evident by the almost exact overlay of contour lines for the two data sets.

Viscosity measurements reported by Ueno et al. for acetonitrile-water mixtures up to pressures of roughly 2000 bar were used in a similar manner to generate a contour plot, which was displayed as dashed lines in Figure 3-13.[28] The literature and CTOF viscometer measurements agree in the general shape of the viscosity trend in volume-pressure space. The absolute viscosity values disagree somewhat, but in a fashion that is consistent with the

5ºC difference in temperature between the experiments. The Ueno et al. data was collected at 30ºC, and roughly 10% lower viscosity was observed over most of the contour plot, compared to the CTOF data obtained at 25ºC. A roughly ten percent decrease in viscosity for acetonitrile-water mixtures with a temperature increase from 25ºC to 30ºC was reported previously.[37] It is not clear why the data seem to coincide so closely at 100 percent acetonitrile.

Several interesting observations can be made from these contour plots. As pressure increases, the mixture composition at which the maximum viscosity occurs changes to higher percent organic. This is true for both mixtures. Methanol-water shows a maximum viscosity shift from roughly 55% organic at atmosphere to 65% organic at 3500 bar. Acetonitrile-water shows a maximum viscosity shift from roughly 20% organic at atmosphere to 50% organic at 3500 bar. This shift of maximum viscosity to higher percent organic with pressure has been used as evidence for the increased inclusion of organic molecules into water cavities, such that pressure allows for a stabilization of the water structure.[27]

It is also interesting to note, when looking at Tables 3-1 and 3-2 and Figures 3-12 and 3-13, that although the mixtures of methanol-water and acetonitrile-water have their viscosity maxima at different compositions at atmospheric pressure and at elevated pressures, both solvent systems observe the maximum viscosity response to pressure (slope) at roughly the same percent organic composition. From Tables 3-1 and 3-2, it can be seen that methanol-water observes its maximum slope (0.36 cP/kbar) at 70 and 80% organic, while the acetonitrile-water mixture observes its maximum slope (0.23 cP/kbar) at 70% organic. This maximum slope of viscosity vs pressure implies that this is the solvent composition at which the solvent structure is most easily altered by external force. This could mean that at ~70%

organic, enough water is present to weaken the interactions typically present in pure organic solvents, and enough organic solvent is present to almost completely inhibit the hydrogen-bonding typically present in liquid water.

3.3.7 Three-Dimensional Visualization

As an informative visualization exercise, three-dimensional plots of viscosity versus composition and pressure were created in Igor Pro 4.08. Figure 3-14 contains the three-dimensional surface plots for methanol-water (top) and acetonitrile-water (bottom). Looking at the plots on the same scale, it is easy to visualize why acetonitrile-water is a preferable mobile phase for ultrahigh pressure liquid chromatography, compared to methanol-water. Acetonitrile-water mixtures exhibit viscosity values roughly half of that of methanol-water mixtures in the moderate mixture region (~50% organic by volume). This translates into half the pressure being required for a desired linear velocity.

3.3.8 Prediction of Mobile Phase Velocity versus Pressure

As previously mentioned, one goal of this research was to generate a set of viscosity data that would be useful for chromatographers working at ultrahigh pressures. If a hypothetical LC experiment were being performed using isocratic elution with 50/50 (v/v) acetonitrile/water at 1000 bar, the average column pressure would be 500 bar. Table 3-2 would then be used to calculate the viscosity of the solvent at 500 bar, and thus the flow rate and dead time of the column could be more accurately predicted. When using solvents with a high water content (>80% by volume), care must be taken to account for the nonlinearity in the pressure versus viscosity trace.

An example can be used to best describe how accurately knowing the viscosity of a mobile phase at ultrahigh pressures allows a chromatographer to more accurately predict the

dead time of a chromatographic column. Recall the Kozeny-Carman equation from Chapter 1:

$$u = \frac{\varepsilon^2 d_p^2 \Delta P}{180(1-\varepsilon)^2 \eta L}$$
(3-3)

In the current example, we assume particle diameter (d_p^2), interparticle porosity (ε), and column length (L) remain constant throughout.[38]

Figure 3-15 shows the velocity versus pressure data obtained during a van Deemter experiment for a 49.3-cm long, 30-μm inner diameter capillary packed with 1.56-μm BEH porous C18 particles. The experimental data, plotted as triangles, shows a significant negative deviation from linearity. Prior to obtaining ultrahigh pressure viscosity data from the CTOF viscometer, the best approximation of the velocity through a column was obtained by using the atmospheric pressure viscosity from the literature.[37] This approximation is shown as solid squares, and is of course linear. As would be expected, the approximation works well near atmospheric pressure, but is off by more than 30% by the time the average column pressure is 2200 bar (pressure at the inlet is 4400 bar, or 64,000 psi).

To try and make a better approximation using our experimentally-determined viscosity values, viscosity was treated as a function of the average column pressure, using the slope and intercept from Table 3-2 for 50/50 acetonitrile/water (0.195 cP/kbar, and 0.81cP, respectively). The resultant velocity prediction, shown as open circles in Figure 3-15, worked well (<10% error) up to 2600 bar (38000 psi). At the maximum pressure of this experiment, the error was approximately 13%.

Interestingly, our viscosity-corrected prediction resulted in a velocity curve that was consistently lower than the actual data obtained in the experiment, and the error was largest

at higher pressures.   A higher-than expected velocity, especially when the deviation increases with increasing pressure, can be qualified by mobile phase compression during isocratic UHPLC. This phenomenon is addressed in Chapter 5.

3.3.9   Prediction of Trends in Diffusion Coefficients

As mentioned in the opening of this chapter, we were interested to see if diffusion coefficients could be correlated to the change in viscosity of the solution by the Stokes-Einstein equation. This equation predicts a simple inverse relation ship between the diffusion coefficient of an analyte and the viscosity of solution.   Diffusion coefficient (D) of hydroquinone at ultrahigh pressures have been measured in our lab in 10/90 v/v acetonitrile/water and 50/50 v/v acetonitrile/water. These measurements were performed by a stopped-flow method utilizing an open tube capillary and two UV detectors, as described in detail elsewhere.[1, 39] The experiments are very time-consuming, requiring approximately 24 hours for a diffusion coefficient measurement in a single mobile phase at a single pressure. Alternatively, viscosity measurements using the CTOF viscometer can be performed in duplicate for two to three mobile phase systems, from atmosphere to 3500 bar, during a single day. If small molecule diffusion coefficients could be strongly correlated to viscosity, then a huge throughput advantage could be realized by measuring D at atmospheric pressure using a stopped-flow method, then using the change in viscosity to predict change in D at elevated pressure.

Initial comparisons of measured diffusion coefficients for hydroquinone at elevated pressure to values predicted by viscosity changes showed that changes in viscosity alone cannot very accurately predict changes in D. This realization and the subsequent desire to

77

modify the CTOF instrument to obtain diffusion coefficients as well as viscosity, is the subject of the ensuing chapter.

3.4   Summary of Results

Using a new type of viscometer, the viscosities of the complete series of methanol-water and acetonitrile-water mixtures up to 3500 bar have been elucidated within a predicted error of 3%. Data corresponded well with the available literature. In its current design, the CTOF viscometer utilized contactless conductivity detectors and a very small inner diameter capillary in order to minimize band-broadening. Possible improvements to this design call for still more accurate pressure measurement and thermostatting the system to maintain temperature with a lower fluctuation (preferably ± 0.1ºC). In addition, chromatography is often performed at temperatures other than 25º C, so it would be of interest to measure high-pressure viscosity at elevated or depressed temperatures.

At the conclusion of the ultrahigh pressure viscosity study, I looked back at the data and realized that although this instrument was designed to minimize C-term broadening, there still was significant bandspreading that occurred between the two detectors (note the difference in the peak widths in Figure 3-5B, bottom). Because of the fast experiment times (~ 1 minute), C-term broadening still outweighed the B-term broadening, so this led me to design an experiment whereby we might quantify the C-term variance accumulated between the detectors, and use it to calculate the diffusion coefficient of an analyte molecule. In this embodiment, the CTOF instrument could employ a very long capillary with a larger inner diameter, perhaps ten meters of 50 μm inner diameter capillary. Taylor dispersion would be amplified and would far outweigh any B-term band broadening, and the Taylor-Aris method

could be used to calculate diffusion coefficients, while solution viscosity is determined by the

same method employed with the current CTOF viscometer. In this way, it might be possible

to measure the viscosity of a solution of interest and the diffusion coefficient of an analyte of

interest in a single experiment. It is this instrument which is described in Chapter 4.

3.5 References

(1)   Mellors, J. S., University of North Carolina at Chapel Hill, Chapel Hill, NC, 2005.

(2)   Karger, B. L.; Snyder, L. R.; Horvath, C. *An Introduction to Separation Science*; John Wiley & Sons, Inc.: New York, 1973.

(3)   Neue, U. D. *HPLC Columns: Theory, Technology, and Practice*; Wiley-VCH, Inc.: New York, 1997.

(4)   Martin, M.; Blu, G.; Guiochon, G. *J. Chrom. Sci.* **1973**, *11*, 641-654.

(5)   MacNair, J. E.; Patel, K. D.; Jorgenson, J. W. *Anal. Chem.* **1999**, *71*, 700-708.

(6)   MacNair, J. E.; Lewis, K. C.; Jorgenson, J. W. *Anal. Chem.* **1997**, *69*, 983-989.

(7)   Patel, K. D.; Jerkovich, A. D.; Link, J. C.; Jorgenson, J. W. *Anal. Chem.* **2004**, *76*, 5777-5786.

(8)   Martin, M.; Guiochon, G. *J. Chrom. A* **2005**, *1090*, 16-38.

(9)   Bridgman, P. W. In *The Physics of High Pressure*; Andrade, E. N. d. C., Ed.; G. Bell and Sons, Ltd.: London, 1931, pp 330-356.

(10)   Harris, K. R.; Woolf, L. A. *J. Chem. Eng. Data* **2004**, *49*, 1064-1069.

(11)   Forst, P.; Werner, F.; Delgado, A. *Rheol Acta* **2000**, *39*, 566-573.

(12)   Mattischek, H. P.; Sobczak, R. *Meas. Sci. Technol.* **1994**, *5*, 782-785.

(13)   Reamer, H. H.; Cokelet, G.; Sage, B. H. *Anal. Chem.* **1959**, *31*, 1422-1428.

(14)   Huss, V.; Chevalier, J. L.; Siouffi, A. M. *J. Chrom.* **1990**, *500*, 241-255.

(15)   Snyder, L. R. *J. Chrom. Sci.* **1977**, *15*, 441-449.

(16)   Aminabhavi, T. M.; Gopalakrishna, B. *J. Chem. Eng. Data* **1995**, *40*, 856-861.

(17)   Abbott, S. R.; Berg, J. R.; Achener, P.; Stevenson, R. L. *J. Chrom.* **1976**, *126*, 421-437.

(18)   Bidlingmeyer, B. A.; Hooker, R. P.; Lochmuller, C. H.; Rogers, L. B. *Sep. Sci.* **1969**, *4*, 439-446.

(19)   Bidlingmeyer, B. A.; Rogers, L. B. *Sep. Sci.* **1972**, *7*, 131-158.

(20)   McGuffin, V. L.; Evans, C. E. *J. Microcol. Sep.* **1991**, *3*, 513-520.

(21)   Guiochon, G.; Sepaniak, M. J. *J. Chrom.* **1992**, *606*, 248-250.

(22)   McGuffin, V. L.; Evans, C. E.; Chen, S. H. *J. Microcol. Sep.* **1993**, *5*, 3-10.

(23)   Macko, T.; Berek, D. *J. Liq. Chrom. Rel. Technol.* **2001**, *24*, 1275-1293.

(24)   Giddings, J. C. *Sep. Sci.* **1966**, *1*, 73-80.

(25)   Mellors, J. S.; Jorgenson, J. W. *Anal. Chem.* **2004**, *76*, 5441-5450.

(26)   Kubota, H.; Tsuda, S.; Murata, M.; Yamamoto, T.; Tanaka, Y.; Makita, T. *Rev. Phys. Chem. Japan* **1979**, *49*, 59-69.

(27)   Isdale, J. D.; Easteal, A. J.; Woolf, L. A. *Int. J. Thermophys.* **1985**, *6*, 439-450.

(28)   Ueno, M.; Ueyama, S.; Hashimoto, S.; Tsuchihashi, N.; Ibuki, K. *J. Solution Chem.* **2004**, *33*, 827-846.

(29)   Thompson, J. W.; Kaiser, T. J.; Jorgenson, J. W. *J. Chrom. A* **2006**, submitted.

(30)   Jones, G.; Dole, M. *J. Am. Chem. Soc.* **1929**, *51*, 2950-2964.

(31)   Lencka, M. M.; Anderko, A.; Sanders, S. J.; Young, R. D. *Int. J. Thermophys.* **1998**, *19*, 367-378.

(32)   Van Wazer, J. R.; Lyons, J. W.; Kim, K. Y.; Coldwell, R. E. *Viscosity and flow measurement*; Wiley & Sons, Inc.: New York, 1963.

(33)   Jerkovich, A. D.; Mellors, J. S.; Thompson, J. W.; Jorgenson, J. W. *Anal. Chem.* **2005**, *77*, 6292-6299.

(34)   Zemann, A. J.; Schnell, E.; Volgger, D.; Bonn, G. K. *Anal. Chem.* **1998**, *70*, 563-567.

(35)   van der Gulik, P. S. *Physica A* **1998**, *256*, 39-56.

(36)   Maini, B. B.; Kokal, S. *Rev. Sci. Instrum.* **1991**, *62*, 2742-2747.

(37)   Colin, H.; Diez-Masa, J. C.; Guiochon, G.; Czajkowska, T.; Miedziak, I. *J. Chrom.* **1978**, *167*, 41-65.

(38)   Giddings, J. C. *Unified Separation Science*; John Wiley & Sons, Inc.: New York, 1991.

(39)   Mellors, J. S.; Jorgenson, J. W. *Anal. Chem.* **2006**, *submitted.*

Percent Methanol in Water (v/v)	Pressure Range (kbar)	α (cP/kbar)	η_0 (cP)
0	0-1	0.0026	0.89
	1-3.5	0.052	0.84*
10	0-1	0.011	1.07
	1-3.5	0.064	1.02*
20	0-3.5	0.049	1.34
30	0-3.5	0.113	1.48
40	0-3.5	0.203	1.56
50	0-3.5	0.263	1.54
60	0-3.5	0.317	1.47
70	0-3.5	0.363	1.30
80	0-3.5	0.364	1.05
90	0-3.5	0.308	0.82
100	0-3.5	0.241	0.55

Table 3-1: Viscosity of methanol-water mixtures as a function of composition (percent by volume) and pressure. α is the slope of the viscosity versus pressure curve for that composition, given in cP per kbar. η_0 is the viscosity at atmospheric pressure (the y-intercept of the viscosity versus pressure curve). Asterisked values are simply the intercept of the high-pressure region and have no physical meaning.

Percent Acetonitrile in Water (v/v)	Pressure Range (kbar)	α (cP/kbar)	η_0 (cP)
0	0-1	0.0026	0.89
	1-3.5	0.052	0.84*
10	0-1	0.036	0.96
	1-3.5	0.077	0.92*
20	0-1	0.063	0.98
	1-3.5	0.097	0.95*
30	0-3.5	0.132	0.92
40	0-3.5	0.163	0.89
50	0-3.5	0.195	0.81
60	0-3.5	0.214	0.75
70	0-3.5	0.232	0.63
80	0-3.5	0.219	0.53
90	0-3.5	0.216	0.39
100	0-3.5	0.190	0.34

Table 3-2: Viscosity of acetonitrile-water mixtures as a function of composition (percent by volume) and pressure. α is the slope of the viscosity versus pressure curve for that composition, given in cP per kbar. η_0 is the viscosity at atmospheric pressure (the y-intercept of the viscosity versus pressure curve). Asterisked values are simply the intercept of the high-pressure region and have no physical meaning.
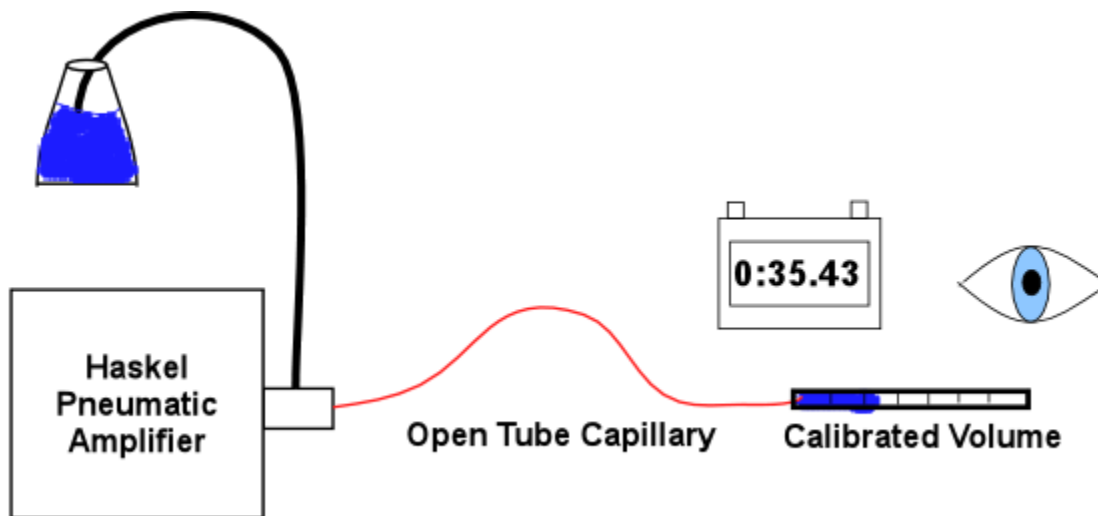
Figure 3-1: Cartoon schematic of the open tube method for viscosity determination. A Haskel pump is used to drive flow at a known pressure through an open tube capillary of known diameter, and the flow rate is measured (volume per unit time) using a calibrated pipette and a stopwatch. Viscosity is then determined using the Poiseuille Equation. Drawing is not to scale.
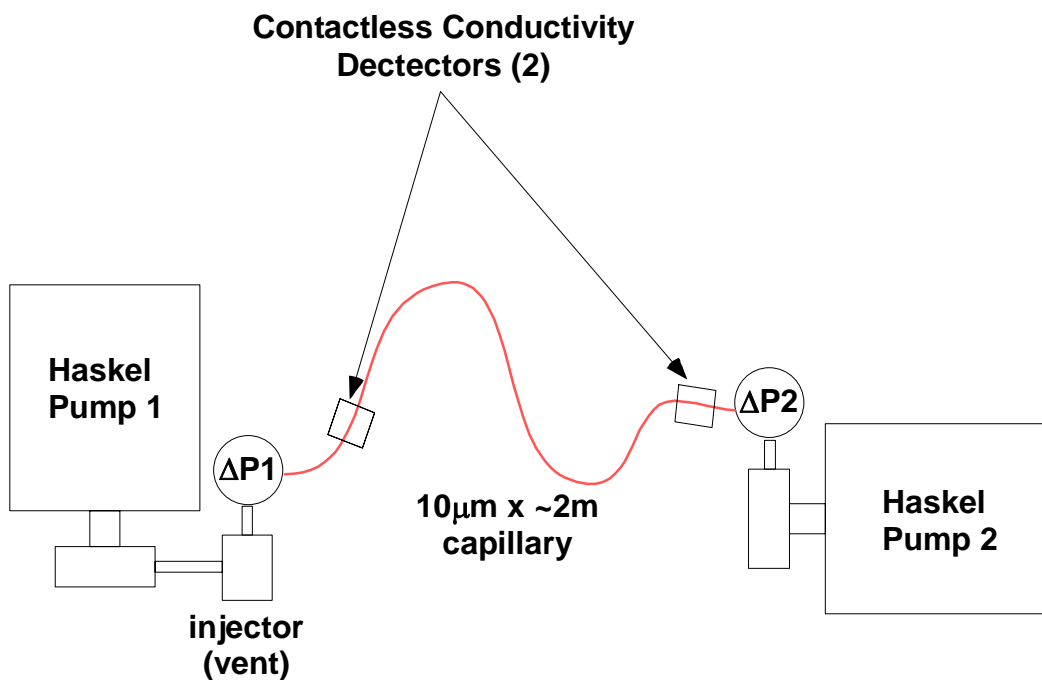
Figure 3-2: Dual-pump configuration for determination of viscosity by time-of-flight of a conductive front through an open tube. Mobile phases in the two pumps are identical, except mobile phase in the Pump 1 has a slightly higher conductivity than that in Pump 2. ΔP denotes a pressure sensor. Drawing is not to scale.
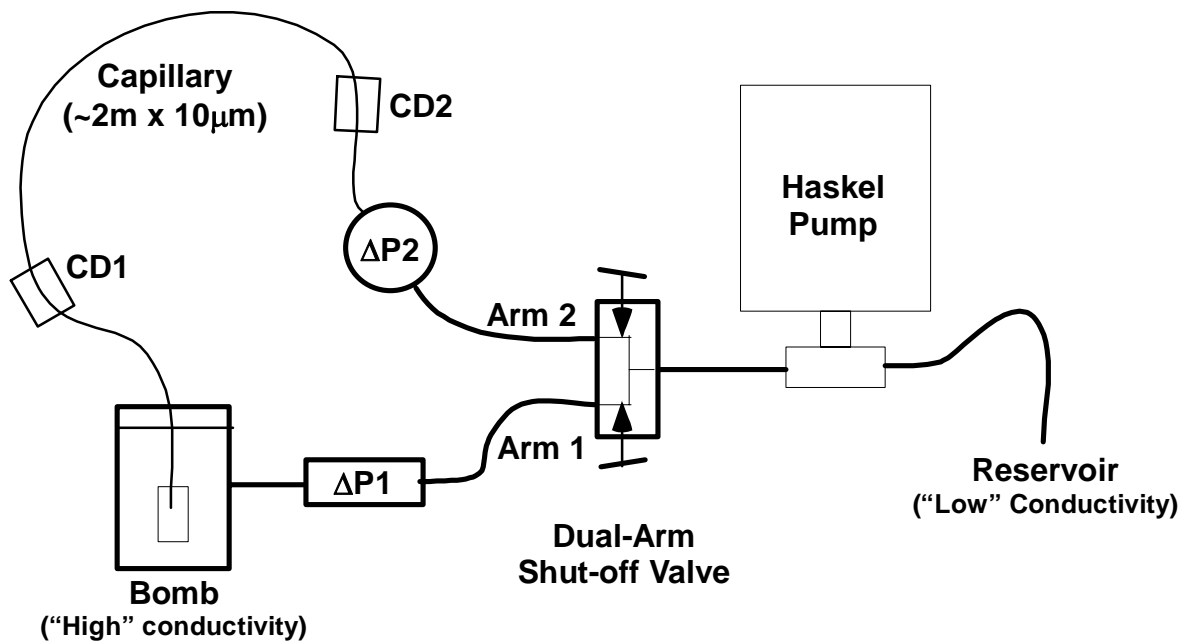
Figure 3-3: Scheme of the capillary time-of-flight (CTOF) viscometer. Mobile phases in the bomb and the reservoir are typically identical, except mobile phase in the bomb has a slightly higher conductivity. Abbreviations; CD: contactless conductivity detector, ΔP: pressure sensor. For detailed explanation of operating principles, see text. Drawing is not to scale.
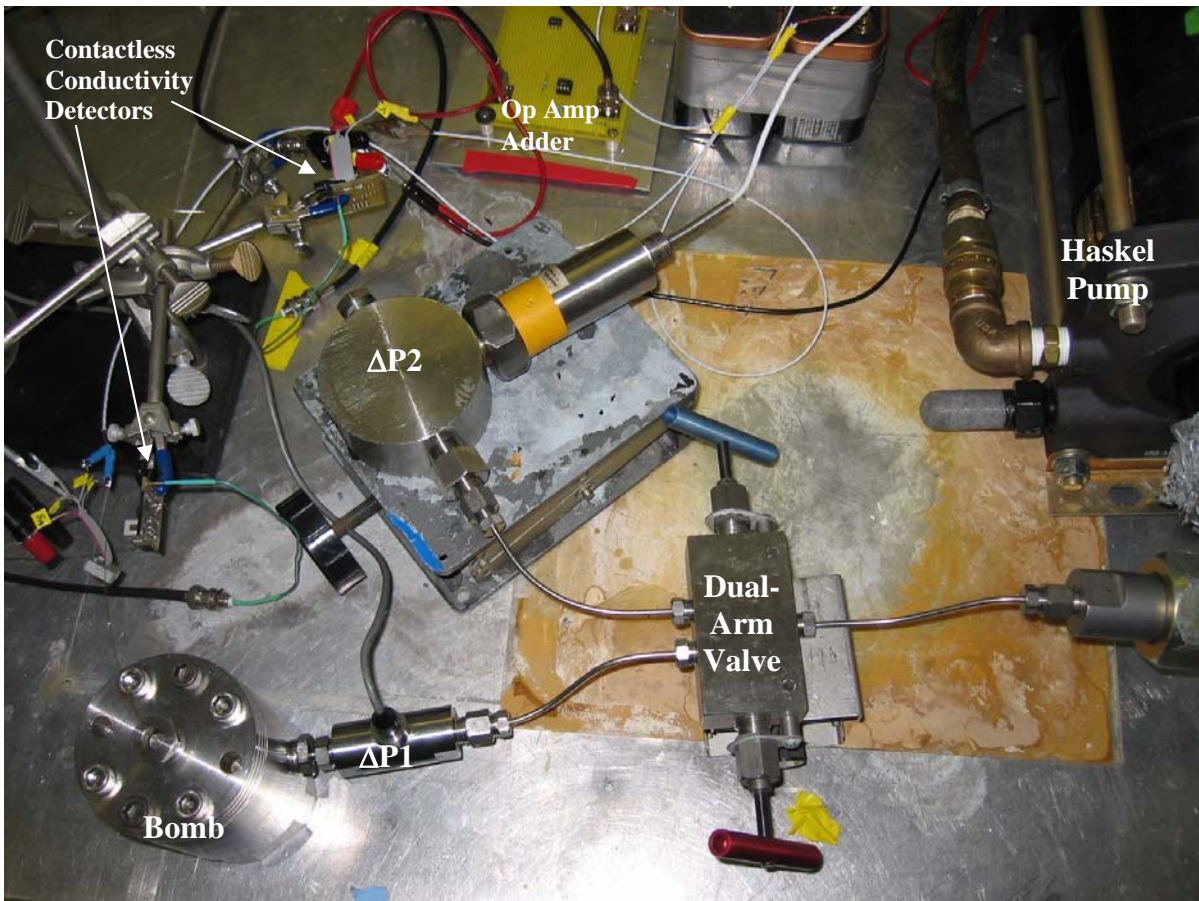
Figure 3-4: Photograph of the CTOF viscometer configured as shown in the schematic Figure 3-3. The capillary is present, but is not plainly visible in the photograph.
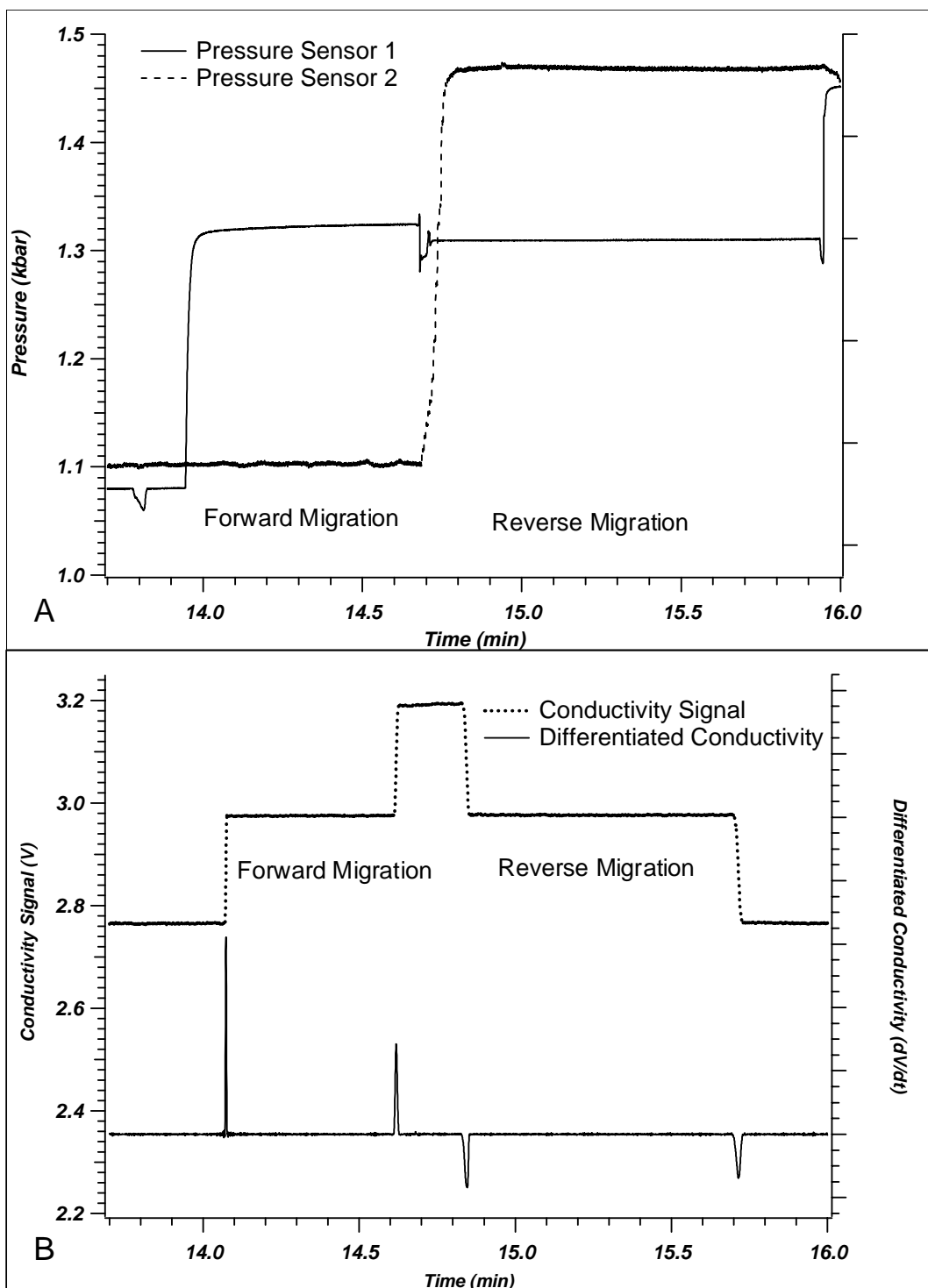
Figure 3-5: Raw data collected during the viscosity measurement of 50/50 v/v acetonitrile/water. (A) Pressure traces from Sensors 1 and 2. Sensor 1 is used for all pressure measurements. Sensor 2 is only used to ensure that the pressure at the outlet end of the capillary is constant during the forward migration. Sensor 2 has been offset by 0.02 kbar for visualization. (B) Conductivity signal (top) as collected from the conductivity detectors, and the differentiated signal (bottom) used to accurately determine migration times.
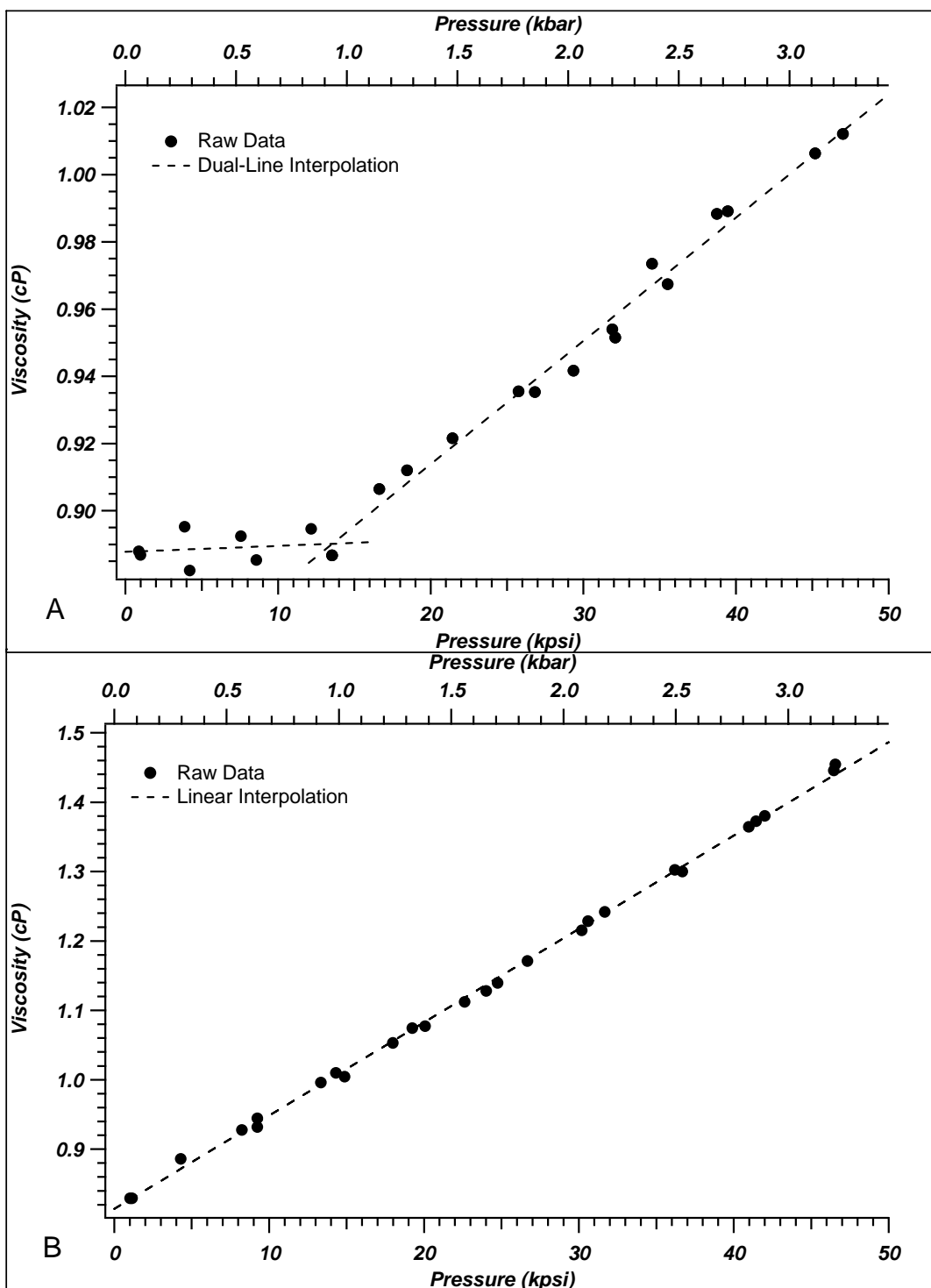
Figure 3-6: Raw data points for viscosity as a function of pressure and the linear fits performed to the data. (A) Raw data for 100% water with < 0.1% TFA. Interpolation is performed in two linear regions, one below and one above roughly 1 kbar. (B) Raw data for 50/50 v/v acetonitrile/water with < 0.1% TFA. Interpolation is perfomed in with a single linear regression.

Figure 3-7: Viscosity of water at 25ºC under ultra-high pressures. (●): Combination of two data sets from the CTOF viscometer. (□): Data from Harris and Woolf (2004) using a falling body viscometer.
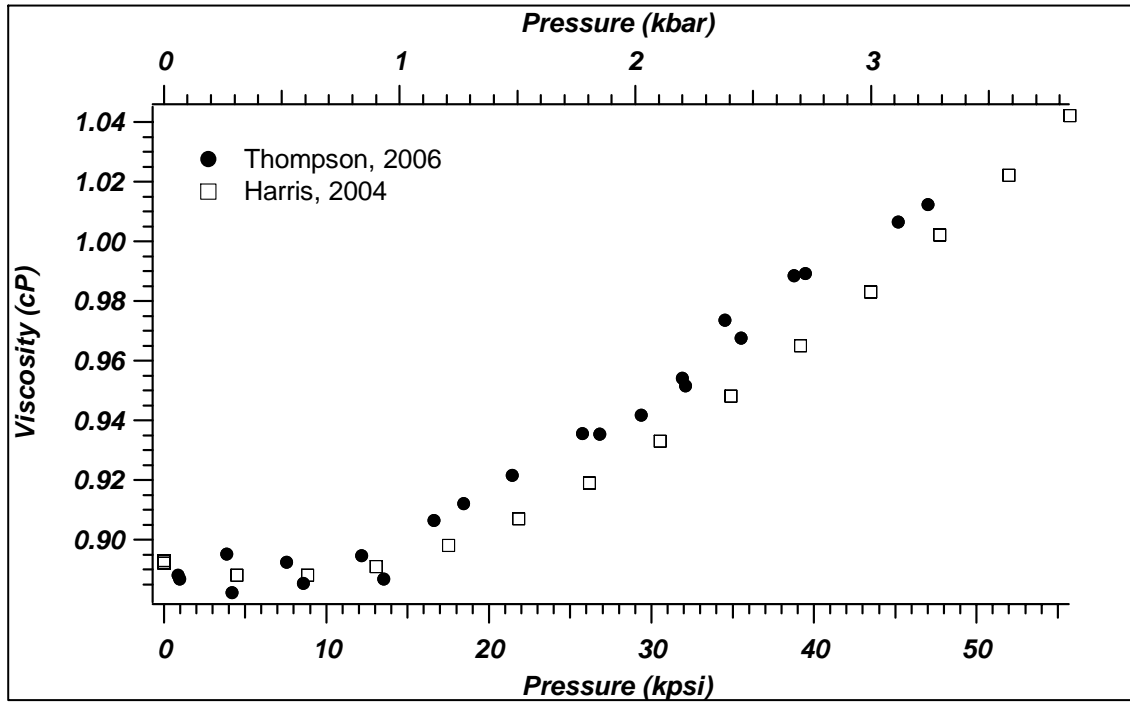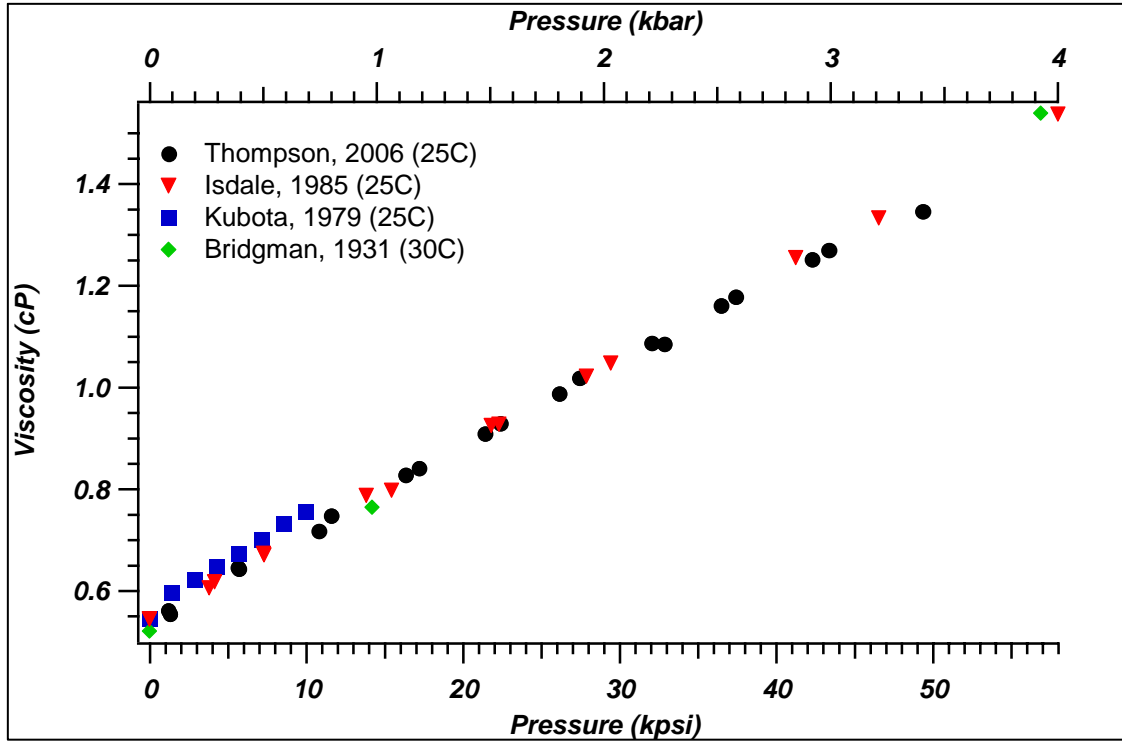
Figure 3-8: Viscosity of methanol under ultra-high pressures. (●): Combination of two data sets from the CTOF viscometer at 25ºC. (▼): Data from Isdale et al. (1985) using a falling body viscometer at 25ºC. (■): Data from Kubota (1979) using a falling body viscometer at 25ºC. (♦): Data from Bridgman (1931) using a falling body viscometer at 30ºC.
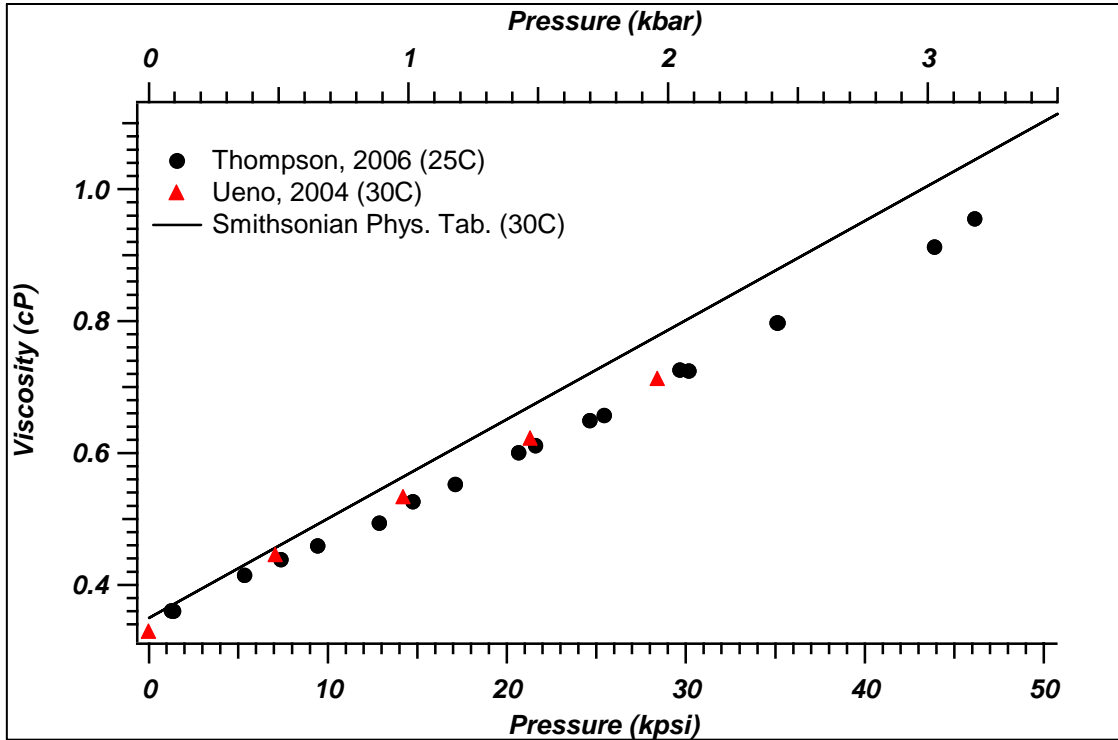
Figure 3-9: Viscosity of acetonitrile under ultra-high pressures.(●): Combination of two data sets from the CTOF viscometer at 25ºC. (▲): Data from Ueno et al. using a falling-body viscometer at 30 ºC. (-): Slope and intercept from the Smithsonian Physical Tables at 30ºC.
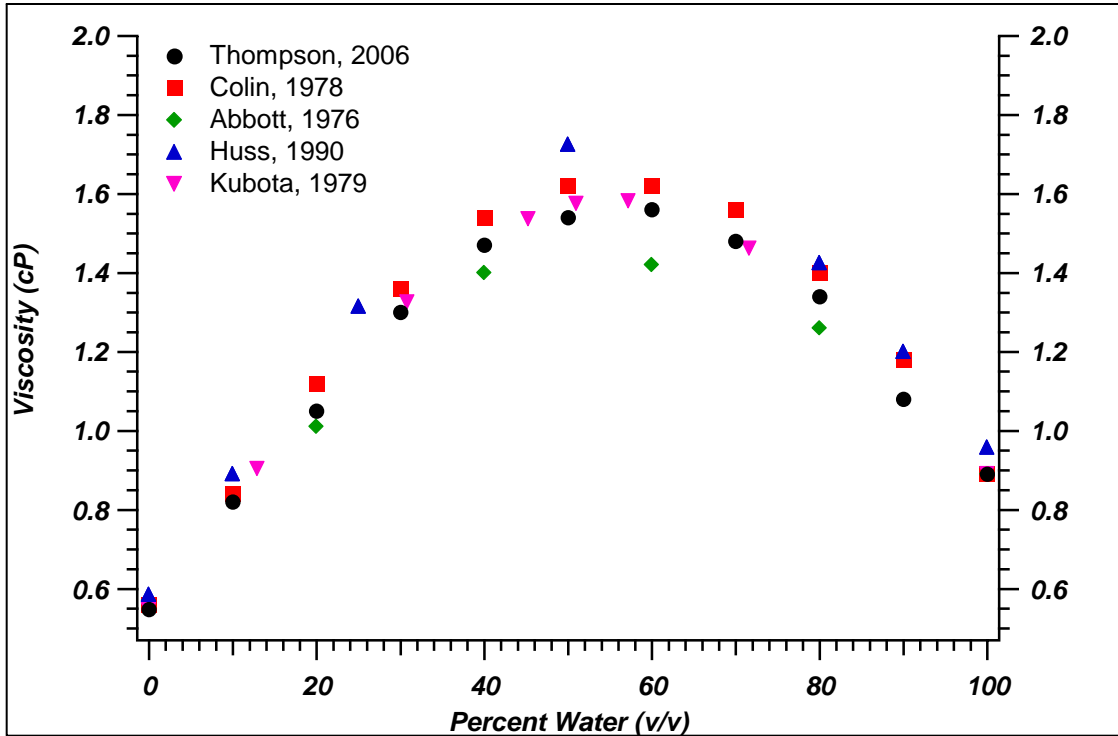
Figure 3-10: Atmospheric pressure viscosity of methanol-water mixtures as a function of composition, at 25° C. (●) denotes the data generated from experiments with the CTOF viscometer; literature values are identified by the first author's last name and date of the reference.
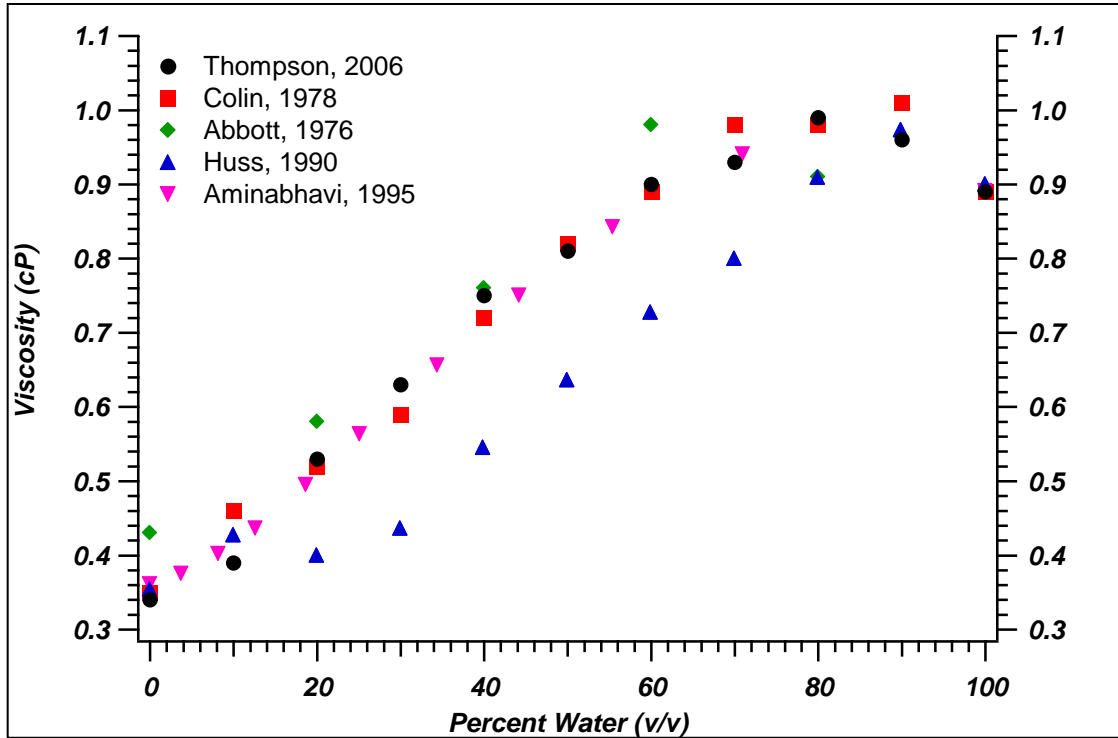
Figure 3-11: Atmospheric pressure viscosity of acetonitrile-water mixtures as a function of composition, at 25° C. (●) denotes the data generated from experiments with the CTOF viscometer; literature values are identified by the first author's last name and date of the reference.
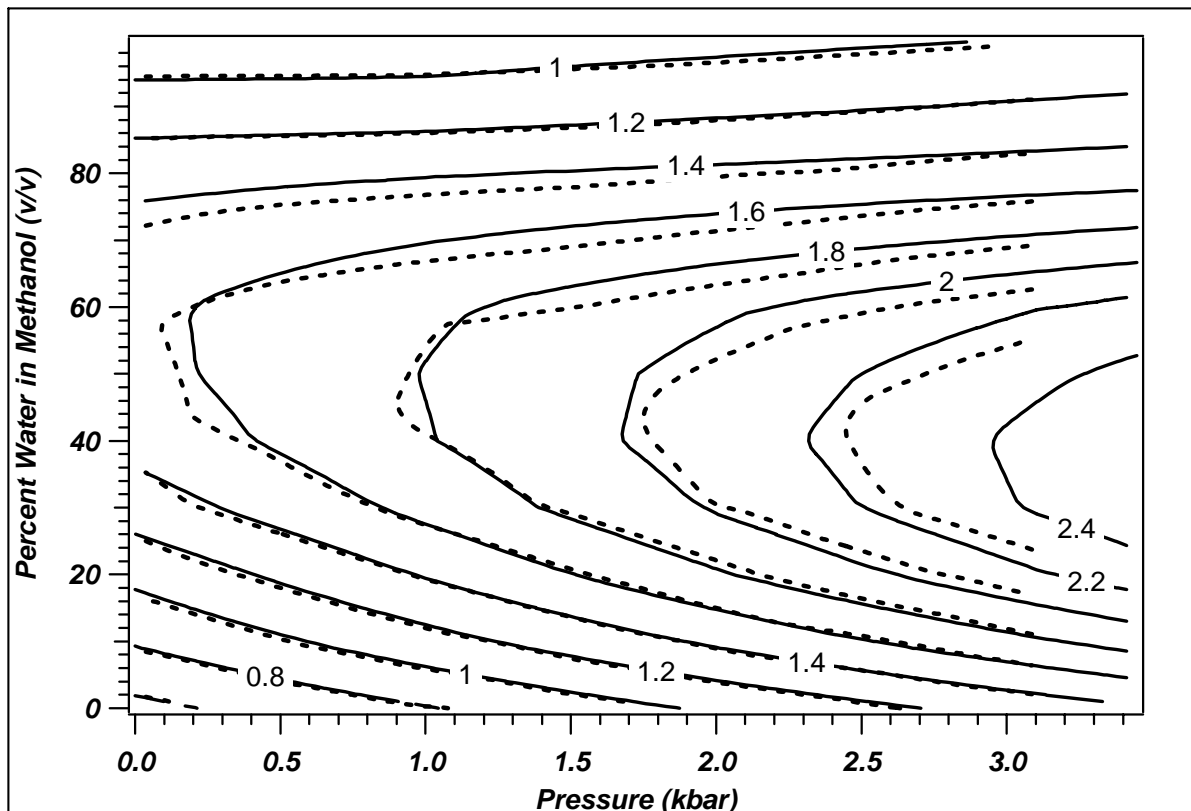
Figure 3-12: Contour plots for the viscosity of methanol-water mixtures as a function of composition (percent water by volume) and pressure (kbar). Viscosity is shown in units of centipoise (cP). Each contour line corresponds to a viscosity change of 0.2 cP. Solid lines represent a matrix interpolation of data obtained using the CTOF viscometer at 25°C. Dashed lines represent an interpolation of data reported by Isdale et al., using a falling body viscometer, at 25°C.
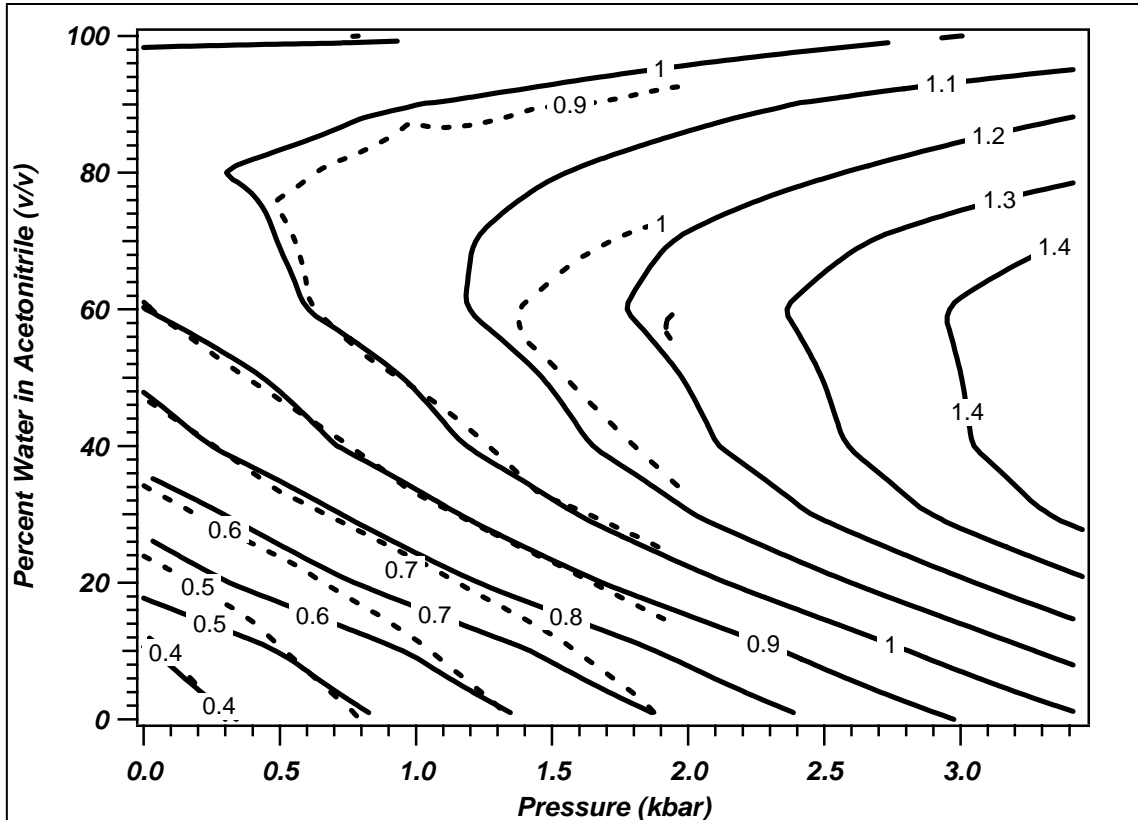
Figure 3-13: Contour plot showing viscosity of acetonitrile-water mixtures as a function of composition (percent water by volume) and pressure (kbar). Viscosity is shown in units of centipoise (cP). Each contour line corresponds to a viscosity change of 0.1 cP. Solid lines represent a matrix interpolation of data obtained using the CTOF viscometer at 25°C. Dashed lines represent an interpolation of data reported by Ueno et al., using a falling body viscometer, at 30°C. The deviation is consistent with that expected of a five degree temperature difference.
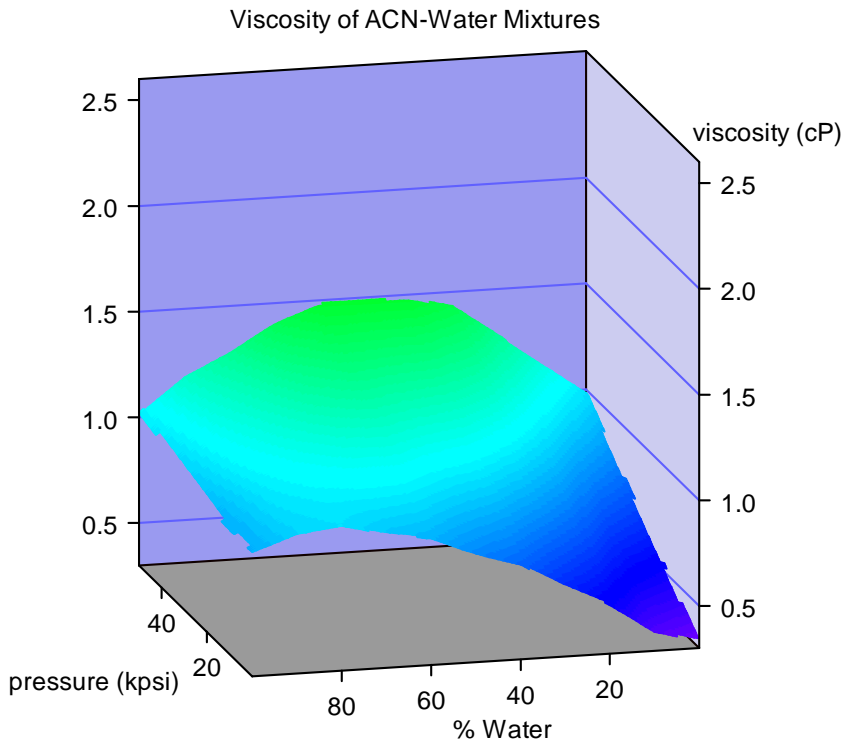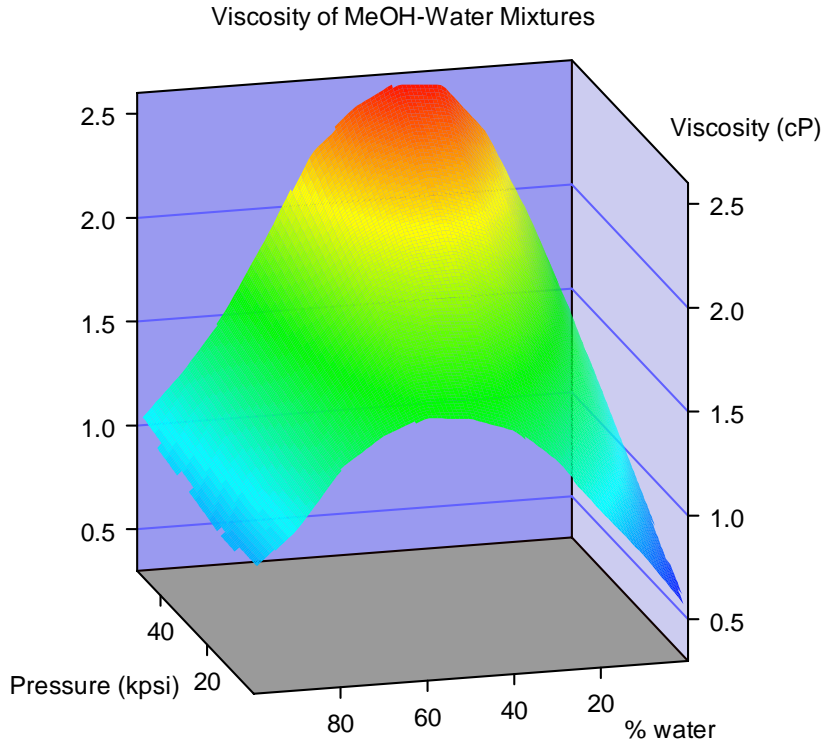
Figure 3-14: Three-dimensional visualization of viscosity for methanol-water (top) and acetonitrile-water (bottom) mixtures at pressures up to 50,000 psi (3500 bar). Scales are identical to enable a more direct comparison. Plots created in Igor Pro 4.08 using the surface plot function.
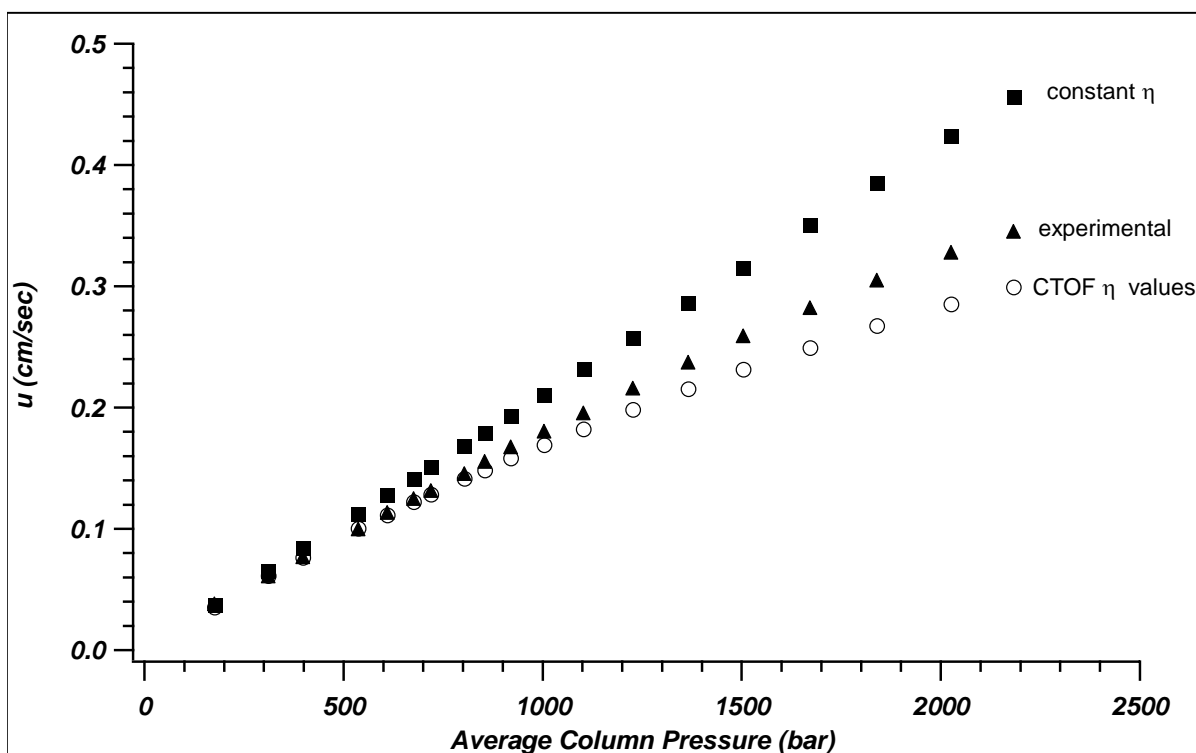
Figure 3-15: Linear velocity versus average column pressure for a 49.3-cm capillary column packed with 1.56 μm BEH C18 particles, with 50/50 v/v acetonitrile/water, 0.1% TFA as the mobile phase. (▲) Experimentally determined values based on the dead time of the column. (■) Calculated velocity using a constant (atmospheric) mobile phase viscosity (η) in the Kozeny-Carman equation. (○) Calculated velocity using the mobile phase viscosity (η) as determined by the CTOF viscometer.

4 SIMULTANEOUS MEASUREMENT OF SOLUTE DIFFUSION AND SOLUTION VISCOSITY

4.1 Introduction

In the previous Chapter I described an instrument designed to measure solution viscosities at ultrahigh-pressures, dubbed the capillary time-of-flight (CTOF) viscometer.[1] In this chapter another embodiment of this instrument design is introduced which uses Taylor dispersion to measure an analyte's diffusion coefficient at the same time as poiseuille-flow is used to measure solution viscosity. The motivation behind this work was to develop a time-effective method for measuring diffusion coefficients at ultrahigh pressures so that these values can ultimately be applied to assist in van Deemter evaluation of chromatography columns.

4.1.1 Diffusion Theory

Diffusion refers to the random process by which molecules move. The importance of molecular diffusion to the *B*- and *C*-terms in chromatographic bandspreading was discussed in Chapter 1. In general, net molecular flux due to a concentration gradient can be described simply by Fick's first law, which defines a diffusion coefficient (*D*) as a molecular constant characteristic of the molecule of interest:

$$J = -D\frac{\partial C}{\partial x} \qquad (4\text{-}1)$$

where J is the flux in mol sec^{-1} of the molecule due to the concentration gradient dC/dx.[2] Note the right side of the equation is negative, because net molecular flux always occurs in the general direction of high to low concentration. The change in concentration with time due to molecular diffusion can be defined by Fick's second law:[2]

$$\frac{\partial C}{\partial t} = D\frac{\partial^2 C}{\partial x^2}$$

(4-2)

On the basis of Fick's second law, two general mechanisms by which molecular diffusion can be measured in a capillary tube have been described in the literature. The first is the so-called "stopped-flow method", in which molecular diffusion is observed as a change in concentration with time over a prescribed distance, absent of any induced flow. The second is the Taylor-Aris method, in which the dispersion of a solute in a flowing stream of solvent can be used to measure the diffusion coefficient.

4.1.2   Stopped-Flow Method for Measuring Molecular Diffusion

The stopped-flow method of measuring diffusion takes advantage of the chromatographic B-term, or longitudinal diffusion, to measure a molecule's diffusion coefficient. In an open tube, the spatial variance (σ_L^2, cm^2) generated by diffusion per unit time (t) can be described by the Einstein equation:[3]

$$\sigma_L^2 = 2Dt$$

(4-3)

To measure diffusion by this mechanism, all that is needed is a method by which to measure the accumulated variance in a specified length of time.

In order to perform this experiment, it is typically necessary to push a solvent front into a capillary tube, where it will be paused to allow for longitudinal diffusion. During this

migration, variance is accumulated due to flow (C-term) and time (B-term). Therefore the most accurate way to perform this experiment is to set up a system where the initial variance is subtracted from the total variance, to obtain a measure that is due solely to molecular diffusion during the pause:

$$\sigma^2_{Lpause} = \sigma^2_{Ltotal} - \sigma^2_{Lmigration} \qquad (4\text{-}4)$$

The pause variance and pause time can then be substituted into (4-3) to obtain D. The most accurate way to perform a stopped-flow diffusion measurement is to migrate a front through the capillary tube and measure the variance accumulated; this is denoted as $\sigma^2_{Lmigration}$. Then perform the same migration but pause the front in the center of the tube for the desired amount of time to allow for longitudinal diffusion, and call the accumulated variance in this case σ^2_{Ltotal}. Equation (4-4) can then be used to obtain the variance that accumulated only during the pause. Mellors used this type of system to measure diffusion coefficients at atmospheric pressure and at pressures up to 4200 bar.[4] The elevated-pressure experiments were performed by migrating the analyte to the middle of a capillary tube, then pressurizing both ends of the capillary tube for the extent of the pause period. The capillary was then depressurized and the analyte front was migrated through the detector to measure σ^2_{Ltotal}.

This stopped-flow method was expected to be the most accurate way to measure molecular diffusion coefficients in a capillary at atmospheric pressure because of the lack of influence of instrumental variables such as capillary diameter. However, a major drawback to this method is time. For a small molecule with $D \sim 1\text{x}10^{-5}$ cm^2/sec, approximately 24 hours of pause to allow diffusion is needed in order to obtain an accurate measurement. This makes the stopped-flow technique impractical for measuring diffusion coefficients of

biomolecules ($D \sim 1\times10^{-6}$ cm^2/sec), which by analogy would need approximately 10 days of diffusion time to accumulate the same level of dissipation.

I should state here for completeness that I have only considered stopped-flow devices of the conventional (capillary) design in this discussion. It is possible that if the dimensions of the UV detectors were reduced such that the capillary length could be shortened significantly, it might be feasible to perform stopped-flow experiments requiring much shorter pause times. Microfluidic devices might provide an excellent avenue for stopped-flow diffusion measurements, although appropriate "universal" detection techniques like UV are not currently available on microfluidic devices.

4.1.3 Taylor-Aris Method for Measuring Molecular Diffusion

In a series of papers in the 1950's, Geoffrey Taylor and Rutherford Aris described a method by which molecular diffusion could be measured by the dispersion of a solute in a stream of fluid flowing in a tube.[5-7] This type of dispersion was later related to C-term (mass transfer) band broadening in open tubular chromatography. Golay described the spatial variance contribution (σ_L^2, cm^2) from flow-induced dispersion for an unretained solute in an open tube as:

$$\sigma_L^2 = \frac{d_c^2 u L}{96 D} \tag{4-5}$$

where d_c is column diameter, u is the mobile phase linear velocity, and L is the migration distance.[8] This equation can be rearranged so that variance, linear velocity, and capillary dimensions can be used to solve for the molecular diffusion coefficient:

$$D = \frac{d_c^2 u L}{96 \sigma_L^2} \tag{4-6}$$

Using this equation or variations thereof, Taylor dispersion has been used to measure molecular diffusion with systems using detection techniques from UV-Vis and fluorescence spectroscopy to mass spectrometry.[9-12]

In most chromatographic systems, variance is much more easily measured as a function of time (σ_t^2, sec^2), than space (σ_L^2, cm^2). The conversion from temporal variance to spatial variance is performed by multiplying by the linear velocity squared:

$$\sigma_L^2 = \sigma_t^2 u^2 \tag{4-7}$$

Substituting (4-7) into (4-6) and simplifying, we obtain:

$$D = \frac{d_c^2 L}{96\sigma_t^2 u} \tag{4-8}$$

Most diffusion-measurement systems utilizing Taylor dispersion in the literature have used a single detector and have assumed an infinitely narrow band at the introduction of a front to the capillary.[9-12] To make a very accurate measurement of accumulated variance over a defined distance, two detectors can be used. With a dual-detector setup, u is calculated as:

$$u = \frac{L_m}{\Delta t} \tag{4-9}$$

where L_m is the migration distance between the detectors and Δt is the time it takes for the analyte front to migrate from one detector to the next. In addition, if variance is measured by flowing a front past the detector, the sigmoid-shaped front can be differentiated to generate a Gaussian peak. The width at base of the Gaussian peak (w_b, sec) is defined as:

$$w_b = 4\sigma_t \tag{4-10}$$

The difference in the Gaussian "peak" widths at the two detectors can be used to calculate the temporal variance accumulated between the detectors:

$$\sigma_t^2 = \left(\frac{w_{b2} - w_{b1}}{4}\right)^2 \qquad (4\text{-}11)$$

Substituting (4-9) and (4-11) into (4-8), we obtain:

$$D = \frac{d_c^2 \Delta t}{6(w_{b2} - w_{b1})^2} \qquad (4\text{-}12)$$

(4-12) is the equation used to translate raw data from a dual-detector Taylor-Aris experiment into a molecular diffusion coefficient. The capillary diameter (d_c) in expression (4-12) refers to the average capillary dimensions between the two detectors, or the capillary over which the variance being measured is accumulated. Note that in order for (4-12) to be used to make accurate measurements of D, the capillary diameter must be known to a high accuracy. In addition the volumetric flow rate of the mobile phase must be constant as the front passes the two detectors and at all points in between to enable consistent measurement of w_b.

One final stipulation for diffusion measurements with a Taylor-Aris apparatus is that the instrument configuration must allow for the analyte front to be significantly relaxed by diffusion during the time the analyte flows through the tube. Without this appropriate relaxation time, the front will not assume a sigmoidal shape and measurement of molecular diffusion by equation (4-12) is not possible. Another way to qualify this statement is to say that the apparatus must satisfy at least a minimum number of theoretical plates. The stipulation was quantified by Taylor, who said that in order for an accurate D measurement to be made by flow-induced dispersion, the configuration must meet the requirement:

$$\Delta t \gg \frac{d_c^2}{(28.88)D} \qquad (4\text{-}13)$$

where the variables are as described previously.[6] For an instrument of the configuration described later in this chapter ($\Delta t \sim 20$ sec and $d_c \sim 50$ μm), the diffusion coefficient that

results from rearranging (4-13) and solving for D is roughly 4.3×10^{-8} cm^2/sec. If we assume that a one order of magnitude cushion is enough to satisfy the inequality in expression (4-13), then the minimum diffusion coefficient we might "accurately" measure is roughly 4×10^{-7} cm^2/sec. Therefore, the apparatus described herein should be capable of measuring diffusion coefficients for analytes ranging from small organic molecules to moderately-sized proteins.

The Taylor-Aris method has the main advantage compared to the stopped-flow method that it is relatively fast (c.a. minutes per D measurement, compared to hours for stopped-flow). In addition, since variance contribution from flow is greater for large molecules (see equation (4-5)) the Taylor-Aris method has the potential to work just as well for biomolecules as for small molecules. The main drawback is the heavy dependence on the accurate determination of instrument parameters such as capillary diameter (squared) and mobile phase flow rate.

It has been stated previously that the Taylor-Aris method is not amenable to diffusion coefficient determination at ultrahigh pressures, because of complications due to solvent compression and the difficulty of accurately measuring the capillary diameter.[4] Use of the CTOF instrument as described in Chapter 3 circumvents the compression problem because the capillary is pressurized from both ends, so that the actual pressure drop across the measurement capillary is small. It was hoped the capillary diameter issue could be addressed by using an analyte with a well-known diffusion coefficient to calibrate d_c.

4.2 Molecular Diffusion Estimation Based on Viscosity

In Chapter 3, I described an instrument that was developed to measure solution viscosity at ultrahigh pressures, with the goal of using viscosity to approximate diffusion

coefficients at ultrahigh pressures. This approximation was carried out using a previously-determined atmospheric-pressure diffusion coefficient, and estimating the elevated-pressure value based on the change in solution viscosity. The Stokes-Einstein relationship was used for this purpose:

$$D = \frac{kT}{6\pi r \eta}$$
(4-14)

where k is the Boltzmann constant, T is temperature, and r is the hydrodynamic radius of the solute. Since all terms except η and D are expected to remain essentially constant with pressure, the equation can be rewritten:

$$D = \frac{\delta}{\eta}$$
(4-15)

To define the constant δ, the atmospheric pressure values for D and η were inserted:

$$\delta = D_{atm}\eta_{atm}$$
(4-16)

To then approximate the elevated-pressure D value (D_{elev}), we used:

$$D_{elev} = \frac{\delta}{\eta_{elev}}$$
(4-17)

Tables 4-1 and 4-2 contain values of diffusion coefficients for hydroquinone in two different solvent systems that were obtained by Mellors at pressures up to 4200 bar using a stopped-flow system.   Also included are the viscosity values at elevated pressure and the estimated diffusion coefficients resulting from the approximation method described by (4-14) through (4-17). Figures 4-1 and 4-2 allow a graphical comparison of the actual measured D values and those estimated using the Stokes-Einstein relationship. It is obvious from this comparison that the data observed by Mellors cannot be fully explained by viscosity change.

As shown in Figure 4-1, the diffusion coefficient measured by the stopped-flow method increased for hydroquinone in 10/90 (v/v) acetonitrile/water, when pressure was applied.[4] If the trend in D were solely due to viscosity change, this would require the viscosity to decrease with applied pressure, which only occurs for pure water at temperatures below 20°C.[13] The viscosity change predicted a shallow decrease in D with pressure, so it appeared from this analysis that for the system of hydroquinone in 10/90 (v/v) acetonitrile/water, estimation of D based on Stokes-Einstein performed poorly.

For the system of hydroquinone in 50/50 (v/v) acetonitrile/water shown in Figure 4-2, the estimation worked somewhat better (at least predicting the direction of the trend correctly). However, the viscosity data again predicted a much larger change in D than actually occurred according to Mellors.[4] Looking at these two systems, it seemed that the simple method of estimating D based on change in η at ultrahigh pressures was inadequate for purposes of evaluating chromatographic columns. My motivation for developing the CTOF instrument so that diffusion coefficients and viscosity measurements could be made simultaneously was therefore two-fold. First, the stopped-flow method of measuring D was prohibitively time-consuming for doing any large-scope studies and the idea of measuring D with the CTOF instrument (via Taylor dispersion) provided an enticing throughput incentive. Second, we were interested to see if the diffusion measurements from the CTOF instrument would corroborate those obtained by Mellors' stopped-flow method.

4.3   Experimental

The general concept and design of the capillary time-of-flight (CTOF) instrument was described in Chapter 3, in an embodiment that used contactless conductivity detectors, a

narrow-diameter capillary and pressurization of this capillary from both ends to allow for viscosity measurements at ultrahigh pressures. This experimental section is intended as an extension of that discussion, in which the instrument was modified with the goal of performing diffusion coefficient measurements as well as viscosity measurements. A series of modifications were made to this instrument and this experimental section highlights the motivation behind each of those modifications. The course of this development led to the instrument which was used to perform the measurements discussed in the results section.

4.3.1 Phase 1 Modifications to CTOF Instrument

4.3.1.1 Detection

With the CTOF viscometer, contactless conductivity detection was used because very narrow capillary inner diameters were used (~10 μm) in order to minimize band broadening. These detectors work well for small capillaries, but are limited to detection of ionic (conductive) analytes. In order for the diffusion experiment to be practical, a more universal detection method was desired. Thus, the conductivity detectors were replaced with on-capillary UV-Vis detectors (Linear UVis 200, ThermoElectron, Waltham, MA), as shown in Figure 4-3. UV-Vis was a viable option because of its compatability with a large number of analytes, and these detectors allowed for open tubular capillaries from 30 μm to 150 μm inner diameter. UV detectors were interfaced to separate channels of a BNC-2090 DAQ board (National Instruments, Austin, TX), and data was collected at 21 or 51 Hz with Stripchart Recorder XP (www.alchemistmatt.com/resume/stripchartrecorder.html), written in Labview 6.

4.3.1.2 Maximizing Taylor Dispersion

As discussed above, measurement of diffusion coefficients by Taylor dispersion works best when C-term broadening is maximized and B-term broadening (longitudinal diffusion) is minimized. Examining (4-3) and (4-5), it is apparent that the experimental optimization requires maximizing column diameter, column length, and linear velocity, while minimizing time. With this in mind, the obvious change to the CTOF instrumentation was to use a longer, larger inner diameter capillary.

In the CTOF viscometer, we used a ~10 μm i.d. capillary roughly 2 m long. Assuming a 2,000 psi (138 bar) pressure drop, solution viscosity of 1 cP, and $D = 1x10^{-6}$ cm^2/sec, we can use (4-3) and (4-5) to calculate the B- and C-term variance accumulated, respectively (denoted here as σ_B^2 and σ_C^2). The 2 m x 10 μm capillary has a dead time of 92.8 seconds, gives $\sigma_B^2 = 0.00185$ cm^2, and $\sigma_C^2 = 0.111$ cm^2. If the quantity of interest is σ_C^2, an inherent error of 1.6% will therefore be present due to B-term broadening with this capillary. However, if we switch to a 10 m x 50 μm capillary as shown in Figure 4-3, and keep all other parameters constant, it results in a situation much more favorable for measuring diffusion by Taylor dispersion. With the new capillary the dead time is the same and thus σ_B^2 is the same as the previous case, but $\sigma_C^2 = 70.117$ cm^2, a 625-fold increase. The estimated B-term error was therefore reduced to 0.0026%.

The experimental configuration shown in Figure 4-3 used a 50 μm capillary 973 cm in length, with 820 cm between the two detectors. Figure 4-4 shows one of the very few experiments done with this experimental setup, before a critical flaw was realized. Recalling the experimental procedure for operating the CTOF viscometer from Chapter 3, in order to push a front forward through the capillary it is necessary to close the valve on the ΔP2 side of the instrument and subsequently apply a pressure increase at the bomb. Flow is induced by a

small (~140 bar) pressure drop across the column. For the CTOF viscometer, the capillary was 2m x 10 μm in diameter, and therefore the flow through the capillary was not enough to cause a pressure increase at the outlet side of the capillary. By increasing the capillary dimensions to 10 m x 50 μm, the volumetric flow rate increased by 125-fold. The ~2 mL volume inside pressure sensor 2 was not enough to allow this volumetric flow increase and the resultant pressure increase at ΔP2 during the migration is shown in Figure 4-4 (top, blue traces), starting at 14.4 minutes.

This was a critical flaw because the pressure drop was not constant across the column during the run, so neither viscosity nor diffusion coefficient could be measured. Note the fronts (Figure 4-4 bottom) appear to be tailed because the linear velocity was slowing during the forward migration. The way to fix this was obviously to increase the volume in the region of ΔP2, so that the flow through the column would not cause the pressure to increase. A large reservoir placed on the "outlet" (ΔP2) side of the system would act like a fluidic spring by allowing flow into that region while maintaining relatively constant pressure.

4.3.2   Phase 2 Modifications to CTOF instrument

4.3.2.1 Fluidic Spring

To increase the volume in the ΔP2 region, our idea was to add a large volume reservoir between ΔP2 and the dual-arm valve, as shown in Figure 4-5 ("fluidic spring"). This was much simpler in concept than to implement. Using the isothermal compressibility equation for fluids, both the volume decrease caused by adding pressure to a liquid, and the pressure increase caused by adding fluid into a fixed volume can be calculated.[14] The approximate flow expected through our 10m x 50 μm capillary during a one minute

109

experiment was 13 μL, and we empirically set a target pressure increase of 10 psi at the outlet during an experiment.

With these parameters, a reservoir filled with water (isothermal compressibility = 4.52×10^{-4} MPa^{-1}), required a volume of ~300 mL. Therefore, we were faced with finding or manufacturing a reservoir with a volume greater than 300 mL that could withstand pressure on the order of 50,000 psi. To reduce the volume required, we decided to use a very compressible fluid in the reservoir (somewhat analogous to using a spring with a lower spring constant). However, the caveats to this idea were that the fluid had to be totally immiscible with our mobile phase (so as to not disturb the h and D measurements), and also more dense than water in order to sit at the bottom of the reservoir. It turned out that perfluorocarbons were an appropriate fit. No data for isothermal compressibility for perfluorcarbons was available, but personal communication with Dr. Andy Joel (F2 Chemicals, Preston, UK) revealed a value of 3.28×10^{-3} MPa^{-1} for perfluorohexane at 35°C. Fluorinert FC-5320 was obtained from 3M Corporation, and contained mostly C9-C11 perfluorocarbon. This material had an estimated isothermal compressibility of ~2×10^{-3} MPa^{-1} at 25°C and a density of 1.6 g/mL. By using FC-5320 in the fluidic spring, the estimated volume required to accommodate 13 μL with only 10 psi increase in pressure was decreased to ~50 mL.

At this point, I set out to design and machine a reservoir that had a volume of 50 mL and pressure capability of greater than 50,000 psi (3500 bar). The draft documents for this reservoir, which was machined from a single 3-inch diameter piece of 17-4 PH stainless steel round stock, are shown in Figure 4-6 (Solidedge v11, drawings performed by Ted Kaiser). The reservoir bomb was machined with dimensions as noted in the draft. A one-piece seal

was machined out of polyether-ether-ketone (PEEK) polymer. Figure 4-7 is a cutaway rendering of the reservoir as it would be assembled.

The reservoir was connected to the CTOF instrument using 60,000-psi HiP fittings and tubing (High Pressure Equipment Company, Erie, PA), positioned between ΔP2 and the dual-arm valve, as shown in Figure 4-5. The fluidic spring proved to be effective at removing the increase in ΔP2 readings when flow was in the forward direction. The practical pressure limitation for the system with this reservoir was roughly 2400 bar (34,000 psi), for two reasons. At this pressure the PEEK seal started leaking so that pressure could not be maintained. Also, the pressure started to rise again at ΔP2 when forward migration was performed near 30,000 psi, presumably because the FC-5320 perfluorocarbon was significantly compressed at this pressure and it was not as effective at taking up the volumetric flow.

4.3.2.2 Capillary Positioning

The second change we made to the CTOF instrument in this series of modifications was to move the first UV detector away from the inlet (bomb) end by a distance of one meter. The reason for moving the capillary can be explained by examining Figure 4-4. Note in this experiment, the front passed the first detector (UV1) prior to the pressure leveling off (ΔP1 trace). As discussed previously, pressure (and thus velocity) variations while the front is passing a detector will cause a non-sigmoidal front, and prevent accurate variance measurement. By moving the detector back another meter, our hope was that the pressure would level off prior to the front reaching the first detector.

With these two modifications made, a few experiments were performed. Both the aforementioned modifications were successful at correcting the problems they were meant to

address, but there still remained an unacceptable amount of error (±15%) in the diffusion coefficient measurements. We realized the majority of this was coming from pressure drift in the inlet region of the capillary during the migration between the detectors. This drift was on the order of 50 to 100 psi, likely caused by nonidealities in the pneumatic amplifier pump performance. In order to address this pressure drift, two further modifications were performed.

As can be seen in comparing Figure 4-3 with Figure 4-5, the second UV detector was moved much closer to the first one, to a position 2 meters after UV1 and 4 meters from the inlet of the capillary. The overall capillary dimensions were left constant to maintain flow resistance. The reason we moved UV2 was to reduce the flight time between the two detectors. The variance accumulated between detectors was reduced dramatically by taking this step, but variance at UV2 was still double that at UV1. The inter-detector flight time was reduced from 1 minute to roughly 15-20 seconds, so as to reduce the amount of time over which pressure drift could occur. The final instrument modification came in the form of adding a manual pump, which (with proper operation) was able to reach the target pressure more quickly and maintain a much more consistent inlet pressure than the Haskel pump alone.

4.3.2.3 HiP Ship's Wheel Pump

A Ship's Wheel pump (Model 37-5.75-60, High Pressure Equipment Company, Erie, PA) capable of 60,000 psi (4200 bar) was added into the system as shown schematically in Figure 4-5. The purpose of this pump was to provide the ~2,000 psi pressure-jump required to push the front forward through the capillary. Prior to installing the ship's wheel pump, the

Haskel pneumatic amplifier pump was used for this purpose. However, the Haskel pump had a significant time-constant to reach the target pressure, which it approached asymptotically.

The ship's wheel pump was operated manually, by turning the "wheel" clockwise. By manually turning the wheel while watching the pressure readout from pressure sensor 1 ($\Delta P1$ in Figure 4-5), the pressure desired could be reached within ~2 seconds, and held within ±10 psi of the target. One unforeseen advantage of using the two pump system was that it allowed several measurements to be obtained at the same pressure, before moving on to the next pressure. The addition of this pump changed the operating procedure slightly for the CTOF instrument compared to that described in Chapter 3. The operating procedure is next described in detail.

4.3.3 CTOF Operating Procedure for Determination of Diffusion Coefficients and Viscosity

The operating procedure for the CTOF instrument shown in Figure 4-5 is very similar to that described for the CTOF viscometer in Chapter 3, with one very important difference. The CTOF viscometer used one pump (Haskel), which provided the pressure to move fronts back and forth in the capillary and the "overpressure" at which the viscosity determination was desired. In the embodiment described here, two pumps are used. The Haskel pump still determined the overall pressure at which the viscosity and diffusion measurement was to be made, but the newly-included Ship's wheel pump was used to push the analyte back and forth through the capillary.

The system, including the capillary, was first flushed with mobile phase from the Haskel pump, with the capillary removed from the bomb. The pressure was released, and the analyte solution was added to the bomb (typically 5mM analyte in mobile phase). The fitting was

113

tightened into the bomb and both valves opened, so that both ends of the capillary were at atmosphere.

At the start of the experiment, the Haskel pump was engaged to the lowest pressure possible, typically ~2,000 psi, and the entire system was allowed to equilibrate at this pressure. An analyte front was then pushed through the capillary by closing the valve at Arm 2 and turning the HiP Ship's Wheel pump clockwise to achieve a ~2000 psi pressure increase (to ~4,000 psi total) at $\Delta P1$ (see Figure 4-5).

The pressure drop across the capillary was measured using pressure sensor 1 (Model 602160-2, Senso-Metrics Inc., Simi Valley, CA) in the same manner as was described in detail in Chapter 3. Recall that the pressure reading prior to migration of the front was used as the outlet pressure, and the average pressure at $\Delta P1$ during migration of the front was used as the inlet pressure. The function of pressure sensor 2 was simply to ensure that no pressure change occurred in Arm 2 of the system during the forward migration.

After the front was sufficiently past UV2, the valve at Arm 2 was opened to equilibrate the pressure at both ends of the capillary, and therefore stop flow through the capillary. Since the volume of Arm 2 was significantly larger than Arm 1, the pressure of the entire system decreased to the initial (Haskel pump-determined) pressure once the Arm 2 valve was opened. To push the front backward, Arm 1 valve was closed and the Ship's Wheel was turned counterclockwise to decrease the pressure at the inlet of the capillary. After the reverse migration, both valves were opened to stop flow and allow equilibration at the pressure determined by the Haskel pump. The procedure typically repeated at the same average pressure for the desired number of points (typically 4 or 5). The Haskel pump

pressure was then increased to the next desired experimental pressure. This CTOF instrument proved reliable from ~2000 to 30,000 psi (~140 to 2100 bar).

4.3.4 Thermostatting

An additional step which was not taken with the CTOF viscometer was to thermostat the system, in order to enable more accurate and consistent determination of diffusion coefficients. The insulated box used for these experiments has been described previously.[4] Thermostatting was performed by inclosing the system in a 4'x2'x2' insulated box, which was accessed via a hinged front. A hole was cut in the rear of the box so the front half of the two UV detectors were inside the box, while the back half of the detectors housing the UV lamps remained outside. A Haake A82 temperature-controlled bath circulated 22°C water through a 120-mm radiator inside the box. One computer fan was attached to the radiator, and another had a coiled Ni:Cr wire suspended in front of it to act as a heating element. The element was attached to an Omega SSR330DC50 solid state relay, then to the output of an Omega Series 6000 microprocessor-based temperature controller. Two 4-L bottles of water were included to increase the thermal mass of the system. The temperature was monitored with a T-type thermocouple attached to an Omega model i/32 process meter, then fed via serial connection to a PC. Temperature was typically recorded every 30 seconds during a run, and the box was found to remain steady at 25°C ±0.1°C over the course of an experiment (~2 hours). A mercury thermometer was used to monitor the actual temperature, and the thermocouple provided a means of ensuring long-term stability to ± 0.1°C.

4.3.5 Sample Preparation

All solutions were prepared at 25 ± 0.5 °C by mixing HPLC-grade acetonitrile (Fisher Scientific, Fair Lawn, NJ) with Nanopure water (Barnstead-Thermolyne, Dubuque, IA). For

experiments reported herein, the mobile phase used was 50/50 (v/v) acetonitrile/water with 0.1% trifluoroacetic acid (TFA) (Sigma-Aldrich, St. Louis, MO). 1,4-dihydroxybenzene (hydroquinone, HQ) and egg white lysozyme were used as received from Sigma-Aldrich. Samples were prepared by enriching an aliquot of the mobile phase to the desired concentration in order to ensure uniform solvent composition.

4.4 Results

4.4.1 Raw Data Collection and Manipulation

Raw data from the CTOF instrument that was used for determinations of diffusion coefficients and viscosity was very similar to that described in Chapter 3 for the CTOF viscometer. The main difference for this instrument was that for the UV detectors a separate channel was collected for each detector, as opposed to both signals being combined as with the conductivity detectors. Figure 4-8 shows the raw data from a two-hour experiment in which forward and reverse migrations were carried out at five separate pressures between roughly 5,000 psi (340 bar) and 30,000 psi (2,100 bar). The absorbance traces have been differentiated in this Figure in order to show the data as it was used for variance calculations, using Gaussian fits. Figure 4-8A shows the entire two hour experiment; Figure 4-8B shows a section of the experiment in which 4 migrations were performed at an average pressure of 14,000 psi (30-47 minutes); Figure 4-8C shows data from a single forward migration (40-41 minutes).

Figure 4-8C can be used to fully understand how an experiment was performed with this CTOF instrument. The pressure traces at the two detectors are shown in blue; solid blue is $\Delta P1$ and dashed blue is $\Delta P2$. Prior to roughly 40.1 minutes, the pressure traces overlap,

indicating both valves were open and the pressure was in equilibrium at both ends of the capillary. At roughly 40.1 minutes, ΔP1 rose sharply from ~13,000 psi to ~15,000 psi, and shortly thereafter the front passed UV1 (red trace). This migration was caused by closing the valve at Arm 2 and turning the ship's wheel. Between ~40.1 minutes and ~40.9 minutes, the ship's wheel was used to keep the pressure constant at ΔP1. Once the front completely passed UV2, the valve at Arm 2 was opened to stop the migration (~40.9 minutes).

Gaussian fits to the differentiated fronts at UV1 and UV2 are shown in black in Figure 4-8C. As can be seen in this figure, a Gaussian curve provides an excellent fit to the experimental data. For the two curves shown here, the retention times were 40.398 min and 40.634 min, giving a flight time of 14.21 seconds between detectors. The widths at base were 3.32 sec and 4.40 sec. Using this data and a calibrated capillary diameter of 52 μm, (4-12) was used to calculate a D value of 7.41×10^{-6} cm^2/sec. The same procedure was then performed with each of the migrations at the same pressure, and these values were averaged to give the experimental diffusion coefficient for hydroquinone in 50/50 (v/v) acetonitrile/water at 13,000 psi. The raw data migration time and peak widths given here are not in themselves significant but serve to give a sense of the average values obtained with this CTOF instrument.

4.4.2 Viscosity Data Obtained Compared to the CTOF Viscometer

Hydroquinone (MW = 110 g/mol) and lysozyme (MW ≈ 14,400 g/mol) were dissolved in 50/50 (v/v) acetonitrile/water with 0.1% TFA and experiments were performed using the CTOF instrument to determine the solution viscosity and solute diffusion coefficient. For experiments with hydroquinone, the solute concentration was 5 mM. For lysozyme the concentration was roughly 0.12 mM, or 1.7 mg/mL. These solutions were

analyzed independently, with three separate experiments performed with hydroquinone and two with lysozyme.

Data was collected and evaluated as described in Section 4.4.1, and the retention time ("flight time") data was used to calculate solution viscosity using Equation 3-2. Figure 4-9 shows viscosity data obtained from the new configuration of the CTOF instrument. Figure 4-9A shows three the three replicate data sets obtained for 5mM hydroquinone, and Figure 4-9B shows two data sets for 0.12 mM lysozyme. The solid lines in the figures are not linear regressions for the data shown, but instead represent the viscosity data obtained for 50/50 acetonitrile/water from the CTOF viscometer, data previously presented in Chapter 3.

The capillary diameter used in the new CTOF instrument configuration was roughly 50 um, but the exact value was unknown. Therefore, the CTOF viscometer data (Chapter 3) was used to calibrate the new CTOF instrument. In order to get the data shown in Figure 4-9A to overlay with viscosity data obtained previously, the capillary diameter for the new instrument was adjusted to 52 μm. This diameter was therefore also used in the viscosity determination using lysozyme, presented in Figure 4-9B. There is excellent agreement in both data sets, which implies that marker molecules over a very wide range of molecular weight (~100 to >14,000 g/mol) may be used to obtain accurate solution viscosity measurements using this instrument configuration. The only requirements seem to be that the analyte solute must be UV-absorbing and must give an appropriate sigmoidal-shaped front upon migration through the capillary. The data obtained for hydroquinone and lysozyme were next evaluated for diffusion coefficient determination.

4.4.3 Ultrahigh Pressure Diffusion Coefficient Determination for Hydroquinone

The diffusion coefficient for hydroquinone in 50/50 acetonitrile/water with 0.1% TFA was determined from roughly 100 bar to 2000 bar using the CTOF instrument. Data was collected and evaluated as described in Section 4.4.1. Three data sets for hydroquinone are shown in Figure 4-10. Either two or three diffusion/viscosity determinations were performed at each desired pressure in each of the three data sets. All told, approximately 60 independent diffusion/viscosity determinations are plotted in Figure 4-10 for hydroquionone. The three data sets overlap reasonably well; there is very little scatter at low pressure and the scatter in the calculated diffusion coefficient values increase slightly as pressure increases. The relative standard deviation of the data set was determined at three different pressures; RSD was determined to be 1%, 3% and 5% at 200, 1000, and 1900 bar, respectively. This is likely due to the fact that as pressure increases it is more difficult to maintain the pressure exactly constant at the inlet and outlet of the capillary during the migration.

The average capillary diameter was calibrated using known viscosity data, as discussed in Section 4.4.2. In that case the capillary diameter of interest was the overall average capillary diameter, which along with the pressure determines the flow rate through the capillary. A fine point arises here, which is that the diameter of interest for the diffusion coefficient determination is not the overall average diameter, but only the average diameter *between* the two detectors. This is because the variance accumulated between the detectors is dependent only on the local capillary diameter in that region, whereas the flow rate between the two detectors is a function of the average diameter over the entire capillary length. It is not uncommon for fused silica capillaries to vary in diameter by a micron or two along their length. It was therefore desirable to independently calibrate the 1.5-meter section of capillary between the two detectors for diffusion coefficient measurements.

The diffusion coefficient for hydroquinone in 50/50 acetonitrile/water at atmospheric pressure was previously determined by a stopped-flow method to be 9.1×10^{-6} cm^2 sec^{-1}.[4] As a first approximation, a linear regression was performed to the three combined data sets shown in Figure 4-10 (linear regression not shown). The intercept of this linear regression was then set to equal 9.1×10^{-6} by adjusting the capillary diameter to 50.0 μm. This capillary diameter was then used as the "migration region" diameter for all further diffusion coefficient measurements.

As discussed in Section 4.2, elevated pressure is expected to shift the molecular diffusion coefficient based on the change in solution viscosity. The Stokes-Einstein relationship (Equation 4-13) predicts an inverse relationship between D and η. To compare the diffusion coefficient data obtained for hydroquinone from the CTOF instrument to the expected change in diffusion coefficient simply due to an increase in viscosity, the viscosity-predicted diffusion trend from Table 4-2 and Figure 4-2 was replotted as a dashed line on Figure 4-10. It was immediately obvious that the change in viscosity seemed to provide a very close estimation of the change in diffusion coefficient with pressure for hydroquinone.

The diffusion coefficient measurements from all three data sets were then collectively fit to the following equation, which allowed for nonlinearity due to a change in solution viscosity:

$$D = \frac{\delta}{\eta_0 + \alpha P} \qquad (4\text{-}18)$$

where δ is an adjustable fit parameter, P is the pressure in bar, and η_0 and α are the viscosity parameters for 50/50 acetonitrile/water from Table 3-2 (0.0081 Poise and 1.95×10^{-6} Poise bar^{-1}, respectively). The best-fit line to the data for Equation 4-18 is shown as the solid line in Figure 4-10. It appears as if the only difference between a best-fit to the data collected and

a prediction based on solution viscosity is a slight offset. It is possible that this offset is simply due to a slight miscalibration (~0.5 μm) of the capillary diameter between the detectors.

From the diffusion coefficient data obtained for hydroquinone in 50/50 acetonitrile/water using the CTOF instrument, it appears that the change in viscosity with pressure provides a very good estimation of the change in diffusion coefficient from atmospheric pressure to 2000 bar. Measurements from the CTOF instrument suggest a roughly 30% decrease in diffusion coefficient from 1 to 2000 bar. This is approximately double the change that Mellors observed utilizing his stopped-flow technique.[4] Figure 4-11 shows the best-fit line from the CTOF diffusion data and the viscosity prediction from Figure 4-10, along with a comparison to Mellors data for hydroquinone at 1 bar, 1000 bar, and 2000 bar. Although Mellors' data had a smaller standard deviation between measurements than our method, the data from the CTOF instument seems to agree much more strongly with the prediction based on viscosity. Mellors suggested that although solution viscosity increases with pressure, the diffusion coefficient of hydroquinone may decrease less than expected because of the disruption of hydrogen bonds due to the applied pressure.[5] However there is no direct evidence to support such an effect in 50/50 acetonitrile/water. The discrepancy between diffusion coefficient data reported from the stopped-flow experiments and that observed using our CTOF instrument prompted further critical evaluation of the two methods to find any experimental flaws which might lead to the difference.

The discrepancy between ultrahigh-pressure D data obtained by the stopped-flow method and the CTOF instrument might be explained by a simple thought experiment, which explains how the ultrahigh pressure diffusion coefficients from the stopped-flow method may

be artificially elevated over the actual D value. The argument for the error in the stopped-flow method centers on compression of the solvent at elevated pressures.

In the stopped-flow method of measuring D at elevated pressures, recall that although the variance was allowed to accumulate at elevated pressure, the actual variance measurement was at atmospheric pressure. For example, to measure the diffusion coefficient of hydroquinone at 1000 bar, an analyte front was migrated into the center of the column using gravity. Both ends of the capillary were then pressurized to 1000 bar, and diffusion was allowed to occur for the predetermined time (typically 24 hours). The pressure was then released from the capillary, and the variance was measured by migration of the diffusion-broadened front through the detector.

This experiment would perform without error for an incompressible solvent. However, for a solvent that compresses under pressure an unexpected (and heretofore unrealized) error is possible. For a solvent that compresses 10% under the aforementioned 1000 bar of pressure, the same 10% expansion will occur upon release of the pressure. It would therefore be expected for this case that any band (or front) in the capillary during the pressure release will experience the same 10% expansion. This means that whatever variance accumulated in the pause period will then be expanded by an amount directly proportional to the compressibility of the solvent, prior to measurement. It was postulated that the measured diffusion coefficient using the stopped-flow method would therefore be elevated by an amount directly proportional to the solvent compressibility at the pressure of the experiment.

To test this theory in a hypothetical sense, a calculation was carried out that incorporated the additional variance that would be generated due to expansion of the band

122

during decompression of the solution in the capillary. Assume an actual diffusion coefficient of 8×10^{-6} cm^2 sec^{-1} and a solution compressibility of 10% at 1000 bar. Assume an infinitely narrow initial front was compressed 10% and then allowed to diffuse for 24 hours. After this pause the spatial variance generated from diffusion would be 1.38 cm^2 (calculated using equation (4-3)). The 4σ width while still under pressure was therefore 4.703 cm. If the pressure was then released from the capillary containing the front, an expansion of 10% would occur resulting in a 4σ width of 5.226 sec. The measured variance at the detector would therefore be 1.707 cm^2 and D would be calculated to be 9.87×10^{-6} cm^2 sec^{-1}. This evaluation therefore predicts that a solution compressibility of 10% would lead to 23% error in the measured D value from Mellors' stopped-flow ultrahigh pressure diffusion experiment.

A specific evaluation of the difference between the stopped-flow D measurements and the CTOF measurements was carried out using the above hypothesis. For hydroquinone in 50/50 ACN/water at 1000 bar, the CTOF measurement gave $D = 7.50 \times 10^{-6}$ cm^2 sec^{-1} while the stopped-flow method gave $D = 8.4 \times 10^{-6}$ cm^2 sec^{-1} (see Figure 4-11). Performing an evaluation as described above, solvent compression of 5.5% could result in this 12% error. At 2000 bar, the reported D values were 6.28×10^{-6} cm^2 sec^{-1} and 7.5×10^{-6} cm^2 sec^{-1} for CTOF and stopped-flow methods, respectively. Solvent compression of 8.5% could lead to this 19% error.

From density data previously reported for mixtures of acetonitrile/water at 30°C and up to 2000 bar, the percent compression of this mobile phase as a function of pressure was calculated.[15] Figure 4-12 is a plot of percent reduction in volume versus pressure and composition. This plot reveals that for 50/50 (v/v) acetonitrile/water, the mobile phase is compressed approximately 5% and 8% at 1000 bar and 2000 bar, respectively. These

quantities agree very closely with the compression values calculated in the thought experiment outlined above (5.5% and 8.5%). Noting this agreement, it is highly likely that the error in the stopped-flow diffusion measurement method is due to compression and expansion of the mobile phase.

Citing the newly-recognized error in the stopped-flow D measurement at ultrahigh pressure and the consistency of the CTOF data with that predicted by viscosity, it is now believed that the CTOF instrument provides a more reliable method of measuring diffusion at ultrahigh pressures. The stopped-flow method still provides the most accurate way to determine diffusion coefficients at atmospheric pressure. In addition, it appears that a reasonably accurate estimation of D at ultrahigh pressures (<5% error) can be made by adjusting the atmospheric pressure diffusion coefficient based on viscosity data at ultrahigh pressures with the Stokes-Einstein relationship (Equation (4-13)).

4.4.4   Ultrahigh Pressure Diffusion Coefficient Determination for Lysozyme

It was desirable to show the CTOF instrument's capability to measure diffusion coefficients of large molecules, since these measurements are somewhat inaccessible to the high-pressure stopped-flow method because of the long wait times required. Figure 4-13 shows the data obtained for the diffusion coefficient of the small protein lysozyme in 50/50 acetonitrile/water up to 2000 bar. The diffusion coefficient of lysozyme was measured to change from approximately 1.05×10^{-6} cm^2/sec at 200 bar to 0.65×10^{-6} cm^2/sec at 1900 bar. There is good agreement between the two data sets collected. The solid line is a linear regression for the combination of the two data sets; for the lysozyme data set a linear regression provided a better fit than a fit of the form shown in Equation 4-18.

The dashed line is a prediction of the change in diffusion coefficient for lysozyme based strictly on viscosity increase. Interestingly, the measured diffusion coefficient for lysozyme is lower at elevated pressure (in the region from 1000 to 2000 bar) than predicted by the viscosity increase, which could be the result of an increase in hydrodynamic radius of the protein at elevated pressure. However, the difference between the diffusion coefficient data obtained and the viscosity-based prediction is too small to make any conclusive arguments centered around protein denaturation.

We were aware that when measuring the diffusion coefficient of a protein using our CTOF instrument, we would be near the low "theoretical limit" discussed in Section 4.1.3. Recall from the evaluation of Equation (4-13) that the theoretical low limit for "accurate" measurement of diffusion coefficients via Taylor Dispersion with our instrument was roughly 4×10^{-7} cm^2/sec for a flight time of 20 seconds. The lowest diffusion coefficients measured for lysozyme (at ~1900 bar) were within roughly 20% of this limiting value, so it is possible that the difference between the observed diffusion coefficients and that predicted by viscosity change is the result of a measurement error. To extend the measurement dynamic range to lower diffusion coefficient limits, either the flight time of the instrument can be increased or the capillary diameter decreased.[6, 16]

It should be pointed out here the throughput advantage gained by using the CTOF instrument to measure high-pressure protein diffusion as opposed to a stopped-flow capillary method. In two two-hour experiments, 43 diffusion coefficient measurements were made for lysozyme in the solvent system of interest (~6 minutes/measurement). According to Mellors, approximately 7 days would be required to obtain a reasonable amount of accumulated variance to use the stopped-flow method for a single diffusion coefficient measurement for a

protein (~10,000 minutes/measurement). This corresponds to an approximately 1600-fold throughput advantage for the CTOF method.

4.4.5   Improved Chromatographic Column Evaluation with Correct D_m Values

The main goal for seeking accurate measurements of diffusion coefficients is to enable more accurate chromatographic evaluation of ultrahigh pressure LC columns. We have long assumed that some change in solvent viscosity and solute diffusion coefficient occurs with increased pressure, but the amount of the change was undetermined. It has been stated that UHPLC suffers from unusually large C-terms (~0.3 to 0.5) compared to typical "well-packed" chromatographic columns (~0.1 to 0.25).[4, 17-20]   This statement has been somewhat troubling because it implies that UHPLC does not give very good performance, when in fact capillary UHPLC has given some of the best chromatographic performance ever reported in terms of reduced plate heights.

Recall from Equation (1-12) that in reduced van Deemter parameters, the reduced velocity (v) is inversely proportional to the molecule's diffusion coefficient in the mobile phase (D_m). Therefore if the diffusion coefficient were to decrease with increasing pressure, the reduced velocity would also increase. The result would be a shift of the high-velocity portion of the van Deemter curve to the right, and a lowering of the C-term.

The data shown in red in Figure 4-14 is a reduced van Deemter curve for hydroquinone, collected by J.S. Mellors on a 49.3-cm long capillary column packed with 1.5-μm BEH porous particles. For this evaluation, which was published in 2004, the D_m value was held constant at 9.1×10^{-6} cm^2/sec, which was the atmospheric-pressure D_m value determined for hydroquinone.[21]   At the time the data was published the diffusion coefficient was obtained from a stopped-flow method at atmospheric pressure, and neither accurate high

pressure diffusion coefficient nor viscosity measurements were available. The van Deemter evaluation with constant D_m gave a C-term equal to 0.28, which is considered to be on the high side for "well-packed" columns.[3, 21]

Based on the data reported in Figure 4-10, the reduced van Deemter parameters were reevaluated for this column. To find D_m as a function of pressure for this exercise, the fit equation 4-13 was used with $\delta = 7.54 \times 10^{-6}$ (from data in Figure 4-10) and the pressure used was half the inlet pressure, to estimate for the pressure drop across the column. The black data shown in Figure 4-14 is the reevaluated van Deemter curve. Because of the corrected diffusion coefficients, the apparent C-term for this column was reduced almost in half, to 0.16. Taking into account the change in diffusion coefficient with pressure and the mobile phase compression phenomenon (discussed further in the next chapter), the actual C-term for this column may actually be near 0.1 as opposed to 0.28, as originally reported.

The other reduced van Deemter coefficients (A- and B-term) also changed to compensate for the decreased C-term. A significant increase in the A-term occurred, from 0.19 to 0.59. The second value is more in line with typically-observed A-terms.[3] The observed B-term decreased slightly, from 1.7 to 1.51. Only a small change in the B-term was expected since the low-pressure end of the van Deemter curve largely establishes the B-term, and the diffusion coefficient in the low-pressure region is much closer to the previously-used atmospheric pressure value.

4.5   Summary and Conclusions

A capillary time-of-flight (CTOF) instrument has been developed that is able to determine the diffusion coefficient of a solute and the viscosity of solution in the same experiment. Diffusion coefficients are determined using a method similar to the classic

Taylor-Aris method, and viscosity using the Poiseuille model for flow through an open tube. This method typically gives viscosity values with roughly 3% RSD, and diffusion coefficient values with ~5% RSD at a pressure of 2000 bar. The instrument provides a straightforward, fast way to determine the diffusion coefficient of any UV-absorbing analyte of interest from small organics to moderately-sized proteins (~30 kDa), in any liquid mobile phase, at pressures from roughly 200 bar to 2,000 bar.

The instrument was shown capable of measuring diffusion coefficients of both small molecules and proteins. In addition, diffusion coefficient measurements for hydroquinone at ultrahigh pressures helped in the reevaluation of capillary UHPLC data obtained previously in our laboratory, and showed that the C-term for a column was actually almost 50% lower than previously thought. Diffusion coefficients obtained with the CTOF instrument for hydroquinone and lysozyme up to 2000 bar trend very closely for the change in diffusion that is predicted with viscosity change of the solvent. This suggests that if the atmospheric pressure D value is known accurately then Stokes-Einstein relationship (along with high pressure viscosity data from Chapter 3) should provide a relatively accurate estimation of D at ultrahigh pressure for chromatographic purposes. Analytes with strong hydrogen-bonding capability in solvents containing large mole fraction water may be the exception to this rule, but more data needs to be collected in order to make this determination.

Current limitations to the CTOF instrument include its theoretical low-limit of accurate D_m measurement to ~4×10^{-7} cm^2/sec, and its limitation to only 2000 bar. A longer flight time could help to increase the dynamic range of the method. A better seal on the "fluidic spring", possibly made of ultrahigh molecular weight polyethylene (UHMWPE), could increase the pressure capability. Another downside is that the instrument requires a

good amount of user skill in order for accurate measurements to be obtained, so it would be nice to make some portions of the instrument automated to decrease user intervention.

Because of the higher efficiency and faster separations capability at ultrahigh pressures, and as evidenced by the recent introduction of several commercial LC systems capable of 15,000 psi (1000 bar), the average pressure at which commercial and research-oriented liquid chromatography is performed will likely continue to increase. Knowledge of analyte properties such as diffusion coefficients will be crucial to understanding of the effects of elevated pressure on the separations. The CTOF instrument provides a relatively straightforward method for this information to be obtained.

4.6   References

(1)   Thompson, J. W.; Kaiser, T. J.; Jorgenson, J. W. *J. Chrom. A* **2006**, *submitted.*

(2)   Giddings, J. C. *Unified Separation Science*; John Wiley & Sons, Inc.: New York, 1991.

(3)   Neue, U. D. *HPLC Columns: Theory, Technology, and Practice*; Wiley-VCH, Inc.: New York, 1997.

(4)   Mellors, J. S., University of North Carolina at Chapel Hill, Chapel Hill, NC, 2005.

(5)   Aris, R. *Proc. Royal Soc. London A* **1956**, *235*, 67-77.

(6)   Taylor, G. *Proc. Royal Soc. London A* **1953**, *219*, 186-203.

(7)   Taylor, G. *Proc. Royal Soc. London A* **1954**, *225*, 473-477.

(8)   Golay, M. J. E. *J. Chrom.* **1979**, *186*, 341.

(9)   Pratt, K. C.; Wakeham, W. A. *Proc. Royal Soc. London A* **1975**, *342*, 401-419.

(10)   Alizadeh, A.; Neito de Castro, C. A.; Wakeham, W. A. *Int. J. Thermophys.* **1980**, *1*, 243-284.

(11)   Atwood, J. G.; Goldstein, J. *J. Phys. Chem.* **1984**, *88*, 1875-1885.

(12)   Clark, S. M.; Leaist, D. G.; Konermann, L. *Rapid Comm. Mass. Spectrom.* **2002**, *16*, 1454-1462.

(13)   Forst, P.; Werner, F.; Delgado, A. *Rheol Acta* **2000**, *39*, 566-573.

(14)   *CRC Handbook of Chemistry and Physics*, 77th ed.; CRC Press, Inc.: New York, 1996.

(15)   Ueno, M.; Ueyama, S.; Hashimoto, S.; Tsuchihashi, N.; Ibuki, K. *J. Solution Chem.* **2004**, *33*, 827-846.

(16)   Pratt, K. C.; Wakeham, W. A. *Proc. Royal Soc. London A* **1974**, *336*, 393-406.

(17)   MacNair, J. E.; Patel, K. D.; Jorgenson, J. W. *Anal. Chem.* **1999**, *71*, 700-708.

(18)   MacNair, J. E.; Lewis, K. C.; Jorgenson, J. W. *Anal. Chem.* **1997**, *69*, 983-989.

(19)   Jerkovich, A. D.; Mellors, J. S.; Thompson, J. W.; Jorgenson, J. W. *Anal. Chem.* **2005**, *77*, 6292-6299.

(20)   Patel, K. D.; Jerkovich, A. D.; Link, J. C.; Jorgenson, J. W. *Anal. Chem.* **2004**, *76*, 5777-5786.

(21)   Mellors, J. S.; Jorgenson, J. W. *Anal. Chem.* **2004**, *76*, 5441-5450.

Pressure (psi)	Pressure (bar)	D (Mellors)[1] (cm^2/sec)	η (cP)	D (Predicted)[2] (cm^2/sec)
14.5	1	7.7E-06	0.96	7.7E-06
15000	1034	8.2E-06	1.00	7.4E-06
30000	2069	8.2E-06	1.08	6.8E-06
45000	3103	8.0E-06	1.16	6.4E-06
60000	4138	8.0E-06	1.24*	5.9E-06

Table 4-1: Diffusion coefficient of hydroquinone in 10/90 (v/v) acetonitrile/water 0.1% TFA, as a function of pressure. [1] Diffusion coefficients obtained by stopped-flow method, from Reference 4. [2] Diffusion coefficients obtained by using the change in viscosity at elevated pressure to predict the change in diffusion. * Viscosity at 4200 bar was estimated using a continuation of the linear trend from 1500 bar to 3500 bar.

Pressure (psi)	Pressure (bar)	D (Mellors)[1] (cm^2/sec)	η (cP)	D (Predicted)[2] (cm^2/sec)
14.5	1	9.1E-06	0.81	9.1E-06
15000	1034	8.4E-06	1.02	7.2E-06
30000	2069	7.5E-06	1.22	6.0E-06
45000	3103	6.7E-06	1.42	5.2E-06
60000	4138	6.0E-06	1.62*	4.5E-06

Table 4-2: Diffusion coefficient of hydroquinone in 50/50 (v/v) acetonitrile/water 0.1% TFA, as a function of pressure. [1] Diffusion coefficients obtained by stopped-flow method, from Reference 4. [2] Diffusion coefficients obtained by using the change in viscosity at elevated pressure to predict the change in diffusion. * Viscosity at 4200 bar was estimated using a continuation of the linear trend from 1 bar to 3500 bar.
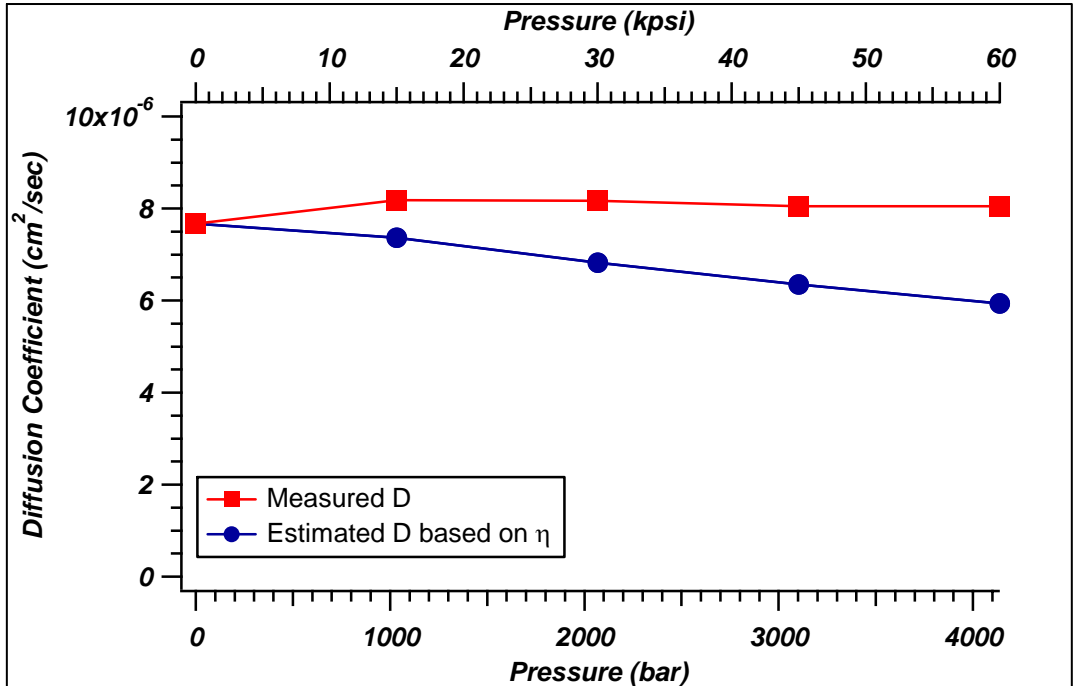
Figure 4-1: Diffusion coefficient vs pressure for hydroquinone in 10/90 (v/v) acetonitrile/ water with 0.1% TFA. (■) Measured values from stopped-flow experiment, from Ref X. (●) Values predicted for diffusion coefficient at elevated pressure, based solely on the change in solution viscosity.
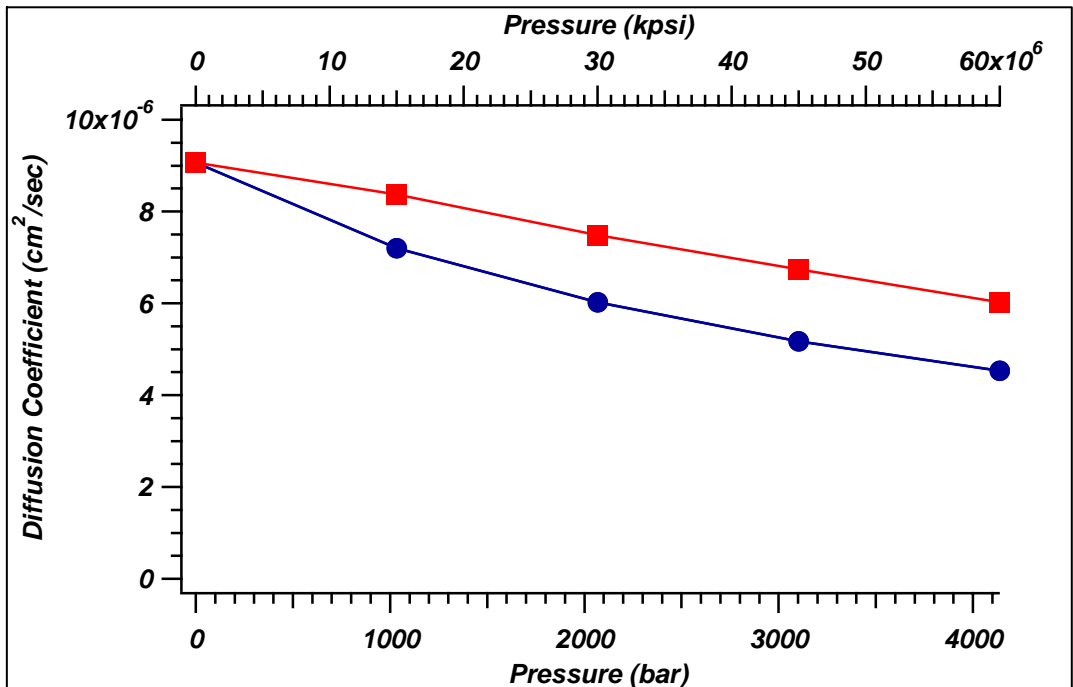
Figure 4-2: Diffusion coefficient vs pressure for hydroquinone in 50/50 (v/v) acetonitrile/ water with 0.1% TFA. (■) Measured values from stopped-flow experiment, from Ref X. (●) Values predicted for diffusion coefficient at elevated pressure, based solely on the change in solution viscosity.
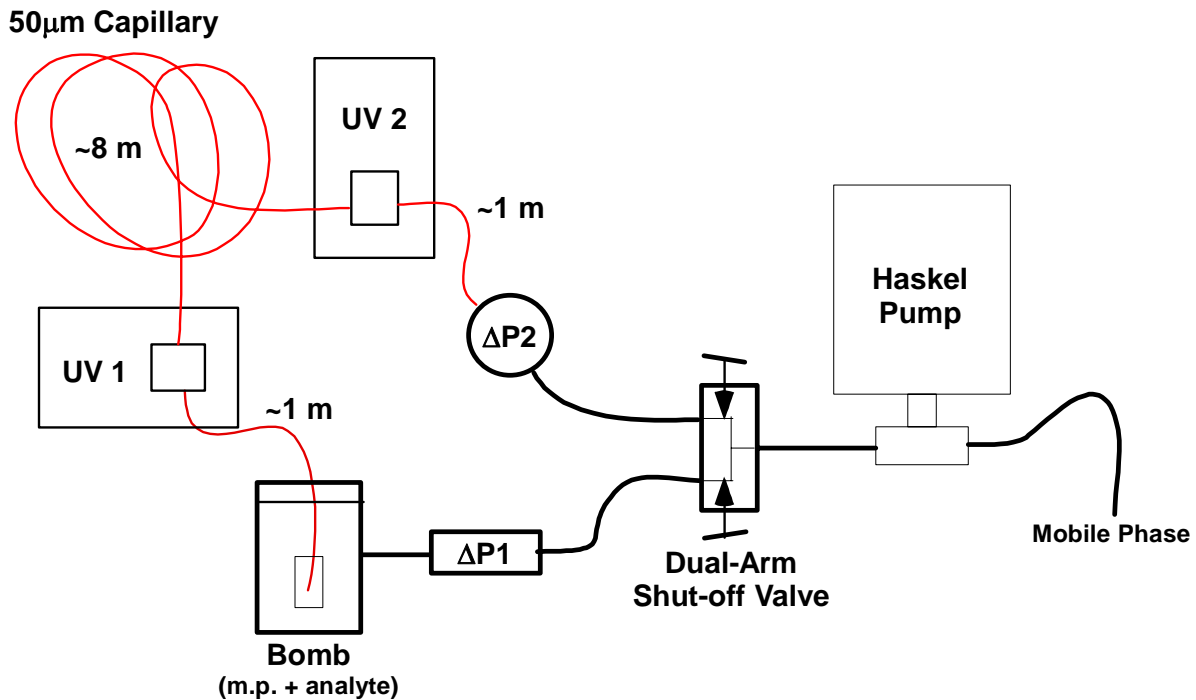
Figure 4-3. Phase 1 of the CTOF instrumental configuration intended for measuring both diffusion coefficients and viscosity. The major changes from the CTOF viscometer are the replacement of conductivity detectors with UV detectors, and the replacement of the 2m x 10 μm i.d. capillary with a ~10m x 50 μm i.d. capillary.
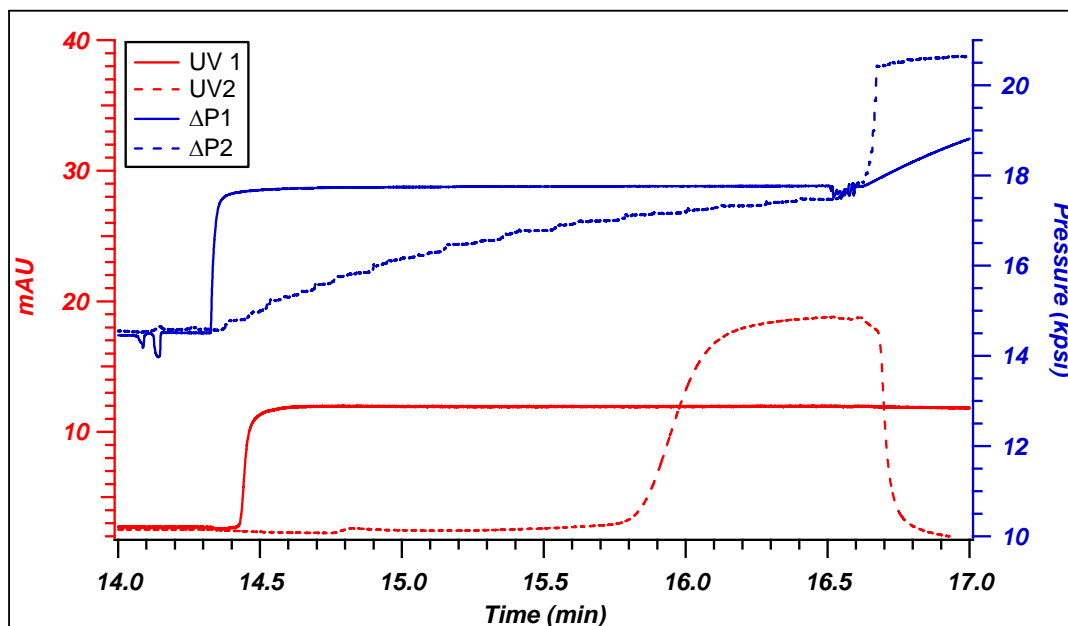
Figure 4-4: A portion of the raw data from experiment Feb13_01, using 5mM hydroquinone in 10/90 (v/v) acetonitrile/water and performed with the instrument configuration in Figure 4-3. Note that the flow out of the capillary at ΔP2 causes the pressure at ΔP2 to rise during the migration of a front from the bomb through the capillary, slowing the front.
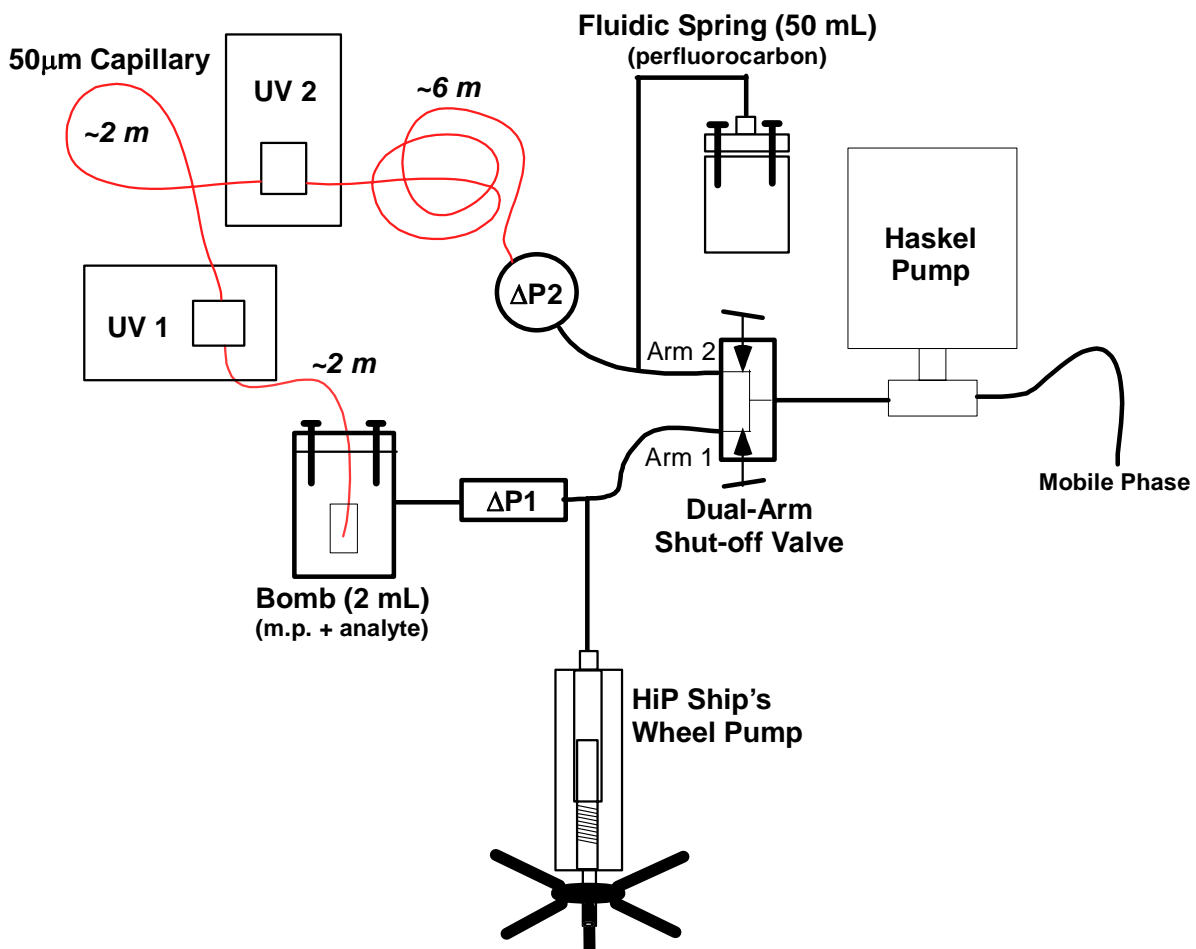
Figure 4-5: Phase 2 of the CTOF instrumental configuration. Changes from Phase 1 include the installation of the fluidic spring, repositioning of the UV detectors, and installation of the HiP Ship's Wheel pump to use for forward and reverse migration of the pump. Drawing is not to scale.
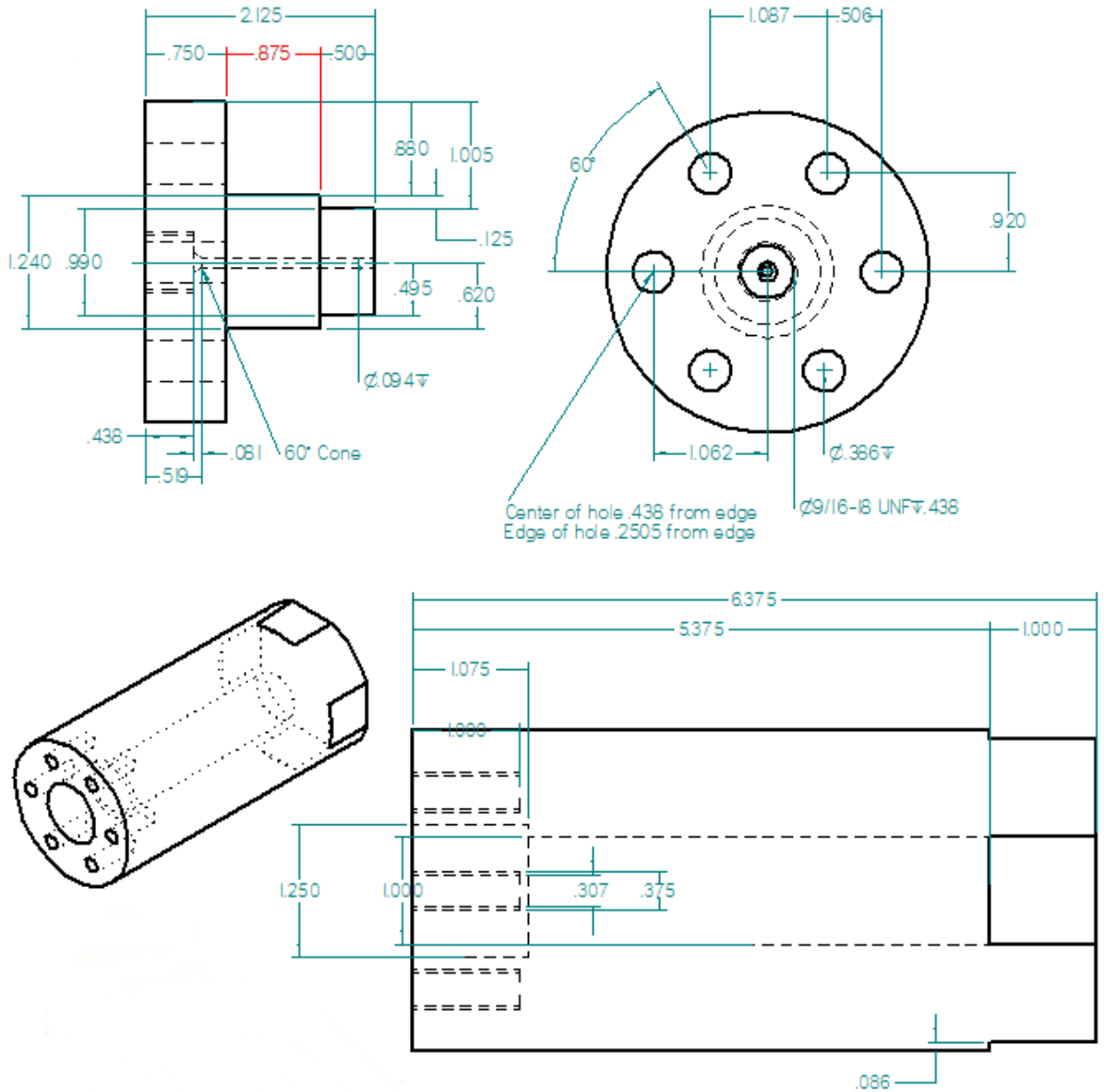
Figure 4-6   Draft (.dft) document from Solidedge v11 for the reservoir used as the fluidic spring in Figure 4-5. Both the lid (top) and the reservoir body (bottom) were machined from a piece of 3"-diameter 17-4 PH stainless steel.

136

Bolts (A268 Super Alloy)

Lid (17-4 PH stainless steel)

Seal (PEEK)

Reservoir Body (17-4 PH stainless steel)

Figure 4-7: Assembly (.asm) document from Solidedge v11 showing an exploded view of the fluidic spring, as machined for the CTOF instrument. Location at which this device was included in the CTOF instrument is shown in Figure 4-5. The reservoir had a volume of 50 mL and was filled with Fluorinert FC-5320.
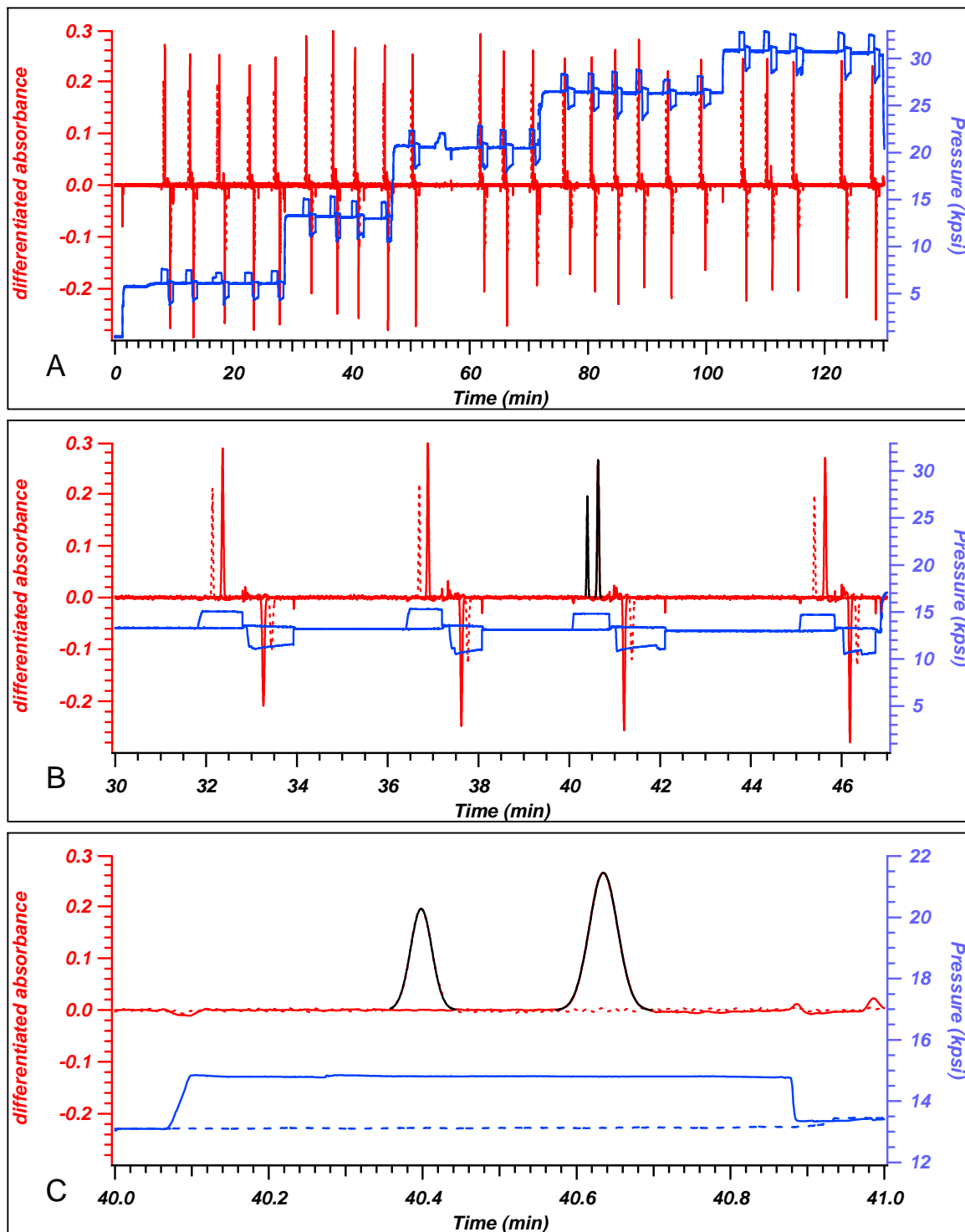
Figure 4-8: Raw data for an experiment performed with 5mM hydroquinone in 50/50 (v/v) acetonitrile/water. Absorbance traces are differentiated to give peaks. Panel (A) shows the entire experiment, with between 4 and 6 forward and reverse migrations performed at each desired pressure. (B) 30-47 minutes; four forward and reverse migrations performed at an average pressure of ~14,000 psi. (C) 40-41 minutes; one forward migration with Gaussian fits to the absorbance signals.
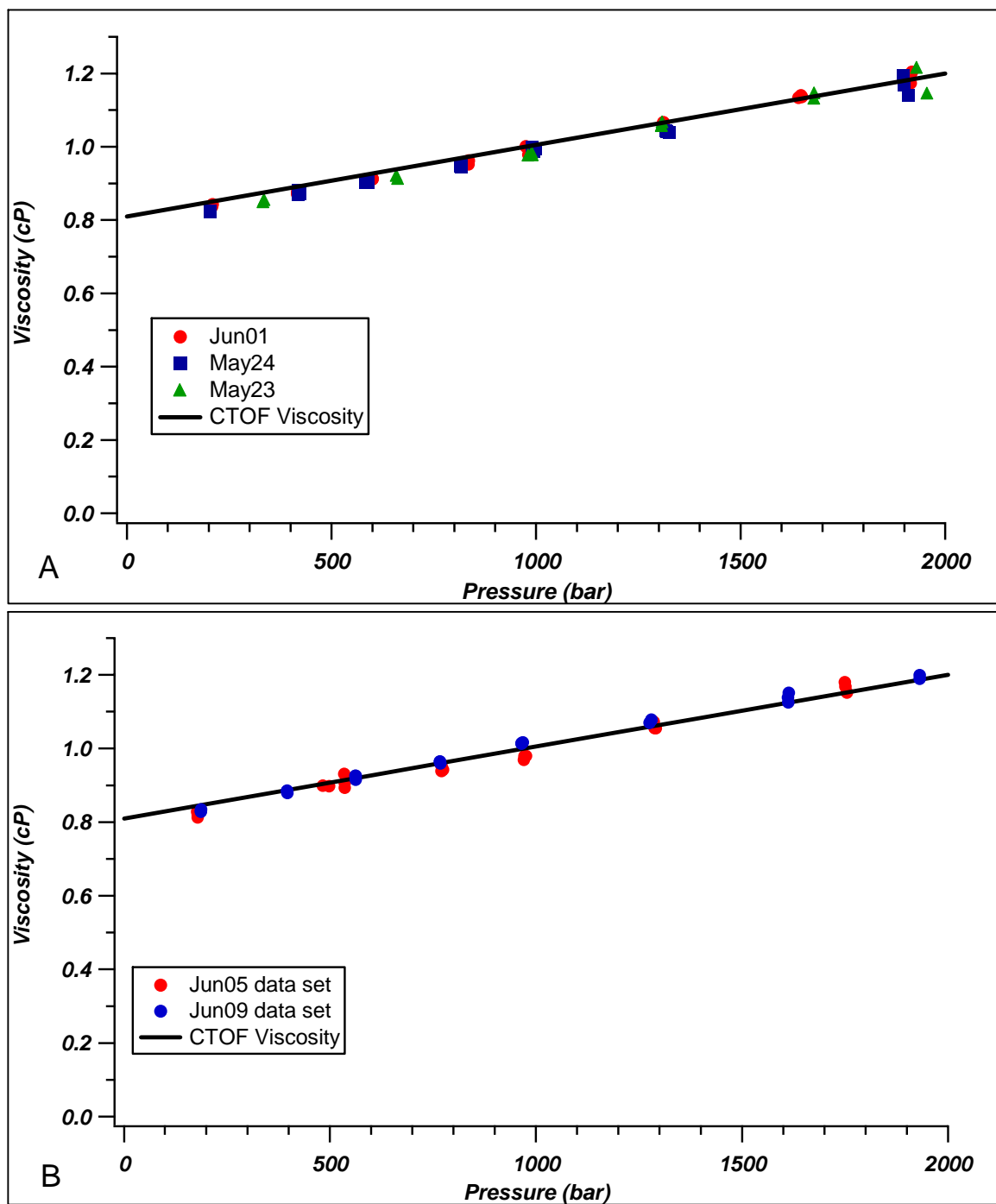
Figure 4-9: Viscosity data obtained for 50/50 (v/v) acetonitrile/water with 0.1% TFA, from the instrument configuration shown in Figure 4-5. The three data sets in (A) were obtained using hydroquinone as the marker analyte. Data in (B) was obtained using lysozyme as the analyte. The solid line in both (A) and (B) is not a linear regression of the data shown, but represents viscosity determined for 50/50 acetonitrile/water in a separate experiment, using the CTOF viscometer discussed in Chapter 3.

139
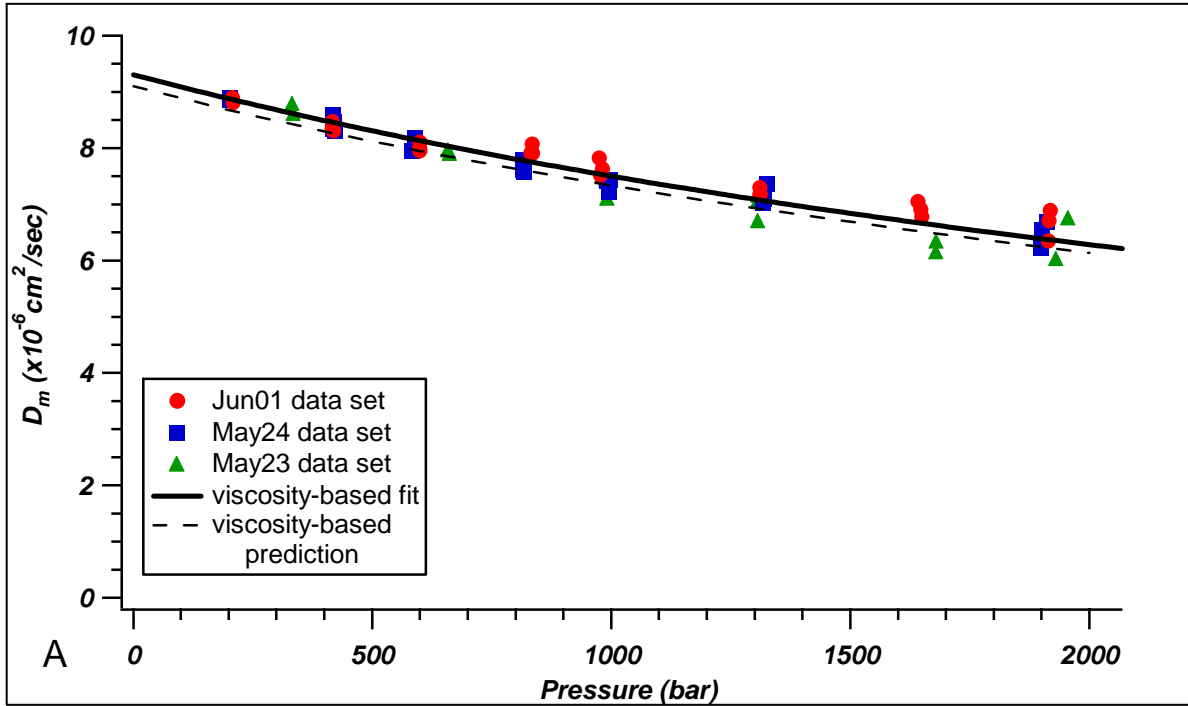
Figure 4-10: Diffusion coefficient determination for hydroquinone in 50/50 (v/v) acetonitrile/water with 0.1% TFA, at pressures from ~100 to 2000 bar using the CTOF instrument.
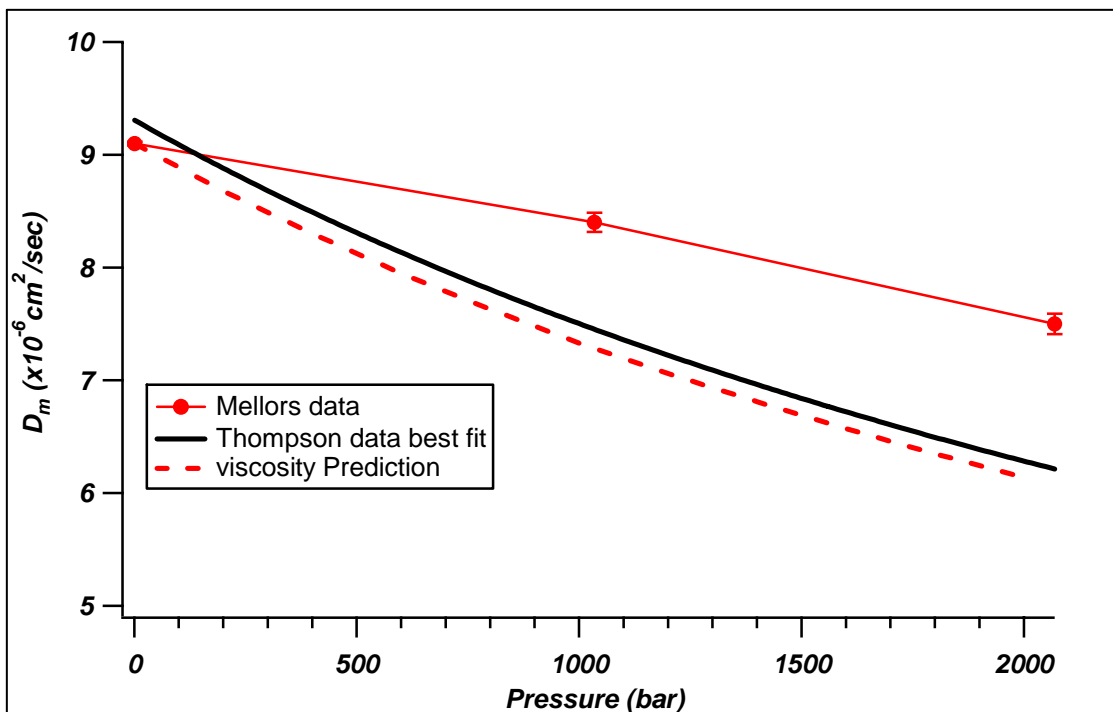
Figure 4-11: Comparison of data obtained for high-pressure diffusion coefficient for hydroquinone in 50/50 acetonitrile/water with 0.1% TFA, from the stopped-flow method developed by Mellors (reference 4) and the CTOF method described here. The viscosity-predicted change in diffusion with pressure is shown as well for reference.
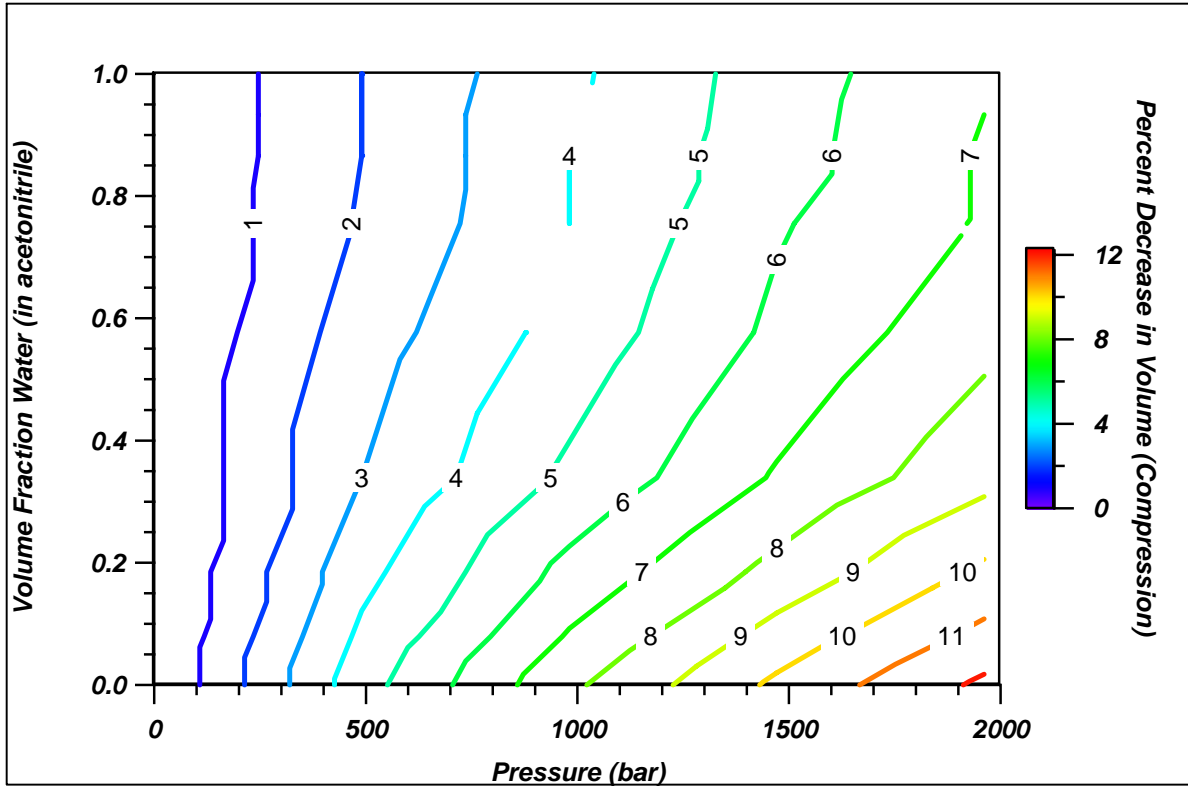
Figure 4-12: Mobile phase compression (percent reduction in volume) as a function of pressure and volumetric composition for water/acetonitrile mixtures. Contour plot was generated from density data collected at 30°C, from reference 15. Contour lines denote a 1 percent change in volume.
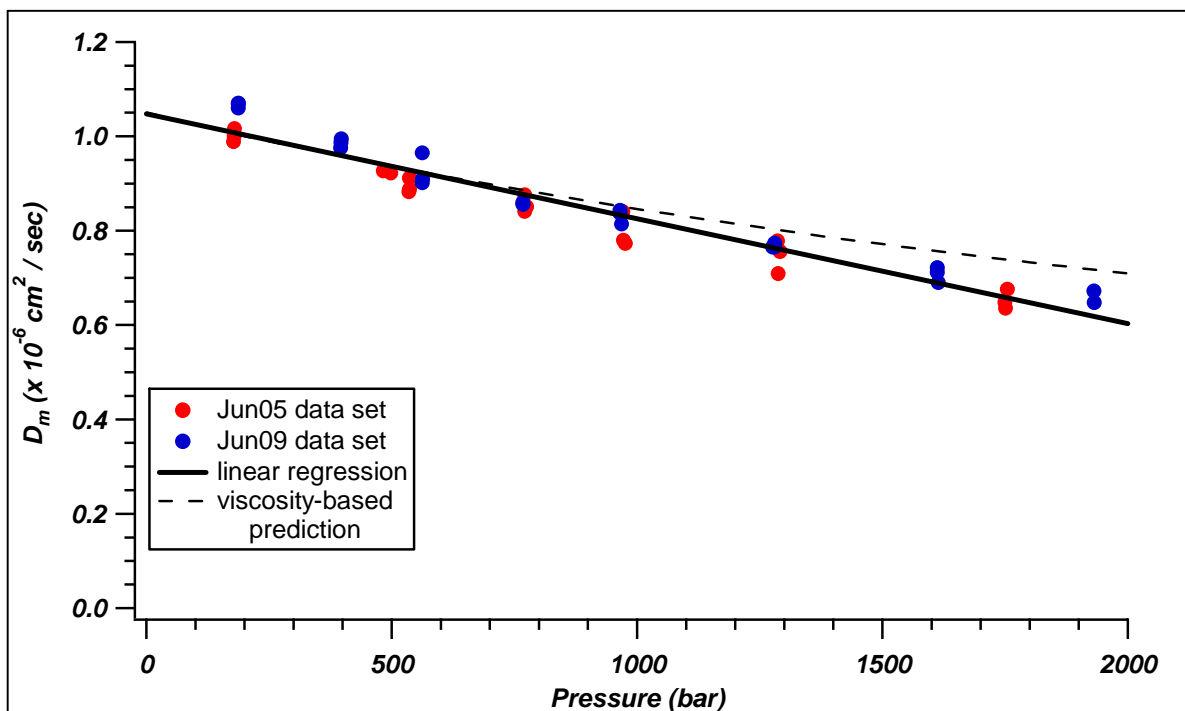
Figure 4-13: Measurement of the diffusion coefficient for the protein lysozyme in 50/50 acetonitrile/water as a function of pressure, obtained with the CTOF instrument. Two data sets are shown, and the solid line represents a linear regression of the combined data sets. The dashed line represents the predicted change in diffusion due to viscosity increase with pressure.
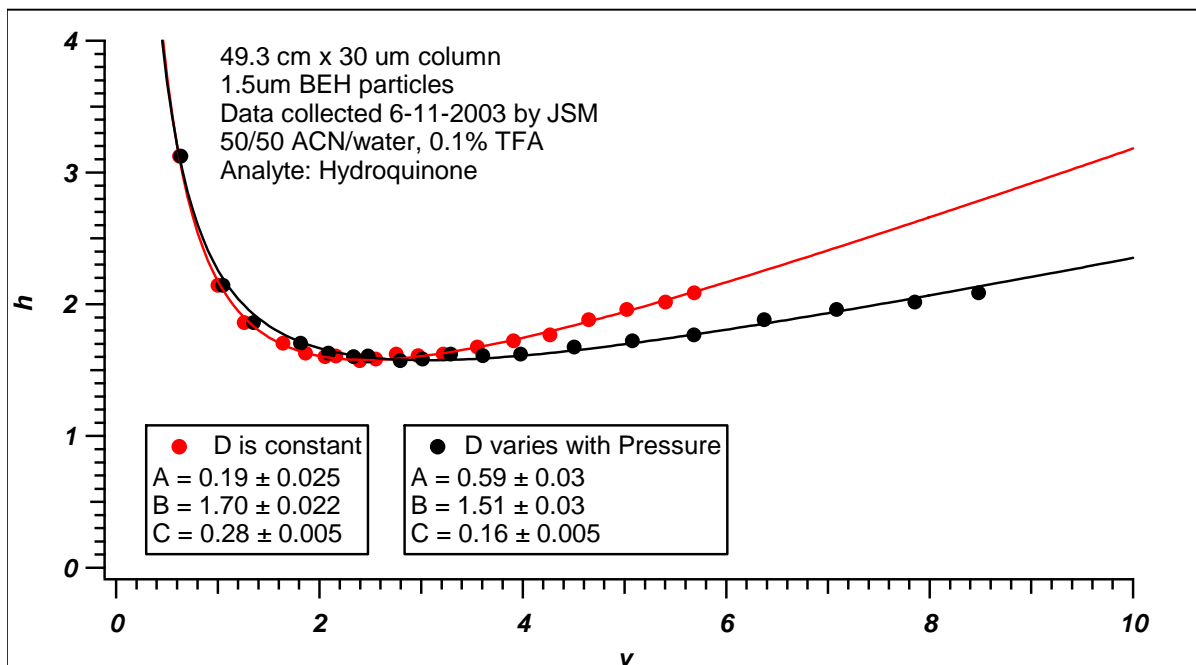
Figure 4-14: Reevaluation of UHPLC van Deemter data with proper diffusion coefficients at ultrahigh pressures. Red data: original reduced van Deemter curve for hydroquinone on a 49.3-cm x 30-um i.d. capillary column on 6-11-2003 by J.S. Mellors, using D_m= 9.1x10^{-6} cm^2 sec^{-1}. This data was originally published in Reference 21. Black trace: the reduced velocity was recalculated using a diffusion coefficient that was allowed to properly vary with pressure based on data shown in Figure 4-10.

5 EFFECTS OF MOBILE PHASE COMPRESSION ON RETAINED ANALYTES IN UHPLC

5.1 Introduction

In 2003, Jerkovich performed experiments in our lab which showed that mobile phase compression at the beginning of a UHPLC run caused a significant linear velocity surge at the inlet of the chromatography column.[1, 2] He correlated this velocity surge to the possibility for increased C-term broadening, since the mobile phase was effectively traveling much higher than the optimum linear velocity for a short period at the beginning of the run. He then used experimental data to develop a theory to approximate the additional variance accumulated during this velocity surge, and showed that for an isocratic UHPLC experiment, an unretained analyte might observe a 50% increase in C-term due to mobile phase compression.[2]

Being involved with these experiments led me to consider other ways in which mobile phase compression might affect the observed chromatographic results in UHPLC. The implications of the linear velocity surge were fairly clear for unretained analytes: the dead-time marker eluted before it would have otherwise been predicted (without compression) and the velocity surge also caused additional variance from the mass-transfer mechanism, which artificially increased the C-term. Likewise, the situation was fairly simple for highly-retained solutes; if the analyte was not migrating it would not undergo additional

C-term broadening, so mobile phase compression was not expected to be an important practical issue for gradient elution chromatography.

My interests turned to moderately retained analytes, those with retention factor (k') ranging from 0.1 to 10. Based on a very simple model, I hypothesized that mobile phase compression and the resulting linear velocity surge would cause artificially-inflated values of k' to be measured during isocratic UHPLC. Also, I was interested in examining how the additional variance contribution from mobile phase compression changed with analyte k'. In this chapter I will present research carried out to examine the trend of k' versus pressure at pressures up to 4000 bar. An experiment was designed to eliminate virtually all influences from pressure drop across the column and mobile phase compression. I compare the "corrected" curves to those of normal k' vs. pressure curves for isocratic UHPLC. I then use an extension of Jerkovich's theory for mobile phase compression at the column inlet to quantify how a linear velocity surge could cause an artificial increase in the measured k' at the outlet of the column. Finally, I will briefly discuss the implications of this theory for velocity surge contributions to C-term variance for retained species in isocratic UHPLC.

5.2   Theory and Background

5.2.1 Mobile Phase Compression in UHPLC

Although mobile phase compressibility has historically been taken into account for gas chromatography because of the readily compressible nature of gases, it is rarely considered in liquid chromatography. In GC, mobile phase enters the column as a stream of compressed gas and expansion occurs near the outlet of the column, giving rise to an increase in linear velocity in that region. Thinking in a similar vein, Martin and coworkers examined

the theoretical effects of mobile phase expansion for liquid chromatography at pressures up to 1500 bar.[3] Only small errors due to expansion were revealed by this study; roughly 3% error in void time was predicted for aqueous mobile phases because of their relatively low compressibility.

As identified by Jerkovich et al., a more significant compression event occurs at the beginning of an isocratic UHPLC run in the special case where injection is done at low pressure, followed by quick application of the desired run pressure.[1, 2] In this case, the mobile phase in the pump, injector, and column compresses quickly, resulting in a velocity surge at the inlet of the column for a short period of time until the mobile phase is completely compressed. The pressures used in UHPLC (up to 7000 bar) are high enough to compress aqueous mobile phases on the order of 20 percent, so it was predicted that this surge may penetrate a significant distance into the column.[4]

To quantify this compression event, Jerkovich devised an experiment in which the position of an unretained ionic marker was monitored as a function of time after an injection was performed.[1, 2] Long capillary columns were used (up to 206 cm) in order to observe the compression event over an appreciable distance. Figure 5-1 shows the results of this experiment for pressures ranging from 2600 bar to 6300 bar. Compression of the mobile phase is obvious from the nonlinear nature of this distance vs. time plot within the first ~30 cm of the column. An empirical equation was formulated to describe the position of the unretained marker as a function of time ($x(t)$):

$$x(t) = A\left(1 - e^{-t/\tau}\right) + ut \qquad\qquad (5\text{-}1)$$

The equation contains two parts, an exponential portion to describe the beginning of the run when the compression event occurs, and a linear portion to describe the remainder of the run.

The constant A is the y-intercept of the linear portion of the curve, and corresponds to the distance effectively "gained" by the void volume marker during the velocity surge. τ is the time constant for the exponentially decaying velocity as the mobile phase reaches its fully compressed state. u is the slope of the linear part of the curve, or simply the mean velocity after the compression event is finished. Looking at Figure 5-1, it is also apparent that no mobile phase expansion was observed near the outlet of the column, as would be evidenced by an upward slope of the distance vs. time curve near the outlet.

By differentiating (5-1) a relationship for the instantaneous mobile phase velocity ($u'(t)$) at any time during the experiment can be generated:

$$u'(t) = \left(\frac{\partial x}{\partial t} \right) = \left(\frac{A}{\tau} \right) e^{-t/\tau} + u \qquad (5\text{-}2)$$

The constants A, τ, and u were obtained for each run pressure from the data shown in Figure 5-1. Then, by plotting instantaneous velocity from expression (5-2) versus position from (5-1), the velocity as a function of column position can be visualized, as is shown in Figure 5-2A. This figure shows that the linear velocity at the start of the run is approximately 8-fold higher than the terminal velocity u, for the 6300-bar (91,000 psi) case. The linear velocity surge penetrates a distance into the column proportional to the applied pressure, from ~15 cm at 2600 bar to ~35 cm at 6300 bar for the 206-cm capillary column.

Since linear velocity is directly proportional to C-term band broadening, an estimation of additional variance due to the velocity surge can be made by integrating the curve shown in Figure 5-2A. The result is shown as Figure 5-2B. For a normal chromatography column, variance of an analyte band should grow linearly as a function of column position. It is obvious from Figure 5-2B that in the case of a linear velocity surge, a disproportionate amount of the total C-term variance for an unretained solute is accumulated

148

during the first ~10% of the column. In the results section of this chapter, the compression theory developed by Jerkovich is extended to make predictions about the effects a velocity surge would have on retained species.

5.2.2 Theory for Pressure Effects on Retention Factor

Retention factor (k'), as defined in Chapter 1, has historically been observed to increase with increasing pressure.[5-8] Numerous reports in the literature have cited changes in equilibrium constant (and thus retention factor) with changes in the run pressure for a separation.[9-14] McGuffin et al. observed a k' increase of 25 percent over a pressure range of only 100 to 350 bar, and along with others suggested that such large k' increase over a low pressure range could extrapolate to prohibitive k' increases at ultrahigh pressures.[14-17] By contrast, Figure 5-3 displays the k' increase with pressure observed for UHPLC using porous particles packed into capillary columns, using two different mobile phases for isocratic elution of several dihydroxybenzenes. The data show roughly a 30 percent increase in k' over a pressure range of 4000 bar, for analytes with a wide range of k' ($\sim 0.1 - 10$). This data is typical of that observed in our laboratory for reversed-phase UHPLC using porous and nonporous silica-based stationary phases. Comparing observations in the literature with our own observations for the trends of k' vs. pressure, one can see that although k' does increase with applied pressure, the amount of the increase is certainly not prohibitive for liquid chromatography with inlet pressures up to ~7000 bar.

From thermodynamics, one can show that the expected change in retention factor with pressure ($\partial \ln k' / \partial P$) will follow the relationship, assuming a constant column phase ratio:

$$\frac{\partial \ln k'}{\partial P} = -\frac{\Delta V}{RT} \tag{5-3}$$

where ΔV is the change in partial molar volume (mL/mol) upon sorption of the analyte to the stationary phase.[18] Several observations can be made from (5-3). ΔV is a constant that is roughly proportional to the molecular weight of a solute, so for small molecules the expected change in k' with increased pressure will be small, and for large molecules (such as proteins) the expected shift will be large. As a specific example using (5-3), a small organic molecule (MW~10^2 g/mol) will typically have a ΔV value near -2 mL/mol, and would observe a k' increase of only ~30% from atmosphere to 3500 bar. In contrast, a protein may have $\Delta V\sim$ -100 mL/mol or larger. This molecule would go from having a k' of 1 to being completely retained ($k' > 100$) within a 1000 bar pressure increase. The pressure range used in commercial instrumentation is relatively small (<300 bar), so the expected change in k' due to pressure is typically ignored, although it is not inconsequential for large solutes.[9, 12] Isocratic reversed-phase chromatography of large analytes such as peptides and proteins is not practical in most cases because of the steep slope of k' vs. organic modifier.[12] Small molecules will only be considered from this point forward in our discussion, since they are the most amenable to isocratic UHPLC and are expected to observe small and roughly linear increases in k' with pressure applied.

It is obvious from the above discussion that k' is a function of pressure for all retained solutes in reversed phase LC. Since there is a linear pressure drop across all chromatography columns utilizing pressure driven flow, k' will not be constant along the length of a column. The k' measured at the outlet is therefore the average retention factor the solute observes as it travels down the column. Since pressures used in UHPLC are significantly higher than traditional HPLC, the change in k' along the column will be much greater in magnitude. In order to obtain a true measure of k' at ultrahigh pressures, devoid of effects from a pressure

drop, an experiment was designed to enable k' measurement in a region that was at ultrahigh pressure (several kbar) but contained only a very small pressure drop (200 bar or less).

5.2.3 Simple Theory for Compression Effect on Retention Factor

I performed a simple thought experiment to help formulate my hypothesis that the compression event and ensuing linear velocity surge could cause an artificially elevated k' measurement at the outlet of a UHPLC column. Recall from Chapter 1 that k' is measured as follows:

$$k' = \frac{(t_r - t_m)}{t_m} \qquad (5\text{-}4)$$

where t_r is the retention time of your analyte and t_m is the void time. As our starting case, assume a column run at ultrahigh pressures (~4000 bar) with measured $t_m = 1$ min, and an analyte with a measured $k' = 1$ ($t_r = 2$ min).

As a rough approximation, it is safe to say that upon the start of an isocratic UHPLC run, a linear velocity surge will occur over approximately 10 percent of the column. Assume that this surge means that the dead-time marker will instantaneously move from the inlet to the position 10 percent into the column, then continue down the column at a constant (much lower) velocity after that. The dead-time marker would essentially "skip" the first 10 percent of the column. Recalculating the dead time for the column in a case without compression (t_m'), assuming the measured value (1 minute) was actually for only 90% (9/10[ths]) of the column follows as:

$$t_m' = t_m + \frac{1}{9} t_m \qquad (5\text{-}5)$$

So in this example the dead time without compression (t_m') is 1.111 minute.

Looking at the retained species, assume that with a $k' = 1$, the analyte migrates at half the velocity of the dead-time marker. Assume this also holds true for the compression event, since reversed-phase desorption kinetics are fast relative to the chromatographic time scale. Therefore, the analyte with $k' = 1$ will only move half the distance down the column during the compression event, or 5% into the column. The observed retention time (t_r) of 2 minutes therefore occurred over 95% of the column length ($19/20^{ths}$). Recalculating the predicted retention time without compression (t_r') , including the first 5% of the column therefore follows as above:

$$t_r' = t_r + \frac{1}{19} t_r \qquad (5\text{-}6)$$

Which gives t_r' equal to 2.105 minutes. Recalculating what the retention factor would be without compression (k'') simply follows as:

$$k'' = \frac{(t_r' - t_m')}{t_r'} \qquad (5\text{-}7)$$

The resulting k'' value for this example is 0.895.

With a simple set of assumptions we have shown that a linear velocity surge due to mobile phase compression could cause an actual retention factor of 0.895 to be measured as a k' of 1. Of course, it was understood that the actual effect should be less than this prediction because the example assumed *instantaneous* compression. Nonetheless, this thought experiment validated our desire to try to measure the trend of k' with pressure in UHPLC, void of effects from mobile phase compression.

5.3   Experimental

5.3.1   Chromatography Column for Dual-Detector Setup

A capillary column was desired that had two sections, a low flow resistance section at the inlet over which the pressure drop would be very small (ideally zero), and an outlet section to act as a flow restrictor, over which the majority of the pressure would be dropped. One way to achieve this is to pack the two sections with particles of drastically different diameter, since flow resistance scales with the particle diameter squared. A column was fabricated that had a 65.5-cm section packed with 4.5-μm porous particles at the inlet to act as the analytical column, and a 25.0-cm section packed with 0.5-μm nonporous silica particles at the outlet to act as the flow restrictor. This configuration was such that approximately 3 percent of the applied pressure was dropped over the first 65.5 cm, and the other 97 percent was dropped over the remaining 25-cm section.

This column was fabricated in the following manner. A 1.5-m section of 50-μm i.d. TSU (UV transparent) fused silica capillary (Polymicro Technologies, Phoenix, AZ) was cut and one end was tightened into a UHPLC fitting.[8] At the other end, a frit was manufactured by tapping the end of the capillary into a vial of 2.5 μm nonporous silica beads (Eichrom Technologies, Chicago, IL) and sintering the particles in place with an electric arc device.[19] A slurry of 4.5-μm BEH particles (Batch NLL-3-90, Waters Corporation, Milford, MA) was prepared at a concentration of 5 mg/mL in acetone, and suspended by sonication for 15 minutes. Approximately 2 mL of the slurry was loaded into a custom-built packing bomb,[5] and the column was packed to ~70 cm by ramping the pressure to ~9000 psi over the course of approximately 10 hours. Packing was stopped by releasing the pressure slowly through a leak valve. The column was removed from the bomb, and the remaining 4.5-μm particle slurry was rinsed from the bomb with ~50 mL of acetone from the pump.

The slurry was then replaced with 0.5-μm nonporous silica that had been manufactured in-house via a tetraethylorthosilicate (TEOS) condensation, and derivatized with octadecyltrimethoxysilane (C18).[20] A slurry of these particles was made at 5 mg/mL in 67/33 (v/v) hexane/acetone. The slurry was sonicated for ~20 minutes and loaded into the bomb, and packing was resumed. Pressure was ramped to ~30,000 psi over the course of ~5 hours, and the packing was allowed to continue for 3 days. Upon depressurization, the total packed bed length for the 0.5-μm material was ~29 cm.

The column (~99 cm total length) was rinsed with acetone and pressurized to ~50,000 psi using 35/65 (v/v) acetonitrile/water with 0.1% TFA for one hour. Pressure was slowly released to ~10,000 psi, at which point a resistive heating wire stripper (Teledyne Interconnect Devices, San Diego, CA) was used to make a frit so that 25 cm of the 0.5-μm bed remained in the column.[7] The column was then clipped at the frit (~95 cm total length) and the flow direction was reversed so that the 4.5-μm particles were at the inlet.

The column was reinstalled in a UHPLC fitting with the 4.5-μm section at the inlet, and pressurized to 50,000 psi for one hour to compress the bed in this region. The column was then depressurized slowly to ~10,000 psi, the wire stripper was used to make another frit at the inlet, and the capillary was clipped such that the total column length was 90.5 cm. After allowing the column to dry for ~1 hour, the electric arc device was used to heat the frits at each end of the capillary in order to make them more robust.

5.3.2 Chromatography Column for Isocratic Elution with a Single Detector

A column was prepared for normal UHPLC experiments, which was used to obtain "normal" data for k' vs pressure; i.e., data that had not been corrected for compression. Fifty-μm i.d. TSU fused silica capillary was used, and the column was packed with 1.5 μm BEH

particles (Batch KHG-6-55, Waters Corporation, Milford, MA) as previously described.[7] The length of the column used for these studies was 54.4 cm.

5.3.3 Dual-Detector Setup

In order to perform k' measurements that were independent of pressure drop and compression effects, two on-column UV detectors were used on the separation column. Using two UV detectors, k' can be determined by the difference in the retention time for analytes between each detector. The instrument setup is shown in Figure 5-4. A 75,000 psi Haskel pneumatic amplifier pump (Model DSXHF-903, Haskel, Burbank, CA) and an in-house machined static-split flow injector were used to perform isocratic elution, as described previously.[2, 5-8] Two Linear UVis 200 on-column detectors with capillary flowcells were situated in the section of the column containing the 4.5 μm particles, and set at a wavelength of 214 nm.

For experiments performed with 35/65 acetonitrile/water, the overall column length was 90.5 cm, with 65.5 cm of 4.5 μm packing and 25.0 cm of 0.5 μm packing. Detectors were positioned at 34.1 cm and 51.6 cm from the inlet. The column had to be refitted on both ends prior to the 10/90 acetonitrile/water experiments. The overall column length for those experiments was 86.0 cm with 64.0 cm of 4.5-μm packing and 22.0 cm of 0.5-μm packing. The first detector was always placed at least 30 cm from the inlet of the column, such that the compression event would be complete by the time the analyte reached the first detector.

Data was recorded from the UV detectors at 11 Hz using a BNC-2090 break-out box (National Instruments Corp., Austin, TX) connected to a PC, and Stripchart Recorder XP (www.alchemistmatt.com) written in LabView 6 (National Instruments Corp., Austin, TX).

Data processing was performed in Igor Pro 4.08 (Wavemetrics, Inc., Lake Oswego, OR), with several in-house written macros.[21, 22]

5.3.4   Single-Detector Experiments

For the experiments performed as normal UHPLC runs a single Linear UVis 200 detector was used at a wavelength of 214 nm. The detector was positioned 4.5 cm from the outlet of a 54.4 cm-long column packed with 1.5 μm BEH particles (see section 5.3.1.2). Average column pressure with respect to this detector was taken as the average between the inlet pressure and the approximate pressure at the on-column detector, assuming a linear pressure drop along the length of the column.

5.3.5   Materials and Reagents

Two mobile phase compositions were used in these experiments, 10/90 (v/v) acetonitrile/water and 35/65 (v/v) acetonitrile/water. Mobile phases were made using HPLC-grade acetonitrile (Fischer Scientific) and 0.2-μm filtered water. Mixtures were made volumetrically, by mixing a premeasured volume of organic with a premeasured volume of water; i.e., 10/90 (v/v) acetonitrile/water was made by mixing 100 mL acetonitrile with 900 mL water. One mL of trifluoroacetic acid (TFA, Sigma-Aldrich) was added per liter of mobile phase to all mobile phases. Samples were made by diluting chemicals as received from Sigma-Aldrich in mobile phase to the desired concentration. Analytes were ascorbic acid (or AA), 1,4-dihydroxybenzene (hydroquinone, or HQ), 1,3-dihydroxybenzene (resorcinol, or Res), 1,2-dihydroxybenzene (catechol, or Cat), and 4-methyl-1,2-dihydroxybenzene (4-methyl catechol, or MCat). All solutions were made and data was collected at room temperature, which was 25±2°C.

5.4   Results of Experimental Measurements

5.4.1 k' vs. Pressure for Single Detector, Isocratic UHPLC

Figure 5-5 contains two plots of k' vs pressure, as obtained for isocratic UHPLC with the 54.4-cm column packed with 1.5-μm BEH porous particles. For 10/90 acetonitrile/water (Figure 5-5B), methyl catechol was fairly heavily retained, giving a k' value that ranged approximately between 9 and 11. On the other hand, hydroquinone was only lightly retained when 35/65 acetonitrile/water was the mobile phase, giving a k' value between 0.2 and 0.3. Pressure plotted on the bottom x-axis in each plot is the average column pressure between the inlet and the detector. This was done in order to allow comparison of this data with data obtained using the dual-detector system (with which k' is determined independent of pressure drop).

Between the four analytes and two mobile phases shown in Figure 5-5, the range of k' values covered is fairly extensive, from ~0.2 to ~10. These two systems therefore provided a fairly wide range of k' over which to evaluate our hypothesis, that compression was infact causing an artificial increase in the measured value. This data is referred to as "normal" UHPLC k' vs. pressure data in the remainder of this manuscript.

5.4.2 k' vs. Pressure for Dual-Detector, Isocratic UHPLC

Retention factor vs. pressure experiments were performed in two mobile phases using the long (~90 cm) column described previously (Section 5.3.1). Figure 5-6 shows raw data from a typical experiment using the dual-UV detector setup. This particular experiment was run with 10/90 acetonitrile/water mobile phase at an inlet pressure of 3920 bar (56,800 psi). Immediately noticeable in Figure 5-6 is the long run time. This was one of the higher pressure runs, and in fact run times extended to greater than 10 hours for the experiment

performed at 1830 bar (26,500 psi). The long run times were a consequence of the high flow resistance of the 0.5-μm packing in the outlet of the column, and the high k' values observed for our analytes in 10/90 acetonitrile/water mobile phase.

Retention times from the data shown in Figure 5-6 are reported in Table 5-1. The "difference" retention time was simply calculated as the difference between the UV 2 and UV 1 retention times for each analyte. Table 5-1 also contains the calculated retention factors for the column segment between the detectors, which were presumed to be completely free of effects from compression and virtually free of effects from pressure drop.

Experiments such as that shown in the example Figure 5-6 were performed from 1250 to 4200 bar inlet pressure for 10/90 acetonitrile/water, and from 1300 to 3800 bar for 35/65 acetonitrile/water. Since there was only a very small pressure drop in the region of the column packed with 4.5 μm particles, the pressure at the inlet was used as the average pressure between the two UV detectors. The detection region (between the two UV detectors) was outside the region of the column that experienced a linear velocity surge due to compression, so this data was called "compression-corrected".

Figure 5-7 shows the k' vs. average column pressure data for 10/90 acetonitrile/water (Figure 5-7A) and 35/65 acetonitrile/water (Figure 5-7B). Compression-corrected and normal UHPLC data (shown also in Figure 5-5), were compared in this figure for three analytes, hydroquinone (HQ), catechol (Cat), and 4-methyl catechol (MCat). Linear regressions for each data set are also shown, with the compression-corrected as solid lines and normal UHPLC as dashed. It is obvious from Figure 5-7 that mobile phase compression caused an increase in slope and an artificial increase in observed k' for every analyte in both

mobile phases. Values for slope ($\mathrm{d}k'/\mathrm{d}P$) and y-intercept (k_0') from the analytes shown in these plots (and also for resorcinol) are recorded in Table 5-2.

Table 5-2 shows that the percent difference in the k' vs. pressure curves (% Δ ($\mathrm{d}k'/\mathrm{d}P$)), comparing compression-corrected UHPLC to normal UHPLC, is between 36% and 76%. For 10/90 acetonitrile/water, the difference in the measurements is greatest for the low values of k', and decreases as k' increases. This would lead one to believe that the error in observed k' values is greatest in UHPLC for lightly retained analytes. The trend is less clear for 35/65 acetonitrile/water, although the highest retained analyte still had the lowest percent difference.

Since 35/65 acetonitrile/water is a more compressible mobile phase than 10/90 acetonitrile/water, we expected the k' artifact from compression to be greater for 35/65. The data in Table 5-2 does not support this hypothesis, since the average percent change is actually higher for the 10/90 acetonitrile/water case. However, we cannot draw any solid conclusions from this because the range of k' studied is different for each mobile phase system.

Note as well that the k' values at atmospheric pressure, denoted k_0' in the table, are different for the "normal" UHPLC case and the compression-corrected case. If the experiment performed ideally, the predicted k' at atmospheric pressure should be the same for a given mobile phase and analyte (one row in Table 5-2). Recall that the compression-corrected experiments were done using a column packed with 4.5-μm material, while the "normal" UHPLC experiments used 1.5-μm particles. Although the 1.5-μm and 4.5-μm BEH material used in the two columns was nominally the same composition, it was from different batches and had slightly different pore diameters by mercury porosimetry (Kevin

Wyndham, Waters Corporation, Milford, MA). For the 4.5-μm material, the pore diameter was 158 Å, while for the 1.5-μm particles, it was 145 Å. Larger pore diameters typically mean a lower specific surface area, so this could explain the slightly lower value of k_0' obtained for the compression-corrected case.

5.4.3 Error in Change in Partial Molar Volume (ΔV) Values due to Compression

The change in partial molar volume (ΔV) upon sorption of an analyte to the stationary phase is a thermodynamic parameter that can be calculated from data for retention factor as a function of pressure, as discussed in Section 5.2.2. ΔV for an analyte at infinite dilution is roughly proportional to molecular weight in a biphasic system, and is also related to the various intermolecular forces at work between the analyte and the two-phase system. As such, it is sometimes measured to investigate solute-surface interactions and has even been suggested as a parameter through which pressure could be used to perform a separation.[23] Recall that ΔV can be solved for using:

$$\Delta V = -\frac{\partial \ln k'}{\partial P} RT \qquad (5\text{-}8)$$

where ($\partial lnk'/\partial P$) is simply the slope of a plot of ln k' versus pressure from our experimental data. Therefore, ΔV was calculated for each of our analyte/mobile phase pairs for the normal UHPLC and compression-corrected UHPLC. The value for RT used in the calculation was 2478.97 J/mol. Values for $\partial lnk'/\partial P$ and ΔV are reported in Table 5-3 for each analyte.

As expected, artifacts due to compression caused all the ΔV values to be larger in magnitude for the normal UHPLC case than when compression-corrected. In general, compression caused an average measurement error between 30 and 70 percent for ΔV. The

average ΔV value for all analytes was around -2 mL/mol, which fits with literature values for small molecules in reversed-phase LC.[18] The ΔV values were smaller for all analytes in the more hydrophobic mobile phase; this is consistent with theory because a lower ΔV value is expected when the two phases in a biphasic system are more alike.

5.4.4 Experimental Results Summary

In general, the experiments performed revealed that the linear velocity surge caused by mobile phase compression in UHPLC can cause an artificial inflation of measured k' values. This means that the k' values measured with a static split-flow style injection system in isocratic UHPLC will be slightly elevated over the value that would be measured using a hypothetical loop-style injection system, in which case the mobile phase would be already compressed before the injection. In addition, values for change in partial molar volume (ΔV) calculated from k' vs. pressure plots will have error of roughly 30 to 70 percent when measured using a system that does not account for compression of the mobile phase.

Jerkovich used experimental data to come up with an empirical relationship to describe the linear velocity surge due to compression of the mobile phase, as discussed in the introduction of this chapter. I was eager to know if the model he developed could be extended, so as to predict the experimental observation of elevated retention factor due to compression, as investigated above. In addition, I was interested to see what the model predicted about the mobile phase C-term variance contribution for retained species during a compression event, which had not been addressed experimentally. The ensuing set of theoretical exercises was intended to address these two questions.

5.5 Results of Theoretical Treatment of Mobile Phase Compression

5.5.1 Extension of Compression Theory to Retained Compounds

As described in Section 5.2.1, the distance vs. time profile for a velocity surge caused by mobile phase compression can be fit with the empirical equation (5-1):

$$x(t) = A\left(1 - e^{-t/\tau}\right) + ut \qquad (5\text{-}1)$$

and the derivative of (5-1) with respect to time yields an expression that can describe the instantaneous mobile phase velocity at any point in time:

$$u'(t) = \left(\frac{\partial x}{\partial t}\right) = \left(\frac{A}{\tau}\right)e^{-t/\tau} + u \qquad (5\text{-}2)$$

To attempt to describe the behavior of a retained species ($k' > 0$), I made the assumption that a compression event would occur over the same period of time as for an unretained species, but that the retained analyte band would move down the column at a lower velocity. This was a safe assumption because reversed-phase partitioning kinetics are known to be very fast relative to the chromatographic time scale. The velocity at which the analyte band moves (u^*) can be related to the mobile phase velocity (u) by the expression:

$$u^* = \frac{u}{(1 + k')} \qquad (5\text{-}9)$$

where k' is the analyte retention factor.

Recall also that the experimental parameter A in (5-1) is the effective distance migrated during the velocity surge event, and is empirically dependent on the mobile phase composition, column length, and pressure. The same logic used to find u^* can be used to

adjust A for analyte retention, since the analyte migration distance during a fixed time is also related to k'. Therefore the value A^* for the retained case is defined as:

$$A^* = \frac{A}{(1+k')} \qquad (5\text{-}10)$$

Substituting expressions for u^* and A^* into (5-1) and (5-2) for u and A, expressions for a retained species' position and instantaneous velocity as a function of time can be obtained:

$$x(t) = \frac{A\left(1 - e^{-t/\tau}\right) + ut}{(1+k')} \qquad (5\text{-}11)$$

$$u'(t) = \left(\frac{A}{(1+k')\tau}\right)e^{-t/\tau} + \frac{u}{(1+k')} \qquad (5\text{-}12)$$

Using (5-11) and (5-12) plots of velocity versus column position, similar to that shown in Figure 5-2A, can be generated for a retained species.

5.5.2   Estimation of Constants

Before (5-11) and (5-12) can be used to estimate the change in k' vs. pressure due to compression, the constants A, τ, k' and u must be obtained, so that the only unknown for a specific case is time. First a set of starting conditions was required, so column conditions were assumed as follows: 50-cm column length, 50-μm column diameter, and 1.5-μm particle diameter. From data obtained by Jerkovich for 10/90 acetonitrile/water, the constants A and τ were calculated in 10,000 psi increments from atmosphere to 50,000 psi. Values for u were calculated based on the Kozeny-Carman relationship for flow through a packed bed (Equation 1-7). Values for k' were then varied in order to generate a series of

velocity vs. position curves which provided an avenue for predicting compression effects on measured k' and C-term variance. For the initial simulation k' was assumed constant at the average value between the inlet and outlet, and actual k' change due to pressure drop along the column was ignored.

As an example, assume the case where pressure is 50,000 psi. Under these conditions, it was gathered from Jerkovich's data that the linear velocity surge event occurred over roughly 11% of the column length, and 5% of the measured dead time of the column. Using this information, the constants A and τ in (5-11) and (5-12) were calculated to be 2.75 cm and 1.72 sec, respectively. Linear velocity (u) was found to be 0.29 cm/sec in this case. The solution to (5-11) is shown in Figure 5-8A, in a plot of distance (or column position) versus time for a deadtime marker ($k' = 0$). Figure 5-8B is the solution to (5-12), velocity versus time. Plotting the y-axes of Figures 5-8A and 5-8B against one another, Figure 5-8C is obtained, which is a plot of velocity versus column position for an unretained species.

5.5.3   Prediction of k' vs. Pressure for Retained Species

The same procedure as noted above was followed for k' values of 0.22, 0.34, 0.59 and 1.00. These values were the average k' expected for the retained analytes in 35/65 acetonitrile/water mobile phase on a BEH column at 50,000 psi (3400 bar) inlet pressure. The resulting velocity vs. position plot for analytes with these retention factors is shown in Figure 5-9. In this figure, migration velocity of the respective analyte band was plotted on the Y-axis and column position on the X. From this figure, it is obvious that the terminal velocity of an analyte was based on its retention factor (higher k' has lower terminal velocity). In

addition, analytes with higher k' exhibited both a slower initial velocity and a shorter distance traveled during the linear velocity surge.

One final modification was necessary in order to make the model as accurate as possible. That was to allow k' to vary along the column length, based on the actual data obtained for k' vs. pressure from the dual-detector experiments discussed in section 5.4.2. To make this modification, the k' value was not assumed constant as in the above example, but was allowed to vary based on the pressure in the column. The intercept values (value at atmospheric pressure) for k' were 0.21, 0.31, 0.47, and 0.82. Figure 5-10 shows a plot of band velocity versus column position for the 50,000 psi (3400 bar) case when k' was allowed to vary along the column length. Figure 5-10 looks very similar to Figure 5-9, with one major exception. Note that after the compression event reaches completion, the velocity of each retained analyte actually increased as it traveled down the column. This of course was a result of the analyte becoming less retained as it moved down the column, as a function of decreasing pressure.

To calculate modeled k' with compression included, the final step was to calculate the retention times of the dead-time marker and retained species, using the data shown in Figure 5-10. The total retention time of each analyte was calculated simply by adding together the time elapsed during the migration, as the sum of the time elapsed in 0.1 cm distance segments:

$$t_r = \sum_{n=1}^{n=500} u_n (0.1 cm) \qquad (5\text{-}13)$$

The above calculations were performed for the modeled conditions at pressures of 10, 20, 30 and 50 kpsi (700, 1400, 2100, and 3400 bar). The case without compression was modeled in the same manner, except the exponential portion of equations (5-11) and (5-12) were eliminated.

The retention time results from these simulations are presented in Tables 5-4 and 5-5. Table 5-4 shows the retention times that were calculated for the case where no mobile phase compression occurs, i.e. the mobile phase linear velocity was constant as a function of time. Table 5-5 shows the retention times calculated in the case of a compression-induced linear velocity surge. Note that the dead time and retention time for each analyte was faster in the compression case than the constant velocity case, and that the difference between the compression-and non-compression cases was largest for the highest pressure (in proportion to the migration time).

Tables 5-6 and 5-7 show the retention factors calculated for the non-compression and compression case, respectively. The values were calculated using retention times reported in Tables 5-4 and 5-5. Mobile phase compression caused an increase in the observed k' that became more obvious for higher pressures. The model predicted roughly a 5% increase in measured k' for the compression case over the non-compression case, for all analytes when the inlet pressure was 50,000 psi (3400 bar). The data is displayed graphically in Figure 5-11. To compare with the experimental data, the compression case was referred to as "normal" UHPLC data in Figure 5-7, and the non-compression case was referred to as "compression corrected". Comparing Figures 5-11 and 5-7B, it is obvious that for similar analyte k' the compression model does a good job of predicting the increase in slope of k' versus pressure curves.

It was thus confirmed with some degree of certainty that a linear velocity surge due to compression was the cause of the difference in slope of k' vs. pressure between the normal UHPLC data and the compression-corrected UHPLC data as presented in Section 5.4.2. The model described herein was able to describe the linear velocity of a retained analyte in the case where a linear velocity surge was expected due to mobile phase compression, and predict the effect on measured k'.

5.5.4 Prediction of Variance Contribution from Compression for a Retained Species

The final area of interest for this model was to see what predictions it made about the mobile phase variance contribution for retained analytes that would occur from the linear velocity surge. The equation that describes the variance contribution from mobile phase C-term $((\sigma_L^2)_{CM})$, as a function of retention factor (k') is:

$$\left(\sigma_L^2\right)_{CM} = H_{CM}L = \left(\frac{1+6k'+11k'^2}{(1+k')^2}\right)\frac{d_p^2 u}{24D_M} \tag{5-14}$$

where d_p is particle diameter, u is linear velocity, and D_M is diffusion coefficient in the mobile phase.[24] Using the linear velocity values as calculated in the previous section, expression (5-14) was evaluated for the special case where the inlet pressure was 50,000 psi (3400 bar). The expression was evaluated in both the compression and non-compression cases, so that the absolute additional variance due to the linear velocity surge could be examined. In this simulation, k' was also varied from approximately 0.1 to 25, in order to see what the effect would be for analytes from very lightly retained to essentially fully retained.

167

Figure 5-12 shows the excess mobile phase C-term variance expected from the linear velocity surge as a function of retention factor. The function experienced a maximum around $k' = 1$, which means that the variance contribution due to mobile phase compression is expected to be at its worst when the analyte is partitioned half in the mobile phase and half in the stationary phase. However, the fractional contribution to total C-term variance from the velocity surge is greatest for a deadtime marker, as shown in Figure 5-13. The excess variance from the linear velocity surge is depicted here as a percentage of the total C-term variance. Since the total C-term variance goes up as the retention time goes up, the contribution from the linear velocity surge makes the largest impact for lightly retained species. The percent contribution from compression decreased from 16% of the total C-term variance at $k' = 0$ to 2% at $k' = 25$. This suggests that evaluation of columns using isocratic UHPLC with static split-flow injection should be done with as high a retention factor as is practical, in order to reduce the variance contribution from mobile phase compression.

5.6   Conclusions

A linear velocity surge due to mobile phase compression was shown through both experimental evidence and theoretical modeling to cause artificially elevated retention factor values. The velocity surge event was found to cause error in k' values on the order of 10% at pressures of 50,000 psi (3400 bar). Until recently, no injection system was capable of performing loop-style injections at pressures above 15,000 psi (1000 bar). Very recently, a commercial injector from VICI has been reported to perform injections up to 40,000 psi (2700 bar).[25, 26] This injector would serve to circumvent the problems caused by a linear-

velocity surge as described in this chapter, and would help optimize the performance of UHPLC. The static-split flow injector as used in our lab is still the only style of injector capable of performing reproducible injections at greater than 40,000 psi (2700 bar); its operational limit is roughly 100,000 psi (7000 bar).

In addition, the compression-induced velocity surge was modeled to have the greatest impact on the chromatographic efficiency of a capillary UHPLC column at low retention factors. Our columns have historically been evaluated with analytes having k' ranging from 0.1 to 1. Data presented here argues for using at least one analyte with k' around 3, where the expected contribution from compression would be reduced to roughly 5% of the C-term variance at 50,000 psi (3400 bar).

5.7   References

(1)   Jerkovich, A. D., University of North Carolina at Chapel Hill, Chapel Hill, 2003.

(2)   Jerkovich, A. D.; Mellors, J. S.; Thompson, J. W.; Jorgenson, J. W. *Anal. Chem.* **2005**, *77*, 6292.

(3)   Martin, M.; Blu, G.; Guiochon, G. *J. Chrom. Sci.* **1973**, *11*, 641.

(4)   *CRC Handbook of Chemistry and Physics*, 77 ed.; CRC Press, Inc.: New York, 1996-1997.

(5)   MacNair, J. E.; Lewis, K. C.; Jorgenson, J. W. *Anal. Chem.* **1997**, *69*, 983-989.

(6)   MacNair, J. E.; Patel, K. D.; Jorgenson, J. W. *Anal. Chem.* **1999**, *71*, 700-708.

(7)   Mellors, J. S.; Jorgenson, J. W. *Anal. Chem.* **2004**, *76*, 5441.

(8)   Patel, K. D.; Jerkovich, A. D.; Link, J. C.; Jorgenson, J. W. *Anal. Chem.* **2004**, *76*, 5777.

(9)   Liu, X.; Zhou, D.; Szabelski, P.; Guiochon, G. *Anal. Chem.* **2003**, *75*, 3999-4009.

(10)   Bidlingmeyer, B. A.; Hooker, R. P.; Lochmuller, C. H.; Rogers, L. B. *Sep. Science* **1969**, *4*, 439-446.

(11)   Bidlingmeyer, B. A.; Rogers, L. B. *Sep. Science* **1972**, *7*, 131-158.

(12)   Chen, S. H.; Ho, C. T.; Hsiao, K. Y.; Chen, J. M. *J. Chrom A.* **2000**, *891*, 207-215.

(13)   Evans, C. E.; Davis, J. A. *Anal. Chim. Acta* **1999**, *397*, 163-172.

(14)   Guiochon, G.; Sepaniak, M. J. *J. Chrom.* **1992**, *606*, 248-250.

(15)   McGuffin, V. L.; Chen, S. H. *Anal. Chem.* **1997**, *69*, 930-943.

(16)   McGuffin, V. L.; Evans, C. E.; Chen, S. H. *J. Microcol. Sep.* **1993**, *5*, 3-10.

(17)   McGuffin, V. L.; Evans, C. E. *J. Microcol. Sep.* **1991**, *3*, 513-520.

(18)   Martin, M.; Guiochon, G. *J. Chrom A.* **2005**, *1090*, 16-38.

(19)   Hoyt, A. M., Jr.; Beale, S. C.; Larmann, J. P., Jr.; Jorgenson, J. W. *Journal of Microcolumn Separations* **1993**, *5*, 325-330.

(20)   Mellors, J. S., University of NC at Chapel Hill, Chapel Hill, NC, 2005.

(21)   Monroe, M. E., Univ. of North Carolina, Chapel Hill,NC, 2002.

(22)   Fadgen, K. E., Univ. of North Carolina, Chapel Hill, NC, 2001.

(23)   Giddings, J. C. *Sep. Science* **1966**, *1*, 73-80.

(24)   Neue, U. D. *HPLC Columns: Theory, Technology, and Practice*; Wiley-VCH, Inc.:
New York, NY, 1997.

(25)   Anspach, J. A.; Maloney, T. D.; Brice, R. W.; Colon, L. A. *Anal. Chem.* **2005**, *77*,
7489-7494.

(26)   Xiang, Y.; Lin, Y.; Stearns, S. D.; Plistil, A.; Lee, M. L. *Anal. Chem.* **2006**, *78*, 858-
864.

retention time	Detector Position (cm)	AA (t_d)	HQ	Res	Cat	Mcat
UV Detector 1	31.6	12.19	33.13	64.34	84.06	247.34
UV Detector 2	51.6	20.26	49.83	93.81	122.6	354.87
Difference	20.0	8.07	16.70	29.47	38.54	107.53
Difference k′	20.0	0	1.07	2.65	3.78	12.32

Table 5-1: Retention times for Dual-UV detector experiment Mar07_02, shown in Figure 5-6. Time values are in minutes. Retention factor was calculated using equation (5-4) for the difference retention times. This experiment was performed in 10/90 acetonitrile/water mobile phase at an inlet pressure of 3920 bar (56,800 psi). Detector position is in cm from inlet of the column.

		Normal UHPLC		Compression-Corrected		
Mobile Phase	Analyte	k_0'	dk'/dP	k_0'	dk'/dP	% Δ (dk'/dP)
10/90	MCat	8.74	1.5E-03	8.03	1.1E-03	36%
10/90	Cat	3.11	4.0E-04	2.74	2.7E-04	48%
10/90	Res	1.99	3.9E-04	1.77	2.3E-04	67%
10/90	HQ	0.78	1.7E-04	0.69	9.6E-05	76%
35/65	MCat	1.01	1.5E-04	0.88	1.1E-04	36%
35/65	Cat	0.61	5.7E-05	0.51	3.6E-05	57%
35/65	Res	0.41	4.3E-05	0.34	2.9E-05	48%
35/65	HQ	0.27	1.8E-05	0.22	1.2E-05	51%

Table 5-2: Retention factor extrapolated to P = 0 bar (k_0'), and slope of k' vs.pressure curves (*dk'/dP*) for normal UHPLC data and compression-corrected UHPLC data. Mobile phase ratios refer to the volumetric ratio of acetonitrile to water, and assume inclusion of 0.1% TFA. The slope is reported in units of bar^{-1}. Data is shown in graphical form (except for resorcinol) in Figure 5-7.

		Normal UHPLC		Compression-Corrected		
Mobile Phase	Analyte	*dlnk'/dP*	ΔV (mL/mol)	*dlnk'/dP*	ΔV (mL/mol)	% error (ΔV)
10/90	MCat	1.4E-04	-3.5	1.0E-04	-2.5	38%
10/90	Cat	1.1E-04	-2.7	7.7E-05	-1.9	42%
10/90	Res	1.6E-04	-3.9	9.7E-05	-2.4	61%
10/90	HQ	1.7E-04	-4.2	1.0E-04	-2.5	68%
35/65	MCat	1.3E-04	-3.3	9.6E-05	-2.4	37%
35/65	Cat	8.6E-05	-2.1	6.1E-05	-1.5	42%
35/65	Res	9.6E-05	-2.4	7.1E-05	-1.8	36%
35/65	HQ	6.3E-05	-1.6	4.9E-05	-1.2	28%

Table 5-3: Calculated values of change in partial molar volume (ΔV) for our analytes using k' vs.pressure data from normal UHPLC and compression-corrected UHPLC. Calculations were performed using the same data as Table 5-2. *dlnk'/dP* data is in units of bar^{-1}. Percent error is calculated as the error in the normal UHPLC ΔV values compared to the compression-corrected values.

NO VELOCITY SURGE, retention time						
Inlet P (bar)	Avg P (bar)	AA	HQ	Res	Cat	Mcat
690	345	14.40	17.42	19.03	21.39	26.68
1379	690	7.20	8.74	9.59	10.78	13.60
2069	1034	4.80	5.84	6.44	7.25	9.24
3448	1724	2.88	3.53	3.92	4.42	5.75

Table 5-4: Retention time results of simulated ultrahigh pressure runs for a 50cm column packed with 1.5 μm particles, allowing k' to vary with pressure, but omitting the velocity surge due to mobile phase compression. Results obtained using a combination of Equations (5-11) and (5-12), omitting the exponential portions from the linear velocity surge. Retention times listed in minutes.

COMPRESSION-INDUCED VELOCITY SURGE, retention time						
Inlet P (bar)	Avg P (bar)	AA	HQ	Res	Cat	Mcat
690	345	14.23	17.25	18.87	21.23	26.52
1379	690	7.05	8.58	9.44	10.62	13.43
2069	1034	4.65	5.69	6.29	7.09	9.09
3448	1724	2.73	3.38	3.77	4.26	5.60

Table 5-5: Retention time results of simulated ultrahigh pressure runs for a 50cm column packed with 1.5 μm particles, allowing k' to vary with pressure, and including velocity surge due to mobile phase compression. Results obtained using a combination of Equations (5-11) and (5-12). Retention times listed in minutes.

NO VELOCITY SURGE, retention factor						
Inlet P (bar)	Avg P (bar)	AA	HQ	Res	Cat	Mcat
690	345	0	0.210	0.322	0.486	0.853
1379	690	0	0.214	0.332	0.498	0.889
2069	1034	0	0.217	0.342	0.510	0.925
3448	1724	0	0.225	0.362	0.534	0.998

Table 5-6: Retention factor results of simulated ultrahigh pressure runs for a 50cm column packed with 1.5 μm particles, allowing k' to vary with pressure, but omitting the velocity surge due to mobile phase compression. Results calculated using the retention times listed in Table 5-4.

COMPRESSION-INDUCED VELOCITY SURGE, retention factor						
Inlet P (bar)	Avg P (bar)	AA	HQ	Res	Cat	Mcat
690	345	0	0.212	0.326	0.492	0.864
1379	690	0	0.217	0.339	0.507	0.906
2069	1034	0	0.225	0.354	0.526	0.955
3448	1724	0	0.238	0.382	0.563	1.052

Table 5-7: Retention factor results of simulated ultrahigh pressure runs for a 50-cm column packed with 1.5 μm particles, allowing k' to vary with pressure, including the velocity surge due to mobile phase compression. Results calculated using the retention times listed in Table 5-5.
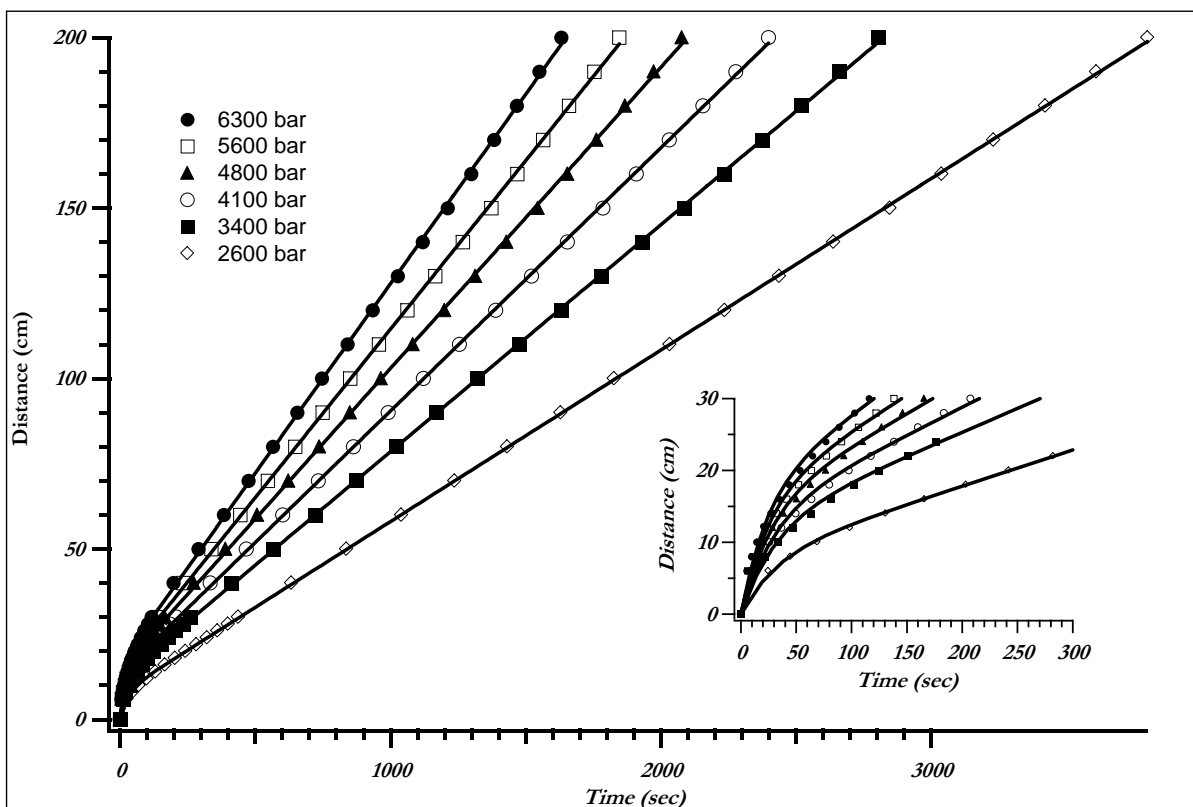
Figure 5-1: Distance versus time plots for runs at pressures from 2600 bar (38,000 psi) to 6300 bar (91,000 psi) performed on a 206-cm long capillary column packed with 1.5 μm nonporous silica. Mobile phase was 10/90 (v/v) acetonitrile/water with 0.1% TFA. The inset shows the first 30 cm of the column in greater detail. Figure reprinted with permission from reference 2.
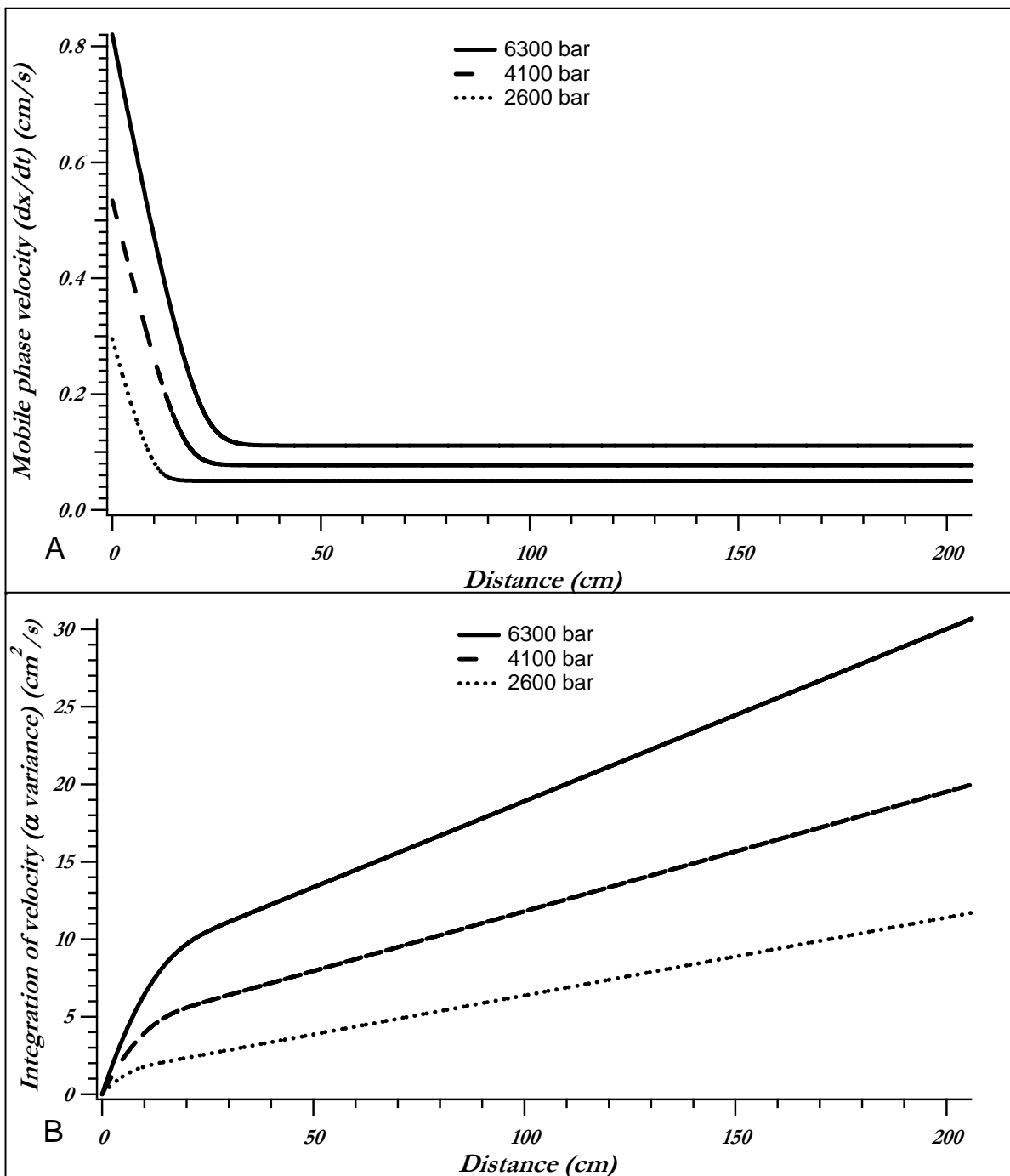
Figure 5-2: Mobile phase velocity (A) and integration of velocity (B) versus distance from the column inlet for various pressures for a 206-cm column packed with 1.5 μm nonporous silica, with 10/90 acetonitrile/water 0.1% TFA as the mobile phase. Figure reprinted with permission from reference 2.
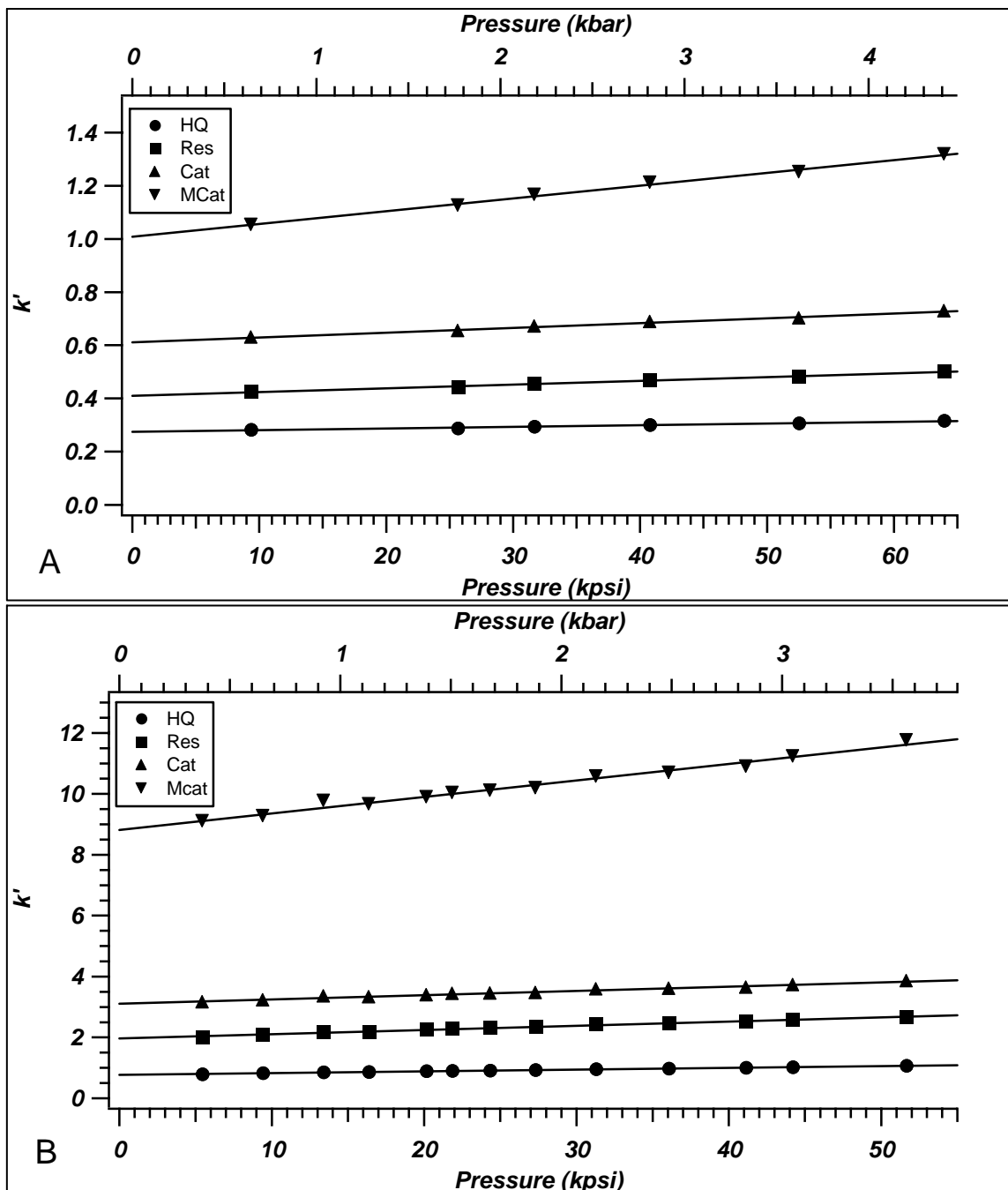
Figure 5-3: The effect of inlet pressure on retention factor in UHPLC. k' vs.pressure on 30-µm i.d. capillary columns packed with 1.5 µm BEH porous particles, run in (A) 35/65 (v/v) acetonitrile/water with 0.1% TFA and (B) 10/90 (v/v) acetonitrile/water with 0.1% TFA. Analytes are hydroquinone (HQ), resorcinol (Res), catechol (Cat) and 4-methyl catechol (MCat).
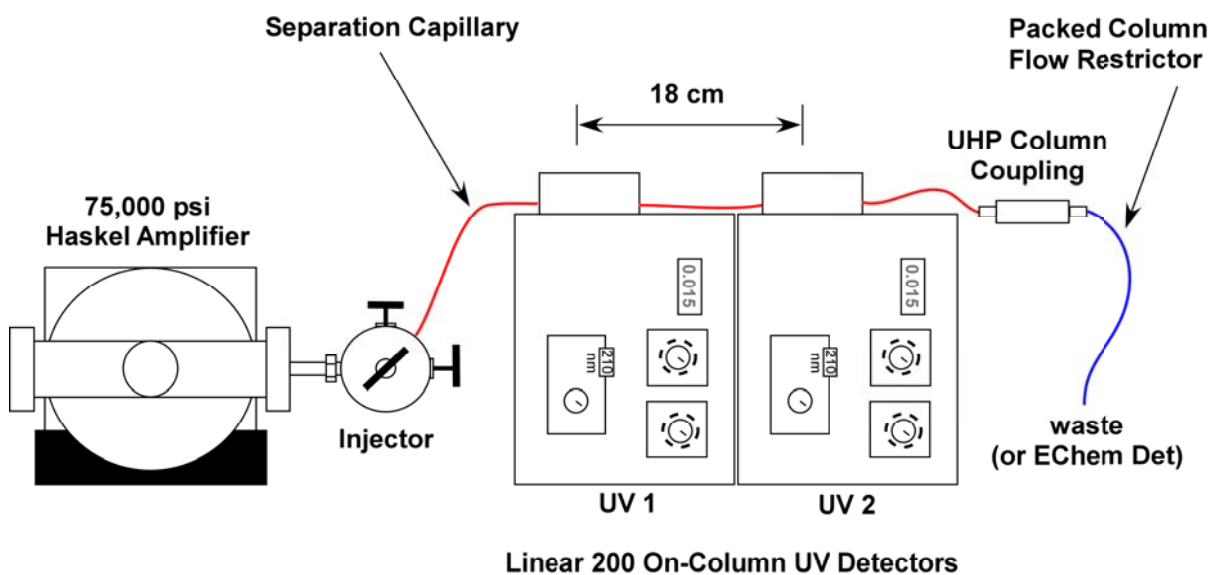
Figure 5-4: Instrument diagram for experiments used in the determination of k' vs. pressure, independent of compression and pressure drop. The column described in the text did not use a column coupling, but a single column packed with two different size particles. The separation section of the column (red) contained 4.5- μm porous particles, and the flow restrictor (blue) contained 0.5-μm particles. The drawing is not to scale.
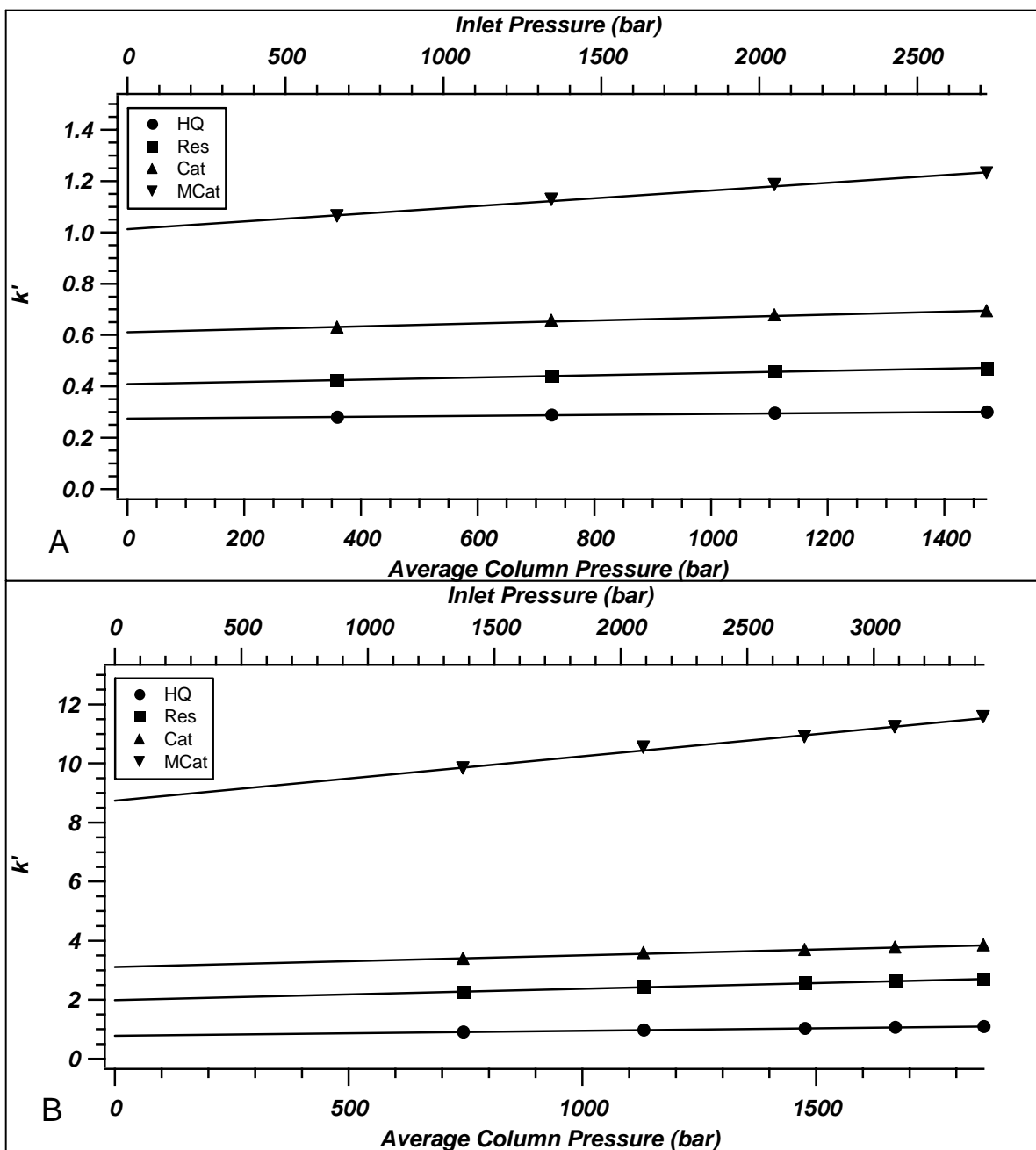
Figure 5-5: Observed effect of k' vs.pressure for "normal" UHPLC using a 54.4 cm x 50 μm i.d. column packed with 1.5 μm BEH particles, with UV detection at 4.5 cm from the outlet. Data collected using (A) 35/65 acetonitrile/water mobile phase, and (B) 10/90 acetonitrile/water mobile phase. Note that the bottom axis in (A) and (B) is average column pressure.
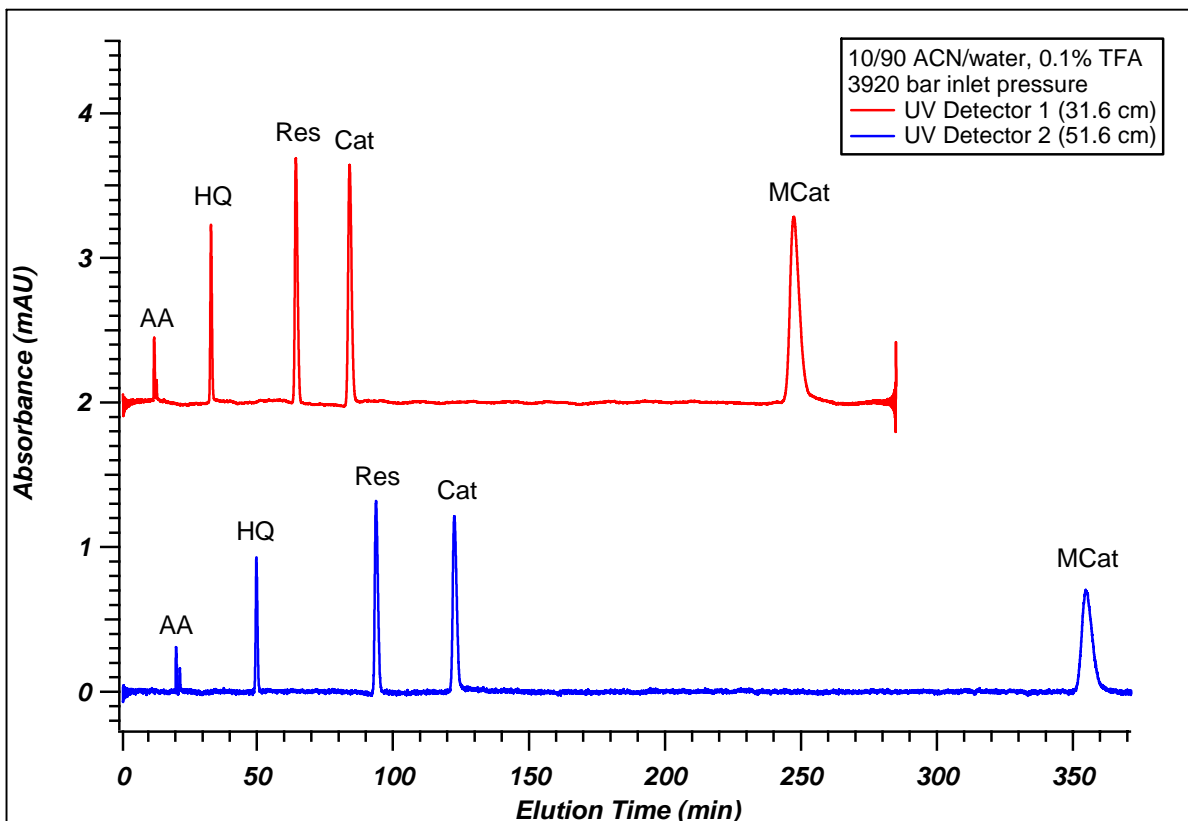
Figure 5-6: Raw data from experiment Mar07_02, a Dual-detector UV experiment with 10/90 acetonitrile/water as the mobile phase. The column used in this experiment was 86.0 cm long, with 64.0 cm of 4.5 μm particles and 22.0 cm of 0.5 μm particles. The pressure at the inlet was 3920 bar (56,800 psi). See Tables 5-1 and 5-2 for retention time and retention factor data. The trace for UV detector 1 was offset by +2 mAU for visualization.
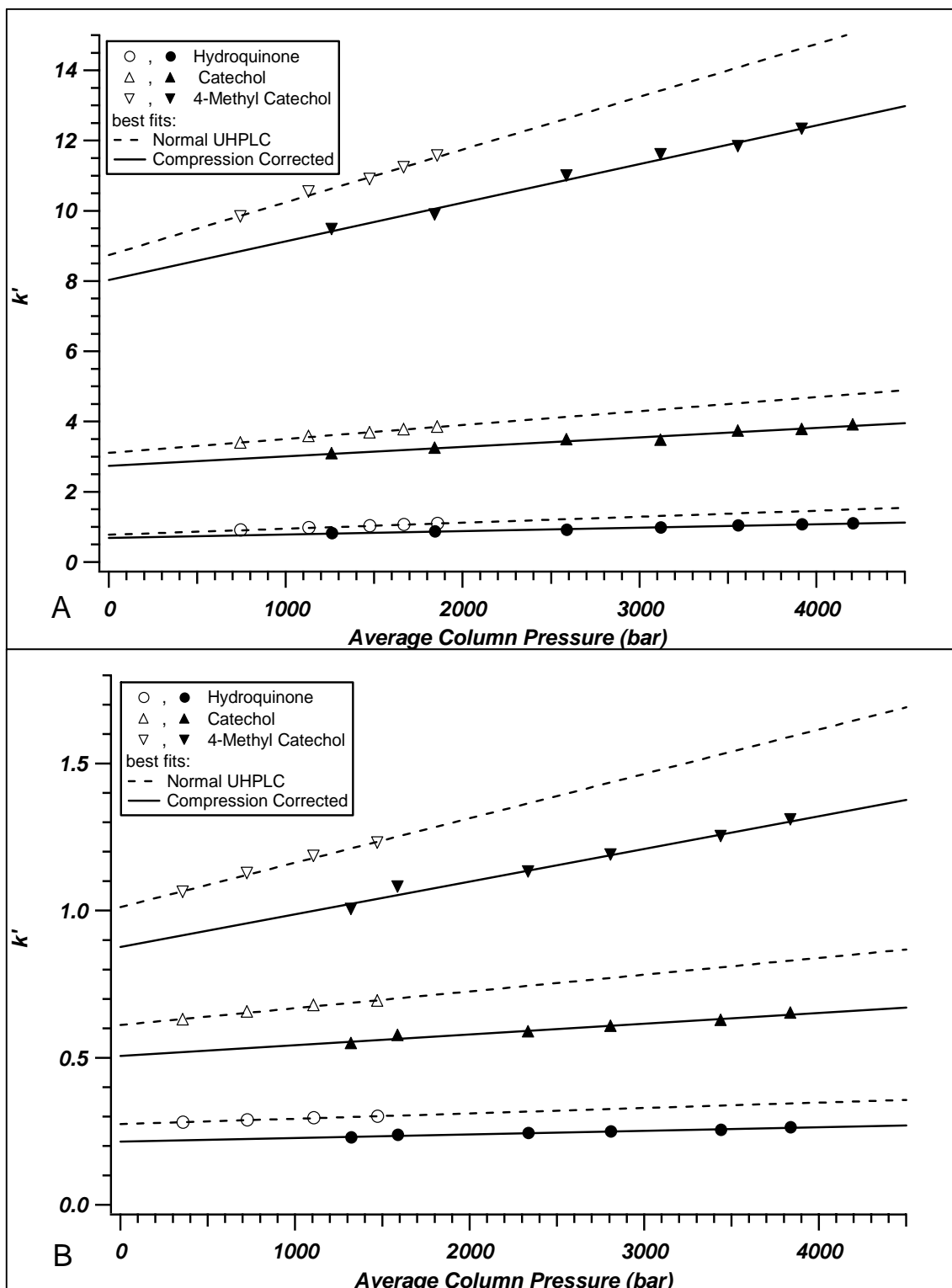
Figure 5-7: Comparison of k' vs.pressure plots observed for the normal UHPLC case (- -) and the compression-corrected case (-), for (A) 10/90 acetonitrile/water and (B) 35/65 acetonitrile/water. The compression phenomenon causes an increase in slope of k' vs.pressure for every analyte and mobile phase condition tested. Data for resorcinol was left off of this figure for ease of visualization. Data is reported in Table 5-3 as well.
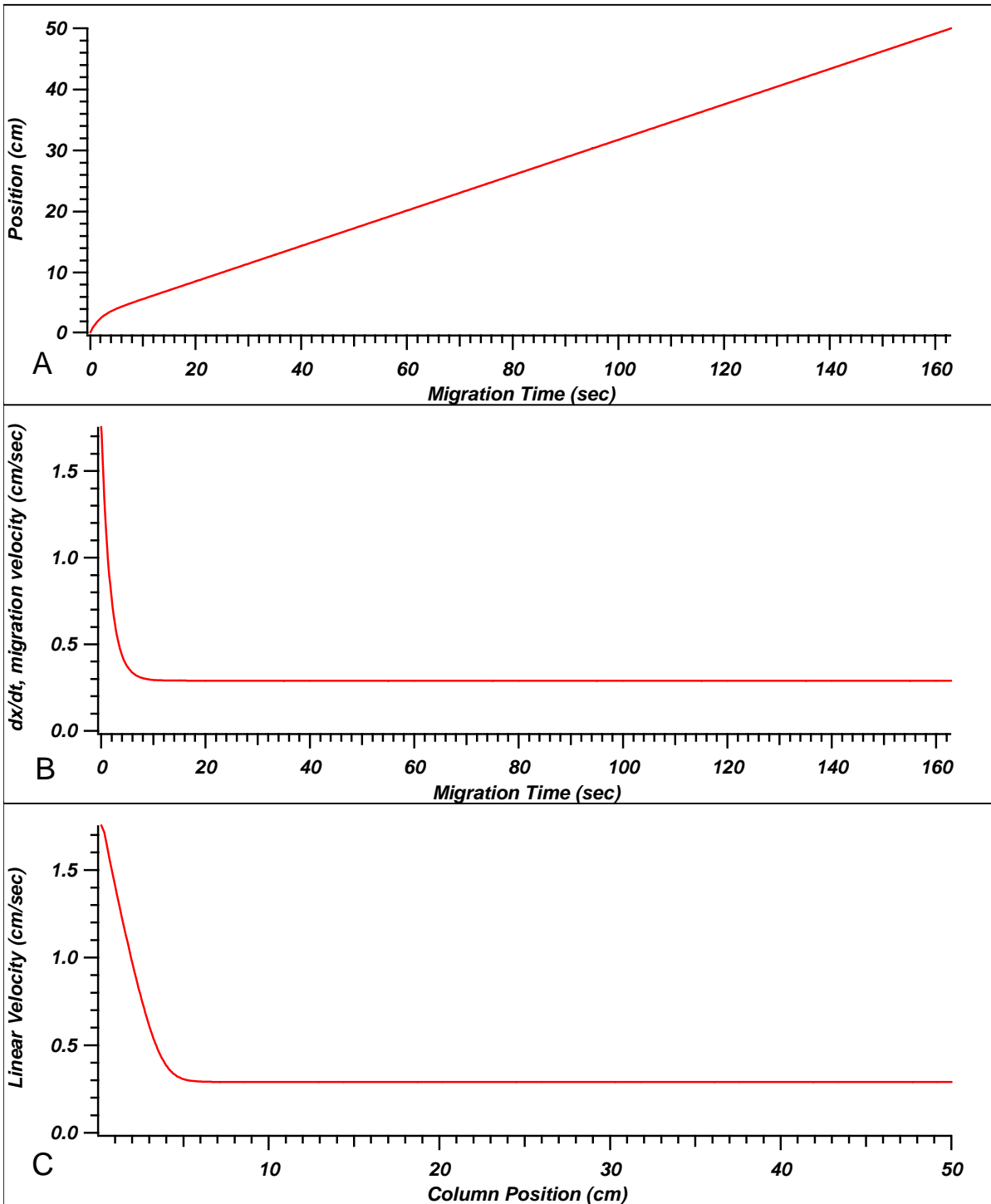
Figure 5-8: Using Equations (5-11) and (5-12) to estimate the velocity vs. column position for a deadtime marker in the case of a 50 cm capillary column packed with 1.5-μm particles, run in 10/90 acetonitrile/water mobile phase at 50,000 psi (3400 bar). (A) Position vs. Time predicted with (5-11) for $k'=0$, $A = 2.75$ cm, $\tau = 1.72$ sec, and $u = 0.29$ cm/sec . (B) Velocity vs. Time predicted with the same constants using (5-12). (C) Combination of the y-axes from (A) and (B), with migration velocity plotted vs. column position.
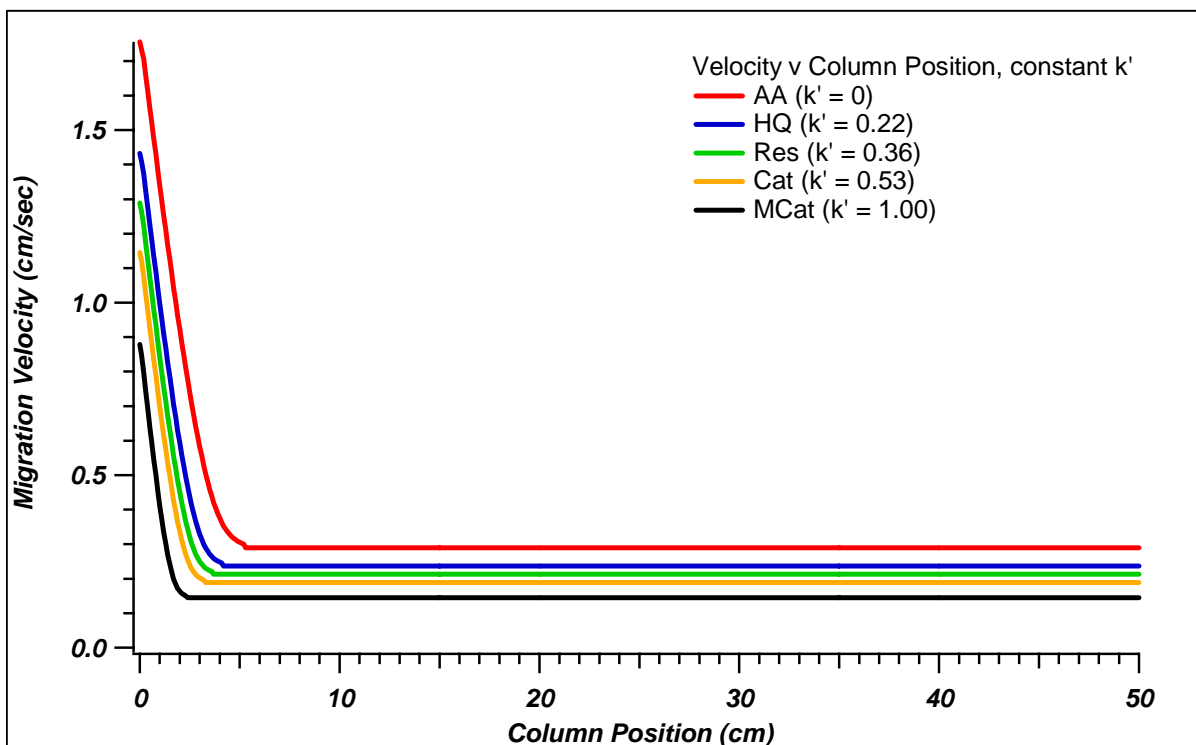
Figure 5-9: Plot of migration velocity of an analyte band (solution of (5-12)) versus column position (solution of (5-11)) for species with constant retention factors (k') listed in the key. The modeled condition shown assumed a pressure of 50,000 psi (3400 bar).
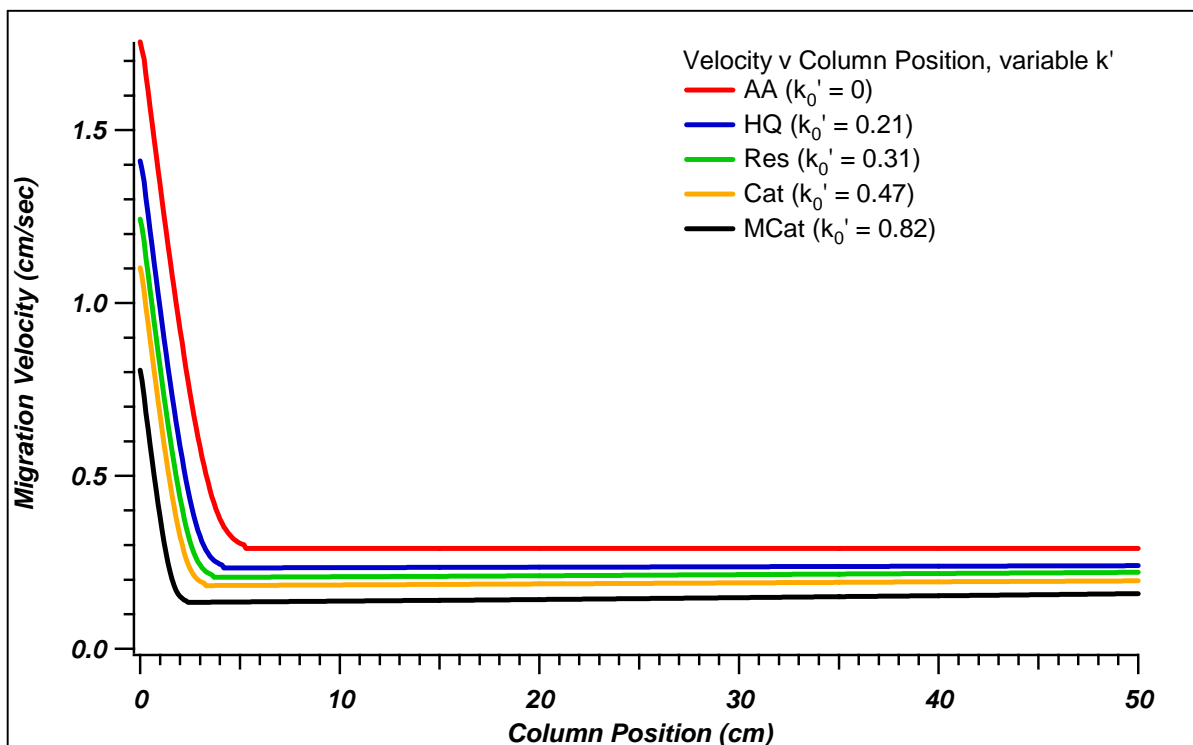
Figure 5-10: Plot of migration velocity of an analyte band (solution of (5-12)) versus column position (solution of (5-11)) for species with retention factors that were allowed to vary along the length of the column, according to the local pressure. The values used for retention factor at atmospheric pressure (k_0') are listed in the key. Note the velocity for retained species actually increases with position along the column, due to decreasing k'. Modeled condition shown was at a pressure of 50,000 psi (3400 bar).
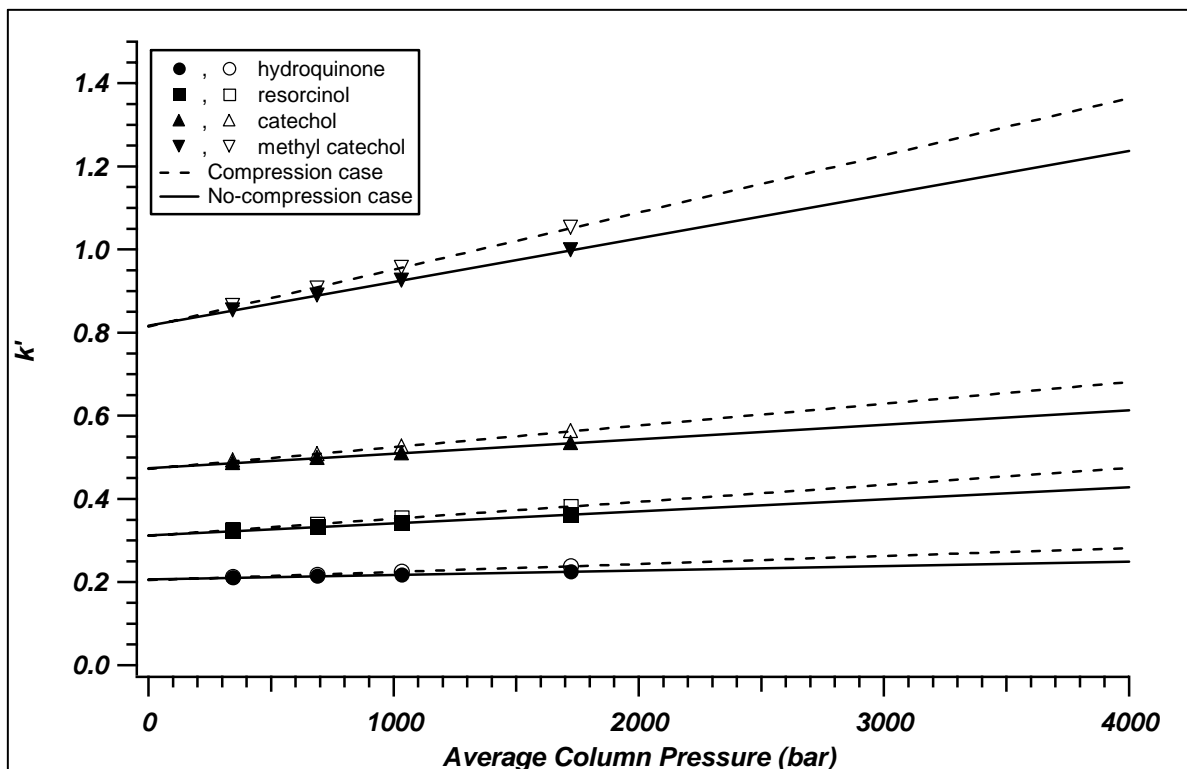
Figure 5-11: Plot of k' vs.average column pressure for the simulated cases where compression was included (- - -) and not included (-) in the simulation. Data plotted is from Tables 5-7 (no compression) and 5-8 (compression). Best fit linear regressions were carried out to 4000 bar to enable easier comparison to experimental data shown in Figure 5-7B.
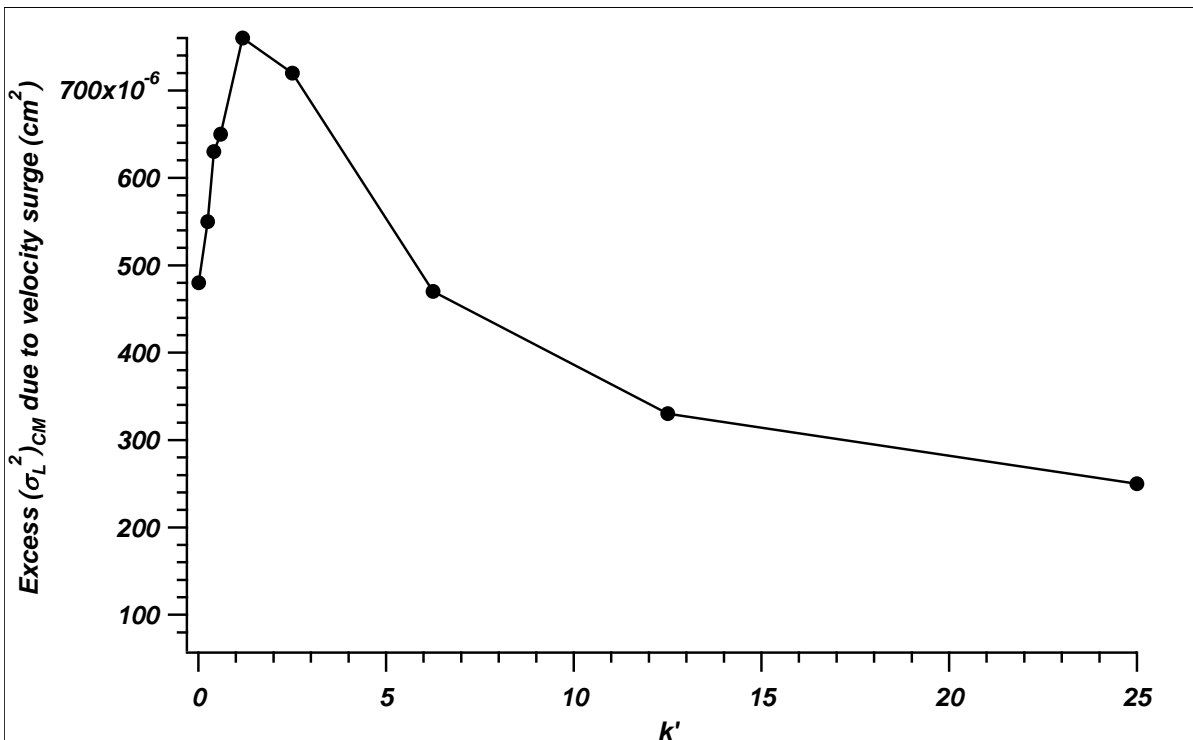
Figure 5-12: The amount of excess mobile phase C-term variance contributed from a linear velocity surge as a function of the retention factor of the analyte. The plot experiences a maximum near k′ = 1.
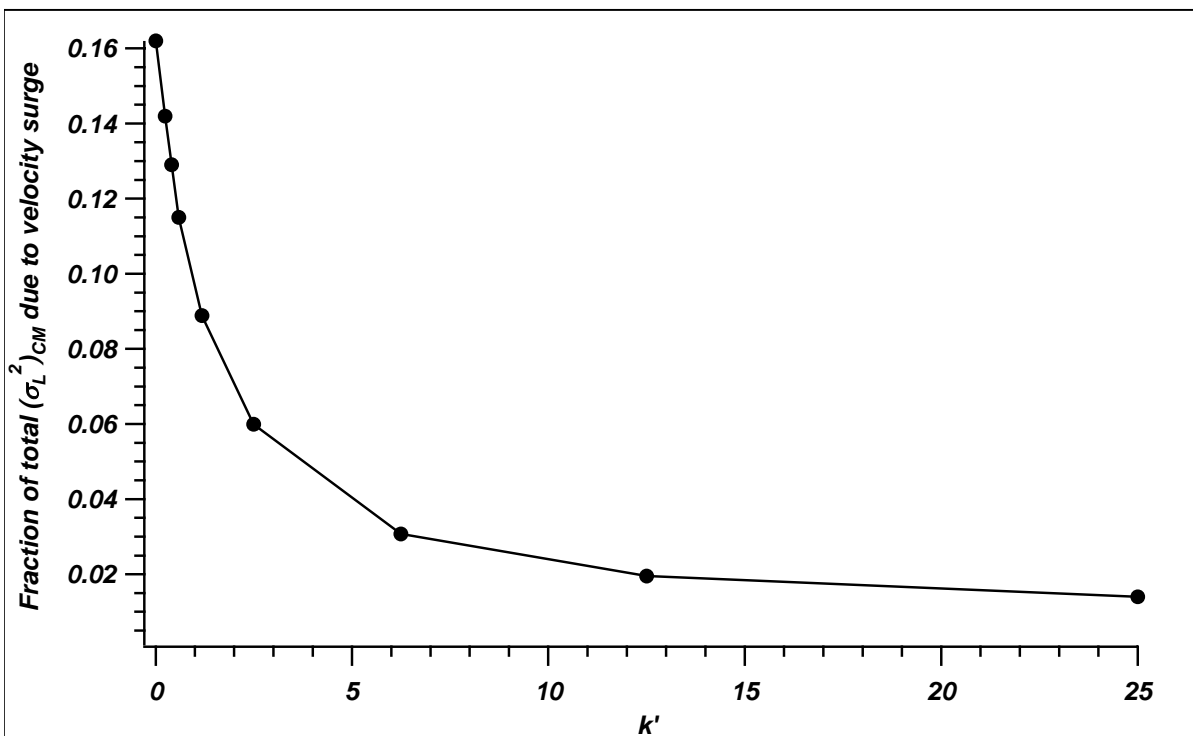
Figure 5-13: The mobile phase C-term variance due to a linear velocity surge (expressed as a percentage of the total mobile phase C-term variance) as a function of retention factor.

6 INVESTIGATION OF NANO-ELECTROSPRAY IONIZATION AND ELECTROSTATIC FOCUSING DEVICES USING A THREE-DIMENSIONAL ELECTROSPRAY CURRENT DENSITY PROFILER

6.1 Introduction

The previous chapters of this dissertation have focused on some aspect of ultrahigh pressure liquid chromatography, either trying to make improvements in UHPLC practice (through advances in stationary phase technology) or advancing our general understanding of column performance (viscosity, diffusion, and compression effects). Part of the goal of my dissertation research was to improve the applicability of UHPLC to the analysis of very complex mixtures, by seeking out ways to increase the sensitivity and dynamic range of UHPLC coupled to mass spectrometry (MS). Thus far, I have talked very little about this topic. The final chapter of this dissertation deals with research carried out with the stated goal of improving the sensitivity of UHPLC-MS by increasing the transmission of ions generated by nano-electrospray ionization into the first orifice of a mass spectrometer.

6.1.1 Aspects of Electrospray Ionization

Since its inception as an ionization technique for mass spectrometry in 1984,[1] electrospray has enjoyed an explosion in use. Two factors have emerged that determine sensitivity for an analyte in electrospray ionization mass spectrometry (ESI-MS): ionization efficiency and ion transfer efficiency.[2-6] Ionization efficiency is the fraction of target

molecules in the liquid phase that evolve into gas phase ions via the ESI mechanism. ESI inherently has high ionization efficiencies due to the large number of excess charges available for protonating or deprotonating analyte molecules (positive and negative modes, respectively).[2, 7] The advent of nanoelectrospray (nano-ESI) further benefited ionization efficiency because lower flow rates lead to smaller initial droplet size and larger amounts of excess charge per unit volume. It is widely accepted that nano-ESI exhibits superior ionization efficiency over conventional ESI or Ionspray techniques, and efficiencies at very low flow rates are thought to approach 100 percent.[8-12]

Ion transmission efficiency is the fraction of analyte ions that enter the mass analyzer out of those gas-phase ions produced, and is largely a characteristic of the mass spectrometer. The number of analyte ions that are transferred from one region to the next is proportional to the current density (J) at the entrance orifice of the mass spectrometer and the gas flow into the MS at that orifice.[13] Since ESI is typically performed at atmospheric pressure, the efficient transfer of gas phase ions from ambient pressure to high vacuum required for mass spectrometry was recognized as an important sensitivity issue during the technique's infancy.[14, 15] Due to the coulombically repulsive nature of an ESI plume and the characteristic losses of skimmer devices, ion transmission from source to detector in ESI-MS has been quoted as being as low as 1 ion transmitted in 10^5 ions created.[2, 16] The largest losses appear to occur between the ESI source and the first sampling orifice. Current measurements behind the first sampling orifice have historically been about two orders of magnitude smaller than the total ESI current, indicating about one percent ion transmission into the first differentially pumped region.[10, 16-18]

6.1.2 Improving Ion Transmission Efficiency in ESI-MS

One attempt to improve transmission between the electrospray source and first sampling orifice included enlarging the entrance orifice and use a higher pumping speed.[19, 20] Although this method is effective, larger pumps are needed, which can lead to prohibitive costs. A thoroughly studied method for improving ion transmission in ESI-MS is the so-called "Ion Funnel," which was based on early work by Bahr et. al. and developed in the lab of Richard Smith.[18, 19, 21-28] This device showed improvement in ion transmission into the mass analyzer, but was not functional at atmospheric pressure. Lee and coworkers have recently shown transmission improvements using a Venturi device, in an approach based on gas dynamic focusing.[29] Perhaps the method of increasing ion transmission that has received the most coverage in the literature is the use of electrostatic lenses, but signal improvements and exact function or benefit of these methods has not been well established.[14, 15, 30-33]

More recently, Schneider and coworkers used an "atmospheric pressure ion lens" in the form of a ring to improve ion transmission by shaping the electric field between the ESI emitter and acceptance orifice.[34] Previously, Beavis et al. used a similar device to assist in electrospray deposition of LC eluate into a small spot for off-column analysis by SIMS.[35, 36] The studies discussed in this chapter focus on the evaluation of these types of electrostatic devices. We have also adopted the terminology "ion lens" to include the use of electrostatic fields to move ions at atmospheric pressure. Previous works have evaluated electrostatic lens effects on ESI strictly on the basis of how transmission of ions into a mass spectrometer is altered; in other words, the ion signal has been the primary quantity measured. Our investigation centers around profiling the effect of electrostatic lenses on the actual shape and current density of the electrospray plume, in addition to directly monitoring the resultant ion transmission into a mass spectrometer.

6.1.3 Electrospray Ionization Profiler Concept

The ESI profiler described herein allows generation of complete three-dimensional current density profiles for nano-ESI plumes. Visualization of electrospray plume geometry is commonly performed using photomicroscopy. The main weakness of this technique is that once the electrosprayed droplets become too small to scatter light, the spray plume is not visible. In our experience with nano-ESI techniques, this can occur within one millimeter or less of the spray tip. Zhou and coworkers have used fluorescence techniques to monitor analyte intensity as a function of location in an ESI plume, and more recently to monitor pH changes that occur in the plume.[37, 38] Although this technique provided the first direct measurement of ion intensities in an ESI plume, the spatial resolution was limited to 1 mm. By monitoring the local current density with a very small probe electrode, our ESI Profiler can detect current density changes with a resolution of roughly 0.5 mm. Simultaneous monitoring of the total ESI current from the ground plane ensures consistent ESI performance over time. This is important because an accurate ESI profile can only be accomplished with the plume at a steady spray state.

To our knowledge, this report contains the first generation of complete geometric current density profiles for electrospray ionization. A goal of this study is to show how electrostatic lenses at a voltage between that of the emitter and electrical ground affect the shape of nanoelectrospray plumes. In addition, the current transmitted into the orifice of a mass spectrometer can be increased by using such an electrostatic lens. We develop a simple way to quantify the increase in current density in the central region of an ESI plume due to compression of the space charge, defined as the "compression factor", or κ. This term is

developed as a ratio of the average current densities of electrospray plumes before and after focusing with electrostatic lenses.

6.2   Experimental

6.2.1   Electrospray Profiler

An instrument to profile the current density of an electrospray ionization plume in three dimensions was fabricated from parts both ordered and machined in-house.   All parts were obtained from McMaster-Carr Supply Company (Atlanta, GA) unless otherwise noted. A simplified schematic of the assembled ESI profiler is shown in Figure 6-1.   Figure 6-2 contains two photographs of the instrument in its assembled form.   The general experimental design involves using a brass plate (15.25-cm square x 0.635-cm thick) at ground potential as the ground plane for electrospray ionization.   The plate has a 1-mm hole drilled into the center, through which a 500-μm diameter copper probe electrode is placed (PE in Figure 1), such that the electrode is exactly level with the brass ground plate surrounding it.   The probe electrode was fabricated by using heat-shrink tubing to surround a piece of 500-μm copper wire (total diameter 1 mm), after which the insulated wire was clipped and polished using 2000-grit sandpaper followed by 0.5-μm diamond compound (Crystalite Corp., Marina del Rey, CA).   The non-polished end was soldered to a low-noise BNC cable.   This small electrode was used to monitor current density as a function of position within the electrospray plume.   Another low-noise BNC cable was connected directly to the brass plate to monitor total electrospray current (labeled I_T in Figure 6-1).

Current from the 500-μm probe electrode was amplified by 10^8 or 10^9 volts/amp using a Keithley Model 427 current amplifier (Cleveland, OH) and subsequently recorded

with a Dell Dimension XPS T700R personal computer (Round Rock, TX), using a BNC-2090 break-out box (National Instruments Corporation, Austin, TX). Total electrospray current was monitored using a Keithley Model 616 digital electrometer (Cleveland, OH).

The probe electrode and ground plate assembly were attached to a moving stage using 7.6-cm long ⅜-16 stainless steel bolts. These bolts were run through a 0.635-cm polycarbonate plate to provide electrical isolation. The polycarbonate plate was then bolted to a low-profile Teflon® guide block that fit into a 75-mm wide x 500-mm long aluminum rail for y-translational movement (labeled "Y" in Figure 6-1). Another polycarbonate block (1.27-cm thick) was used to couple the y-translational rail to a Versa-Mount ball-bearing guide block for x-translation. This guide block fit around a 45.7-cm long hardened steel guide rail (labeled "X" in Figure 6-1). The entire assembly was bolted to a laser table (Technical Manufacturing Corporation, Peabody, MA).

Translation was accomplished in the X and Y directions using linear actuators. Actuators (Model 36341-05-061, Haydon Switch and Instrument, Inc., Waterbury, CN) were attached via aluminum angle brackets to the X and Y translational stages, as shown in Figure 6-1 (X-dimension motor and lead screw not shown). The linear actuators were operated by microcontroller-based stepper motor control boards. The main control board consisted of a BiStep A06 (Peter Norberg Consulting, Inc., Ferguson, MO) operated in 1/16th micro-stepping mode to produce smooth linear motion and increased resolution. The control board was interfaced to a custom data acquisition and motion control program written in LabView 6.1 (National Instruments Corporation, Austin, TX). Positional information of the probe on the X- and Y-axes was calculated from the step number of the linear actuator provided by the stepper control board.

Electrospray ionization was performed via infusion using platinum-coated fused silica Picotips™ (Model FS360-20-5-D and FS360-50-8-D, New Objective, Inc., Woburn, MA) butt-connected to fused-silica tubing with Teflon® tubing (Polymicro Technologies, LLC., Phoenix, AZ). A pressure bomb was used to supply liquid flow and a 5kV DC power supply (Bertan Model MPS-HV10M-05P, Valhalla, NY) was used to couple the spray voltage directly to the spray tip.   The electrospray emitter was positioned vertically, spraying down on the profiling apparatus (see Figure 6-1). Fine control of the vertical position ("Z-dimension") of the spray tip was performed utilizing a micropositioner with 0.01-mm precision, (Narishige Intl., Japan) fitted with an in-house machined polycarbonate bracket to couple the positioner to the butt-connect (Z in Figure 6-1). The micropositioner was bolted to a square polycarbonate stage which was fabricated in-house, having legs approximately 30-cm long that were bolted to the laser table to provide positional stability of the electrospray needle.

6.2.2   Lenses

Lens geometry design was initiated by simulations of roughly 20 designs using SimIon 3D 7.0 (Idaho National Engineering Lab, Idaho Falls, ID), followed by empirical testing of 5 of the designs. More details on the use of SimIon 3D to assist in lens design can be found in Appendix B. Electrostatic lenses were machined out of either stainless steel or brass from ¾-inch round stock. Several lenses were tested, including ring, conical, and hemispherical designs. This chapter will focus on the properties of one lens design that was empirically found to work the best, the inverted hemispherical lens. For this lens, round brass stock was machined to 19.0-mm diameter and 10.6-mm length. A 16-mm ball endmill was used to cut a hemisphere to 9-mm depth. Then a 3.1-mm hole was drilled axially for the

insertion of the ESI needle. Figure 6-3 shows the normal orientation of this lens in relation to a spray needle and the ground plane of the ESI profiler. To hold the lenses in place, a Model RSA-1 rotating optical positioner (NRC, Fountain Valley, CA) was fitted with a specially made aluminum bracket that allowed positional adjustment relative to the electrospray needle. The base of the rotating optical positioner was bolted on the underside of the polycarbonate stage (also used to hold the Z-positioner). This assembly allowed for quick insertion of the lens to a reproducible location. A separate output of the 5-kV DC power supply described above provided the lens voltage.

6.2.3 Chemicals

HPLC-grade acetonitrile, HPLC-grade methanol (Fisher Scientific, Fair Lawn, NJ), 96% formic acid, (Aldrich, St. Louis, MO), and ammonium bicarbonate (Sigma Chemical Co., St. Louis, MO) were used as received. Water used in these experiments was purified (18 MΩ*cm) using a Nanopure ultrapurified water system (Barnstead International, Boston, MA). All solutions except mobile phases for LC-MS experiments were filtered through 0.1 μm nylon syringe filters prior to use (Cameo 30N Syringe Filter, GE Osmonics, Inc., Trevose, PA).

6.2.4 Collecting an Electrospray Current Density Profile

To collect a profile, the ESI needle was first set at the desired distance from the ground plane ("Z"-distance). The brass plate was then translated under the electrospray plume so that the probe electrode traversed a square area in a flat s-fashion. This process was carried out in the following steps: The probe electrode was positioned in the left, lower corner of the plane to be profiled, and then scanned from left to right (+X direction). Next, the probe electrode was moved closer to the center of the ESI plume in a Y-step of

previously determined distance. The probe was then scanned back from right to left (-X direction), followed by another Y-step. This process was repeated until the desired area was covered. Data was collected at 20 Hz only during the ±X-directional scans, and each line scan was saved to an individual file. The typical rate of translation was 0.05 inches (0.13 cm) per second. For normal operation, a survey scan with a Y-step of 1 mm was often used to make sure the profiled area captured the entire electrospray plume. The survey scan typically took less than 2 minutes. Provided the profiled area did not need to be adjusted, this could then be followed with a scan at high resolution, which typically utilized a 0.250 mm Y-step. A 10-mm x 10-mm scan at this resolution could be performed in about 7 minutes. The maximum reproducible resolution in the Y-direction for this instrument is roughly 0.05 mm. For profiles taken at high resolution (Y-step less than 1 mm), only the +X-directional scans were used, in order to eliminate the mechanical actuator hysteresis of about 100 μm.

6.2.5   Data Manipulation

Individual data files for each scan were typically combined in a Labview program to form a slice plane, and subsequently loaded into Igor Pro 4.08 for visualization (Wavemetrics, Inc., Lake Oswego, OR). To improve visual display of data collected from the profiler, a 200 x 200 point grid interpolation was often performed using Igor Pro. Scans could be loaded individually in cases where comparison of electrospray plumes under multiple conditions was needed; in this case the most intense line scan in the two dimensional profile was selected and then plotted as current density versus X-translational distance. Three dimensional volume visualization and data manipulation was performed using a custom module written in AVS/Express (Advanced Visual Systems Inc., Waltham,

MA). The volume was created by first stacking multiple slice planes along the Z-axis and then performing a first-order, nearest-neighbor interpolation into a regular grid. The interpolated grid was equal to or less than the dimensions of the irregularly sampled input grid to produce the most accurate image. Three-dimensional visualization in AVS/Express was performed by John Eschelbach.

6.2.6   Direct Measurement of Ion Transmission

Ion transmission through the acceptance orifice of a mass spectrometer was determined by ratioing the current measured at a small Faraday mesh detector immediately behind the entrance orifice to the total current of the nanospray plume. All MS experiments were performed on a Waters Micromass ZQ single quadrupole mass spectrometer (Waters Corporation, Milford, MA). The orifice diameter on this instrument was 500 μm. The ion block portion of the ZQ was modified to allow a stainless steel mesh electrode to be suspended in the ion flow path at a distance of 17 mm behind the orifice to measure the ion current transmitted through the acceptance orifice, as shown in Figure 6-4. Pressure in the region containing the mesh electrode was measured remotely using a Pirani gauge (model # KJL-912012, Kurt J. Lesker Company, Clairton, PA). The pressure in this region was approximately 3 torr. The mesh used was woven from 50 μm fibers and had approximately 40% open area; this was cut into a 5 mm circle and subsequently soldered to 22 AWG Duobond shielded 50 ohm coax cable (Belden Wire and Cable, Richmond, IN). The mesh electrode current was monitored using a Keithley Model 616 digital electrometer (Cleveland, OH).

Infusion nano-ESI and capillary liquid chromatography ESI-MS experiments were performed to evaluate lens performance. Nano-ESI was performed on-axis with the

acceptance orifice since the electrostatic lens focuses the plume in an axial direction. A Waters Nanospray source was used to hold the electrostatic lens and a second micropositioner was used to hold the nanospray needle. The total electrospray current was monitored by using a digital multimeter floated at high voltage to track the voltage drop across a 4.13 MΩ carbon resistor in series with the applied spray voltage.

6.2.7 Evaluation of Percent Coverage in Protein Digest Experiments

A capillary column (30-μm i.d. fused silica, Polymicro Technologies, Phoenix, AZ) was slurry packed in house to a length of 50 cm with Atlantis 3 μm C18 porous silica particles (Waters Corporation, Milford, MA), using a packing apparatus previously reported.[39] Reversed-phase separations of a tryptic digest of bovine serum albumin (MassPREP BSA Digestion Standard, Waters Corporation, Milford, MA) were performed using a Waters 600 Liquid Chromatograph operated with a flow splitter to achieve flow rates in the low nanoliter per minute range. The capillary column was coupled to a Micromass ZQ single quadrupole mass spectrometer using a Picotip™ electrospray emitter (part number FS-360-50-5-CE, New Objective, Inc., Woburn, MA). Percent coverage was determined using selected ion searching over the mass range of 400 to 1500 m/z with a macro written in Igor Pro 4.08.[40] Injections from approximately 600 amol to 200 fmol protein digest were performed using a pressure bomb and varying dilutions. Percent coverage was compared head-to-head for LC-MS experiments using the hemispherical lens versus not using the lens, operating with the spray needle in the same position (4 mm from sampling orifice).

6.3 Theory

6.3.1 Electric Field

The electric field (E) at an electrospray tip can be calculated using the equation:

$$E = \frac{V}{A \cdot r \cdot \ln\left(\dfrac{4d}{r}\right)}$$
(6-1)

where V is the applied voltage, r is the capillary emitter radius in cm, and d is the distance between the ESI tip and the ground plane in cm.[41, 42] A is an empirical constant found by Smith to be equal to 0.667[42]. It is important to note that (6-1) was derived for the electric field at a point relative to a plane, and thus cannot be used to calculate the field at an electrospray tip in the case where an electrostatic lens is in place.

6.3.2   Current Density

ESI profiles obtained with our system generate two current measurements. The first current measurement comes from the probe electrode, PE, which provides a current density at a specific location in the electrospray plume, defined as current per unit area, J:

$$J = \frac{i_p}{A_p}$$
(6-2)

where i_p is current in amperes at the probe electrode and A_p is probe electrode area in mm^2. Local current density (J) was plotted in our experiments to show changes in the intensity of the electrospray plume as a function of position.

The other current measurement obtained in these experiments is total electrospray current (I_T), in amperes, which should be constant throughout a profiling run for constant ESI conditions. Using this measured current, an average current density for an electrospray plume, or $\bar{J}$, can be described as:

$$\bar{J} = \frac{I_T}{A_T}$$
(6-3)

where A_T is the total area in mm^2 that the electrospray plume covers at the brass ground plane, obtained for each case from the ESI Profiler data. Average current density can therefore be defined for an electrospray plume under any number of varying conditions such as spray voltage, solvent flow rate, emitter-ground plane distance, or various lens parameters.

6.3.3 Compression Factor

Electrostatic lenses, gas dynamics, and other means have been used in attempts to increase ion transmission from ESI into the mass spectrometer, as outlined in the introduction. In reviewing the literature, it was disconcerting that no uniform way has ever been presented to determine the effectiveness of the various techniques at shaping the electrospray plume and getting more ions into the entrance orifice. Improvement in terms of limits of detection always depends on the starting conditions which the experimenter chose and the MS instrument employed. To more accurately compare effectiveness of focusing methods on ESI plumes, the simple concept of compression factor has been developed. Compression Factor, or κ, can be described as:

$$\kappa = \frac{(\overline{J}_L)}{(\overline{J}_N)} \tag{6-4}$$

where $\overline{J}_L$ is the average current density (amps/mm^2) for the lens condition, and $\overline{J}_N$ is the average current density under nominal or unmodified conditions. The ratio κ essentially provides a value for the compression of the space-charge in an electrospray plume, as compared to the null condition. A κ value greater than 1 manifests itself in an electrospray profile as an increase in current density, J, in the central portion of the profile. Assuming the entrance orifice of a mass spectrometer is a fixed diameter, compression of the ion current into a smaller area in front of the orifice should allow for increased ion transmission,

assuming the orifice diameter is smaller than the plume diameter. The parameter κ is normalized by the nominal case for any particular system, and thus eliminates other instrumental variables such as flow rate, spray voltage, and solvent viscosity in determining the focusing effectiveness of any focusing system.

6.4 Results and Discussion

6.4.1 Operation of the Nanoelectrospray Profiler

The technique used for collection of a nano-ESI current density profile was described in the experimental section. Important to the function of this device is that the translation of the brass ground plane is "invisible" to the electrospray emitter; this ensures that the electric field does not change over the course of stage translation and an accurate profile is generated. The ground plane area in this system is large enough that the emitter never approaches the edge of the brass plate, so the distance relevant to the formation of the electric field between emitter and ground remains constant throughout X-Y translation. Total electrospray current is monitored at all times to ensure consistency in the electrospray mode.

6.4.2 Current Density as a Function of Distance from the ESI emitter

Current density profiles were collected as a function of distance from the ESI needle. A New Objective Picotip with 8 μm orifice diameter was used to spray a solution of 50/50 (v/v) acetonitrile/water with 0.1 percent formic acid at 150 nL/min. Current density profiles were collected at 1-mm increments from 2 to 12 mm from the ESI needle, and then stacked in Z-space to create a three-dimensional current density map. The three-dimensional visualization of that current-density profile is shown in Figure 6-5. An important property of this experiment was that as distance was increased, the voltage applied to the ESI needle was

increased to maintain a constant electric field at the ESI tip of roughly 1.1×10^6 V/cm as calculated using equation (6-1). This was confirmed also by consistent I_T during all measurements. It was expected that we would observe a widening spray plume as distance from the needle increased, due to the diverging electric field lines near the emitter and coulombic repulsion of the ions in the plume.[13, 41, 42]

In 1991, Busman et. al. published finite element calculations for the charge density as a function of distance from an electrospray emitter based on a "needle-in-can" geometry.[13] Figure 6-6A shows a contour plot of the calculated charge density, based on a hypothetical source with radius 1 cm at 5 kV and a ground plane at a distance of 5 cm. Figure 6-6B is a contour plot of current density as a function of distance taken using our ESI profiler, which was generated by taking a single slice in the X-Z plane of Figure 6-5, and displaying it as a contour plot. Both the mathematical model (6-6A) and our experimental data (6-6B) point to a collimated spray plume close to the emitter where the ions are in a strong electric field. Then, after the field strength lessens, the plume diverges significantly into more of a mushroom shape. Our experiments reinforce Busman's model that the ions spread more readily in a space-charge dominated region far from the emitter, however it is possible this may be partly due to increased ion mobility as desolvation of the ions occurs. In the Busman model, the expansion was attributed totally to field strength, and ion mobility was held constant. The absolute values of current and charge density, distance, spray voltage and electric field were different for the experimental and calculated systems. Nonetheless, it is noteworthy that there is such strong agreement in the ESI plume geometry predicted from Busman's model and observed in our experiments.

Neither our experiments nor the Busman model include the effects a gas-dynamic acceptance orifice to a mass spectrometer may have on the electrospray plume. The high-velocity gas flow into the acceptance orifice certainly serves to increase the number of ions transmitted, and may change the shape of the ESI plume at small distances from the orifice.

6.4.3 Examination of Spray Tip Integrity

An immediate benefit of the ESI current density profiler was the instrument's ability to recognize nanoelectrospray needles that were in poor condition. Figure 6-7 is a comparison of an ESI profile for a needle in poor condition (6-7A) and a new needle (6-7B). This experiment was performed over a 20 mm x 20 mm area with a Y-step of 1 mm. Both profiles were taken at a distance of 12 mm from the spray tip, with a spray voltage of 3.06 kV, a volumetric flow rate of roughly 200 nL/min (50/50 ACN/H_2O with 20 mM ammonium bicarbonate). The ESI profile displayed in Figure 6-7A was taken using a fused silica needle which was pulled with an electric arcer and etched in-house to make a tip with inner diameter roughly 5 μm. This needle had a small chip at the end, which was observed upon microscopic evaluation. There were multiple jets emitting from the damaged spray tip; in particular, a major jet in the 6 mm region on the y-axis, and a minor jet near 14 mm, as is obvious in the figure. Figure 6-7B was obtained using a new FS360-50-8-N fused silica tip from New Objective; the profile shows an electrospray plume which has a very even distribution. For the damaged emitter, profiles were taken over a wide range of spray voltages to ensure these multiple spray jets were not due to operating outside the most stable cone-jet mode.

Recommendations have been made in the literature for cleaning or unclogging nano-ESI needles by carefully scratching them on the surface of a ground plate.[10] Evidence

presented in Figure 6-7 suggests that jagged nano-ESI emitters, as may be produced by the needles touching a surface, give less than desirable electrospray plume characteristics. In general, our evaluation of several in-house made electrospray needles showed that they gave less reproducible and less uniform spray characteristics than the New Objective needles. Therefore, the commercially made needles were used for all other experiments and the needle was replaced any time there was a chance it had become damaged.

6.4.4 Observation of Multiple Spray Modes Using an Electrostatic Lens

Several different lens designs were tested in our experiments, including ring electrodes and different interior diameters of conical and hemispherical shape. In all cases, the lens orientation was similar to that used by Schneider et. al., although that report only contained data for a ring-like electrostatic lens.[34] Figure 6-3 shows the lens arrangement using a lens with a hemispherical interior, with a 3.1-mm hole in the top where the spray needle was inserted. When a lens with this shape was modeled using SimIon 7.0, the resulting electric field at the spray tip had isopotential lines that were somewhat flattened as compared to a model where no lens was used (see Appendix B, Figures B-7 and B-8). Supporting this modeled system, we observed two regions of steady decrease in total current (I_T), from 0 V to 600 V (lens voltage, V_L) and from 650 V to 1300 V (Figure 6-8A). The current density at the center of the ESI plume also increased linearly in these two regions (Figure 6-8B). This suggests the electric field at the tip of the emitter was modified by the lens, and that the coulombic repulsion of charged droplets inside the electrospray plume were counteracted by the additional electric field from the lens.

The two sudden drops in spray current near $V_L = 600$ V and 1350 V shown in Figure 6-8A correspond to changes in the axial spray mode. Our observations correlate well with

the three axial spray modes reported by Juraschek and Röllgen.[43] At high V_L there were heavy pulsations in I_T, corresponding to axial spray mode I, which occurs at low spray potentials. The region between $V_L = 650$ V and 1350 V corresponds to axial spray mode II, or "cusp-jet" mode, and the highest current region corresponds to the preferred "cone-jet" mode, or axial spray mode III, as labeled in Figure 6-8A.

The horizontal dotted line in Figure 6-8A at 61 nA corresponds to the nominal I_T for this system with no lens in place. An initially surprising result was that I_T was higher with the lens in place and V_L less than 600 V than with no lens present at all. This observation was attributed to having a lens at low potential near the ESI needle, which increased the electric field at the needle and therefore raised I_T. Total spray current returned to its nominal value of 61 nA when V_L reached 600 V.   This data suggests that the lens is located at a position where the usual potential in space, with $V_s = 1600$ V, would be roughly 600 V.

Spray modes II and III appear to be effectively focused by the electrostatic lens, as is evident in Figure 6-8B by the linear increase in current density at the center of the plume during both modes.   Here again, the dotted line indicates the nominal value of J, or the value of current density in the center of the ESI plume when no lens was used. J values lower than the nominal case mean that the ESI plume was widened by the lens because the ions were attracted to the low potential lens. Therefore no compression of the ESI plume, or increase in average current density, occured in the cone-jet spray mode as compared to the nominal case. Local current density (J) at the center of the plume was able to be roughly doubled while maintaining constant V_s, but the plume was operating in the less desirable cusp-jet mode and I_T was significantly diminished.

Total current of an electrospray plume has been studied as a function of a number of parameters, including but probably not limited to, solvent flow rate, spray voltage, emitter-ground plane distance, solvent conductivity, emitter diameter, and solvent viscosity.[2, 3, 5-7, 12, 17, 42, 44-47] The total spray current is directly proportional to the amount of excess charge available to produce gas-phase ions.[48, 49] As a result of our observations discussed above and the literature's noted trend between total spray current and ionization efficiency, V_s was adjusted (for all further studies) as V_L was increased in order to maintain constant total ESI current and keep the electrospray in the desirable cone-jet mode.

6.4.5 Profiling Local Current Density Enhancement Using Electrostatic Lenses

A significant conclusion of the previously mentioned Busman et. al. model was the prediction that no improvement in current density, and thus MS signal, could be obtained by using electrostatic lenses.[13] However, Busman's model used a situation where the lens was at the same potential as the emitter as the focusing case. This is an unrealistic configuration for ESI because the field is so weak at the ESI tip that no Taylor cone can form, and therefore no emission will occur. The analogous case in our data is shown in Figure 6-8A where V_L is 1600 V. Electrospray profiler data indicated that compression of space-charge in ESI, in order to increase current density at the orifice of a mass spectrometer, can be carried out via electrostatic lenses. However, it must be done in a situation where the strong electric field at the ESI tip is maintained and the total spray current is constant. This requires increasing the spray voltage as the surrounding electrostatic lens voltage is increased.

The electrospray profiler was used to image changes in current density that occurred when the voltage was increased on an electrostatic lens positioned as in Figure 6-3. V_s was adjusted to maintain constant I_T. Figure 6-9 is a plot of local current density, J, versus

position as the probe electrode was traversed along the X-axis, for four different V_L values. The exact collection parameters are included in the caption for Figure 6-9. In comparison to the nominal case (Figure 6-9, trace A), the ESI plume was noticeably widened when the lens was at ground potential, and the local current density in the center of the plume was cut in half (Figure 6-9, trace B). This result likely occurred because the ions were attracted to the electrostatic lens acting as a ground plane. It was expected that a broadened plume would lead to a decrease in ion transmission efficiency.

At $V_L = 400$ V, the ESI plume shape is almost identical to the plume where no lens is present (data not shown). Further enhancement of the current density in the center of the plume was noticed as V_L was raised to 800 V and 2000 V (Figure 6-9, traces C and D, respectively). Current density values in the center of the plume were increased from approximately 2 nA/mm^2 in Case A to 10 nA/mm^2 in Case D. If ion transmission were only dependent upon this local J, the increase observed in Figure 6 A to D would correspond to an approximately 5-fold increase in signal.

6.4.6 Increases in Average Current Density and Compression Factor Using Electrostatic Lenses

The orifice of a mass spectrometer functions not as a point, but as an active gas dynamic region. It has a functional diameter that is larger than the actual diameter itself, due to the high gas flow into the orifice (typically tens of milliliters of ambient gas per second). Ion transmission can therefore be better approximated by the average current density ($\overline{J}$) of an ESI plume in the region sampled by the entrance orifice.[13] Figure 6-10A shows the increase in average current density as a function of lens voltage for three different mobile phase compositions. It is immediately noticeable from this figure that the mobile phases with

higher aqueous content, and thus higher conductivity, exhibit higher overall $\bar{J}$ values, which is concurrent with literature.[2, 7, 47] In addition, the slope of $\bar{J}$ versus V_L also decreases with increasing organic content (i to iii). This would prematurely suggest that higher organic content plumes are less effectively focused using atmospheric pressure lenses.

However, when compression factor (κ) was calculated for the same system, a different trend was observed (see Figure 6-10B). This factor took into account the current density of the nominal, or unfocused, case. A κ value of 1 indicates $\bar{J}$ is the same as that of the nominal case, and should correlate to the same ion transmission as in the nominal case. Figure 6-10B shows that for $V_L = 2000$ V, κ was roughly 3, predicting a 3-fold increase in ion transmission over using no lens. It is also important to note from this figure that the slopes of all κ versus V_L curves were nearly the same, indicating that the lens affected the spray plume similarly for all organic solvent compositions. In fact, the absolute values for κ were slightly higher for high organic content under all lens voltages, suggesting that an ESI plume with high organic content may in fact be easier to focus. In a separate experiment, we observed the same optimal V_L conditions for mobile phases of 5 percent to 80 percent acetonitrile composition. Lens voltage therefore was not expected to need adjustment to maintain high ion transmission efficiencies during a gradient liquid chromatography run, for instance.

It is also of interest to note that we observed a consistent decrease in the area of electrospray plumes as the organic content of the sprayed solvent was increased (data not shown). This was attributed to the decrease in ion current with increasing organic content and the consequent decrease in coulombic repulsions. The more slender spray plume with

mobile phases containing higher organic content would likely enable a higher ion transmission efficiency, which supports the traditionally-observed phenomenon of better signal-to-noise with at least some organic content in the mobile phase.[10, 16, 17, 50]

6.4.7 Improving Ion Transmission using an Electrostatic Lens

Results from the ESI profiler led us to believe we could expect roughly 3-fold increase in ion transmission efficiency by using a hemispherical electrostatic lens to focus a nano-ESI plume. In order to experimentally verify this hypothesis, a series of experiments were performed using a single-quadrupole mass spectrometer (Micromass ZQ). The current at a small mesh electrode placed in the first vacuum region was monitored and compared to the total ESI current to determine the ion transmission into the first orifice (see Experimental, and Figure 6-4). In a series of infusion experiments performed, total spray current varied widely depending on the flow rate, spray voltage, mobile phase composition, and needle position used, but followed the trends reported in the literature.[4-6, 9, 12, 17] However, in our ion transmission measurements using nano-ESI, we were surprised to find much higher transmission efficiencies than previously reported.

First, current at the mesh electrode was measured as a function of cone voltage, to make sure that leakage current from the cone to the mesh did not contribute to the current measurements. In order to measure leakage current, the current at the mesh electrode was monitored as a function of cone voltage, with no electrospray performed. The results are presented in Figure 6-11. The leakage current was linear with respect to cone voltage, which was characteristic of a small amount of current traveling through a highly resistive medium (rarefied air). No dielectric breakdown was detected at cone voltages as high as 200 V. Electrospray was then initiated and the current at the mesh was measured again as a function

209

of cone voltage. This experiment is plotted as the red trace in Figure 6-11. Note that the current at the collection mesh increased quickly between cone voltages of 0 and 20 V, as the bias potential was established between the mesh and the cone. Above a cone voltage of 30 V the mesh current increased linearly with the same slope as the leakage current, indicating the mesh electrode had reached its maximum efficiency. The blue trace in Figure 6-11 is the actual transmitted current (total minus leakage) as a function of cone voltage. This function had reached its asymptote by 50 V, so the cone voltage was set to 50 V for experiments measuring ion transmission efficiency. For all experiments, a leakage current characteristic of the particular mesh-cone geometry was subtracted from the mesh collection current value. Values for leakage current varied from 0.5 nA to 5 nA at 50 V bias potential.

At a bias voltage of 50 V between the surrounding ion block and the mesh electrode, the collection efficiency of the mesh was calculated to be 96%. The collection efficiency was calculated by measuring the total ion current at the detector with and without the mesh electrode in place. This was presumed valid because even though the MS detector does not collect all of the ions passing through the mesh, it probably collects a relatively constant percentage. It is important to mention that current measurements behind the first orifice can only approximate the increase in signal that may be seen after at the mass analyzer; there are effects such as ion beam shape and gas dynamics in the interior of the MS that were not taken into account by our experiments. In addition, the mesh electrode collected the total current transmitted into the first orifice; it was not expected to be selective between gas-phase ions, ions that were partially solvated, or even charged droplets.

Figure 6-12 is a plot of transmission efficiency into the first orifice as a function of distance between the needle and the acceptance orifice, for the nano-ESI of 50/50 (v/v)

water/acetonitrile with 0.1 percent formic acid and 950 nM neurotensin at 30 nL/min. Transmission efficiency was calculated simply as the ratio of the current at the mesh electrode to the total ESI current. A leakage current of 0.7 nA was subtracted from the measured current at the mesh. Figure 6-12 indicates that 68 percent ion transmission was obtained for the closest needle-to-orifice position (15.3 nA out of 23.2 nA total current). However, when the mesh was removed and ion intensity was recorded for the (neurotensin+2H)$^{2+}$ ion at 559 m/z, the optimal MS signal was observed when the needle-orifice distance was slightly larger, roughly 2 to 2.5 mm. At this distance, ion transmission was measured to be about 40 percent (Figure 6-12). This observation can be explained by examining the expected mechanism of electrospray ionization. In ESI, the charged droplets require a certain amount of time at atmospheric pressure to create gas-phase ions, as has been indicated by inefficient ionization when ESI was performed directly into vacuum.[51] It is possible that the distance of roughly 2.5 mm in this experiment provided the optimum balance between efficient ionization and ion transfer, assuming these are the two dominant mechanisms in place.

The ion transmission efficiencies in our experiments represent a large departure from the literature, where 99 percent or more of the ion current is reported lost prior to the first vacuum region.[10, 16-18] However, previous reports of direct ion transmission were performed under conditions where flow rates were near 1 μL/min, which is more than an order of magnitude higher than our experimental flow rate. It appears that the faster desolvation and lower space-charge of nanoliter-per-minute flow rates allow the gas dynamics of an orifice to be much more effective at ion conductance. This data also suggests that future efforts undertaken to improve on ion transmission for nano-ESI must recognize that improving upon

a starting condition of 40 percent transmission efficiency may be much more difficult than if the starting condition were 1 percent transmission.

In order to determine if an electrostatic lens could further improve ion transmission, the hemispherical lens was oriented about the ESI emitter in a manner similar to in Figure 6-3, with the spray needle 4 mm from the acceptance orifice of the ZQ mass spectrometer. The starting ion transmission into the first orifice, with the hemispherical lens at 0 V, was roughly 24 percent. This was boosted to about 45 percent transmission by using a lens voltage of 560 V. During this experiment the signal was also monitored for the 559 m/z ion of neurotensin, even though only a small fraction of the ions were reaching the mass analyzer (the majority was being collected by the mesh electrode). With the lens off, the average signal over a 0.4 minute collection period measured 2.84×10^5 counts. With the lens on, the signal was 4.99×10^5 counts, corresponding to an increase of roughly 76 percent.

6.4.8 Percent Sequence Coverage for a BSA Tryptic Digest

In order to evaluate the real-world utility of the apparent signal doubling that was observed with the hemispherical electrostatic lens, a LC-MS experiment was performed which measured percent of BSA sequence coverage as a function of amount injected onto the LC column. It was hypothesized that higher sensitivity using the lens would lead to higher sequence coverage for an equivalent amount injected. Each LC-MS run was performed using a 120-minute gradient elution from 5 to 50 percent acetonitrile with 0.1 percent formic acid, on a 50-cm long column packed with 3 μm Atlantis C18 particles. Two characteristic experiments are shown in Figure 6-13. The experiments shown were performed with nominally the same injection amount (~117 fmol). Figure 6-13A was performed without a focusing lens, Figure 6-13B was performed using a hemispherical lens at 600V surrounding

the electrospray needle. The experiment without a lens gave a calculated peak capacity of 215 in an elution window of approximately 78 minutes (21.4 sec median peak width calculated from 67 peaks). The lens experiment resulted in a chromatogram with a calculated peak capacity of 210 (22.4 sec median peak width calculated from 72 peaks). The two experiments had essentially the same signal-to-noise. The chromatographic characteristics of these runs were typical of LC-MS experiments performed in this study, with higher signal intensity and slightly broader peaks for high injection amounts relative to small injection amounts. For example, 13 fmol injected gave a median peak width of 15.1 sec and a peak capacity of 310. The smallest injection amount that gave enough MS signal to be measured was 0.6 fmol on-column.

The cumulative results of the sequence coverage vs. injection amount experiment are shown in Figure 6-14, with injection amounts ranging from 0.6 to 215 fmol for both the lens and no-lens case. Percent coverage ranged from approximately 40 percent at 0.6 fmol injected to better than 75 percent at 200 fmol. Although the lens helped to pick up a few peptides in most experiments in the middle injection ranges (1-10 fmol injected), the overall improvement in percent coverage was nominal.

6.5   Conclusions

 Electrostatic lenses can be used to focus nano-ESI plumes at atmospheric pressure, but in our experience did not enhance MS signals enough to significantly enhance protein sequence coverage in an LC-MS experiment. Experiments performed in this study showed that nano-ESI-MS performed at significantly higher ion transmission efficiency than previously expected; thus there was less room for improvement in signal-to-noise by

increasing ion transmission into the first orifice in ESI-MS. It is also possible that ionization efficiency suffered as a result of using electrostatic lenses to compress the ESI plume. As droplets are emitted from the Taylor cone, coulombic repulsion between ions typically assists the desolvation-coulombic explosion process which ultimately leads to gas-phase ions.[2-6] We have shown that the electrostatic field from the ion lens was effective at fighting space-charge and thereby increasing current density in the center of the plume. It is possible this effect may also have decreased the rate of desolvation by increasing the local vapor pressure in the center of the plume. In this case, use of electrostatic ion lenses around an electrospray needle would lead to more efficient ion transfer into the MS acceptance orifice, but less efficient gas-phase ionization, resulting in little or no net gain in signal.

The two major weaknesses of the ESI profiler are its inability to function properly at high liquid volumetric flow rates and that it ignores gas dynamic effects on ion transmission into mass spectrometers. At flow rates greater than about 500 nL/min, droplets form on the ground plane during the collection of a profile, even at distances of 4 cm or more. However, we feel that because of the excess space-charge present in ESI at high flow rates, focusing with electrostatics may not be a viable option in that regime. Furthermore, nano-ESI offers superior ionization efficiency and sensitivity as previously discussed, so concentrating on improving ion transmission for nano-ESI is not seen as a hindrance. Although only electrostatic lenses were tested in the experiments reported here, the ESI profiler would likely perform as well in measuring effects of electrodynamic, gas dynamic, or other focusing methods on nano-ESI.

Data presented herein show that 40 percent ion transmission into the first vacuum region of a mass spectrometer is probably not uncommon for what have become typical

nano-ESI conditions (<150 nL/min). The increase in signal observed with decreasing flow rate has previously been almost totally ascribed to increases in ionization efficiency.[9-12, 52] These findings indicate that the increase in signal with nano-ESI is likely due to benefits both in ionization efficiency and ion transmission efficiency.

6.6   References

(1)   Yamashita, M.; Fenn, J. B. *J. Phys. Chem.* **1984**, *88*, 4451-4459.

(2)   Kebarle, P.; Tang, L. *Anal. Chem.* **1993**, *65*, 972A-986A.

(3)   Cole, R. B. *J. Mass. Spec.* **2000**, *35*, 763-772.

(4)   Cech, N. B.; Enke, C. G. *Mass Spectrom. Rev.* **2001**, *20*, 362-387.

(5)   Kebarle, P. *J. Mass. Spec.* **2000**, *35*, 804-817.

(6)   Bruins, A. P. *J. Chrom. A* **1998**, *794*, 345-357.

(7)   Tang, L.; Kebarle, P. *Anal. Chem.* **1991**, *63*, 2709-2715.

(8)   Wahl, J. H.; Goodlet, D. R.; Udseth, H. R.; Smith, R. D. *Anal. Chem.* **1992**, *64*, 3194-3196.

(9)   Mann, M.; Wilm, M. *Int. J. of Mass Spectrom. Ion Processes* **1994**, *136*, 167-180.

(10)   Wilm, M.; Mann, M. *Anal. Chem.* **1996**, *68*, 1-8.

(11)   Feng, B.; Smith, R. D. *J. Am. Soc. Mass Spectrom.* **2000**, *11*, 94-99.

(12)   Schmidt, A.; Karas, M.; Dulcks, T. *J. Am. Soc. Mass Spectrom.* **2003**, *14*, 492-500.

(13)   Busman, M.; Sunner, J.; Vogel, C. R. *J. Am. Soc. Mass Spectrom.* **1991**, *2*, 1-10.

(14)   Smith, R. D.; Olivares, J. A.; Nguyen, N. T.; Udseth, H. R. *Anal. Chem.* **1988**, *60*, 436-441.

(15)   Olivares, J. A.; Nguyen, N. T.; R.Yonker, C.; Smith, R. D. *Anal. Chem.* **1987**, *59*, 1230-1232.

(16)   Smith, R. D.; Loo, L. A.; Edmonds, C. G.; Barinaga, C. J.; Udseth, H. R. *Anal. Chem.* **1990**, *62*, 882-899.

(17)   Zook, D. R.; Bruins, A. P. *Int. J. of Mass Spectrom. Ion Processes* **1997**, *162*, 129-147.

(18)   Shaffer, S. A.; Tang, K.; Anderson, G. A.; Prior, D. C.; Udseth, H. R.; Smith, R. D. *Rapid Comm. Mass Spectrom.* **1997**, *11*, 1813-1817.

(19)   Kim, T.; Udseth, H. R.; Smith, R. D. *Anal. Chem.* **2000**, *72*, 5014-5019.

(20)   Bruins, A. P. *Mass Spectrom. Rev.* **1991**, *10*, 53-77.

(21)   Bahr, R.; Gerlich, D.; Teloy, E. *E. Verh. Dtsch. Phys. Ges.(IV)* **1969**, *4*, 343.

(22)   Shaffer, S. A.; Prior, D. C.; Anderson, G. A.; Udseth, H. R.; Smith, R. D. *Anal. Chem.* **1998**, *70*, 4111-4119.

(23)   Shaffer, S. A.; Tolmachev, A.; Prior, D. C.; Anderson, G. A.; Udseth, H. R.; Smith, R. D. *Anal. Chem.* **1999**, *71*, 2957-2964.

(24)   Belov, M. E.; Gorshkov, M. V.; Udseth, H. R.; Anderson, G. A.; Tolmachev, A.; Prior, D. C.; Harkewicz, R.; Smith, R. D. *J. Am. Soc. Mass Spectrom.* **2000**, *11*, 19-23.

(25)   Lynn, E. T.; Chung, M.-C.; Han, C.-C. *Rapid Comm. Mass Spectrom.* **2000**, *14*, 2129-2134.

(26)   Tolmachev, A.; Kim, T.; Udseth, H. R.; Smith, R. D.; Bailey, T. H.; Futrell, J. H. *Int. J. of Mass Spectrom.* **2000**, *203*, 31-47.

(27)   Kim, T.; Tang, K.; Udseth, H. R.; Smith, R. D. *Anal. Chem.* **2001**, *73*, 4162-4170.

(28)   Tang, K.; Tolmachev, A.; Nikolaev, E.; Zhang, R.; Belov, M. E.; Udseth, H. R.; Smith, R. D. *Anal. Chem.* **2002**, *74*, 5431-5437.

(29)   Zhou, L.; Yue, B.; Dearden, D. V.; Lee, E. D.; Rockwood, A. L.; Lee, M. L. *Anal. Chem.* **2003**, *75*, 5978-5983.

(30)   Potjewyd, J. Doctor of Philosophy, University of Toronto, Torono, Ontario, Canada, 1983.

(31)   Sheehan, E. W.; Willoughby, R. C.: U. S. Patent Appl. 20020011560, 2002.

(32)   Jochen, F.; Bruker-Franzen Analytik GmbH: U. S. Patent 5,747,799, 1996.

(33)   Gulcicek, E. E.; Whitehouse, C. M.: U. S. Patent 5,432,343, 1995.

(34)   Schneider, B. B.; Douglas, D. J.; Chen, D. D. Y. *Rapid Comm. Mass Spectrom.* **2001**, *15*, 2168-2175.

(35)   Beavis, R. C.; Ens, W.; Main, D. E.; Standing, K. G. *Anal. Chem.* **1990**, *62*, 1259-1264.

(36)   Beavis, R. C.; Bolbach, G.; Ens, W.; Main, D. E.; Schueler, B.; Standing, K. G. *J. Chrom. A* **1986**, *359*, 489-497.

(37)   Zhou, S.; Edwards, A. G.; Cook, K. D.; Van Berkel, G. J. *Anal. Chem.* **1999**, *71*, 769-776.

(38)   Zhou, S.; Prebyl, B. S.; Cook, K. D. *Anal. Chem.* **2002**, *74*, 4885-4888.

(39)   MacNair, J. E.; Lewis, K. C.; Jorgenson, J. W. *Anal. Chem.* **1997**, *69*, 983-989.

(40)   Monroe, M. E., Univ. of North Carolina, Chapel Hill,NC, 2002.

(41)   Jones, A. R.; Thong, K. C. *J. Phys. D: Appl. Phys.* **1971**, *4*, 1159-1168.

(42)   Smith, D. P. H. *IEEE Trans. Ind. App.* **1986**, *IA-22*, 527-535.

(43)   Juraschek, R.; Rollgen, F. W. *Int. J. of Mass Spectrom.* **1998**, *177*, 1-15.

(44)   Ikonomou, M. G.; Blades, A. T.; Kebarle, P. *Anal. Chem.* **1991**, *63*, 1989-1998.

(45)   Blades, A. T.; Ikonomou, M. G.; Kebarle, P. *Anal. Chem.* **1991**, *63*, 2109-2114.

(46)   Smith, J. N.; Flagan, R. C.; Beauchamp, J. L. *J. Phys. Chem. A* **2002**, *106*, 9957-9967.

(47)   Loscertales, I. G.; de la Mora, J. F. *J. Chem. Phys.* **1995**, *103*, 5041-5060.

(48)   Enke, C. G. *Anal. Chem.* **1997**, *69*, 4885-4893.

(49)   Cech, N. B.; Enke, C. G. *Anal. Chem.* **2000**, *72*, 2717-2723.

(50)   Geromanos, S.; Freckleton, G.; Tempst, P. *Anal. Chem.* **2000**, *72*, 777-790.

(51)   Dohmeier, D. M. Doctor of Philosophy, Univ. of NC at Chapel Hill, Chapel Hill, NC, 1991.

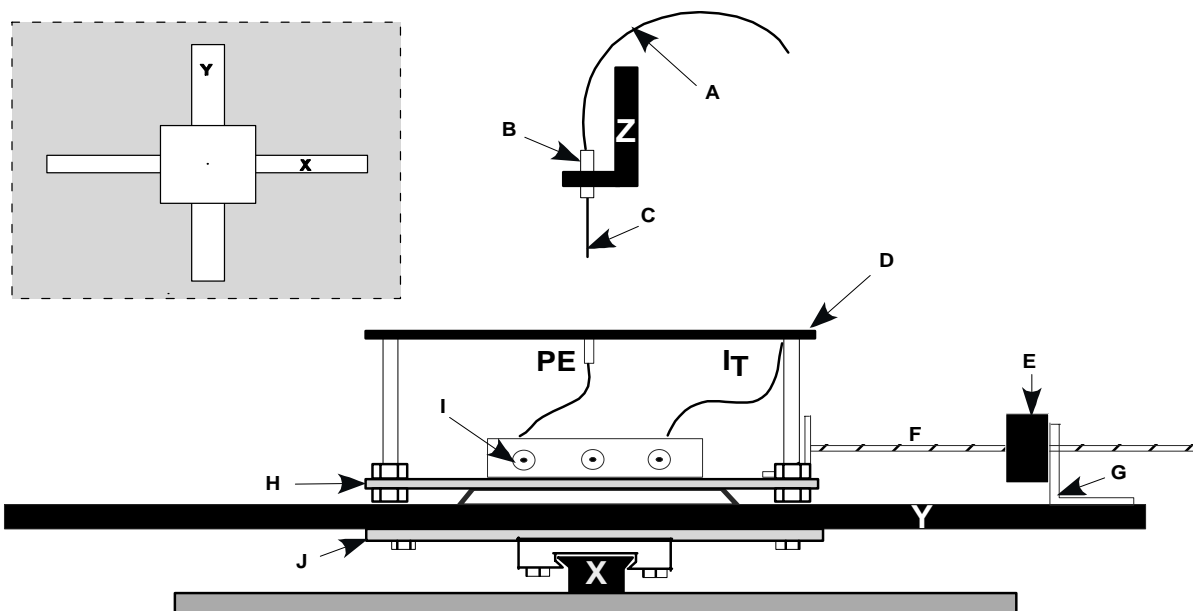(52)   Juraschek, R.; Dulcks, T.; Karas, M. *J. Am. Soc. Mass Spectrom.* **1999**, *10*, 300-308.

Figure 6-1: Schematic of electrospray current density profiler, side view. (A) Fused-silica infusion capillary. (B) Teflon butt-connect. (C) Electrospray needle. (D) Brass ground plane. (E) Linear actuator for Y-translation. (F) Lead screw for Y-translation. (G) Aluminum bracket. (H) Polycarbonate insulator between ground plane and Y-translation stage. (I) BNC connectors. (I_T) Lead to monitor total ESI current. (J) Polycarbonate insulator between X- and Y- translational stages. (PE) Probe Electrode. (X) X-translation track. (Y) Y-translation track. (Z) Z-translation micropositioner. Inset: Top-down layout of ESI profiler. Linear actuator and lead screw for X-translation not shown.
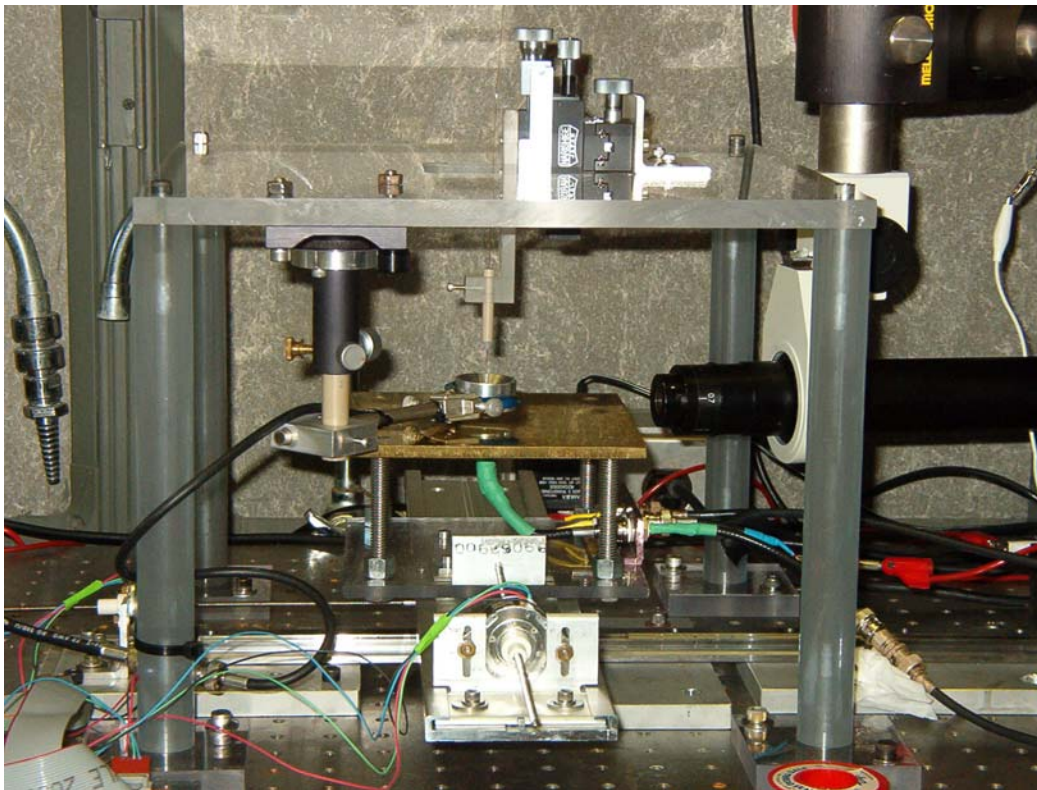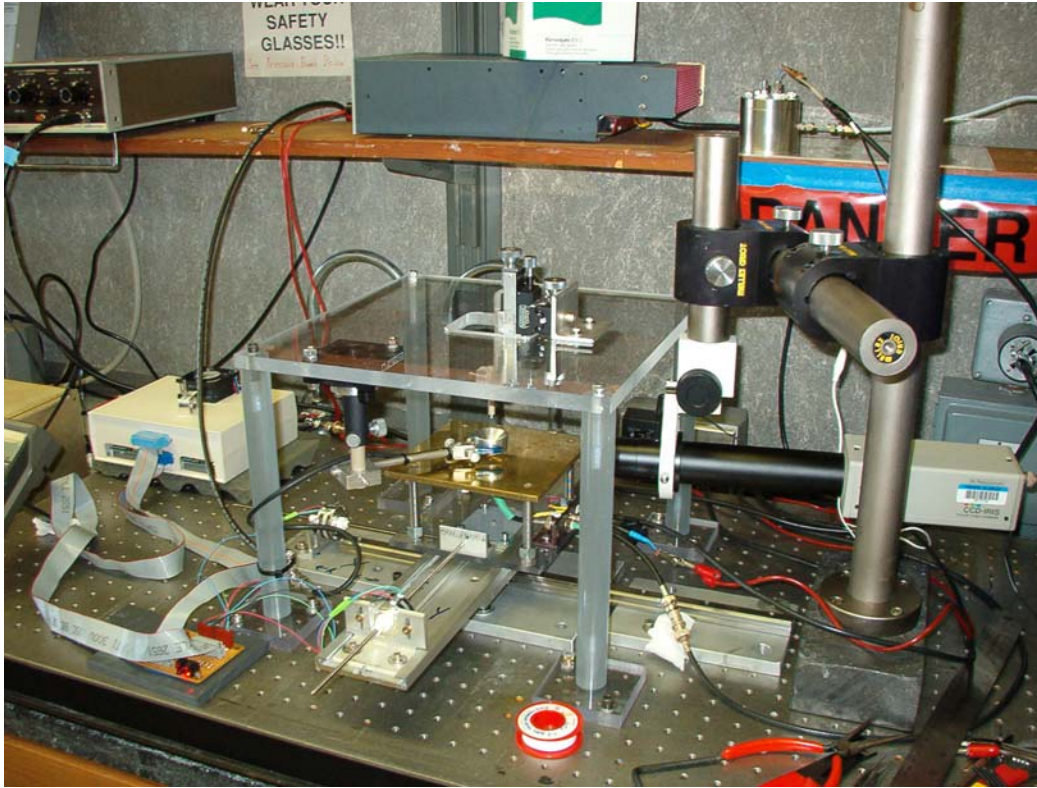
Figure 6-2: Photographs of the ESI current-density profiler displayed schematically in Figure 6-1.
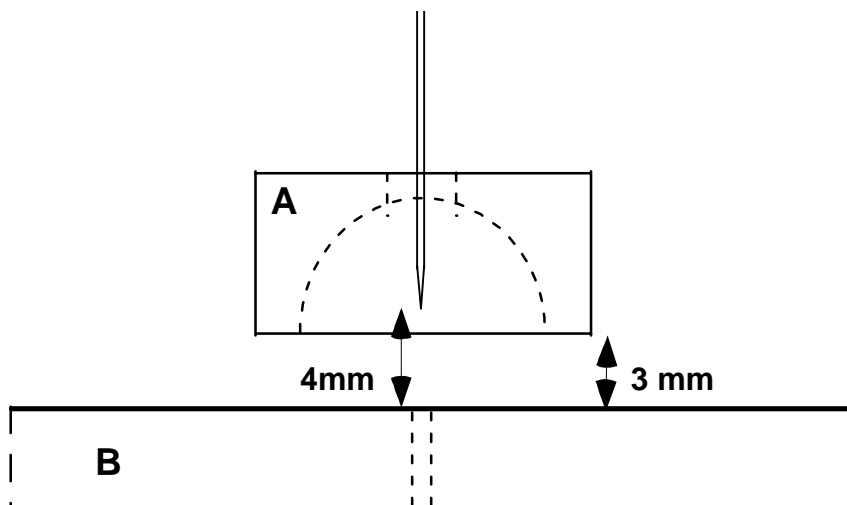
Figure 6-3: Orientation of hemispherically-shaped electrostatic ion lens in relation to a nanoelectrospray emitter. (A) Ion lens in the inverted orientation was found to be the most functional for focusing ESI plumes at atmospheric pressure. The lens was machined from brass tube stock. Dimensions are given in the experimental section. (B) Ground plane of the ESI profiler. The drawing shows the most effective lens geometry in relation to the ESI needle, with the needle 1 mm within the exit of the lens. Drawing not to scale.
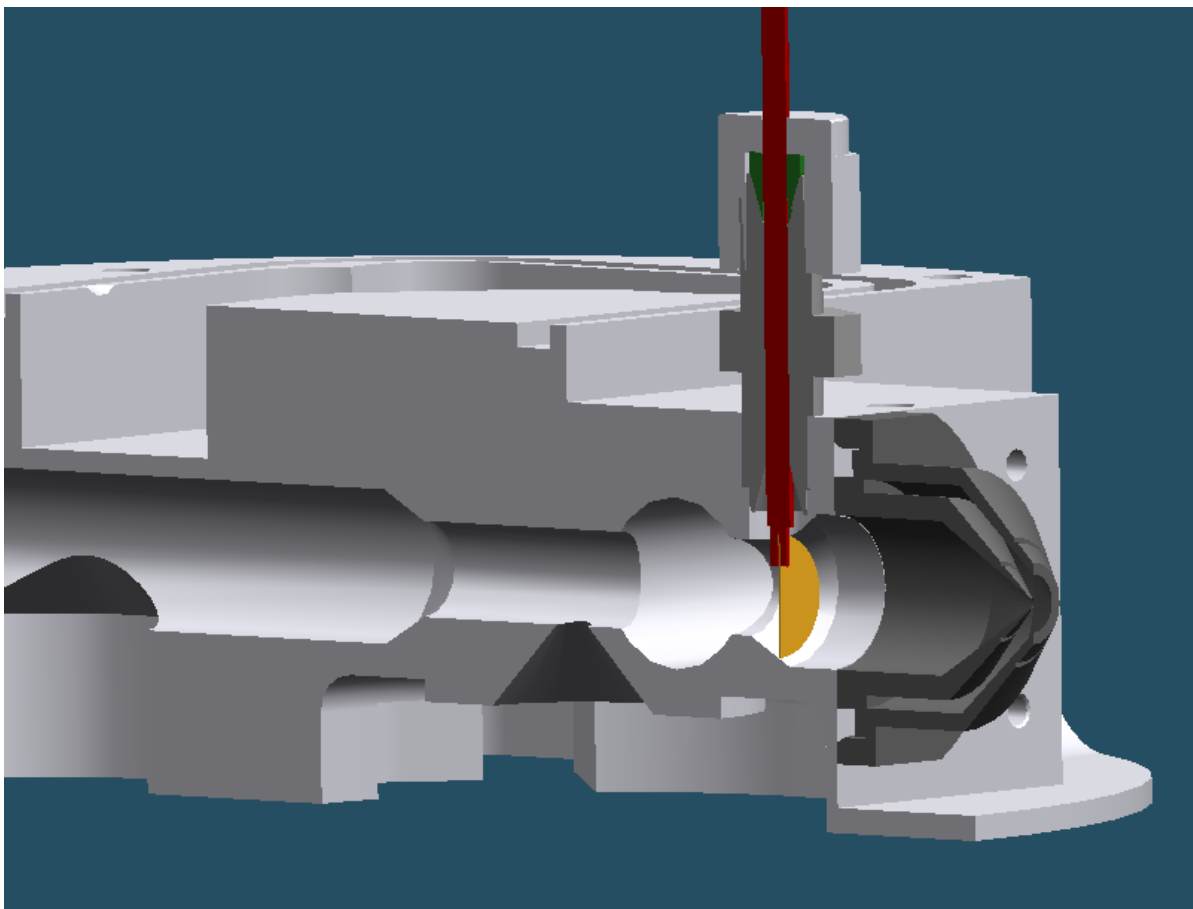
Figure 6-4: Solidedge v11 rendering of the mesh collection electrode placement inside the ion block of the ZQ mass spectrometer. The ion block has been cut in half in this rendering to enable visualization of the mesh electrode (brass color) at a distance approximately 1.7 cm behind the entrance to the ESI sampling cone (dark gray).
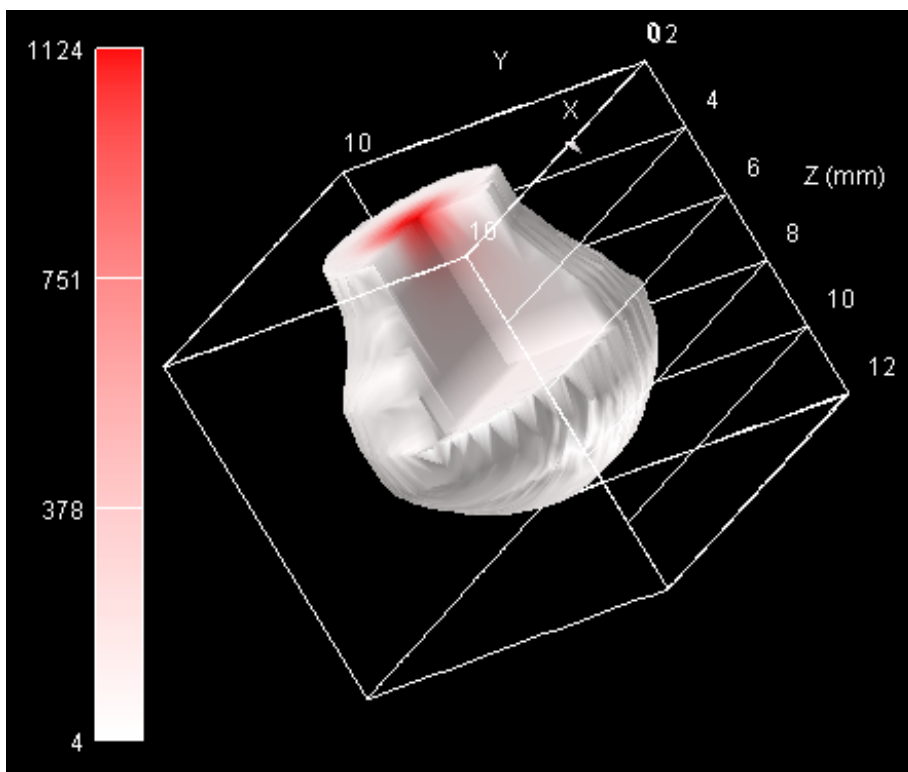
Figure 6-5: Three-dimensional rendering of the current density of an electrospray plume. Three-dimensional volume visualization was performed in AVS/Express by John W. Eschelbach. Data was collected in 1-mm steps from 2 to 12 mm Z-distance. Data in each x-y plane was collected over a 10-mm by 10-mm square with 0.5-mm Y-step size. The flow rate for this experiment was 150 nL/min of 50/50 (v/v) acetonitrile/water with 0.1% formic acid.
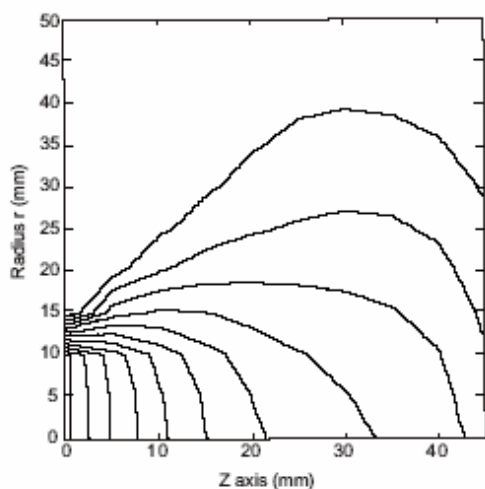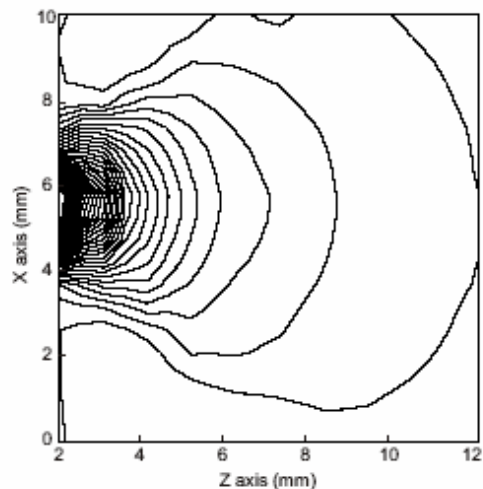
Figure 6-6A   Figure 6-6B

Figure 6-6: Ion density as a function of position within an electrospray plume. (A) Finite-element calculations for needle-in-can geometry. Charge density distribution (-10^{-5} C/mm^3 per step) where the needle is located at (0 meters z, 0 through 0.01 meters r). Reprinted with permission from Ref. 13. (B)   Interpolated current density distribution (-1.53 nA/mm^2 per step) where needle is at position (0 mm Z, 4.7 mm X). Electrospray was performed with the electric field at the tip constant at approximately 1.1×10^6 V/cm. Flow rate was 150 nL/min of 50/50 water/acetonitrile with 0.1% formic acid.
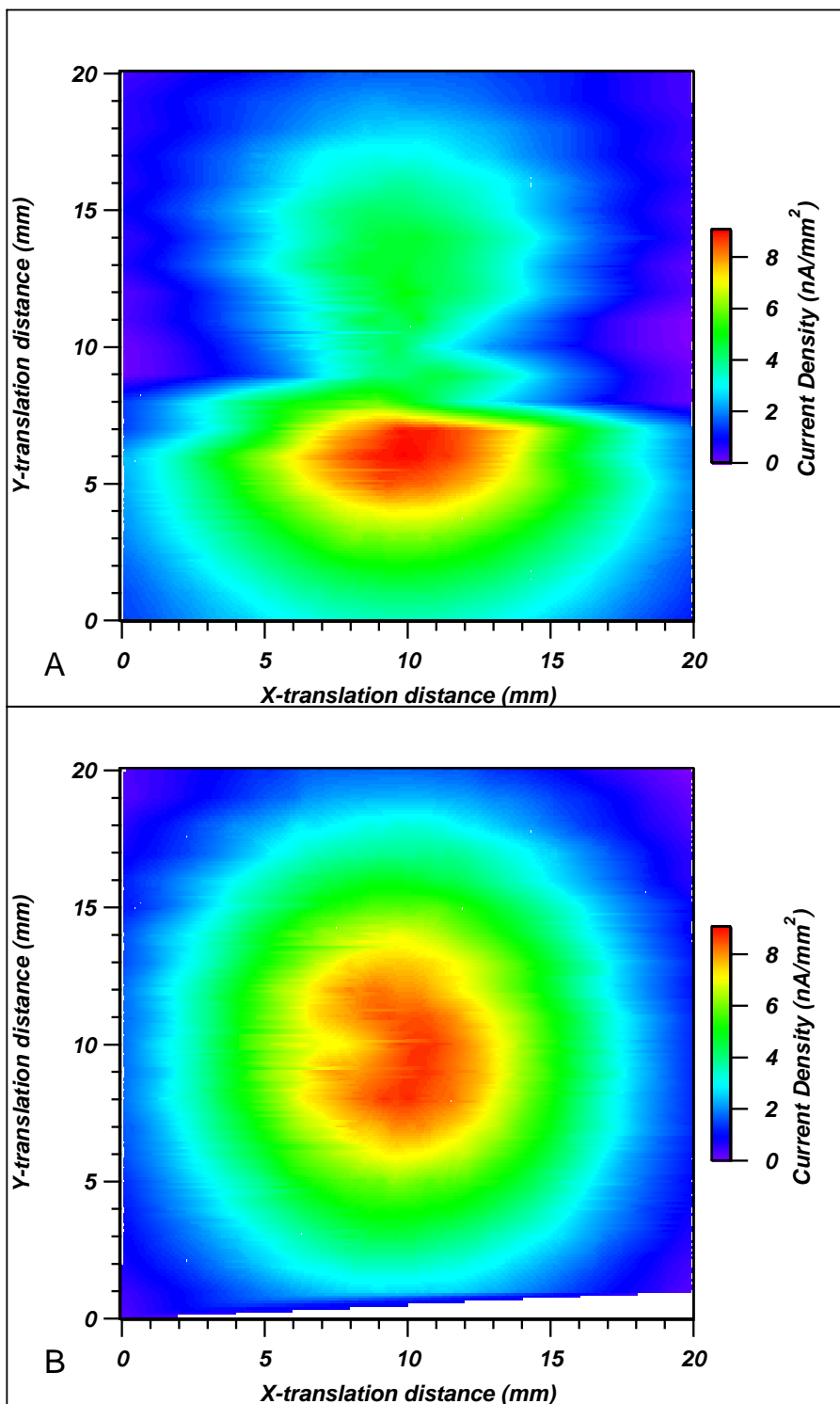
Figure 6-7: Current density profiles of electrospray plumes with electrospray needle in poor condition (A) and with a new New Objective FS360-50-8-D needle (B). Data was interpolated into a 200 x 200 grid using Igor Pro 4.08. Needle to plane distance = 10 mm; spray voltage = 3.02 kV; flow rate was roughly 200 nL/min of 50/50 water/acetonitrile with 0.1% formic acid. Collection was over a 20 x 20 mm square with Y-step size of 1 mm.
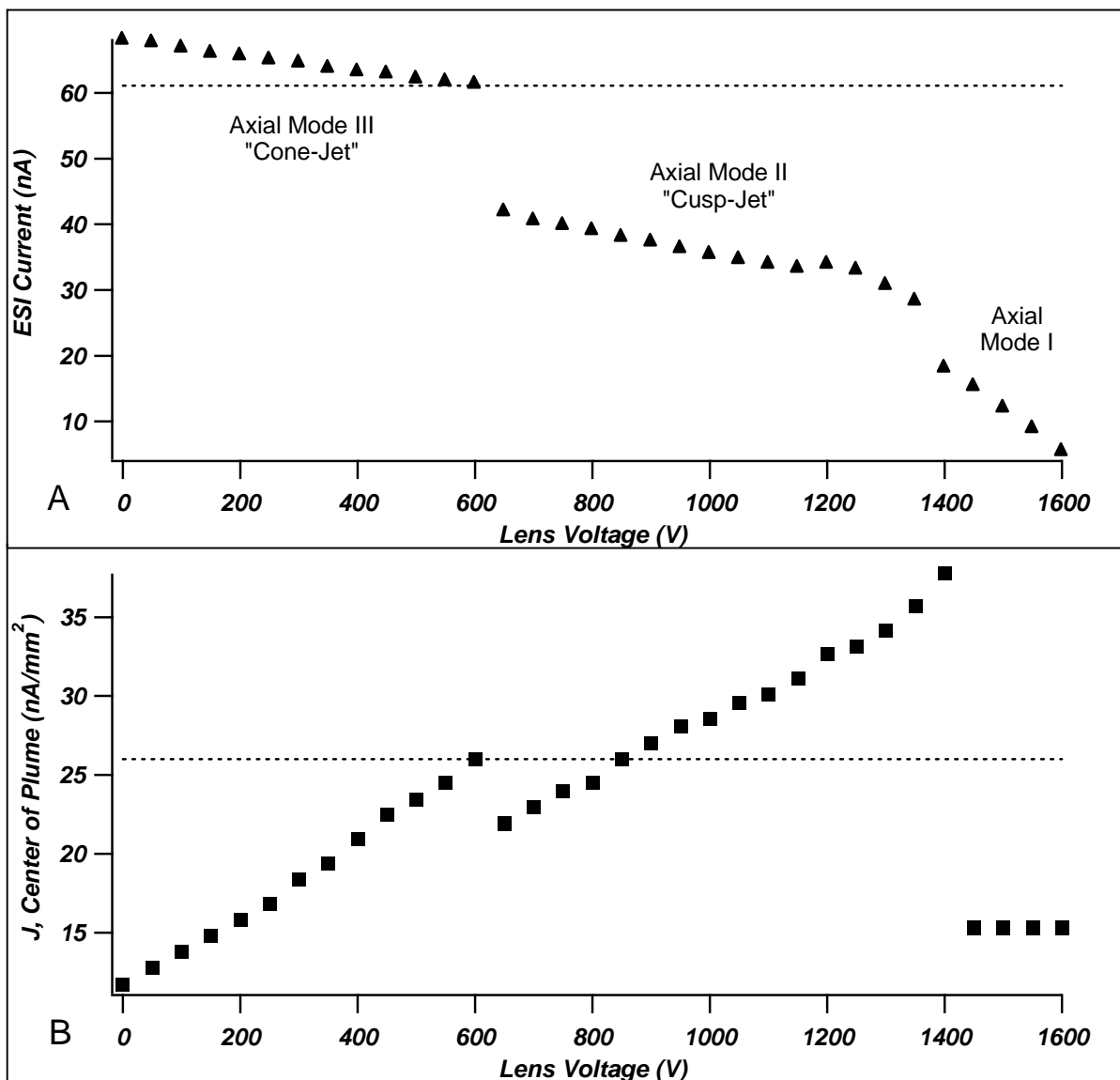
Figure 6-8: Total electrospray current as a function of lens voltage with constant ESI voltage. Data parameters: F=15 nL/min; 90%/10% water/acetonitrile with 0.1% formic acid; ESI voltage 1.6 kV. Needle and lens setup as shown in Figure 6-3. (A) Total ESI Current as a function of lens voltage. (B) Current Density (J) in the center of the ESI plume as a function of lens voltage (monitored at the 0.5-mm probe electrode). Dotted lines correspond to the nominal case, or the values of total current and current density with no lens in place.
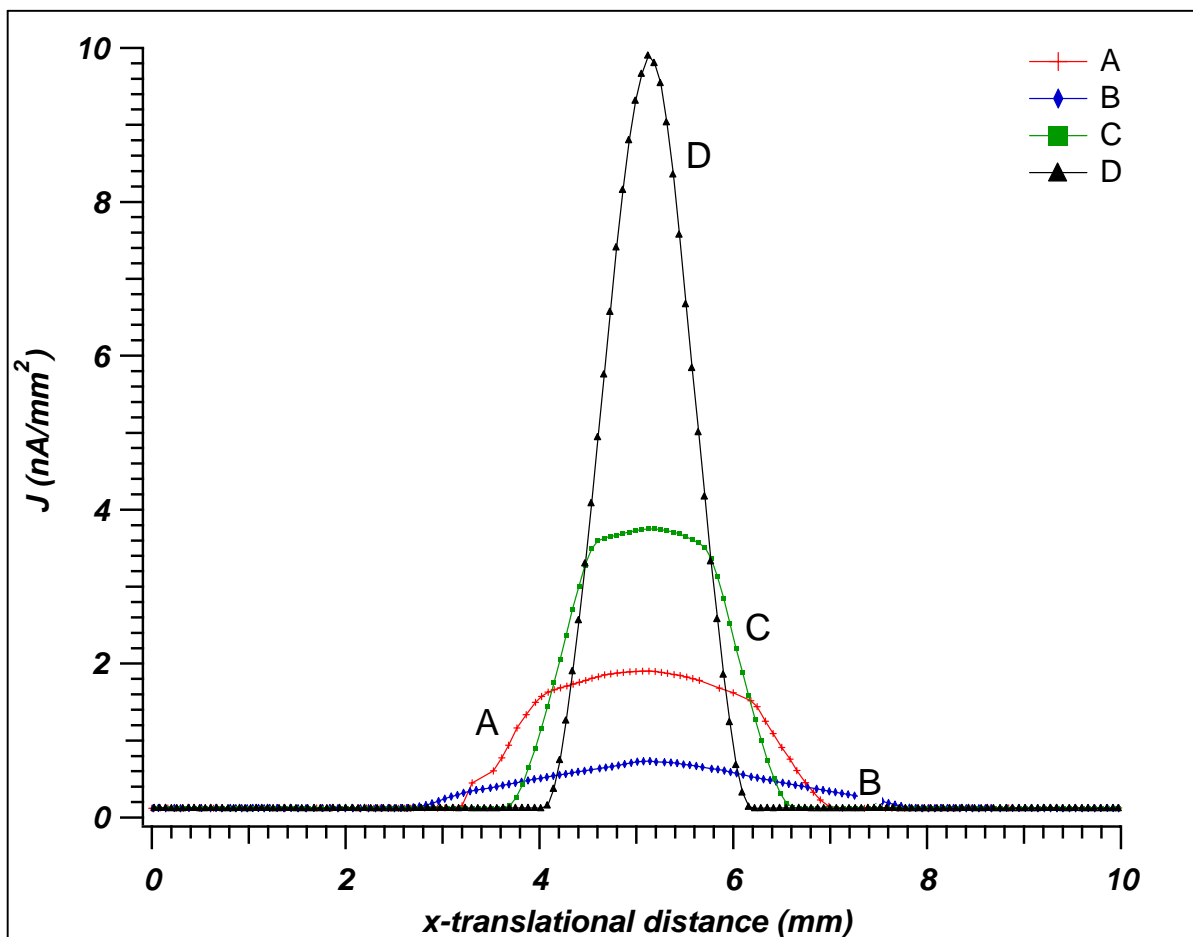
Figure 6-9: The effect of a hemispherical lens on current density profiles of an ESI plume. Plotted are the most intense (center) scans for each of four different conditions. All scans collected with 40/60 (v/v) acetonitrile/water with 0.1% formic acid at a flow rate of 15 nL/min; I_T was constant at 36 nA; needle and lens orientation is as shown in Figure 6-3. Conditions: (A) $V_S = 1600$ V, no lens used. (B) $V_s = 1550$ V, $V_L = 0$ V. (C) $V_s = 1850$ V, $V_L = 800$ V. (D) $V_s = 2680$ V, $V_L = 2000$ V.
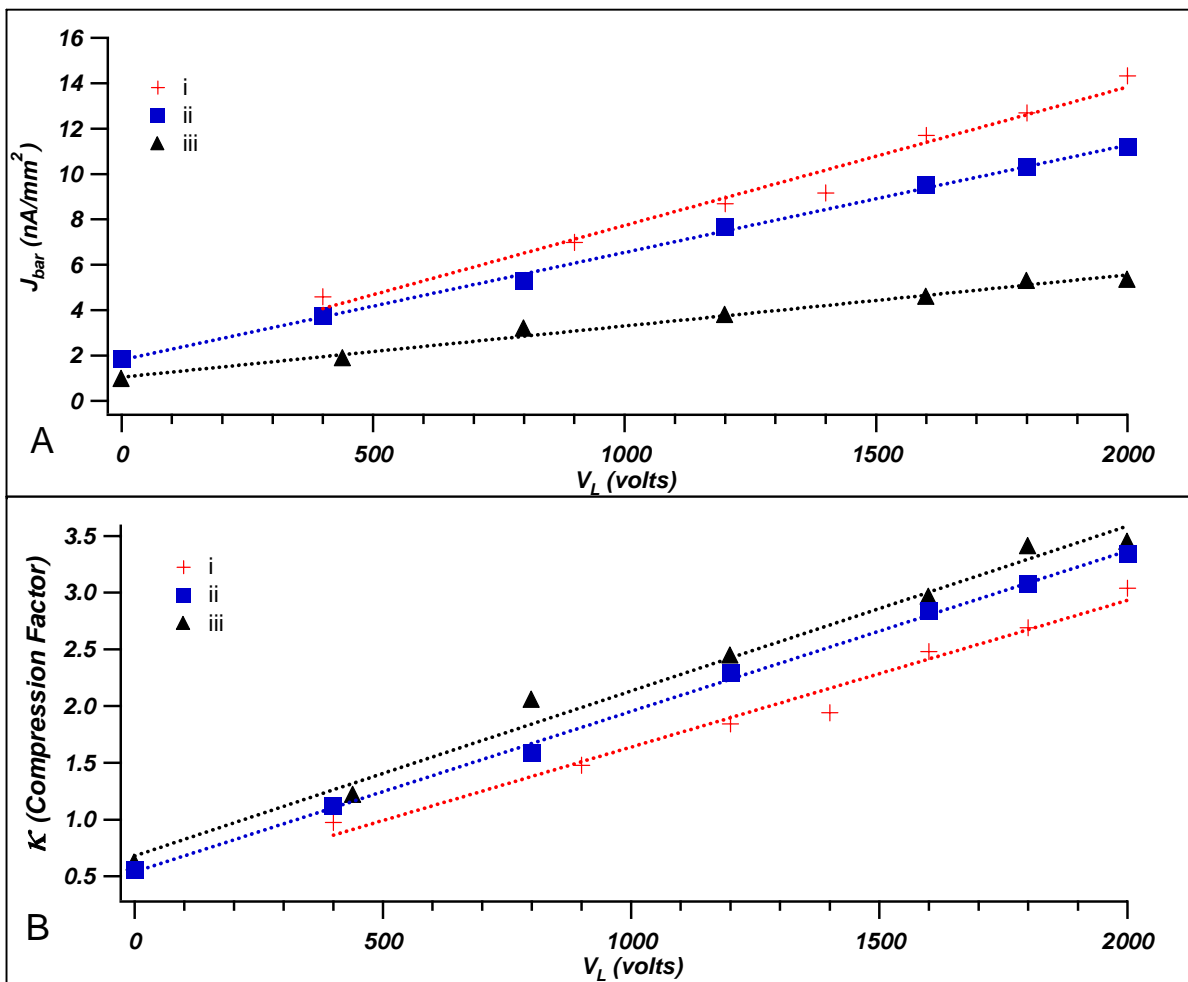
Figure 6-10: The effectiveness of lens with hemispherical interior under different solvent conditions. F~15nL/min. (A) Average current density versus lens voltage. (B) Compression Factor (κ) versus lens voltage. Solvent conditions: (i) 10/90 acetonitrile/water with 0.1% formic acid. (ii) 40/60 acetonitrile/water with 0.1% formic acid. (iii) 80/20 acetonitrile/water with 0.1% formic acid.
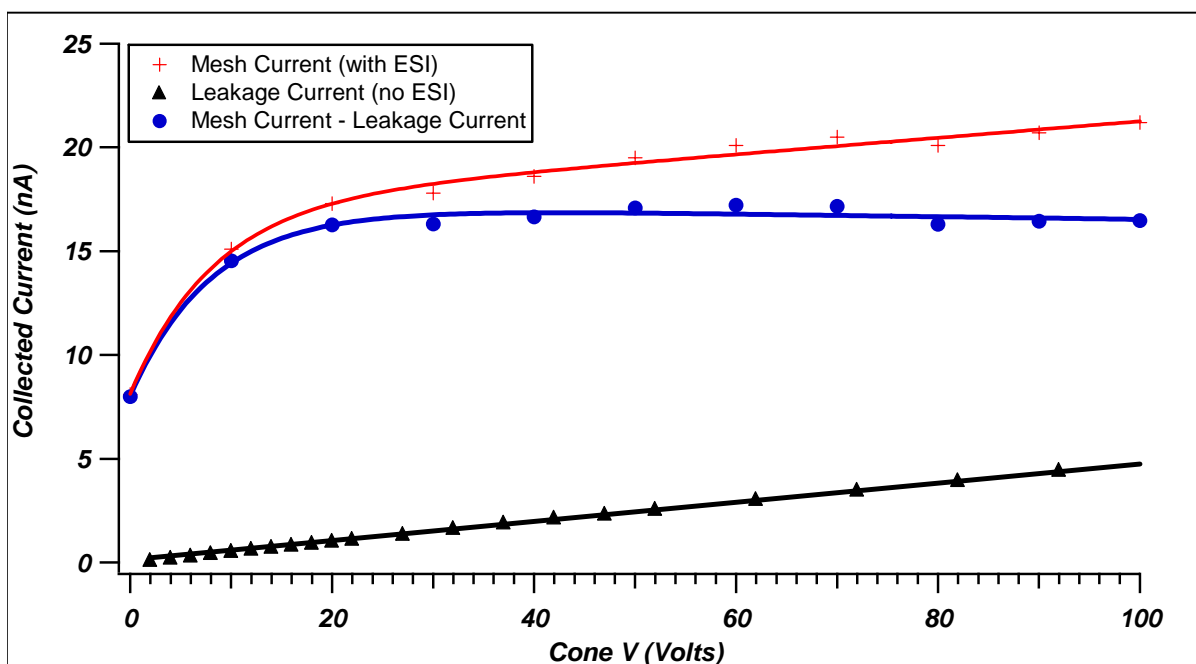
Figure 6-11: Current (nA) collected at the mesh electrode as a function of sampling cone voltage for the cases with and without electrospray. During experiment using electrospray, the flow was approximately 200 nL/min of 50/50 (v/v) acetonitrile/water with 0.1% formic acid, with 1.8 kV spray voltage. The leakage current was subtracted from the total mesh current to give the true mesh current to cone voltage relationship, shown in blue.
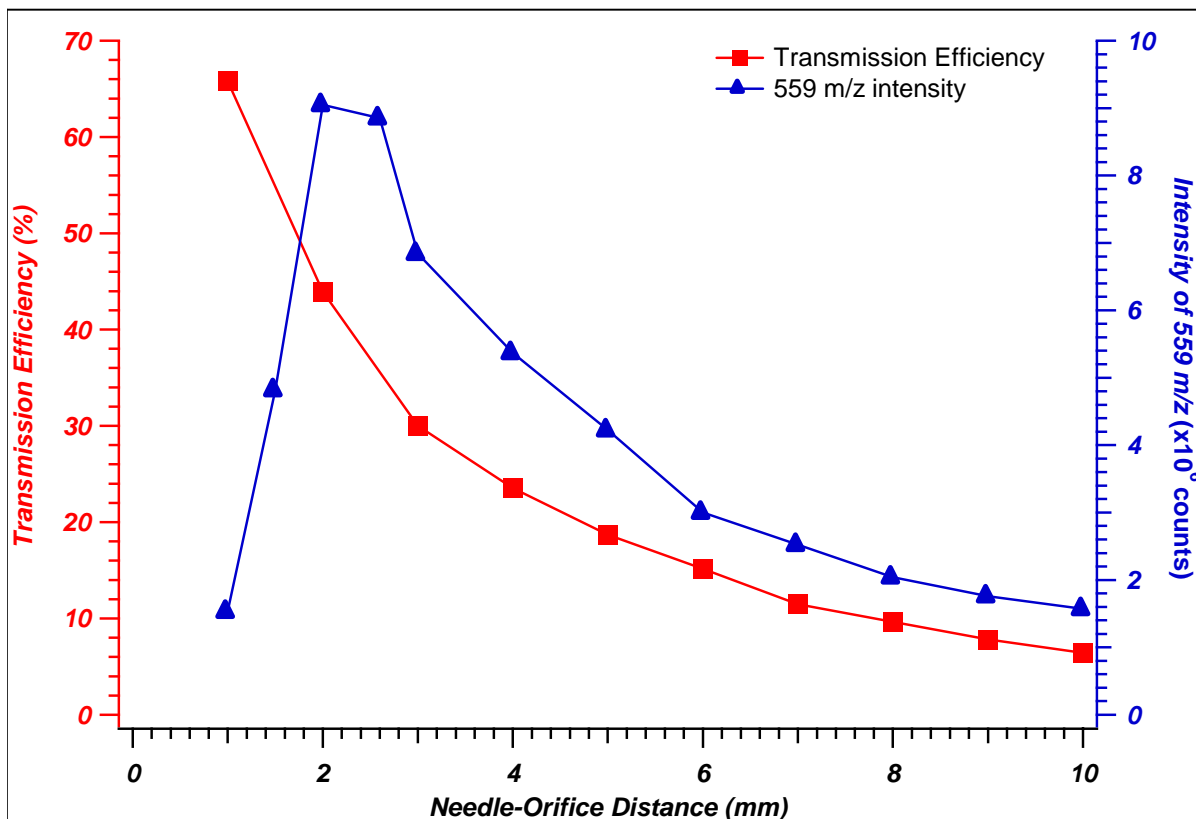
Figure 6-12: Ion transmission efficiency (red) and (neurotensin+2H)$^{2+}$ ion intensity (blue) as a function of needle to orifice distance for nano-ESI.   Experiment was run with a flow rate of 30 nL/min of 50/50 water/acetonitrile with 0.1% formic acid and 950 nM neurotensin, using an FS360-20-5-D spray needle. Spray voltage was increased from 900V at 1-mm to 1.30 kV at 10-mm to maintain roughly constant total spray current. Even though ion transmission is highest at 1 mm (68%), the optimal mass spec signal for the (neurotensin+2H)$^{2+}$ peak occurred between 2 and 2.5 mm, where transmission is 35 to 45%.
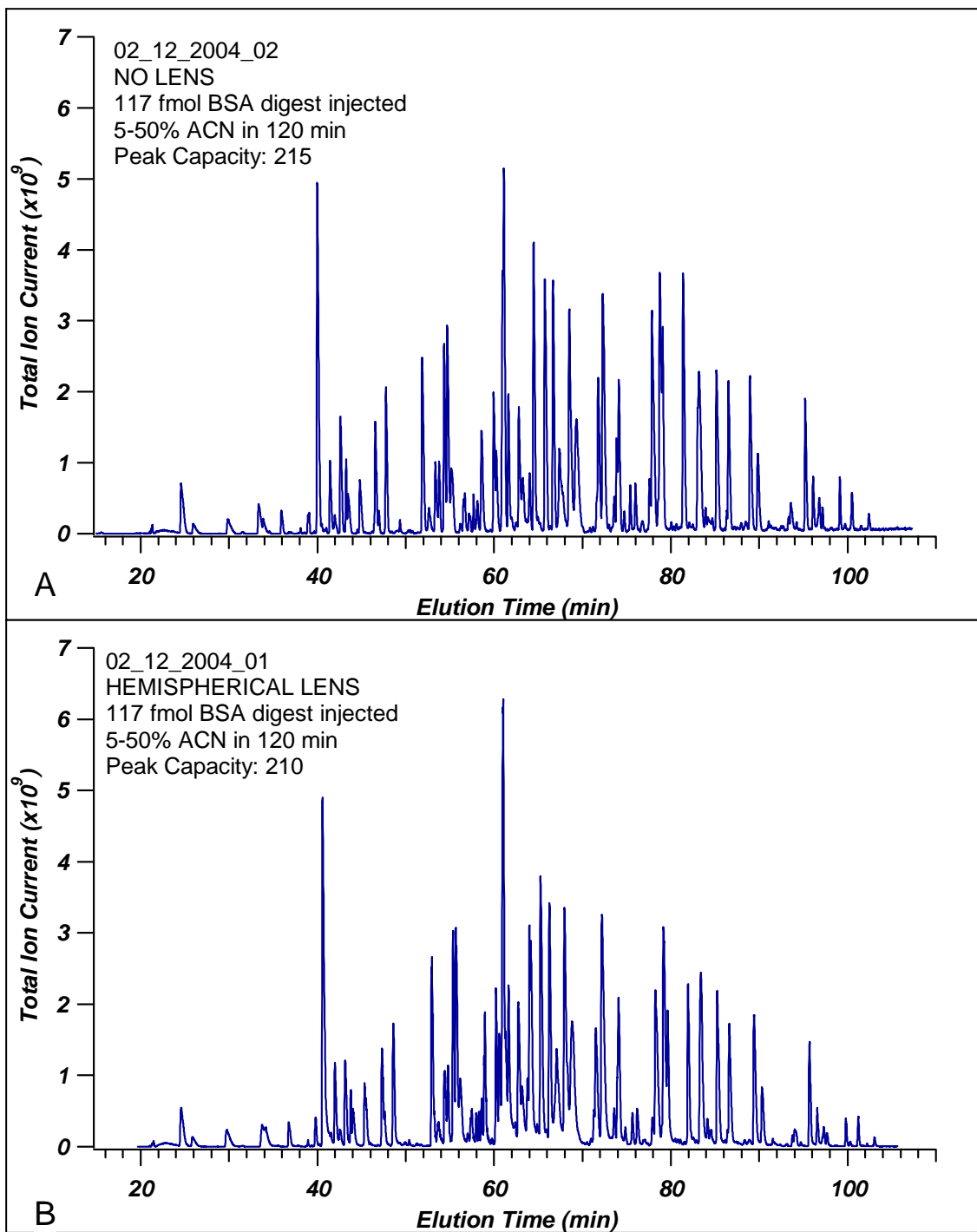
Figure 6-13: TIC (total ion current) chromatograms for a BSA digest sample run on a 50-cm x 30-μm column packed with 3 μm Atlantis C18 particles. Data collected using a ZQ Mass spectrometer. LC run pressure was 3,000 psi (200 bar). Both experiments shown here had an injection amount of roughly 117 fmol. (A) LC-MS experiment without a lens; median peak width was 21.4 sec and peak capacity was 215. (B) LC-MS experiement with the hemispherical lens; the median peak width was 22.4 sec and peak capacity was 210.
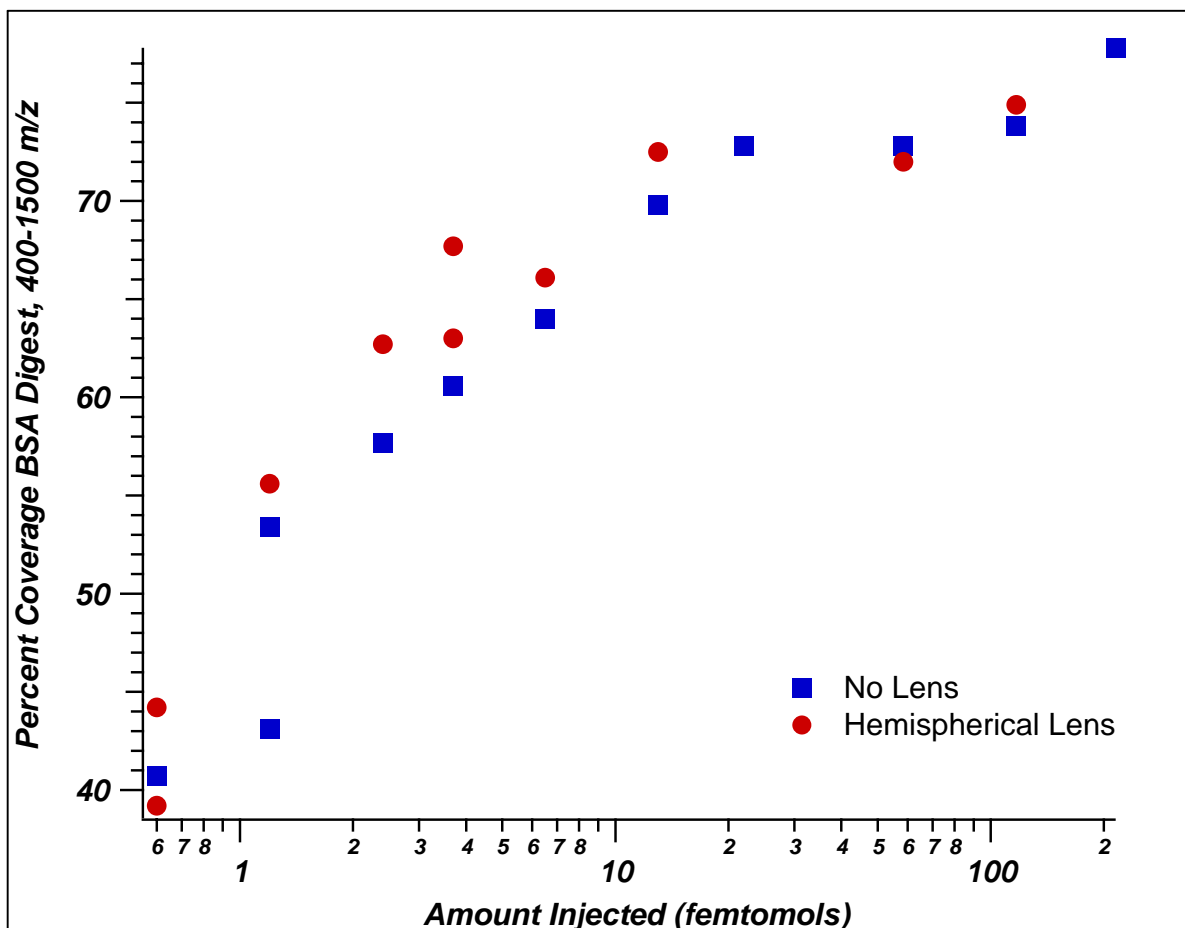
Figure 6-14: Percent coverage of BSA tryptic digest versus quantitiy injected, from an LC-MS experiment using a 50-cm x 30-μm capillary column packed with 3 μm Atlantis C18 particles. Gradient: 5 to 50% acetonitrile with 0.1% formic acid over 120 minutes. F = 15nL/min; V_s=1400V; Hemispherical lens runs were done with V_L = 600 V.

APPENDIX A: INVENTORY OF POROUS AND NONPOROUS PACKING

MATERIALS FOR CAPILLARY HPLC AND UHPLC

A.1   Appendix Purpose

Since 2002 an active collaboration between our lab and Waters Corporation (Milford, MA) has been in place with the purpose of developing technology for commercial UHPLC. As part of this collaboration, we have received a variety of porous packing materials for our use in capillary columns. This appendix is intended to be a compilation of all the porous particles from Waters corporation that are available in-house in the Jorgenson lab as of the summer of 2006. The inventory contains all the known data about each particle type, such that researchers in our lab can be aware of which particles are available and pick those which best suit the particular application under investigation. Also contained in this table are the nonporous particles that have been used for UHPLC, and the known data for those packing materials as well.

A.2   Organization

The table is subdivided into several categories to aid in searching. First, the porous and nonporous particles are segregated, porous material being listed first. Next, if applicable, the material is subdivided by silica support type, such as "Atlantis", "Acquity", or "BEH". Finally, the particles in these categories are ordered approximately from smallest particle diameter to largest. There would certainly have been other ways to subdivide the particles

(for example by stationary phase type), but the organizational scheme utilized was intended

to be the most useful for the chromatographer without being overly complicated. In general,

if a space in the table has been left blank it means that data is not known for those particular

particles.

A.3 Data Categories (Columns)

A.3.1 Lot/Batch

This column gives the manufacturing lot number (for production-scale syntheses) or

the batch number (for research scale particle batches) for each bottle of particles. This

number should be present on every particle container and is the most readily available way to

identify a batch of particles on this list if you find them on the shelf.

A.3.2 Manufacturer/Type

This column contains the particle manufacturer and in most cases the trade name for

the particle type. For nonporous silica, NPS simply means "nonporous silica". "Eichrom

NPS" means nonporous silica manufactured by Eichrom Technologies, while "NPS (Stober)"

means nonporsous silica that was synthesized in our lab using the Stober synthesis.[1]

A.3.3 $d_{p,n}$ (μm)

This column contains data on the number-averaged particle diameter for the particles,

as described in Chapter 2. Values not in quotations have been verified via scanning electron

microscopy. If the value is in quotations, this means that this is the particle diameter claimed

by the manufacturer, but it has not been independently verified by SEM.

A.3.4 σ (μm)

Standard deviation of the number-averaged particle diameter, reported in microns. If

values are reported here, they have been obtained via SEM.

A.3.5 %RSD

Relative standard deviation of the number-averaged particle diameter, reported in microns. If values are reported here, they have been obtained via SEM.

A.3.6 $d_{p,v}$ (μm)

The volume-averaged particle diameter, as discussed in Chapter 3. Values reported with no extra notation were obtained from SEM analysis in our lab. Values with the superscript "cc" were reported by Waters Corporation using a coulter-counter. Values with an asterisk were reported by Waters Corporation using a "Malvern Mastersizer" light-scattering particle distribution analyzer.

A.3.7 SSA (m^2/g)

SSA refers to the particle's specific surface area, reported in m^2 per gram of dry stationary phase. Data provided by Waters Corporation.

A.3.8 SPV (mL/g)

SSA refers to the particle's specific pore volume, reported in mL per gram of dry stationary phase. Data provided by Waters Corporation.

A.3.9 d_{pore} (nm)

Refers to the particle's average pore diameter in nm. This data was provided by Waters Corporation. Numbers listed with a "~" sign before them are approximate.

A.3.10 Bonding

"Bonding" refers to the type of surface modification that has been performed to the stationary phase support as it currently exists. Particles listed as "bare" have not had any surface modification. Otherwise, the type of stationary phase bonded to the surface is listed. In cases where the stationary phase type has a prefix, this is a more detailed description of the

bonding. For instance, "mC18" means a monofunctional octadecylsilane reagent was used to bond the stationary phase to the substrate, "dC18" means difunctional, and "tC18", trifunctional. "C18 (PMM)" refers to bonding that has been performed in the Jorgenson lab using a proprietary method obtained from Peter Myers (PMM = Peter Myers Method).[2]

A.3.11 H_{min}

This column contains the minimum plate height in microns, or the optimum performance, obtained for these particular particles packed into capillary columns. This data was all obtained in the Jorgenson lab, using isocratic evaluation with hydroquinone as the analyte and electrochemical or UV absorbance detection.

A.3.12 Date, Notebook

These columns contain information to allow the user to locate more information about the conditions used to obtain the H_{min} data reported in the previous column. "Date" is (obviously) the date in the notebook which contains the H_{min} data. "Notebook" refers to the person who collected the data or in whose notebook the H_{min} data can be located. For reference, JWT = J. Will Thompson; JSM = J. Scott Mellors; RAL = Rachel A. Lieberman; ADJ = Anton D. Jerkovich; DJS = Dawn J. Stickle.

A.3.13 g available

This column lists the approximate quantity of each particle available in the Jorgenson lab for use.

A.3.14 Packing Solvent

This column lists the preferred packing solvent as determined by that which was used to obtain the H_{min} values. Particles with no solvent listed have never been packed into columns. If a particle type has multiple solvents listed in this column, this means that both

solvent systems seemed to perform equally well at dispersing and packing the particles in capillaries via the slurry method.

A.4   References

(1)   Stöber, W.; Fink, A.; Bohn, E. *J. Colloid Interface Sci.* **1968**, *26*, 62-69.

(2)   Mellors, J. S., University of NC at Chapel Hill, Chapel Hill, NC, 2005.

Table A-1: (see pages 236-238) Inventory of the available porous and nonporous packing materials in the Jorgenson lab for slurry-packing into capillary columns for HPLC and UHPLC.

Lot/Batch #	Manufacturer/Type	$d_{p,n}$ (µm)	σ (µm)	% RSD	$d_{p,v}$ (µm)	SSA (m²/g)	SPV (mL/g)	d_{pore} (nm)	Bonding	H_{min}	Date	Notebook	g avail	packing solvent
Porous silica														
#104	Waters Acquity BEH	"1.7"			1.854cc	184	0.68	13.8	phenyl				2g	
#104	Waters Acquity BEH	"1.7"			1.854cc	184	0.68	13.8	shield RP18				2g	
#111A	Waters Acquity BEH	"1.7"						~13	tC18	3.4	6/17/2005	JWT	2	acetone
#105	Waters Acquity BEH	"1.7"			1.84cc	184	0.68	13.1	tC18				5	
#102	Waters Acquity BEH	"1.7"			1.841cc	183	0.67	12.9	C8				2	acetone
Batch 103	Waters Atlantis	"3.5"						~10	dC18	5.7	11/5/2003	JWT	5	acetone
Batch 109	Waters Atlantis	"5"						~10	dC18				5	
KDW-4-103-CK	Waters BEH	0.58	0.05	8.6%	0.598*	175	0.59	13	bare				4	
NLL-6-95	Waters BEH	0.58	0.05	8.6%	0.598*	175	0.59	13	tC18				1	acetone
KDW-4-103-CL	Waters BEH	0.62	0.13	21.0%	0.589*	177	0.61	13.3	bare				4	
KDW-4-103-CP	Waters BEH	0.62	0.1	16.1%	0.784*	179	0.63	13.4	bare				10	
KDW-3-159	Waters BEH	0.76	0.26	34.2%	0.97	155	0.82	15.5	tC18	4	10/14/2005	JWT/RAL	3	acetone
KDW-4-103-CO	Waters BEH	0.92	0.16	17.4%	1.049*	179	0.63	13.4	bare				20	
KDW-4-36	Waters BEH	0.982	0.189	19.2%	1.07	155	0.82	14.5	tC18	2.9	6/20/2005	JWT	3	acetone
KDW-3-105	Waters BEH	"1.1"			1.15cc	181	0.71	14.5	C18	2.8	10/3/2003	JSM	5	acetone
KHG-6-37	Waters BEH	"1.4"			1.41cc	189	0.74	14.7	mC18	4.2	2/27/2003	JSM	0.6	acetone
KHG-6-87	Waters BEH	1.53			1.52cc	184	0.75	15.0	tC18	2.8	1/20/2005	JWT	3	acetone
KHG-6-55	Waters BEH	1.56	0.17	10.9%	1.62	189	0.74	14.7	tC18	2.3	8/6/2003	JSM	0.05	acetone
NLL-2-90	Waters BEH	"1.7"			1.75cc	190	0.74	14.8	mC18				2	acetone
KDW-3-152A	Waters BEH	"1.7"			1.79cc	192	0.77	14.8	tC18	6	4/9/2004	JSM	1	acetone
#002F3	Waters BEH	1.8	0.4	22.2%	2.06	187.3	0.731	14.5	C18 (PMM)	3.6	1/13/2003	JSM/JWT	20	acetone
#002F3	Waters BEH	1.8	0.4	22.2%	2.06	187.3	0.731	14.5	mC18	3	1/21/2003	JSM/JWT	50	acetone

Lot/Batch #	Manufacturer/Type	$d_{p,n}$ (µm)	σ (µm)	% RSD	$d_{p,v}$ (µm)	SSA (m^2/g)	SPV (mL/g)	d_{pore} (nm)	Bonding	H_{min}	Date	Notebook	g avail	packing solvent
Porous silica (continued)														
DPW-20-145-0	Waters BEH	"1.8"						~10					2	
DPW-20-145-50	BEH-"transformed"	"1.8"						~10					2	
KHG-7-58	Waters BEH	"1.8"			1.80	89	0.58	25.4	tC18	2.9	6/24/2005	RAL/JWT	1	acetone
#002-F3	Waters BEH	"2.0 fines"				187.3	0.731	14.5	bare				100	
KHG-7-59	Waters BEH	"2.5"			2.53^{cc}	90	0.62	25.9	tC18				1	acetone
NLL-3-159	Waters BEH	3.24			3.24^{cc}	188	0.71	13.3	C18				10	acetone
KHG-6-185	Waters BEH	"3.5"			3.24^{cc}	189	0.71	13.3	tC18	8.4	4/19/2004	JWT	2	acetone
NLL-3-190	Waters BEH	4.31			4.31^{cc}	180	0.79	15.8	C18				20	acetone
KHG-7-36	Waters BEH	"4.5"			4.52^{cc}	97	0.74	30.8	tC18				1	acetone
NLL-6-108	Waters BEH	"5"						~13					2	
FM#119	Narrow Pore BEH	0.1-10						~4					3	
NLL-3-54	Waters Symmetry	1.31			1.31^{cc}	321	0.87	10.7	mC18	2.5	6/11/2003	JSM	1	acetone
NLL-3-25	Waters Symmetry	1.42			1.418^{cc}	330	0.89	10.1	mC18				2	acetone
NLL-3-55	Waters Symmetry	"1.47"			1.47^{cc}	315	0.87	10.7	mC18				4.3	acetone
Batch 006	Waters Symmetry	"3.5"						~30	C4	28	5/6/2005	JWT	5	acetone
Batch 118	Waters Symmetry	"3.5"						~30	C18	8.2	11/23/2004	JWT	5	67/33 hexane/acetone
Batch 136	Waters Symmetry	"3.5"						~15	C18				5	
Batch 118	Waters Symmetry	"5"						~30	C4				5	
Batch 166	Waters Symmetry	"5"						~15	C18				5	
Batch 120	Waters Symmetry	"5"						30	C18				5	acetone or IPA

240

Lot/Batch #	Manufacturer/Type	$d_{p,n}$ (μm)	σ (μm)	% RSD	$d_{p,v}$ (μm)	SSA (m^2/g)	SPV (mL/g)	d_{pore} (nm)	Bonding	H_{min}	Date	Notebook	g avail	packing solvent
nonporous silica														
JSM-06-16-04	NPS (Stober)	0.6				n/a	n/a	n/a	C18 (PMM)	1.7	7/7/2005	JWT	0.25	67/33 hexane/acetone
M120794	Eichrom NPS	0.7				n/a	n/a	n/a	bare				20	H2O or acetone
JSM-03-24-05	NPS (Stober)	0.9				n/a	n/a	n/a	C18 (PMM)	1.5	4/20/2005	JSM	0.5	67/33 hexane/acetone or acetone
JSM-04-04-05	NPS (Stober)	0.96				n/a	n/a	n/a	C18 (PMM)				1.5	67/33 hexane/acetone
M012695	Eichrom NPS	1				n/a	n/a	n/a	bare				10	H2O or acetone
"Eddie van Deemter"	Eichrom NPS	1				n/a	n/a	n/a	C18 (PMM)	1.6	8/7/2001	ADJ	0.1	67/33 hexane/acetone
JSM-04-13-05	NPS (Stober)	1.05				n/a	n/a	n/a	C18 (PMM)	2.2	4/28/2005	JSM	0.75	acetone
NPS015ODS2	Micra NPS	1.5				n/a	n/a	n/a	C18	1.6	6/8/2005	JSM/DJS	5	67/33 hexane/acetone
101128	Eichrom NPS	1.5				n/a	n/a	n/a	bare				50	H2O or acetone

241

APPENDIX B: SIMION 3D 7.0 MODELING FOR DEVELOPMENT OF

ATMOSPHERIC PRESSURE ION FOCUSING DEVICES

B.1 Modeling Overview

In chapter 6, SimIon 3D 7.0 was referred to as a tool used for the development of "lens" geometries. The geometries contained in this appendix were part of this development process, and were designed for improving ion transmission into the first orifice of a mass spectrometer, when electrospray ionization was used as the ionization technique. Only about a quarter of the modeling efforts undertaken are included here.

It is important to note that SimIon is best suited for modeling the trajectory of ions in a vacuum. Since our goal was to improve ion transmission by affecting the region between the ESI emitter and the first acceptance orifice of the mass spectrometer, we were using SimIon to model a region at atmospheric pressure. For this reason, the ion trajectories modeled were not considered to be relevant. Only the electric field shapes were evaluated, usually in the form of isopotential lines. It was hoped this evaluation would give a relative measure of the "focusing" ability of each lens.

Ions in general will desire to travel downhill in a potential gradient (and perpendicular to isopotential lines), so in our modeling efforts with SimIon we typically paid more attention to the potential surfaces than the flight paths of the ions. For this purpose,

isopotential lines were drawn and the isopotential surface ("PE View") mode was used frequently.

Five lens designs are discussed below. The first three designs are intended to show a progression of the modeling experiments, by which we were able to generate a lens which we felt would be acceptable to machine and test empirically. The third and fourth lenses discussed were machined and tested, and the fourth design is the modeling for the hemispherical lens discussed in Chapter 6. The final SimIon experiment discussed is a design which looks very favorable but was not constructed due to the difficulties associated with construction of such a design.

B.2   Conical Lens (Test Cone 2B)

Shown in Figures B-1 and B-2 is the conical lens, the initial design for atmospheric pressure focusing. The intent of this lens was to make a region near the acceptance orifice of the cone that was more favorable for the entry of ions. This appeared to have been accomplished (note tight isopotential lines near the orifice of the acceptance cone). However, the overall shape of the isopotential lines near the ESI needle was not affected, and it appeared to be fairly favorable for ions to actually impact the conical lens.

B.3   Wide-Mouthed Conical Lens (Test Cone 5)

In the geometry shown in Figures B-3 and B-4, the "mouth" of the lens at the base closest to the acceptance cone was widened, with the intention of allowing the appropriate isopotential lines to reach further out into the space adjacent to the ESI emitter. This geometry was successful in achieving this goal, but the slope of the isopotential lines was fairly gentle, leading to a weak field and poor focusing.

B.4   Inverted Cone (Inverted Test Cone 2B)

While performing testing of Test Cone 2B with the ESI profiler in an orientation shown previously in Figure B-1, we moved the ESI emitter through the bottom of the lens, and saw favorable narrowing of the ESI plume. As a result of this, we decided to turn the lens around and model it in an inverted geometry, with the emitter protruding through the narrow opening of the lens, and the wide opening toward the acceptance orifice. This geometry is modeled in Figures B-5 and B-6. Note the very steep potential surface from the emitter and lens down toward the orifice. It is important to point out that in this particular case the lens was modeled at a voltage of 2800 V while the needle was at 3500 V. We learned later that this would likely not allow for initiation of electrospray, so the lens voltage should be somewhat lower in actuality (~1500 V).

B.5   Inverted Hemispherical Geometry (Test Cone 7)

Modeling for the lens called "Test Cone 7" is shown in Figures B-7 and B-8. This lens was intended to approximate as closely as possible a hemispherical lens. Note that the block size used in the simulation prevents accurate construction of a hemisphere. Nonetheless, with the emitter and lens voltages at 1500 V and 700 V respectively, the isopotential lines show very favorable shaping of the electric field between the emitter and the acceptance orifice. This geometry is the closest model to the extensively discussed hemispherical lens from Chapter 6 (Figure 6-3). The hemispherical lens (in an inverted geometry) was shown experimentally to be capable of compressing the current density in an electrospray plume at atmospheric pressure.

B.6   Inverted Ion Funnel

The "ion funnel" is a method of increasing ion transmission in the first vacuum region of MS instruments which has been heavily studied by Smith's lab at PNNL.[1-6] This ion optic

device works by drawing ions into a downhill DC potential gradient, while also applying alternating AC fields to prevent impact onto the plates of the ion optic. Figures B-9 and B-10 show a model of the "inverted ion funnel" which I loosely based on the idea from Smith's lab. However, this device uses a series of rings that get larger in diameter as they extend from the ESI emitter, and also increase in voltage, as opposed to decrease. In theory, the lower voltage rings near the emitter allow for ESI to be initiated. The voltage on the rings increases gradually to increase the electric field on the ions as they become desolvated and have increased ion mobility. The idea is that the field should be strongest near the orifice, where the ions have the highest mobility. This device was never constructed because we found empirically that the transmission of ions into the first orifice of the MS with nano-ESI was very high without focusing lenses (as discussed in Chapter 6). Therefore, the possibility of a small amount of signal improvement was not worth the large time investment it would have taken to construct such a device.

B.7 References

(1) Shaffer, S. A.; Tang, K.; Anderson, G. A.; Prior, D. C.; Udseth, H. R.; Smith, R. D. *Rapid Comm. Mass Spectrom.* **1997**, *11*, 1813-1817.

(2) Shaffer, S. A.; Prior, D. C.; Anderson, G. A.; Udseth, H. R.; Smith, R. D. *Anal. Chem.* **1998**, *70*, 4111-4119.

(3) Belov, M. E.; Gorshkov, M. V.; Udseth, H. R.; Anderson, G. A.; Tolmachev, A.; Prior, D. C.; Harkewicz, R.; Smith, R. D. *J. Am. Soc. Mass Spectrom.* **2000**, *11*, 19-23.

(4) Kim, T.; Udseth, H. R.; Smith, R. D. *Anal. Chem.* **2000**, *72*, 5014-5019.

(5) Lynn, E. T.; Chung, M.-C.; Han, C.-C. *Rapid Comm. Mass Spectrom.* **2000**, *14*, 2129-2134.

(6) Tolmachev, A.; Kim, T.; Udseth, H. R.; Smith, R. D.; Bailey, T. H.; Futrell, J. H. *Int. J. of Mass Spectrom.* **2000**, *203*, 31-47.
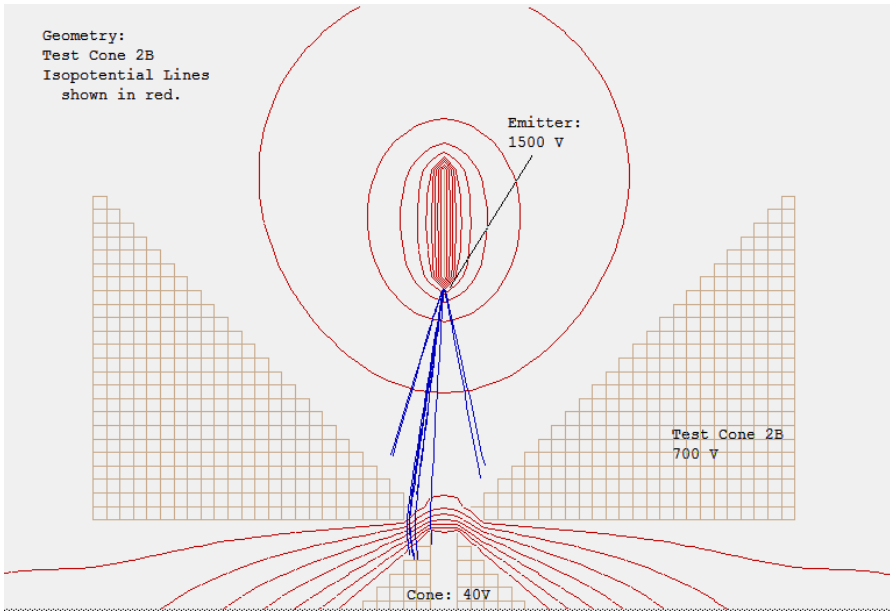
Figure B-1: Initial conical lens geometry, with isopotential lines. Typical emitter, lens (Test Cone 2B) and cone voltage noted. Note that the desired shape of isopotential lines occurs only at the very base of the lens, between the lens and the cone.
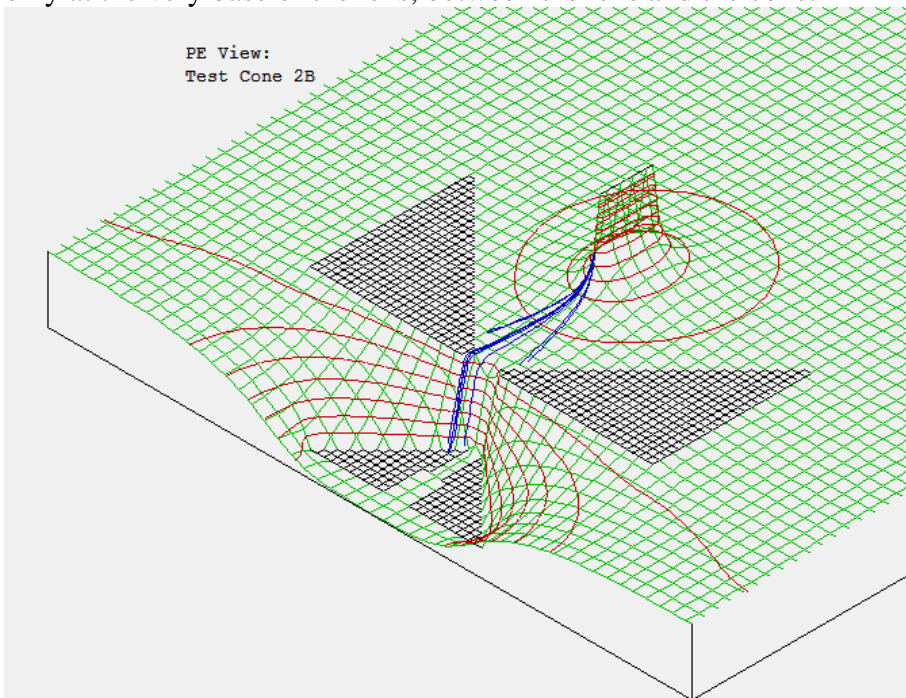
Figure B-2: PE view of Test Cone 2B lens geometry. It is obvious from this view that many ions will impact the lens.
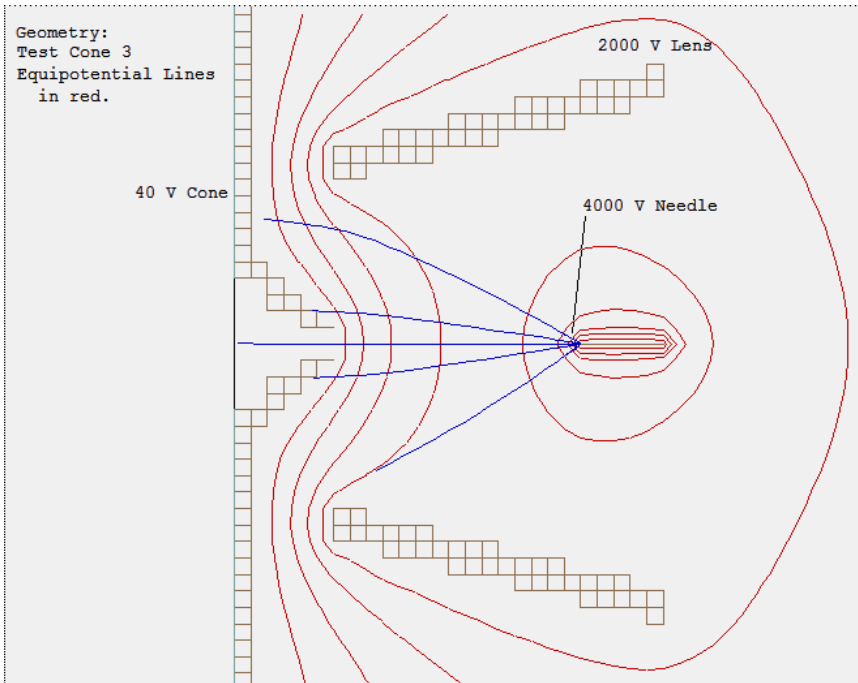
Figure B-3: Wide-mouthed conical lens geometry, with isopotential lines. High-voltage emitter, lens (Test Cone 5) and cone voltage noted. The desired shape of the isopotential lines extends further out from acceptance cone than the previous geometry.
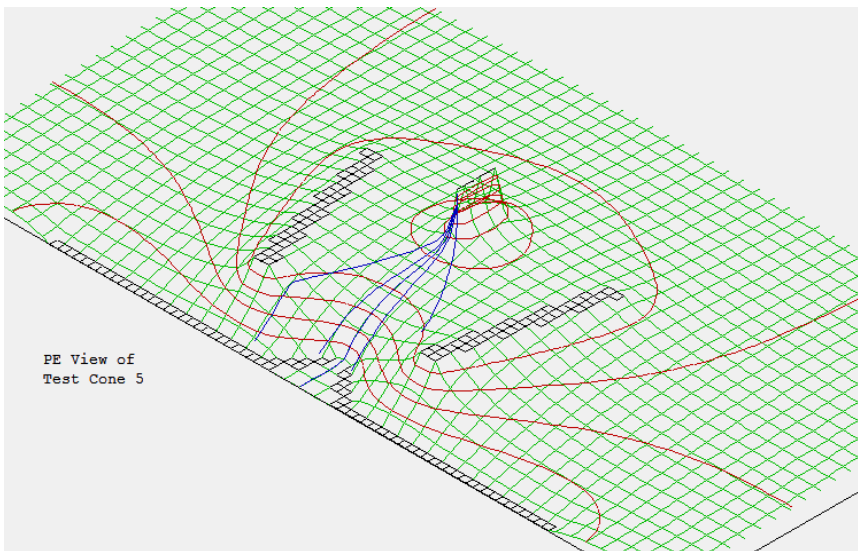
Figure B-4: PE View of Test Cone 5.
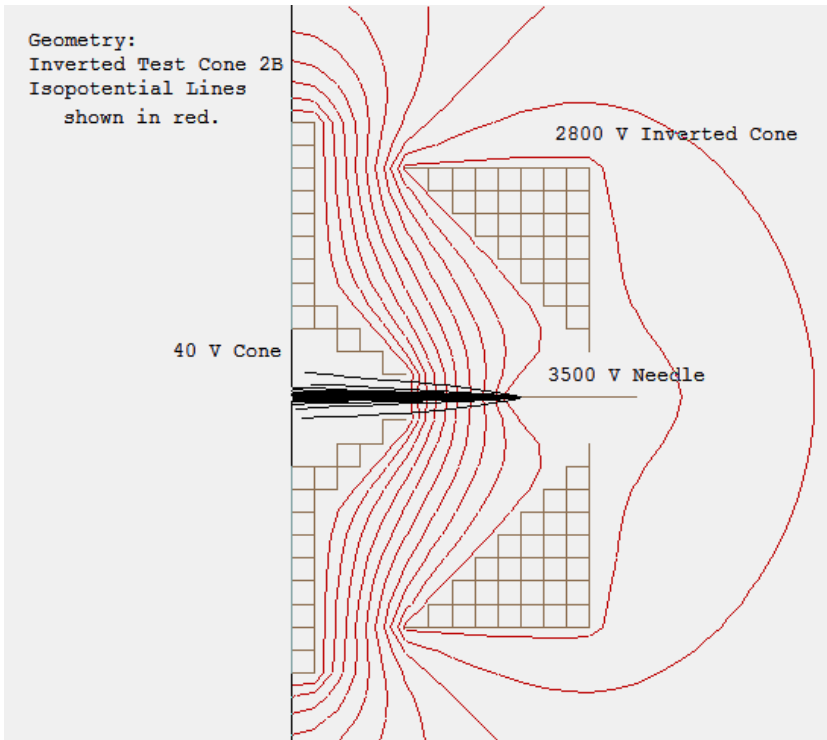
Figure B-5: Inverted version of the lens called "Test Cone 2B", which was shown in the reverse orientation in Figures B-1 and B-2, with isopotential lines. High-voltage emitter, lens, and cone voltage noted. The shape of the field lines is very promising between the emitter and the cone.
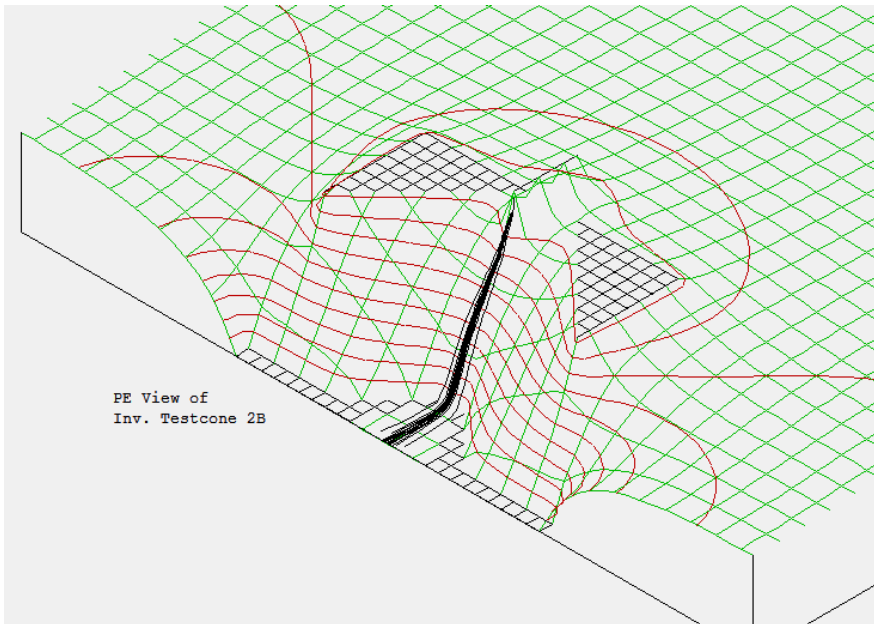
Figure B-6: PE View of Inverted Test Cone 2B. Note steep potential slope between the emitter and the acceptance orifice.
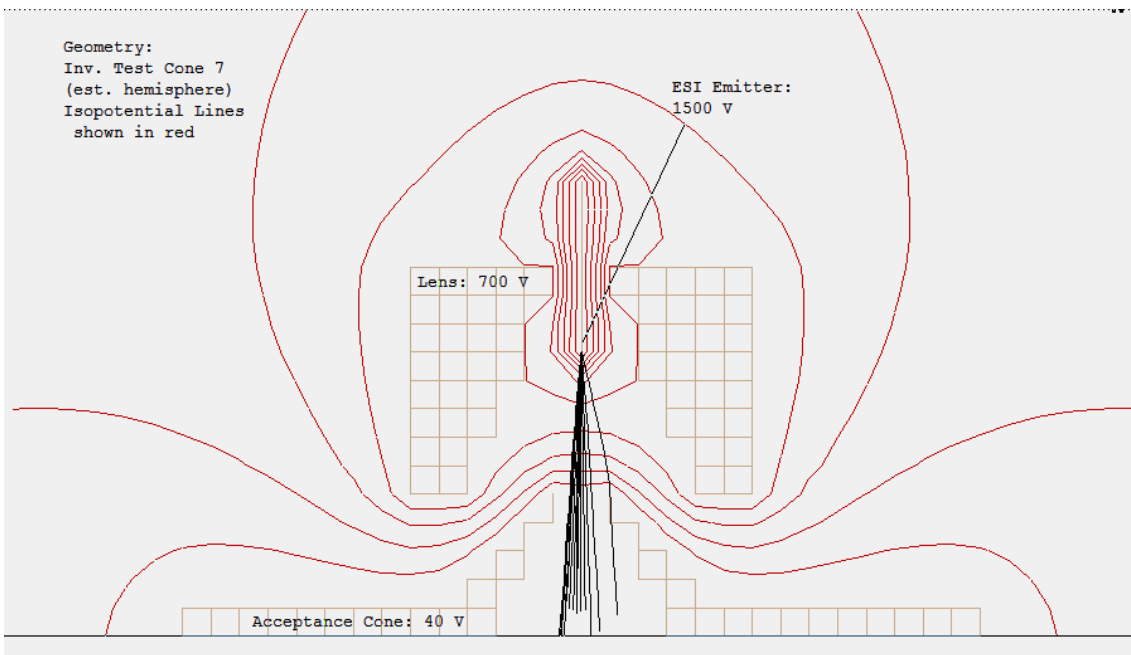
Figure B-7: Inverted Test Cone 7, modeled closely as possible to a hemisphere and as used with the ESI profiler experiments discussed in Chapter 6. Voltages as modeled above were shown experimentally to be effective at focusing ions from an electrospray emission at atmospheric pressure.
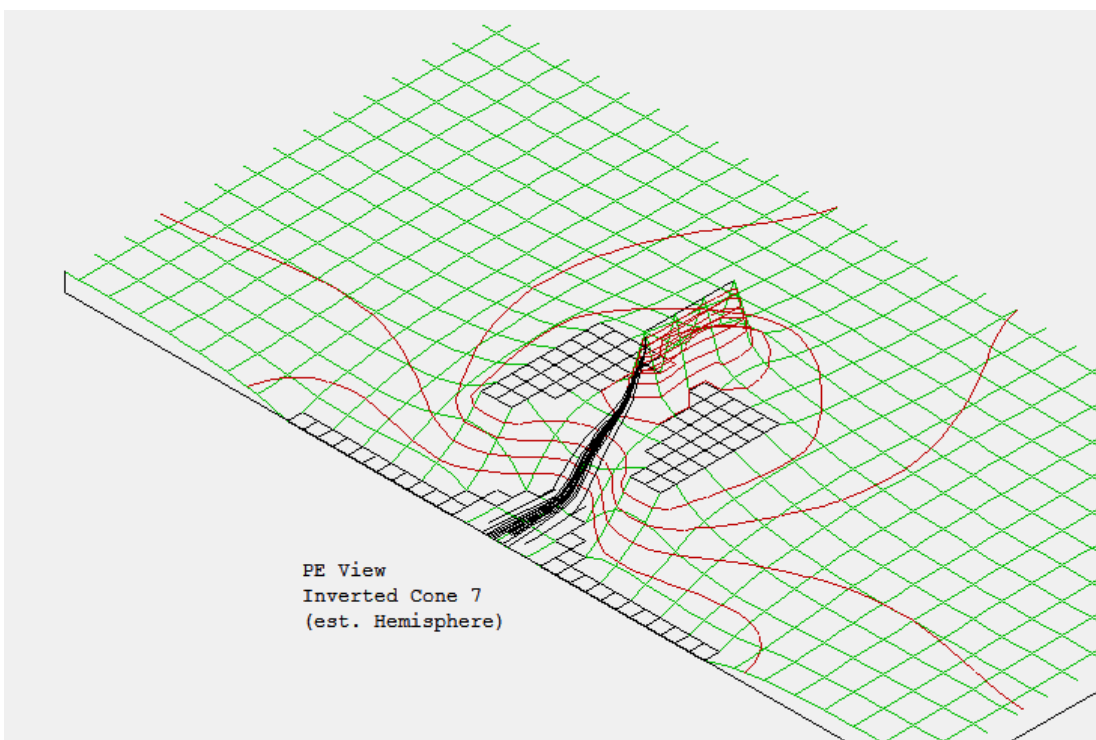

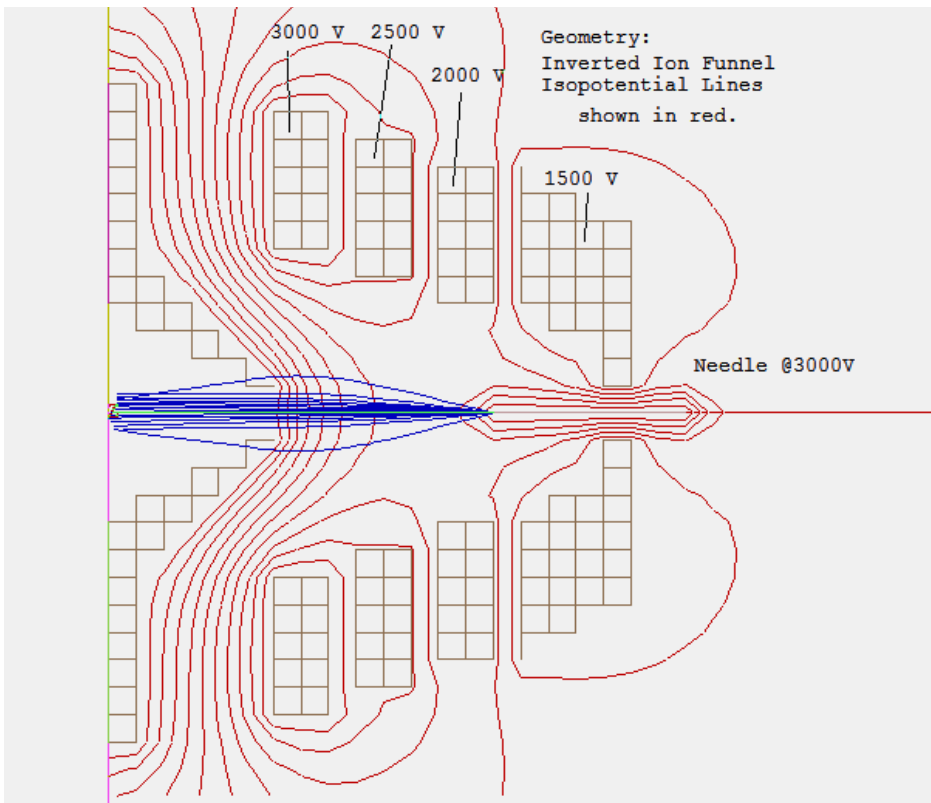Figure B-8: PE View of Inverted Test Cone 7.

Figure B-9: Modeled "Inverted Ion Funnel", modeled loosely after the ion funnel designs from R.D.Smith's lab at PNNL.
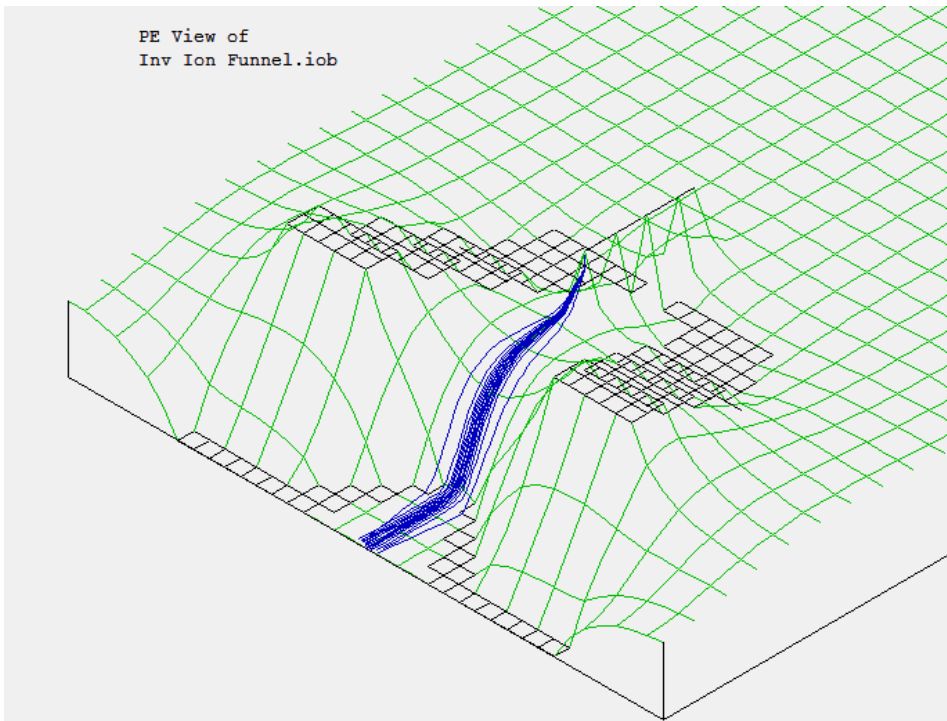

Figure B-10: PE View of modeled "Inverted Ion Funnel".